

Forschungszentrum Karlsruhe
in der Helmholtz-Gemeinschaft

Wissenschaftliche Berichte
FZKA 6720

CBBI-10
Proceedings of the
10th International Workshop
on Ceramic Breeder Blanket
Interactions

Karlsruhe, Germany
October 22 – 24, 2001

L. V. Boccaccini (Hrsg.)

Institut für Kern- und Energietechnik
Programm Kernfusion

Juni 2002

Forschungszentrum Karlsruhe

in der Helmholtz-Gemeinschaft

Wissenschaftliche Berichte

FZKA 6720

CBBI-10

Proceedings of the 10th International Workshop on
Ceramic Breeder Blanket Interactions

Karlsruhe, Germany

October 22-24, 2001

L. V. Boccaccini (Hrsg.)

Institut für Kern- und Energietechnik

Programm Kernfusion

Forschungszentrum Karlsruhe GmbH, Karlsruhe

2002

Als Manuskript gedruckt
Für diesen Bericht behalten wir uns alle Rechte vor
Forschungszentrum Karlsruhe GmbH
Postfach 3640, 76021 Karlsruhe
Mitglied der Hermann von Helmholtz-Gemeinschaft
Deutscher Forschungszentren (HGF)
ISSN 0947-8620

Preface

The Tenth International Workshop on Ceramic Breeder Blanket Interactions was held - under the auspices of the International Energy Agreement for Nuclear Technology of Fusion Reactors (IEA-NFT) and Fusions Materials (IEA-FM) - in Karlsruhe, Germany on October 22-24, 2001 as satellite meeting of the 10th International Conference on Fusion Reactor Materials (14-19 October 2001, in Baden-Baden, Germany). The workshop was attended by 33 participants: Japan (8), Russia(1), Chile(1) and EU(23).

The CBBI-10 has provided a forum of specialists involved in the design, research, development and testing of material and components for lithium ceramic based breeding blankets. The workshop was divided into 4 technical sessions that addressed the general topics of (a) progress in ceramic breeder material development, (b) thermal and mechanical behaviour of pebble beds, (c) irradiation testing, (d) breeder material properties, and a special section dedicated to the question: "Where do we stand in the development of ceramic breeder materials for blanket?". As many as 26 presentations were given and discussed, of which 24 papers have been submitted and published in these Proceedings.

The Meeting was hosted by the Institute of Nuclear and Energy Technologies (IKET) at the Forschungszentrum Karlsruhe (Karlsruhe Research Center).

Programme Advisory Committee

M. Abdou (UCLA), S. Berk (OFES,USA), H. Kawamura (JAERI), S. Malang (FZK), Y. Ohara (JAERI), N. Roux (CEA), J. van der Laan (NRG), M. Yamawachi (Tokyo University)

Local Organizing Committee

L.V. Boccaccini, G. Piazza, J. Reimann (FZK)

Lorenzo Virgilio Boccaccini
Chair, CBBI-10
Forschungszentrum Karlsruhe
Institute of Nuclear and Energy Technologies
P.O. Box 3640
D-76021 Karlsruhe, Germany

Table of Contents

	List of participantsV
	ProgrammeVII
	Session SummaryXI
P1	V. Kovalenko, L. Kiryiak, A. Lopatkin, A. Marachev, Yr. Strebkov, D. Davydov, V. Kapyshev, Yr. Kazennov and V. Tebus: "Breeding Zone Models of DEMO Ceramic Helium Blanket Test Module for Testing in IVV-2M Reactor".1
P2	V. Kovalenko, V. Demidov, A. Zyrianov, V. Kapyshev, L. Menkin, L. Milder, Yr. Strebkov, V. Tebus and V. Tokarev: "Experimental Channel and Gas System of RITM-F Facility for In-Pile Tests".13
P3	J.D. Lulewicz, N. Roux, F. Pourchet and J.P. Joulin: "Status of fabrication of Li_2TiO_3 pebbles by the extrusion-spheronisation-sintering process".21
P4	H. Kleykamp, "Thermal properties of Li_2TiO_3 and phase equilibria in the Li-Ti-O system".	(*)
P5	H. Tanigawa and S. Tanaka, "FT-IR study on hydrogen isotopes in lithium oxide combined with ab-initio analysis of O-H vibration".25
P6	withdrawn	
P7	K. Shimura, K.Yamaguchi, T.Terai and M.Yamawaki, "Cellular Automaton Model for Near-Surface Dynamics for Interaction Between Breeder Materials and Sweep-Gas".29
P8	G. -N. Luo, K. Yamaguchi, T. Terai, and M. Yamawaki: "Study on ceramic breeder and related materials by means of work function measurement under irradiation".35
P9	C. Alvani, P.L. Carconi, St. Casadio, S. Casadio: " Li_2TiO_3 pebbles tritium release mechanism and kinetics by post-irradiation 'Temperature Programmed Desorption' (TPD) spectroscopy".43
P10	C. Alvani, S. Casadio, V. Contini, A. Di Bartolomeo, J.D. Lulewicz and N. Roux: " Li_2TiO_3 pebbles reprocessing, recovery of ^6Li as Li_2CO_3 ".57
P11	G. Dell'Orco, L. Sansone, M. Simoncini and D. Zito: "Progress on pebble experimental activity for the HE-FUS3 mock-ups".67
P12	R.E. Avila, L.A. Peña, L. Padilla-Campos and J.C. Jiménez: "Helium as a temperature moderator in batch irradiation of Li_2TiO_3 pebbles".79
P13	A. Ying, H.L. Huang, M. Abdou: "Numerical Simulation of Ceramic Breeder Pebble Bed Thermal Creep Behavior".85
P14	K. Tsuchiya, M. Uchida, H. Kawamura, S. Casadio and C. Alvani, "Fabrication Tests of Li_2TiO_3 Pebbles by Direct Wet Process".93

P15	J.G. van der Laan, R. Conrad, J.H. Fokkens, H.E. Hofmans, J. Hooijmans, H. Kawamura, J.D. Lulewicz, A.J. Magielsen, S. Malang, M.A.G. Ooijevaar, G. Piazza, B.J. Pijlgroms, N. Roux, M.P. Stijkel and A.Y. Ying: "Key Issues for the 'HICU' Project - A High Fluence Irradiation of Ceramic Breeder Pebble Beds".101
P16	J.G. van der Laan, R. Conrad, J.H. Fokkens, H.E. Hofmans, M. Jong, A.J. Magielsen, S. Malang, B.J. Pijlgroms, J. Reimann, N. Roux and M.P. Stijkel: "Status of the In-Pile Test of HCPB Pebble-Bed Assemblies in the HFR Petten".107
P17	G. Dell'Orco, P. A. Di Maio, M. Simoncini, G. Vella and D. Zito: "TAZZA mock-up pebble beds. Experimental and theoretical investigations".115
P18	M. Nishikawa, S. Beloglazov, N. Nakashima, K. Hashimoto and M. Enoda: "Comparison of inventory of tritium in various ceramic breeder blankets".129
P19	K. Morita, H. Suzuki and K. Soda: "One way diffusion model for the D-H exchange in the ceramics and its potential applications".	(*)
P20	withdrawn	
P21	A.J. Magielsen, R. Conrad, J.H. Fokkens, B.J. Pijlgroms and J.G. van der Laan: "Thermal behaviour and tritium management for in-pile testing of the HCPB pebble bed assemblies in the HFR in Petten".137
P22	J.H. Fokkens: "Thermo-Mechanical Behaviour of Pebble Beds by Finite Element Modelling".143
P23	H. Kawamura and K. Tsuchiya: "Status and Future Plan of Breeding Blanket Development".151
P24	J. Reimann, D. Ericher and G. Wörner: "Influence of pebble bed dimensions and filling factor on mechanical pebble bed properties".161
P25	J. Reimann, J.-D. Lulewicz, N. Roux and G. Wörner: "Thermal creep of metatitanate pebble beds".175
P26	J. Reimann; S. Hermsmeyer and G. Wörner "Thermal conductivity of compressed orthosilicate and metatitanate pebble beds".185
P27	S. Hermsmeyer and J. Reimann: "Particle flow of ceramic breeder pebble beds in bi-axial compression experiments".195
P28	S. Kato, H. Tomimoto, T. Takayama, K. Tsuchiya and H. Kawamura: "Current Status on Li ₂ TiO ₃ Pebble Fabrication by Wet Process".203

(*) Paper not submitted for publication in the Proceedings

List of Participants

Name	Affiliation	E-mail
Avila, Ricardo E.	Comision Chilena de Energia Nuclear	ravila@cchen.cl
Bahm, Werner	FZ Karlsruhe	werner.bahm@pkf.fzk.de
Boccaccini, Lorenzo V.	FZ Karlsruhe	lorenzo.boccaccini@iket.fzk.de
Cardella, Antonino	EFDA, Garching	cardela@post.rzg.mpg.de
Casadio, Sergio	ENEA Casaccia	sergio.casadio@casaccia.enea.it
Dell'Orco, Giovanni	ENEA Brasimone	dellorco@brasimone.enea.it
Di Maio, Pietro	University of Palermo	dimaio@din.din.unipa.it
Fokkens, J.H.	NRG Petten	fokkens@nrg-nl.com
Gasparotto, Maurizio	EFDA, Garching	gasparm@post.rzg.mpg.de
Hermesmeyer, Stephan	FZ Karlsruhe	stephan.hermesmeyer@iket.fzk.de
Kleykamp, Heiko	FZ Karlsruhe	heiko.kleykamp@imf.fzk.de
Kovalenko, Victor	ENTEK, Moscow	koval@entek.ru
Le Marois, Jille	EFDA, Garching	lemarog@post.rzg.mpg.de
Lulewicz, Jean-Daniel	CEA Saclay	jean-daniel.lulewicz@cea.fr
Magielsen, A.L.	NRG Petten	magielsen@nrg-nl.com
Malang, Siegfried	FZ Karlsruhe	malang@iket.fzk.de
Morita, Kenji	Nagoya University	k-morita@mail.nucl.nagoya-u.ac.jp
Nishikawa, Masabumi	Kyushu University	nishikaw@nucl.kyushu-u.ac.jp
Norajitra, Prachai	FZ Karlsruhe	norajitra@imf.fzk.de
Piazza, Giovanni	FZ Karlsruhe	giovanni.piazza@iket.fzk.de
Rabaglino, Elisa	FZ Karlsruhe	elisa.rabaglino@iket.fzk.de
Reimann, Joerg	FZ Karlsruhe	joerg.reimann@iket.fzk.de
Roux, Nicole	CEA, Saclay	nicole.roux@cea.fr
Schulenberg, Thomas	FZ Karlsruhe	thomas.schulenberg@iket.fzk.de
Shimura, Kenichiro	Tokyo University	shimura@tokai.t.u-tokyo.ac.jp
Simoncini, Massimiliano	ENEA Brasimone	msimoncini@brasimone.enea.it
Takayama, T.	Nuclear Fuel Industries, Ltd.	takayama@nfi.co.jp
Tanigawa, Hisashi	University of Tokyo	hisashi@flanker.q.t.u-tokyo.ac.jp
Uchida, Munenori	NGK Insulators, LTD.	uchida@oarai.jaeri.go.jp
Yamada, Hirokazu.	JAERI	yamada@oarai.jaeri.go.jp
Yamawaki, Michio	University of Tokyo	yamawaki@q.t.u-tokyo.ac.jp
van der Laan, Jaap	NRG Petten	vanderlaan@nrg-nl.com
Vella, Giuseppe	University of Palermo	vella@din.din.unipa.it

10th International Workshop on CERAMIC BREEDER BLANKET INTERACTIONS

Programme

Monday, October 22

- 8.30- 9.00 Registration
9.00-9.30 Opening Addresses

1) Progress in Ceramic Breeder Material Development [chairman: N. Roux]

- from 9.30 **P3:** J.D. Lulewicz, N. Roux, F. Pourchet and J.P. Joulin: "Status of fabrication of Li_2TiO_3 pebbles by the extrusion-spheronisation-sintering process".
P23: H. Kawamura and K. Tsuchiya (pres. by M. Uchida): "Status and Future Plan of Breeding Blanket Development".
P28: S. Kato, H. Tomimoto, T. Takayama, K. Tsuchiya and H. Kawamura: "Current Status on Li_2TiO_3 Pebble Fabrication by Wet Process".
P14: K. Tsuchiya, M. Uchida, H. Kawamura, S. Casadio and C. Alvani, "Fabrication Tests of Li_2TiO_3 Pebbles by Direct Wet Process".
to 12.00 **P10:** C. Alvani, S. Casadio, V. Contini, A. Di Bartolomeo, J.D. Lulewicz and N. Roux: " Li_2TiO_3 pebbles reprocessing, recovery of ^6Li as Li_2CO_3 ".

2) Thermal and Mechanical Behaviour of Pebble Beds (Part I) [chairman: J. van der Laan]

- from 14.00 **P25:** J. Reimann, J.-D. Lulewicz, N. Roux and G. Wörner: "Thermal creep of metatitanate pebble beds".
P13: A. Ying, H.L. Huang, M. Abdou (pres. by L.V. Boccaccini): "Numerical Simulation of Ceramic Breeder Pebble Bed Thermal Creep Behavior".
P22: J.H. Fokkens: "Thermo-Mechanical Behaviour of Pebble Beds by Finite Element Modelling".
P24: J. Reimann, D. Ericher and G. Wörner: "Influence of pebble bed dimensions and filling factor on mechanical pebble bed properties".
to 16.30 **P17:** G. Dell'Orco, P. A. Di Maio, M. Simoncini, G. Vella and D. Zito: "TAZZA mock-up pebble beds. Experimental and theoretical investigations".

3) Irradiation Testing (Part I) [chairman: V. Kovalenko]

- from 16.30 **P21:** A.J. Magielsen, R. Conrad, J.H. Fokkens, B.J. Pijlgroms and J.G. van der Laan: "Thermal behaviour and tritium management for in-pile testing of the HCPB pebble bed assemblies in the HFR in Petten".
to 17.30 **P9:** C. Alvani, P.L. Carconi, St. Casadio, S. Casadio: " Li_2TiO_3 pebbles tritium release mechanism and kinetics by post-irradiation 'Temperature Programmed Desorption' (TPD) spectroscopy".

Tuesday, October 23

4) Breeder Material Properties [chairman: M. Yamawaki]

from 9.00 - **P4:** H. Kleykamp, "Thermal properties of Li_2TiO_3 and phase equilibria in the Li-Ti-O system".

P18: M. Nishikawa, S. Beloglazov, N. Nakashima, K. Hashimoto and M. Enoda: "Comparison of inventory of tritium in various ceramic breeder blankets".

P5: H. Tanigawa and S. Tanaka, "FT-IR study on hydrogen isotopes in lithium oxide combined with ab-initio analysis of O-H vibration".

P7: K. Shimura, K. Yamaguchi, T. Terai and M. Yamawaki, "Cellular Automaton Model for Near-Surface Dynamics for Interaction Between Breeder Materials and Sweep-Gas".

P19: K. Morita, H. Suzuki and K. Soda: "One way diffusion model for the D-H exchange in the ceramics and its potential applications".

to 12.00 **P8:** G. -N. Luo, K. Yamaguchi, T. Terai, and M. Yamawaki: "Study on ceramic breeder and related materials by means of work function measurement under irradiation".

5) Irradiation Testing (Part II) [chairman: S. Malang]

from 14.00 **P1:** V. Kovalenko, L. Kiryiaik, A. Lopatkin, A. Marachev, Yr. Strebkov, D. Davydov, V. Kapyshev, Yr. Kazennov and V. Tebus: "Breeding Zone Models of DEMO Ceramic Helium Blanket Test Module for Testing in IVV-2M Reactor".

P2: V. Kovalenko, V. Demidov, A. Zyrianov, V. Kapyshev, L. Menkin, L. Milder, Yr. Strebkov, V. Tebus and V. Tokarev: "Experimental Channel and Gas System of RITM-F Facility for In-Pile Tests".

P16: J.G. van der Laan, R. Conrad, J.H. Fokkens, H.E. Hofmans, M. Jong, A.J. Magielsen, S. Malang, B.J. Pijlgroms, J. Reimann, N. Roux and M.P. Stijkel: "Status of the In-Pile Test of HCPB Pebble-Bed Assemblies in the HFR Petten".

P15: J.G. van der Laan, R. Conrad, J.H. Fokkens, H.E. Hofmans, J. Hooijmans, H. Kawamura, J.D. Lulewicz, A.J. Magielsen, S. Malang, M.A.G. Ooijevaar, G. Piazza, B.J. Pijlgroms, N. Roux, M.P. Stijkel and A.Y. Ying: "Key Issues for the 'HICU' Project - A High Fluence Irradiation of Ceramic Breeder Pebble Beds".

to 17.00 **P12:** R.E. Avila, L.A. Peña, L. Padilla-Campos and J.C. Jiménez: "Helium as a temperature moderator in batch irradiation of Li_2TiO_3 pebbles".

Social event

Wednesday, October 24

6) Thermal and Mechanical Behaviour of Pebble Beds (Part II) [T. Hatano]

from 9.00 **P27:** S. Hermsmeyer and J. Reimann: "Particle flow of ceramic breeder pebble beds in bi-axial compression experiments".

P26: J. Reimann; S. Hermsmeyer and G. Wörner "Thermal conductivity of compressed orthosilicate and metatitanate pebble beds".

to 10.30 **P11:** G. Dell'Orco, L. Sansone, M. Simoncini and D. Zito: "Progress on pebble experimental activity for the HE-FUS3 mock-ups".

7) Summaries of the chairmen

8) Special Session: "Where do we stand in the development of ceramic breeder materials for blanket?"

- Fabrication of breeder materials (M. Uchida, N. Roux)
- Tritium release (M. Nishikawa)
- Impact of irradiation (J. van der Laan)
- Thermal and mechanical behaviour of pebble beds (J. Reimann)
- Compatibility with structural materials (S. Casadio)

12:30 Adjourn

14.00-16.30 Visit to FZK facilities.

CBBI-10 SESSION SUMMARY

Session I: Progress in ceramic breeder material development

[chairman N. Roux]

P3 presented by J. D. Lulewicz

The extrusion-spheronisation-sintering process is developed by CEA and CTI firm. The steps of the process for the production of 1 mm Li_2TiO_3 pebbles were recalled and the characteristics of the pebbles (density, grain size, crush load) as a function of the sintering temperature were reported. Pebbles produced by this process

- 1) fulfil the HCPB requirements
- 2) have excellent purity
- 3) characteristics can be easily adjusted.

Present work to decrease pebbles' diameter 0.7 mm – 1 mm is successfully achieved. Further increase down to 0.5 mm can be expected by adapting the process parameters. Advantages of the smaller diameter pebbles are being checked.

The preliminary evaluation of the production yield was followed by the feasibility study of recycling lithium losses during the steps of the fabrication process. Results are promising.

P23 by H. Kawamura (presented by M. Uchida)

Development of breeding material:

- The survey was made of the methods (melting, rotating, wet process) studied by IAERI for the fabrication of ceramic breeder pebbles, as regard purity, sphericity, cost, mass production.
- Current focus is on the wet process both indirect and direct, the latter being more promising from a reprocessing perspective.

Irradiation test of in-pile mock-up of fusion blanket:

- Results were reported of in-pile mock-ups of Li_2TiO_3 pebble bed in IMTR. ORIENT1 and ORIENT showing that tritium release starts when the outside pebble bed temperature is above 100 °C. The ratio of T_2 released to T_2 generated is about 1 when the outside pebble bed temperature exceeds 300 °C.
- Tritium release under ITER pulsed conditions shows that release rate increases cycle by cycle. After ~ 20 cycles the average tritium release rate is almost constant.
- Breeding blanket design using Li_2TiO_3 pebble bed shows good prospects.

Conclusion:

- A simple, flexible, rather inexpensive process was finalised at semi-industrial scale
- the current production facility at CTI allows to produce 150 kg/y of Li_2TiO_3 pebbles

- no significant difficulty is to be expected for extrapolation of the process to industrial scale

P28 presented by T. Takayama

Fabrication tests were carried out for the fabrication of 30 at% ^6Li enriched Li_2TiO_3 pebbles with 1 mm diameter, using the wet process with dehydration reaction finalised by IAERI and NFI. Characteristics of the pebbles, i. e. diameter, density, grain size, fracture load, impurities, etc., were measured as a function of the fabrication parameters for 0%, 5% and 10 % mol TiO_2 doped Li_2TiO_3 pebbles. Typical characteristics are 1 mm diameter, 80-85 % TD, $< 5 \mu\text{m}$ grain size. Future plan include fabrication of pebbles with various ^6Li enrichments and diameter between 0.3 and 2 mm.

P14 presented by M. Uchida

A parametric study was made of all steps of the direct wet process.

1. 100 % Li_2TiO_3 powder could be dissolved at longer holding times, above 60 °C. Deposit in the solution was decreased by adding citric acid as solvent.
2. Good gel shape was maintained by dropping the Li_2TiO_3 condensed solution in acetone.
3. Adjustment of a solution influenced the cracking rate of the Li_2TiO_3 pebble surface solvent exchange was effective to decrease the crack of Li_2TiO_3 pebble surface and to improve the density of the Li_2TiO_3 pebbles.

Future work will aim at improving density and at controlling pebble shape by adjusting the viscosity of the solutions (target: 80 % of TD, grain size $< 5 \mu\text{m}$).

P10 presented by S. Casadio

- As part of the study of ^6Li reprocessing from Li_2TiO_3 pebbles after service in the blanket, two dissolution methods were investigated to dissolve lithium: 100 % Li dissolution was obtained using HNO_3 attack.
- Precipitating Li_2CO_3 from the nitric solution was investigated. Na_2CO_3 was selected as the best carbonating agent under given pH conditions.
- The pH conditions can be obtained by addition of LiOH , H_2O .
- A further advantage of using LiOH , H_2O is that it allows to adapt the ^6Li enrichment of the solution so as to obtain the target ^6Li enrichment for the Li_2CO_3 powder and of the Li_2TiO_3 pebbles subsequently produced. In addition, a very good homogeneity of the ^6Li distribution is ensured under such conditions.
- First batches of Li_2CO_3 powder were prepared with characteristics close to the specified ones.

Conclusion: the optimisation study of the process was successfully achieved.

Session II: Thermal and mechanical Behaviour of Pebble Beds (Part 1)

[chairman J. van der Laan]

P25 presented by Reimann

Stresses in pebble-beds develop from differential expansion and swelling. Understanding of creep and stress relaxation phenomena is necessary to avoid large deformation and gap formation. Pebble bed creep rate: $\varepsilon_{cr} = A e^{-B/T} \sigma_p t^n$. A large number of experimental data were obtained on a large variety of pebbles (size, grain, surface condition) to determine the fit parameters.

The data trends suggest that the creep strain rate increases with sintering temperature, grain size and density ratio. It is also clear that other factors like geometry, purity, roughness are important. More recent material exhibits slower creep rates.

A specific experiment on stress relaxation at high temperature showed a reduction by a factor 4 within 2 hrs. Presented creep correlations appear sufficient, even for material with higher creep rates.

P13 by A. Ying (presented by L.V. Boccaccini)

Due to the recent events in the US Ying was absent, but the paper was presented by L.V. Boccaccini. The approach is called Discrete Element Modelling. It is not aimed as a full description but serves as a guide in development of ideas on pebble-bed creep.

Coble-creep, grain boundary creep, was considered as the main mechanism in UCT of OSi pebble beds at 740, 800 C. The initial creep rates could be described fairly well, but in the secondary regime they get constant. This arises from too much flattening of the pebbles. E.g. stresses in the pebble drop from 17 to 5 MPa in about 1000 minutes (0.5 MPa in steady state), which quantitatively is significantly different from experimental data.

From the discussion it followed that the DEM approach helps developing real understanding.

P22 presented by J. Fokkens

The main features of pebble-bed behaviour have been implemented in the FEM package MARC to support the design of the Pebble-Bed Assembly irradiation. The implemented model describes all relevant phenomena, i.e. non-linear elasticity, compaction and creep. Application of the model gives reliable results, and can be used for engineering purposes. The model is applied to ceramic breeder beds and beryllium beds for detailed design analyses of the Pebble-Bed Assembly irradiation. Its full use requires large computational effort.

P24 presented by J. Reimann

UCT to determine pebble-bed properties have to be characteristic for typical blanket geometries, i.e. shallow beds. The influence of Height/Diameter ratio has been examined to determine wall friction effects. It is concluded that for 60 mm dia beds, H/D should be < 1 , for pebble size up to 1 mm.

Study of bed packing factors have led to new correlations being proposed for the modulus of deformation.

UCT results for blanket relevant bed geometries and filling system agree with standard UCT if a homogeneous pebble distribution is obtained.

Filling techniques require further development work.

P17 presented by P. Di Maio.

DIN is involved in a collaboration with ENEA and FZK, aiming to theoretically model pebble-bed thermo-mechanical behaviour. The potential use of a quite simple mechanical constitutive model of soil mechanics in theoretical modelling of the Li_2TiO_3 pebble bed mechanical behaviour has been investigated.

The model parameters have been determined on the basis of TAZZA UCT carried out at ENEA, Brasimone on a 100 mm height Li_2TiO_3 pebble bed.

The model seems to work properly but it depends strongly from the adopted friction factor. Model improvements require further TAZZA tests and bi- and tri-axial tests as well.

Session III: Irradiation Testing (Part 1) [chairman V. Kovalenko]**P21 presented by A.J. Magielsen**

In the framework of the Helium Cooled Pebble Blanket Concept of the European Blanket Program, four pebble-bed assemblies are to be irradiated in the HFR in Petten. The objective of these experiments is to study the thermo-mechanical behavior of the lithium ceramic and beryllium pebble beds during irradiation.

The thermo-mechanical behavior of the pebble bed assemblies was calculated in a two-dimensional axi-symmetric model in MARC. In this approach there could not be accounted for the influence of thermocouple tubes on the temperature distribution in the assembly, because these are distributed in the assembly in a non axi-symmetric manner. The solution for this problem was to expand the model to a 3D model used for thermal computations only. Because the pebble bed assembly contains a lithium ceramic breeder bed of 11 mm height and 45 mm diameter, a considerable amount of tritium is generated during irradiation. For safety reasons the tritium production and permeation through the first and second containment must be estimated before the in-pile experimentation begins. In order to do so,

the calculated thermal distribution is used as input for the enhanced two-dimensional finite element model in MARC. Because of the adaptations made by user subroutines in MARC, the 2D model has the capability of performing mass flux calculations.

This paper describes the finite element models used for computation of the temperature distribution and the tritium flux through the pebble bed assembly. The results of these calculations are critical for a safety assessment of the in-pile operation of the experiment and will give a better understanding of the in-pile behavior on temperature and tritium management in advance.

P09 presented by S. Casadio

The interaction of gaseous environments such as air (with moisture and CO₂ impurities) and the purge gas mixture He+H₂ (1000 vpm) (R-gas) with Li₂TiO₃ was examined by TPD/TPR methods. Surface "cleaning" processes were stated and the titanate reduction kinetics to Li₂TiO_{3-x} concerning free and grain boundary surfaces were determined by TPR spectra deconvolution-fitting analysis performed by assuming the reaction rate signal as the overlap of independent first-order steps. Formally near all Ti⁴⁺ on both the grain and grain boundary surfaces around 800 and 950 K respectively was found reduced to Ti³⁺ (i. e. x~1).

Several specimen were shortly irradiated and examined for tritium release by previously annealing them for 1-2 hours at 473 K in flowing R-gas and then by heating at the rate $\beta = 5$ K/min (TBD method). Specimen with density lower than about 82 % TD and nearly full open porosity showed a single broad peak ($T_p = 760 \pm 20$ K) whose first-order deconvolution gave a main contribution of a desorption site-peak characterized by the kinetic rate constant $k = 9.5 \times 10^5 \exp(-1.52 \times 10^4/T)$ [s⁻¹]. Diffusion control was however found to be more compatible with experimental data for these porous materials. Tritium removal from pebbles with density higher than 90 % TD was found to be limited by the above mentioned "reduction" steps, tritium trapped on grain boundaries resulting removable above 900 K where the pebbles reduction occurs.

Session IV: Breeder Material Properties [chairman M. Yamavachi]

P4 presented by H. Kleykamp

Some thermal properties of Li_2TiO_3 and phase equilibria in the Li-Ti-O system were studied. The presence of three intermediate phases, Li_4TiO_4 , Li_2TiO_3 and $\text{Li}_4\text{Ti}_5\text{O}_{12}$ and a high temperature phase, $\text{Li}_2\text{Ti}_3\text{O}_7$ have been introduced. The Li_2TiO_3 phase has two modifications; the low temperature monoclinic Li_2TiO_3 has a homogeneity range between about 49 and 51 at%, while the high temperature cubic Li_2TiO_3 has a very broad homogeneity range. The enthalpy, heat capacity and linear thermal expansion coefficients which were measured by the presenter have been reported. Partial decomposition of Li_2TiO_3 due to reducing atmosphere He-0.1vol.% H_2 was observed at 990 °C after 96 d annealing, where Li_4TiO_4 and LiTiO_2 were formed. The latter LiTiO_2 was also observed in the ceramograph of Li_2TiO_3 pellet irradiated in a reactor.

P18 presented by M. Nishikawa

To understand the tritium behavior in a blanket system packed with sintered pebbles of ceramic breeder material, it is necessary to know the contribution of such tritium transfer steps as

- migration mechanism of bred tritium in grain and
- reaction mechanism on the surface of grain.

At present whole mechanisms of tritium transfer steps are not understood yet.

It may be too early to decide the blanket material in a fusion reactor.

P05 presented by H. Tanigawa

In order to explain multiple peaks observed by FT-IR and clarify the nature of hydrogen isotopes in Li_2O , the vibrational frequency of O-H was calculated with HF and B3LYP methods.

In the case of B3LYP, agreement with experimental data was quite good. The present study affords new approach to analyse infrared absorption spectroscopy of O-H in the ceramic breeder materials.

P07 presented by K. Shimura

In the present work the coarse grained atomic simulation based on the Cellular Automaton (CA) is used to model the dynamics of near-surface interaction between lithium ceramics' surface and sweep gas.

However, CA model is fully discrete in both time and space and the system can be represented by set of microscopic interactions of each cell. In this model, lattice is divided

into 2x2 blocks so called Margolus Block. The cells in each of those blocks can have two states and the transition rules are applied to the whole block at each time step. However, two-dimensional lattice is considered as a layer of the surface sites and the gas phase. The dynamics of adsorption and desorption of H₂ and H₂O at the surface of Li₂O are taken into account as thermally-activated processes through those layers. The model is calculated for various conditions of different partial pressures of H₂ and H₂O. It is seen the results is consistent with the chemical model, which is considered for this model. Although the model is not yet complete to express the transient behaviors, but the result shows a good agreement with DAD model in steady-state condition.

P19 presented by K. Morita

Based on the experimental data on D-H and H-D exchange in oxide ceramics, we have proposed the One Way Diffusion Model for explanation of exp. data: absorption of proton and adsorption of OH⁻ at the surface, diffusion of proton, release of deuteron in the trapping site as H-D molecule to Bulk Molecular Recombination and subsequent trapping of another proton in the vacant trapping site.

Experimental data on T-H exchange has given a clear evidence for the bulk molecular recombination due to release of T-H.

Experimental data on enrichment of H₂ contents in air enclosed with the D-implanted. SrCe_{0.95} Yb_{0.05} O_{3-δ} has also given a clear evidence for room temperature production of H₂ gas as well as the bulk molecular recombination in the oxide ceramics.

A-08

P8 presented by M. Yamawaki

- New devices to apply Kelvin probe for work function measurements have been developed and used in studies of surfaces of ceramic breeder materials, especially under irradiation.
- The WF decreased due to 1 MeV He⁺ or H⁺ irradiation on Ni, which was attributed to desorption of adsorbed species on the surface via electronic energy transfer.
- In the case of low energy ion irradiation (~100 eV), the WF initially decreased due to sputtering of adsorbed atoms, then gradually increased as a result of gradual removal of the oxide layer until reaching saturation. The dominant driving force is ion energy transfer to target atoms via nuclear stopping.
- For oxide ceramics, charge build-up caused difficulty in evaluating true work functions, but the behaviors of measured contact potential gave still useful information on the species at the surface and the status of the specimen. Heating the specimen would enable the work function measurement to give meaningful data on irradiation effects.

Session V: Irradiation Testing (Part 2) [chairman S. Malang]

Two papers (**P1** and **P2**) was presented by **V. Kovalenko** on breeding module testing in the IVV-2M reactor:

- Orthosilicate as pebble beds or as pellets
- Beryllium as pebble bed or as solid ring
- Neon as purge gas

Irradiation ongoing, relevant temperatures and power densities, good idea to decrease breeder pebble bed conductivity by using neon purge gas could help to obtain DEMO-relevant temperatures in ITER in spite of lower flux, more details about the pebble bed models desirable, integrity of orthosilicate pellets remains to be seen.

Two papers on irradiation experiment in HFR Petten was presented by **J. van der Laan**:

P16: Subassembly test

- extensive programme to design, analyse, fabricate and qualify test modules
- improved considerably the understanding of pebble bed behaviour
- will contribute to the selection of breeder material

P15: High fluence irradiation test

- collaboration in IEA-frame
- all candidate breeder materials from JA and EU included
- should help to understand influence of neutron spectrum and mechanical constraints on pebble bed behaviour
- extension of the collaboration into the field of analysing irradiation impact desirable

Finally a paper [**P12**] presented by **R.E. Avila**:

- low temperature irradiation of closed capsules
- influence of capsule atmosphere on tritium release

Session VI: Thermal and mechanical Behaviour of Pebble Beds (Part 2) [chairman G. Vella]

The three papers presented in the last session regard the thermal and mechanical behaviour of pebble beds.

The first work presented by **S. Hermsmeyer [P27]** investigates particle flow process of ceramic breeder beds in bi-axial compression experiments, showing the possible presence of

perfect plasticity effects for high pebble beds and proposing a method of determination of internal friction angle by bi-axial test results alternative to the one based on the tri-axial.

There have been performed numerical calculations, qualitatively reproducing the experiments by the use of Porous Elasticity and Drucker-Prager models.

The second paper **presented by J. Reiman [P26]** showed the experimental results relevant to the thermal conductivity of both compressed orthosilicate and metatitanate pebble beds. Bed deformations up to 4% and maximum temperatures of 800 °C using the hot wire technique has been investigated. A distinct increase of the thermal conductivity with pebble bed deformation was found even if it is quite small and it becomes negligible at high temperatures. A comparison with the Schundler model has been investigated too.

The third work **presented by G. Dell'Orco [P11]** concerns the progress on pebble bed experimental activity for the HE-FUS3 mock-ups. TAZZA and HELICHETTA mock-ups have been presented. The main results of TAZZA confirmed that the filling procedure is fundamental to assure the value and the quality of the Packing Factor and its stability during the reactor operation. The HELICHETTA campaign is still in progress and the data elaboration of the preliminary test results is in progress too. The calculations of the pebble bed thermal conductivity show a good agreement with the FZK ones.

Breeding Zone Models of DEMO Ceramic Helium Cooled Blanket Test Module for Testing in IVV-2M Reactor

V.Kovalenko^a, L.Kiryak^a, A.Lopatkin^a, A.Marachev^a, V.Muratov^a, Yr.Strebkov^a, D.Davydov^b,
V.Kapyshev^b, Yr.Kazennov^b, V.Tebus^b

^a Federal State Unitary Enterprise "Dollezhal Research and Development Institute of Power Engineering", P.O. Box 788, Moscow 101000, Russian Federation

^b Federal State Unitary Enterprise "A.A.Bochvar All-Russia Research Institute of Inorganic Materials", P.O. Box 369, Moscow 123060, Russian Federation

The goal of DEMO Ceramic Helium Cooled Blanket Test Module (CHC BTM) is to demonstrate a breeding capability that would lead to tritium self-sufficiency in ITER reactor and to extract a high-grade heat suitable for electricity generation. Experimental validation of all the adopted design solutions is main important problem at design and calculation works carrying out in order to develop the CHC BTM. One important task for breeding zones feasibility validation is in-pile tests.

Two models were developed and fabricated for testing in the fission IVV-2M reactor. Breeding zone is based on poloidal BIT-conception. The models structural material is ferrito-martensitic steel. Breeder material is lithium orthosilicate in pebble beds and pellet forms. Multiplier material is beryllium in pebble beds and porosity forms. The cooling is provided by helium at 10 MPa. The tritium produced in the breeder material is purged by the helium flow at 0.1-0.2 MPa.

Designs of model description and experimental channel, results of neutronic and thermo-hydraulic calculations are presented in the paper.

1. INTRODUCTION

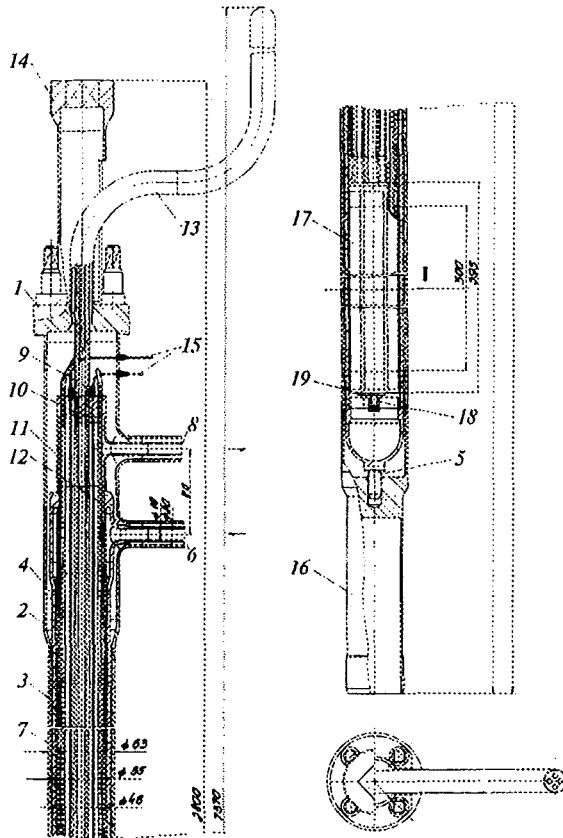
Experimental validation of all adopted design solutions is one of the main problems of design and calculation works carrying out in order to develop the helium-cooled blanket of a demonstration fusion reactor (DEMO) with ceramic breeder. This validation is necessary also for DEMO CHC BTM for testing in ITER. These works include fabrication and technology tests of structural materials, DEMO blanket development, and fabrication. Blanket models are intended for thermal hydraulic tests without irradiation and tests in the neutron field. In this connection the problem of in-pile test facility development for breeding zone models of DEMO blanket has appeared. Taken in account a situation in the RF nuclear industry it was adopted a solution to create the experimental facility on the base IVV-2M of the nuclear reactor in Sverdlovsk Branch of Research and Development Institute of Power Engineering.

Testing objectives on the fission reactor include simulation the neutron irradiation conditions for the design elements of DEMO CHC BTM breeding zone. They can be characterized by the next key parameters: heat power density in materials, breeder and multiplier temperatures and tritium breeding rate in the conditions close to DEMO CHC BTM operation. It is clear these conditions can not be completely simulated in the IVV-2M reactor. The IVV-2M reactor differs by the neutron flux level and spectrum and limited dimensions of experimental loops from a fusion reactor. That is why further loop tests are necessary to solve several design problems. These problems are the following: the combined tests of breeding zone (BZ) elements to demonstrate the material compatibility; tritium extraction modes and extracting gas composition; breeder material burn-up and thermal mechanical behavior of the

design. Tests of BZ models with various design solutions of breeder and multiplier in order to receive the high and reliable tritium breeding will allow to validate preference options of DEMO blanket BZ.

2. DESIGN SCHEME OF THE IVV-2M REACTOR EXPERIMENTAL CHANNEL

The experimental channel (EC) design is shown in figure 1. This channel is intended to test the breeding zone element models (BZEM) of DEMO CHC BTM. It consists of head (1), guard (2) and load-bearing (3) cases. The external diameter of EC in the IVV-2M active core is 63 mm, channel length is 7400 mm. Stainless steel is used as the channel structural material. The vacuum clearance (4) is provided by gap between the guard and load-bearing cases in channel.



1-head, 2-guard case, 3-load-bearing case, 4-vacuum clearance, 5- shank, 6-coolant supply pipeline, 7-separating tube, 8-coolant return pipeline, 9/10-branch-pipe of purge-gas supply/return for breeding element, 11/12-branch-pipe of purge-gas supply/return for multiplying element, 13-guard tube, 14-tip, 15-thermocouple, 16- shank, 17 - BZEM of DEMO blanket, 18 - circle bush, 19 - shank; 1 - active core center of IVV-2m reactor.

Figure 1. Design scheme of IVV-2M reactor experimental channel.

The load-bearing case is centered by shank (5) in the guard case. The guard case is mounted on the bracket flange with the help of a load-bearing rod. The bracket in its turn is fixed on the Control Protection System (CPS) site of the reactor. The channel external wall is cooled by water of the reactor pool.

The load-bearing case is centered by shank (5) in the guard case. The guard case is mounted on the bracket flange with the help of a load-bearing rod. The bracket in its turn is fixed on the Control Protection System (CPS) site of the reactor. The channel external wall is cooled by water of the reactor pool.

Gas cooling contour is U-shaped. Helium coolant is supplied through the pipeline (6) into the cavity between the load-bearing case and separating tube (7). Then it lowers down (flowing around the model external chamber), rotates in the lower collector and flows out into the upper part of the separating tube on the clearance gap between the tube and separating tube (7). The pipelines (6) and (8) have the guard vacuum gaskets.

The supply (9 and 11) and return (10 and 12) purge-gas tubes are welded to the corresponding outlets of the model. These tubes passing from the channel through the head during which are located inside the vacuum guard tube (13).

The head has the tip (14) in the upper part to connect the load-bearing rod and the vacuum guard tube. Four tubes for purge-gas supply and return of breeding and multiplying elements of BZ model for DEMO CHC BTM. The thermocouples leads (15) are located in the middle part of the head.

A guard case of the channel is intended to create a thermal clearance between the channel wall load-bearing case and water in the reactor pool. The guard case is the barrier for gas coolant ingress into the reactor pool in case of wall break of channel load-bearing case. Moreover, the thermal clearance is intended to control the tritium permeation.

The guard case is a tube (63x2.5 mm). The shank (16) is welded to the lower part of the tube and intended to center the EC in the support lattice hole of the reactor core. Three ribs are welded to the upper part of the tube. The EC load-bearing case is installed on these ribs.

The EC load-bearing case is intended to install BZEM (17) inside it and provides the coolant supply to the model. The load-bearing case is a tube (55x3 mm). The shank is located in the lower part of this tube to provide the load-bearing case centering in the guard case. The circle bush (18) centers the BZEM.

One end of the model is welded to the separating tube (46x1 mm). This tube is connected to the load-bearing case. Another end of the model is installed into the circle bush with the help of a shank (19). The leads of BZEM thermocouples and purge-gas tubes are welded to the corresponding tubes that are located inside the separating tube and are leaded out of EC through the upper collector.

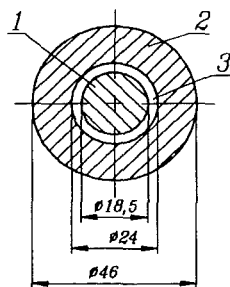
3. BREEDING ZONE ELEMENT MODELS OF DEMO CHC BTM

Basing on the RF DEMO project [1] the Breeder Inside Tube (BIT) concept is adopted as reference option for BZ design of steady-state fusion reactor DEMO-S with ceramic breeder [2]. The following materials have been used in BZEM:

structural material	Cr (12-13.5%), Mo (1.2-1.4%), Nb (0.25-0.55%);
breeder	lithium orthosilicate (Li_4SiO_4),
type	pellet spheres (diameter 11 mm)/pebble-bed (diameter 1-1.5 mm);
multiplier	beryllium (Be),
type	Be porosity (20%)/binary pebbles-bed (diameter 1.5-2.5mm + 0.2-0.3 mm).

Helium with inlet temperature of 350°C and pressure of 8 MPa is used as a coolant. Helium (neon) + 0.1% hydrogen with pressure of 0.15-0.2 MPa is used as a tritium purge-gas.

The BZEM design (Figure 2) is a coaxial assembly of cylindrical elements: a breeding element (1)



1 - breeding element; 2 - multiplying element; 3 - annular

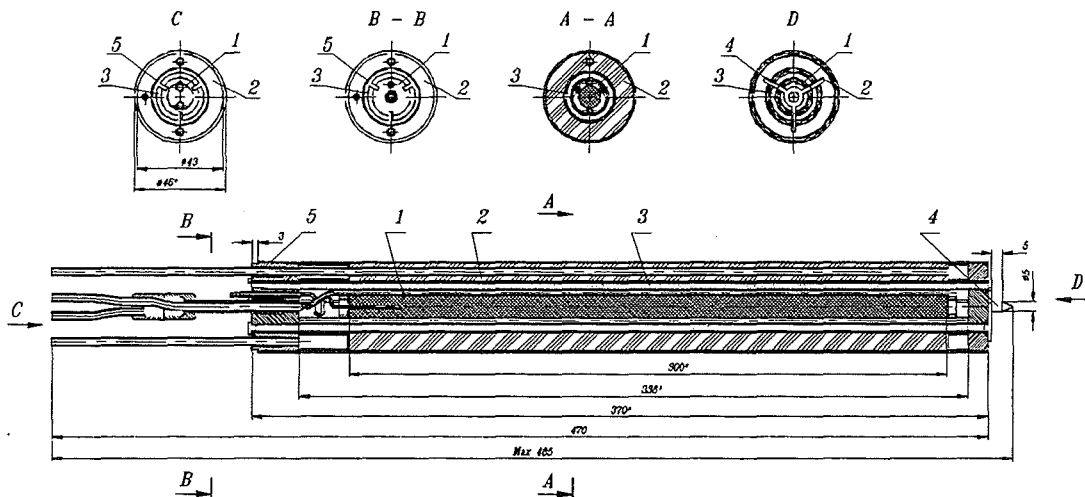
Figure 2. Cross-section of BZEM of DEMO CHC BTM

(18.5 mm in diameter) and a multiplying element (2) (46 mm in diameter) with 24 mm central hole. The annular (3) 2.75 mm - gap is provided by two face distance-providing elements and used for the coolant circulation.

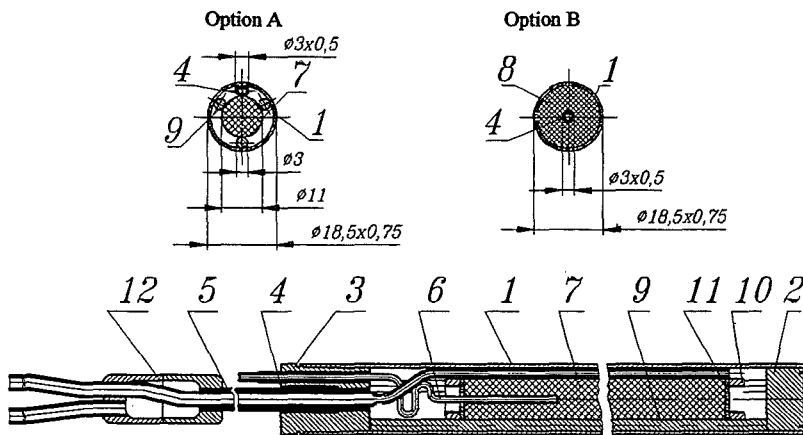
BZEM (Figure 3) is located inside the channel (diameter 55x3 mm) as it is shown in figure 1. The channel guard case is a tube (63x2.5 mm).

The breeding element (Figure 4) is cylindrical 18.5x1 mm tube (1). The plug (2) is welded to one channel face and creates the space for tritium purge-gas supply to the ceramic. The plug (3) with purge-gas supply (4) and return (5) channels and thermocouple (6) are welded to the another channel face. The channel internal space is used for ceramic breeder arrangement. The ceramic breeder is the set of the pellet (7) 11 mm in diameter and 10 mm in height or the pebble-bed (8) of spheres 1-1.5 mm in diameter. The ceramic pellets are placed into the band consisting of three steel rods (9), which are connected with two rings (10). Gauze elements (11) are located between the plugs and lithium ceramic breeder. These elements inhibit ceramic particles ingress into the channels and the purge-gas (12).

The multiplying element (Figure 5) of BZEM is a set of two coaxial cylindrical tubes (1 and 2) of 46x1 mm and 26x1 mm diameter respectively. The annulus between these channels is filled with the multiplier (3) Be (20% porosity) or binary pebble-bed spheres. The circular plug (4) is welded into one face of channels and creates the space for tritium purge-gas supply into the multiplier. The plug (5) with supply (6) and return (7) purge-gas branch-pipes and thermocouple (8) are welded into the another face. The gauze elements (9) are located between the plugs and multiplier. These elements inhibit the multiplier particles ingress into the purge-gas channel.

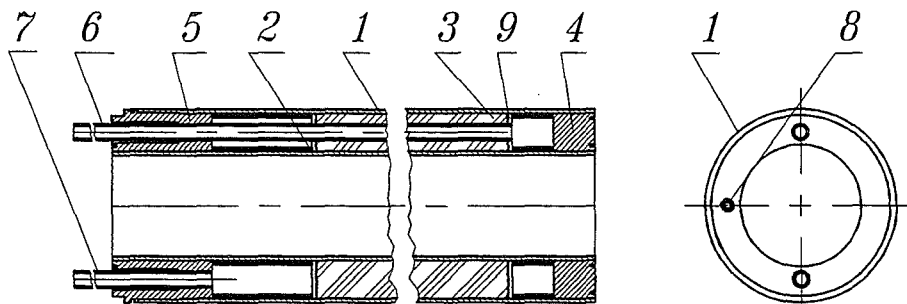


1 - breeding element; 2 - multiplying element; 3 - coolant channel; 4 and 5 - distance-providing elements.
 Figure 3. Model of DEMO CHC BTM breeding zone element.



1 - cylindrical tube; 2 and 3 - plugs; 4 - purge-gas supply channel; 5 - purge-gas return channel; 6 - thermocouple; 7 - Li_4SiO_4 pellets; 8 - Li_4SiO_4 pebble-bed; 9 - steel rod; 10 - ring; 11 - gauze element; 12 - purge-gas channel.
 Breeder option A - pellets 11 mm in diameter and 10 mm in height.
 Breeder option B - pebble-bed spheres 1-1.5 mm in diameter.

Figure 4. Breeding element of BZEM.



1 and 2 - cylindrical tubes (diameter 46 and 26 mm); 3 - beryllium; 4 and 5 - plugs; 6 - purge-gas supply branch-pipe; 7 - purge-gas return branch-pipe; 8 - thermocouple; 9 - gauze element

Figure 5. Multiplying element of BZEM.

4. NEUTRONIC CHARACTERISTICS OF BZEM

The neutronic calculations for the considering BZEM of RF DEMO CHC BTM have been performed with the MCNP (Monte-Carlo transport code [3-6]). A 3-D model of the whole reactor has been developed. This model includes 36 heat producing assemblies (HPA) and beryllium reflector. The layout of HPA and beryllium reflector corresponds to the typical layout of the IVV-2M reactor. The model of the reactor active core (AC) has not controlled rods and the fuel compositions correspond to the fresh fuel burn-up and poisoning. The calculated model of loop channel (LC) containing the BZEM is placed into one of the periphery trap. This trap is formed by six adjacent HPA. All calculation results are normalized to the reactor thermal power of 15 MW.

4.1. Calculation model

The radial layout of LC and BZEM are described in Table 1. The model is presented on figures 6 and 7. The breeding lithium-containing material was divided on the radial 1 mm layers (the first layer is 0.5 mm) in order to account non-uniformity radial distributions of nuclear power density and neutron flux.

Table 1. Calculation model

N°	Name	Material	Mass, g	Vol., cm ³
1	LC guard case	Cr(12-13.5%), Mo(1.2-1.4%), Nb(0.25-0.55%)	1850	240
2	Vacuum clearance gap	Gas		
3	LC load-bearing case	Cr(12-13.5%), Mo(1.2-1.4%), Nb(0.25-0.55%)	1910	245
4	Coolant channel	Gas		
5	Multiplier external cover	Cr(12-13.5%), Mo(1.2-1.4%), Nb(0.25-0.55%)	400	55
6	Multiplier	Be	See tab. 2	See tab. 2
7	Multiplier internal cover	Cr(12-13.5%), Mo(1.2-1.4%), Nb(0.25-0.55%)	220	30
8	Coolant channel	Gas		
9	Breeding element cover	Cr(12-13.5%), Mo(1.2-1.4%), Nb(0.25-0.55%)	180	25
10	Breeder	Li ₄ SiO ₄	See tab. 2	See tab. 2
11	Breeding element plug	Cr (17-19%), Ni (9-11%), Mn (2%)	110	15

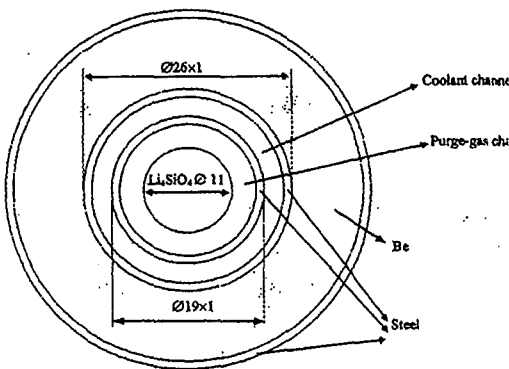


Figure 6. Cross-section of calculation model.

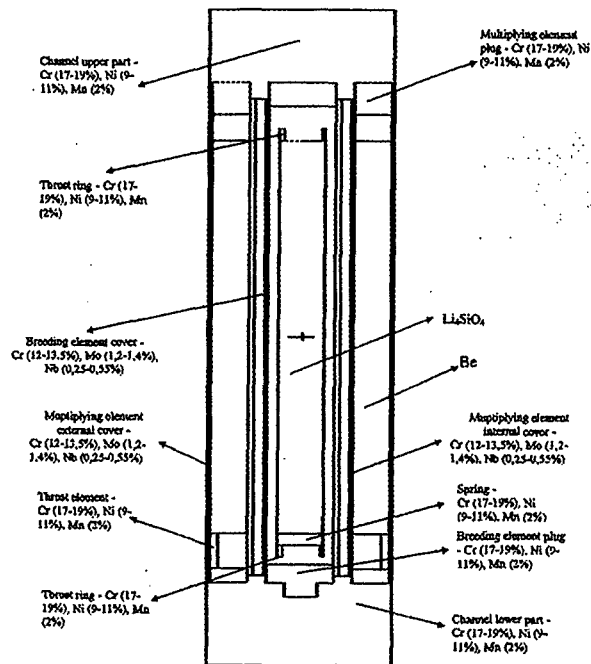


Figure 7. Longitudinal cross-section of calculation model.

Two design options of RF DEMO CHC BTM BZ have been considered:

option 1 – pellet breeding element (Figure 4, option A) and Be multiplier porosity (Figure 5). In this case the part of beryllium and lithium-containing material is 80%;

option 2 - breeding (Figure 4, option B) and multiplier elements of BZEM are made as spheres (diameter 1-1.5 mm) pebble-bed. The part of beryllium and lithium-containing material is 60% by volume.

The radial compositions of multiplying and breeding elements for two options of BZEM are presented in Table 2.

Table 2. Multiplying and breeding zones characteristics of the calculation model

Zone Number	Option 1		Option 2	
	Mass, g	Volume, cm ³	Mass, g	Volume, cm ³
6	428.2	296.8	321.1	296.8
Lithium orthosilicate as breeder				
10 - 1	9.0	4.9	10.6	7.8
10 - 2	15.5	8.5	19.3	14.1
10 - 3	12.0	6.6	16.8	12.3
10 - 4	8.6	4.7	14.2	10.4
10 - 5	5.2	2.8	11.6	8.5
10 - 6	1.7	0.9	9.0	6.6
10 - 7	-	-	6.5	4.7
10 - 8			3.9	2.8
10 - 9			1.3	0.9

4.2. Nuclear power density in the design elements

The table 3 contains the heat power density components calculated in zones of BZEM and averaged over the height of model active part (30 cm) for two model options. The peak values are 10% higher.

Table 3. Heat power density components (W/cm³) in the calculated model zones (option 1/option 2)

Zone number	Neutrons	Photons	Total
5	0.379/0.367	26.6/26.0	27.0/26.4
6	1.36/1.03	3.88/2.84	5.24/3.87
7	0.356/0.344	26.2/25.1	26.6/25.4
10-1	37.8/25.7	5.47/3.79	43.2/29.5
10-2	31.6/22.3	5.49/3.88	37.1/26.2
10-3	27.1/20.0	5.41/3.88	32.5/23.9
10-4	24.9/18.0	5.37/3.78	30.3/21.8
10-5	24.0/15.6	5.38/3.83	29.3/19.4
10-6	22.6/14.4	5.35/3.99	28.0/18.4
10-7	-/14.6	-/3.94	-/18.5
10-8	-/14.7	-/3.85	-/18.5
10-9	-/13.7	-/4.04	-/17.7
11	0.19/0.165	18.4/16.6	18.6/16.8

4.3. Neutron flux density evaluation

Zone averaged neutron fluxes calculated in 4 energy groups for two design option are presented in tables 4 and 5. The maximum values are higher on 10%.

4.4. Gas production rate

Table 6 contains calculation results of gas production rates (hydrogen, tritium, helium) in BZEM. After 500 hours of irradiation 93 Ci (T) and 8x10⁻⁴ Ci (T) and 32 appm He will be accumulated in LCM and Be, respectively, in the first model elements.

Table 4. Neutron flux density in the calculated zones (option 1)

Energy range zone	5	6	7	10-1	10-2
0-1 eV	4.8+13*	5.0+13	4.3+13	3.2+13	2.7+13
1-1000 eV	7.1+13	7.5+13	7.0+13	7.0+13	7.0+13
0.001-0.1	6.0+13	6.4+13	6.1+13	6.4+13	6.4+13
0.1-15.1	1.6+14	1.5+14	1.5+14	1.5+14	1.5+14
Total	3.3+14	3.4+14	3.2+14	3.2+14	3.2+14
Energy range zone	10-3	10-4	10-5	10-6	11
0-1 eV	2.4+13	2.2+13	2.1+13	2.0+13	2.6+13
1-1000 eV	6.9+13	6.9+13	6.6+13	7.0+13	5.1+13
0.001-0.1	6.4+13	6.5+13	6.5+13	6.8+13	4.4+13
0.1-15.1	1.5+14	1.5+14	1.5+14	1.5+14	1.1+14
Total	3.1+14	3.1+14	3.1+14	3.1+14	2.3+14

* 4.8+13=4.8x10¹³

Table 5. Neutron flux density in the calculated zones (option 2)

Energy range zone	5	6	7	10-1	10-2
0-1 eV	4.5+13	4.4+13	3.8+13	2.9+13	2.5+13
1-1000 eV	7.0+13	7.2+13	6.8+13	6.8+13	6.6+13
0.001-0.1	5.9+13	6.2+13	5.8+13	6.3+13	6.3+13
0.1-15.1	1.5+14	1.5+14	1.5+14	1.5+14	1.5+14
Total	3.2+14	3.3+14	3.1+14	3.1+14	3.1+14
Energy range zone	10-3	10-4	10-5	10-6	10-7
0-1 eV	2.4+13	2.1+13	1.8+13	1.7+13	1.7+13
1-1000 eV	6.7+13	6.3+13	6.3+13	6.3+13	6.4+13
0.001-0.1	6.3+13	6.2+13	6.2+13	6.3+13	6.4+13
0.1-15.1	1.5+14	1.5+14	1.5+14	1.5+14	1.5+14
Total	3.1+14	3.0+14	2.9+14	2.9+14	3.0+14
Energy range zone	10-8	10-9	11		
0-1 eV	1.7+13	1.7+13	2.9+13		
1-1000 eV	6.5+13	6.4+13	5.3+13		
0.001-0.1	6.3+13	6.7+13	4.4+13		
0.1-15.1	1.6+14	1.6+14	1.0+14		
Total	3.0+14	3.0+14	2.3+14		

Table 6. Gas production rates (1/cm³.s) option 1/option 2

Zone number	Helium	Tritium	Hydrogen
5	3.9+11/3.6+11	7.4+4/6.647+4	3.6+10/3.5+10
6	1.7+12/1.3+12	3.3+7/3.0+7	
7	3.5+11/3.0+11	2.5+4/1.1+05	3.3+10/3.5+10
10-1	4.8+13/3.3+13	4.8+13/3.2+13	
10-2	4.0+13/2.8+13	4.0+13/2.8+13	
10-3	3.4+13/2.5+13	3.4+13/2.5+13	
10-4	3.2+13/2.3+13	3.2+13/2.3+13	
10-5	3.0+13/2.0+13	3.0+13/2.0+13	
10-6	2.8+13/1.8+13	2.8+13/1.8+13	
10-7	/1.8+13	/1.8+13	
10-8	/1.8+13	/1.8+13	
10-9	/1.7+13	/1.7+13	
11	4.4+9/3.1+9	1.859+4/1.081+4	5.1+10/4.3+10

5. THERMAL HYDRAULIC CHARACTERISTICS

Coolant temperature characteristics and maximum temperatures in BZEM materials are given in this section for two model options.

The design scheme of BZEM (Figure 3) for in-pile testing is a coaxial assembly of cylindrical elements: breeding and multiplying Helium with 350°C inlet temperature and 8 MPa pressure is used as coolant, and helium (neon) with 0.1% hydrogen under pressure of 0.15-0.2 MPa as a purge gas.

5.1. Model design scheme and materials thermal properties

In accordance with the BZEM and LC designs presented in sections 2 and 3 the two calculation schemes (Figures 8 and 9) for thermal hydraulic calculation were developed.

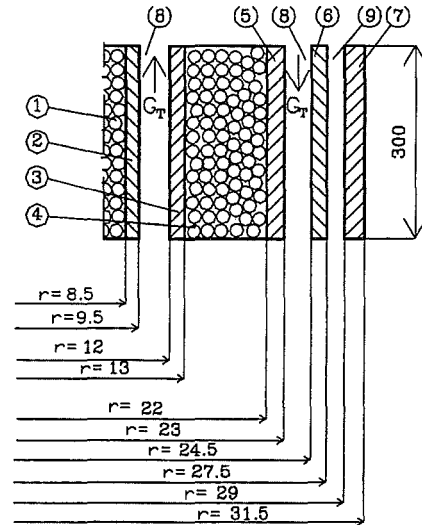
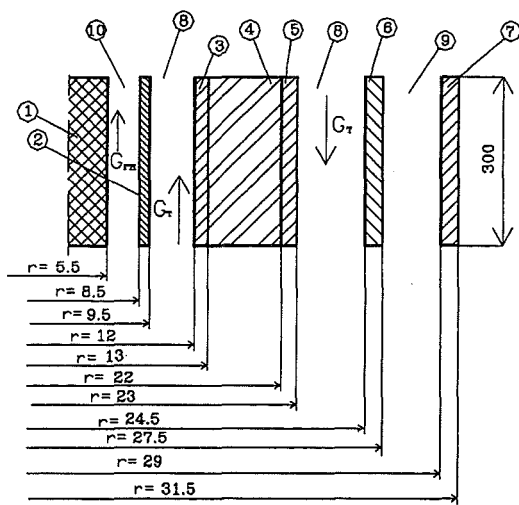


Figure 8. Calculation scheme of EC model with Li_4SiO_4 pellets and porosity beryllium (Option 1)

Fig. 9. Calculation scheme of EC model with Li_4SiO_4 and beryllium spheres pebble-bed (Option 2)

1 - breeder; 2 - breeding element cover; 3 - multiplying element internal cover; 4 - multiplier; 5 - multiplying element external cover; 6 - load-bearing case of LC; 7 - guard case of LC; 8-coolant channel; 9 - vacuum clearance; 10 - purge-gas channel; G_c - coolant (helium under pressure of 8 MPa); G_{pg} - purge-gas (helium + 0.1% hydrogen under pressure of 0.15-0.2 MPa).

The coolant flowing cross-section area between the external cover of multiplying element and the channel load-bearing case is $2.238 \times 10^{-4} \text{ m}^2$, and the flowing cross-section area between the internal cover of multiplying element and breeding element cover is $1.836 \times 10^{-4} \text{ m}^2$ (for 1-st and 2-nd options). The purge-gas area is $1.06 \times 10^{-4} \text{ m}^2$ (option 1 - lithium orthosilicate pellets) and in case of spheres pebble-bed using (option 2) the purge gas flows directly through it.

The average heat conductance factor of 28 W/mxK at temperature of 400°C [7] was used for structural steel elements.

In accordance with [8] the heat conductivity factor of breeder pellets (Li_4SiO_4) is 0.82 W/mxK. The heat conductivity factor for the porosity beryllium varies from 138 to 80 W/mxK at the temperature range of 100-700°C.

The effective thermal conductivity (λ) for spheres pebble-bed (Li_4SiO_4 and Be) is determined in accordance with [9] as:

$$\lambda_{cpb} = 0.708 + 4.51 \times 10^{-4} T + 5.66 \times 10^{-7} T^2 \text{ [W/mxK] for } \text{Li}_4\text{SiO}_4 \text{ pebble-bed,}$$

where T - breeder material temperature [°C].

$$\lambda_{bpb} = 6.2351 + \{353[\alpha_B(T_{Bav} - T_o) - \alpha_w(T_{wav} - T_o) + ((1 + \Delta V/V)^{1/3} - 1)]\} \text{ [W/mxK] for beryl-}$$

lium pebble-bed,

where α_B - thermal expansion factor of Be at T_{Bav} [K^{-1}];

- α_w - thermal expansion factor of wall at T_{wav} [K^{-1}];
- T_{Bav} - pebble-bed average temperature [$^{\circ}C$];
- T_o - temperature of pebble-bed filling (240C);
- T_{wav} - average temperature of element steel cover [$^{\circ}C$];
- $\Delta V/V$ - irradiation-induced volume swelling of beryllium.

An initial state ($\Delta V/V=0$) when the maximum pebble-bed temperatures are expected has been adopted in the present calculations.

Average power densities in the BZEM materials as a result of neutronic calculations are collected in Table 7.

Table 7. The average heat power densities in the model materials (W/cm^3)

Element	Option 1	Option 2
Breeder	27.37	23.40
Breeding element cover	22.93	23.58
Multiplying element internal cover	23.43	23.43
Multiplier	4.418	3.372
Multiplying element external cover	23.71	24.22
Load-bearing case of LC	24.31	24.39
Guard case of LC	26.12	25.93

5.2. Calculation results

The calculations for the Option 1 - model (Li_4SiO_4 pellets and porosity beryllium) have been performed with the code [10] at the following coolant parameters:

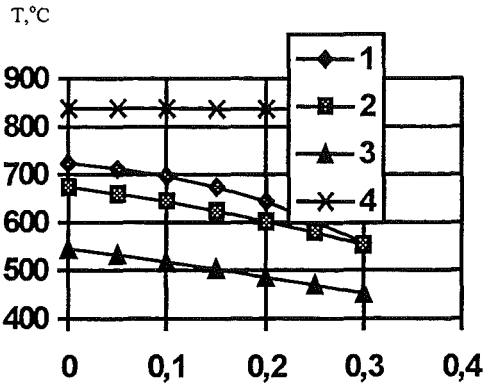
- purge-gas mass flow rate varied from 0.0005 to 0.003 kg/s at the constant coolant mass flow rate – 0.025 kg/s;
- purge-gas mass flow rate– 0.003kg/s and the coolant one varied from 0.005 to 0.065 kg/s;
- zero purge-gas mass flow rate and the coolant one of 0.065 kg/s.

The calculation results for the first option model are presented in table 8 and in figures 10 and 11. It can be seen from table 10 that the maximum breeder temperature under irradiation in IVV-2M reactor (837 $^{\circ}C$) can be reached in case of coolant mass flow rate (MFR) 0.065 kg/s (21 m/s) when the purge-gas MFR through the breeding element is absent. Figures 12 and 13 show the temperature variation in the model (Option 1) in the lower ($Z=0$ m) and upper ($Z=0.3$ m) cross-sections of the Option 1 model for various coolant and purge-gas flow rates.

Table 8. Maximum temperatures in model materials and coolant and purge-gas outlet temperature parameters at the varying mass flow rates (1-st option model)

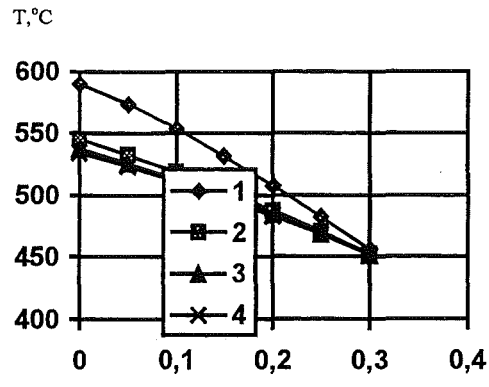
MFR, kg/s	$T_C, ^{\circ}C$	$T_{St}, ^{\circ}C$	$T_{Be}, ^{\circ}C$	$T_{Cl}, ^{\circ}C$	$\Delta T_{Cl}, ^{\circ}C$	$T_{Pg}, ^{\circ}C$	$\Delta T_{Pg}, ^{\circ}C$
$G_{Pg} = 0.0$ kg/s							
$G_{Cl}=0.025$	837	388	376	372	22	-	-
$G_{Pg} = 0.0005$ kg/s							
$G_{Cl}=0.025$	723	434	416	403	53	502	252
$G_{Pg} = 0.001$ kg/s							
$G_{Cl}=0.025$	673	433	416	401	51	434	184
$G_{Pg} = 0.003$ kg/s							
$G_{Cl}=0.005$	590	690	647	558	208	385	135
$G_{Cl}=0.025$	545	433	416	397	47	343	93
$G_{Cl}=0.045$	537	400	388	376	26	337	87
$G_{Cl}=0.065$	593	387	377	368	18	334	84

Note: (here and further in the section): T_C - ceramic maximum temperature; T_{St} - steel maximum temperature; T_{Be} - beryllium maximum temperature; T_{Cl} - coolant maximum temperature; ΔT_{Cl} - coolant heat-up; T_{Pg} - purge-gas maximum temperature; ΔT_{Pg} - purge-gas heat-up.



1 - purge-gas MFR is 0.003 kg/s; 2 - purge-gas MFR is 0.001 kg/s;
3 - purge-gas MFR is 0.0005 kg/s; 4 - purge-gas MFR is 0.000 kg/s

Figure 10. Maximum temperature distribution along the breeding element length (Option 1) at various purge-gas MFR (coolant MFR is constant 0,025 kg/s)



1 - coolant MFR is 0.005 kg/s; 2 - coolant MFR is 0.025 kg/s;
3 - coolant MFR is 0.045 kg/s; 4 - coolant MFR is 0.065 kg/s

Figure 11. Maximum temperature distribution along the breeding element length (Option 1) at various coolant MFR (purge-gas MFR is constant 0,003 kg/s)

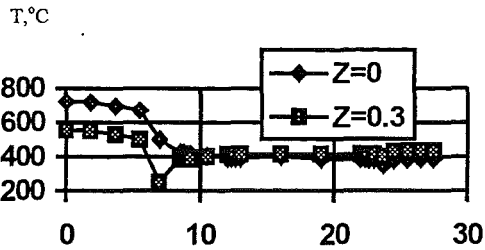


Figure 12. Temperature variations in the model (Option 1) cross-section (purge-gas MFR 0.0005 kg/s, coolant MFR 0.025 kg/s).

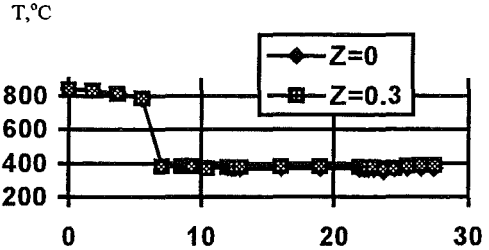


Figure 13. Temperature variations in the model (Option 1) cross-section (purge-gas MFR 0.000 kg/s, coolant MFR of 0.025 kg/s).

Calculation results for the Option 2 model are presented in table 9 and in the figure 14 for coolant MFR in the range 0.02 – 0.08 kg/s. It is seen from figure 14 that the maximum ceramic temperature reaches 820°C at the coolant MFR of 0.02 kg/s. Figure 15 shows the temperature variation in the lower (Z=0 m) and upper (Z=0.3 m) cross-sections of the model (Option 2) at the coolant MFR of 0.02 kg/s. In this case the maximum breeder temperature does not exceed 820°C, the multiplier temperature is lower 450°C at the coolant inlet temperature of 350°C.

Table 9. Maximum temperatures in materials (Option 2) and the outlet coolant temperature parameters for different MFRs

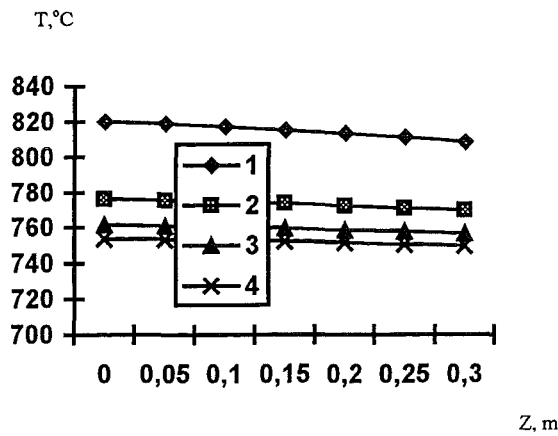
Coolant MFR, kg/s	T_C , °C	T_{St} , °C	T_{Be} , °C	T_{Cl} , °C	ΔT_{Cl} , °C
0.02	820	480	430	428	78
0.04	776	420	391	389	49
0.06	761	398	378	376	26
0.08	776	420	391	389	49

6. FABRICATION TECHNOLOGY.

Technology used for the design element manufacturing includes the breeding (lithium orthosilicate) and multiplying (beryllium) materials fabrication of the required form and properties and models tightness tests. Fabrication technology includes the following sequence steps:

- pellet and pebble fabrication from lithium orthosilicate for breeding elements;
- porous and pebbled beryllium fabrication for the model multiplying element;
- the protective anti-tritium coating deposition on the breeding element casing;

- welding and brazing of the model design elements;
- post-operation quality inspection;
- final inspection and tightness tests.



1 - coolant MFR is 0.02 kg/s; 2 - coolant MFR is 0.04 kg/s;
3 - coolant MFR is 0.06 kg/s; 4 - coolant MFR is 0.08 kg/s
Figure 14. Maximum temperature distribution along the breeding element (Option 2) at various of coolant MFRs.

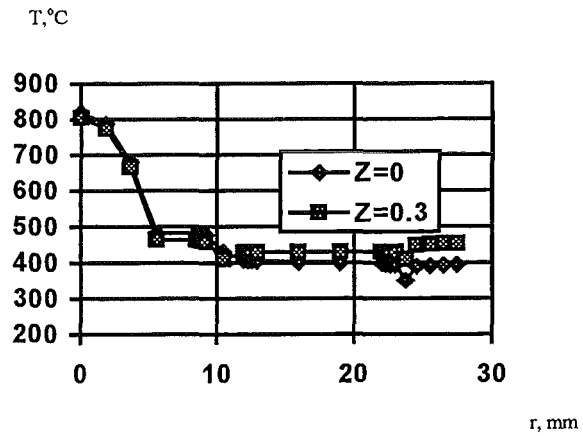


Figure 15. Temperature variation in the model (Option 2) cross-section

The fabrication of lithium orthosilicate is based on its component synthesis: the lithium carbonate of the natural isotope composition and silicon oxide one used as initial materials. The lithium orthosilicate pellets have been fabricated by the extrusion from the press-powder, and their sintering at 800°C. In order to fabricate the orthosilicate pebbles, the disperse powder extrusion is used. The lithium orthosilicate disperse powder is used with the 4% spirit solution of cellulose as the adhesive material.

The porous beryllium has been fabricated by the heat treatment of the pressed powder mixture of metallic beryllium and beryllium hydride. In order to fabricate the pebbled beryllium, the pelletizing method of milled beryllium groats was used.

The aluminizing has been used for the protective coating deposition in order to reduce the tritium leakage and coolant contamination. The aluminizing has been performed in the tight container.

Brazing by Cu-Ni-Mn-solder and automatic argon-arc welding were used for the fabrication of the model design elements preparation.

The RAP device has been used for quality inspection. Measurements of a possible leakage in the breeding zone models have been performed with a special device. A warmed autoclave and filter for the beryllium dust have been developed especially for these measurements.

7. CONCLUSION

In 1997 the design documentation was prepared and the two breeding zone models with ceramic breeder were fabricated. The first in-pile tests of pebble-bed breeding zone model have been performed on the RITM-F facility since March 1999. Irradiated materials examination was started at the end of 2000. The in-pile testing of breeding zone model with the porous beryllium and lithium orthosilicate pellets are performing from the end of 2000 up to the present time.

REFERENCES

- [1] RF DEMO Project. Concept fundamentals of a demonstration fusion reactor, part 2.
- [2] Ceramic helium cooled blanket design concept of RF DEMO fusion reactor and its neutron-physical characteristics, RDIPE report, 31.198 Re.

- [3] MCNP-4A, Manual, LA-12625M.
- [4] ENDF-6: IAEA-NDS-76 Rev.4.
- [5] R.E.MacFarlane, New thermal neutron scattering files for ENDF/B-VI release 2, La-12639-MS, 1994.
- [6] R.E. MacFarlane and D.W. Muir, The NJOY nuclear data processing system, Version 91, LA-12740-M (October 1994).
- [7] M. Solonin et al., Problems of blanket materials in the Russian fusion reactor concept, paper, October conference in Japan, 1997.
- [8] Design Description Document. RF Ceramic Helium Cooled Test Blanket Module, version 2, 07.21.1997.
- [9] Design Description Document. European Helium Cooled Pebble Bed Test Blanket, status:1.12.1996.
- [10] A program description "Calculation of non-steady temperature fields in a multilayer finite-length cylinder", RDIPE.

Experimental Channel and Gas System of RITM-F Facility for In-Pile Tests

V.Kovalenko^a, V.Demidov^b, A.Zyrianov^c, V.Kapyshev^b, L.Menkin^c, L.Milder^c, Yr.Strebkov^a, V.Tebus^b,
V.Tokarev^c

^a Federal State Unitary Enterprise “Dollezhal Research and Development Institute of Power Engineering”, P.O. Box 788, Moscow 101000, Russian Federation

^b Federal State Unitary Enterprise “A.A.Bochvar All-Russia Research Institute of Inorganic Materials”, P.O. Box 369, Moscow 123060, Russian Federation

^c Sverdlovsk Branch of Research and Development Institute of Power Engineering, P.O. Box 29, Zarechniy 624051, Sverdlovsk prov., Russian Federation

For validation breeding zones feasibility of DEMO, ITER and the next generations of fusion reactors we constructed and built the RITM-F (Functional in-Reactor Investigations of Tritium-breeding Models) facility, based on the IVV-2M nuclear reactor. Parameters of the reactor are presented. The test program will be distinguished as functional tests.

Experimental channel and gas system is main units of the RITM-F facility. Main characteristics of RITM-F facility: models irradiation environment - Helium-Neon mixture, pressure - 0.04 MPa; minimum pressure in channel cavity - 10^{-2} mm of Mercury column; tritium purge-gas - Neon + 1% Hydrogen, pressure - 0.1-0.2 MPa, flow rate - 0.1-10 cm³/s; purge-gas channel temperature - 490°K; examination time of channel parameters monitoring - 2-10 s; registration time - 60, 600, 3600 s.

1. INTRODUCTION

Experimental validation of all design solutions is one of the main problems of the DEMO ceramic helium cooled blanket and it's experimental module for testing in ITER. It includes a choice of a manufacturing technology and structural materials tests, as well as out-of-pile and in-pile tests of blanket various units models. In this connection a need in a special in-pile test facility for tritium-breeding blanket models tests. The RITM-F facility was built in the beginning of 1999 year on the base of the IVV-2M reactor.

The test problem on fission reactor enters reproduction of key parameters (for example, heat power densities, breeder and multiplier materials temperature and tritium breeding rate) in neutron irradiation conditions. It is known that they can not be completely realized in IVV-2M reactor, which differs from a fusion reactor by the neutron flux level and spectrum and due to limited sizes of an experimental channel and loops. Therefore forthcoming loop tests are directed mainly on the separate engineering questions decision necessary for validation of blanket breeding zone ability to operation.

2. BRIEF DESCRIPTION OF IVV-2M REACTOR

IVV-2M (Figure 1) is a research pool-type water-cooled nuclear reactor. It operates in a cyclic regime: 300 hours at a permanent power and a short-term (2 days) to discharge cooling period. The reactor stops twice a year for one-week to preventive maintenance (PM). The main characteristics are listed in table 1.

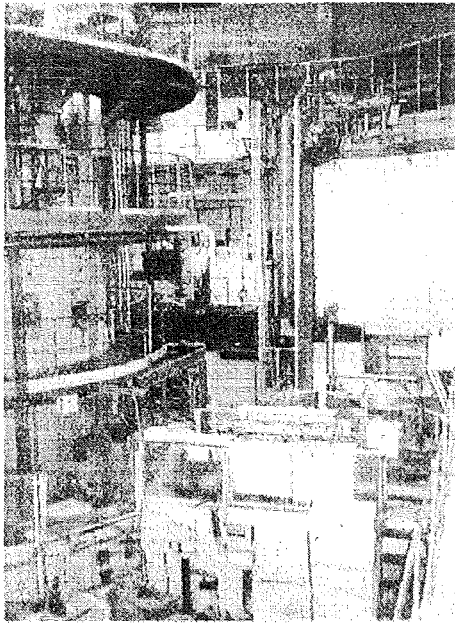


Figure 1. IVV-2M reactor

up to 20 MW. A core height is 50 cm. HGA and moderator blocks are installed in a triangular lattice with 64 mm spacing and minimum allowable clearance. HGA contains 5 tubular heat-generating elements with a hexagonal profile. The fuel is a dispersion type mixture from uranium dioxide in an aluminum matrix. The uranium-235 (enrichment 90 %) nominal load in HGA is 225 g. In the HGA center a water cavity 30 mm in diameter is located for control rods of the reactor control protection system (CPS).

There are cavities in the reactor core: a central one 120 mm diameter, six peripheral cavities 64 mm in diameter, and twenty central cavities in HGA 29 mm in diameter. The reactor is equipped with 8 horizontal channels and two vertical experimental channels (diameters 160 and 210 mm) to transport neutron beams. If desired, water cavities up to 250 mm in diameter can be arranged in the core and the reflector to locate experimental devices.

3. RITM-F FACILITY

RITM-F facility is intended to realize functional reactor investigations of tritium-produced models of fusion reactor blankets in the IVV-2M, in conditions of continuous tritium extraction from a breeder material. The existing set of experimental reactor facilities on the IVV-2M reactor is the basis for RITM-F facility creating. The main technical characteristics of RITM-F facility are listed in table 2.

The main systems and elements are the following:

- experimental channel device (ECD);
- gas system (GS);
- model cooling system (MCS);

Table 1. IVV-2V technical characteristics

Fuel	Uranium dioxide in an aluminum matrix
Reflector	Beryllium and graphite
Coolant	Chemically demineralized water
Thermal power, MW	15
Maximal density of neutron flux, $\text{cm}^{-2}\text{s}^{-1}$	
fast ($E > 0.1 \text{ MeV}$)	2×10^{14}
thermal	5×10^{14}

The core (Fig. 2) is composed from identical heat generating assemblies (HGA) and moderator-reflector blocks (beryllium, graphite). Uniformity and interchangeability of HGA permits to create various configurations of the core, to change section quantity, their sizes and accommodation on a support lattice. One of the possible core configurations consist of 36 up to 58 HGAs with neutronic "traps" of the required sizes. The reactor thermal power can be varied from 10 MW

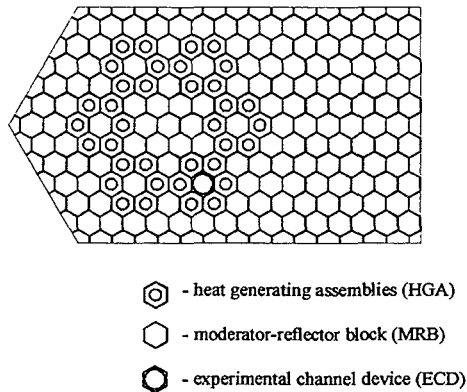


Figure 2. IVV-2M core cartogram

- control and monitoring system (CMS);
- experimental data processing system (EDPS).

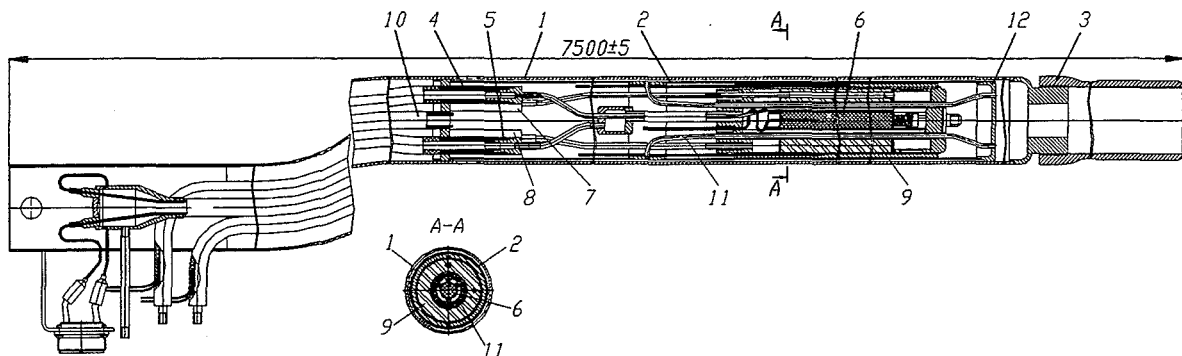
Table 2. Technical characteristics of RITM-F facility

Irradiation process fluid of models pressure	He-Ne mixer 0.04 MPa
Pressure in the vacuum ECD cavities	1.33 Pa
Tritium purge gas pressure flow rate	Ne+1%H ₂ 0.1 – 0.2 MPa 0.1 - 10 cm ³ /s
Polling periodicity of parameters monitoring channels	2 -10 s
Periodicity of sensors readings recording	60, 600, 3600 s
Sensors types	Chromel-alumel graduation
Heating-up channel temperature	490 K

4. EXPERIMENTAL CHANNEL DEVICE (ECD)

The ECD is intended to model irradiation. Helium and tritium release from candidate materials are determined during the reactor tests at a given heat power density and temperature levels.

ECD (figure 3) includes a channel and irradiation device - a capsule with a breeding zone element model (BZEM) of a test module for helium-cooled DEMO blanket with ceramic breeder. The technical characteristics of ECD and capsule are presented in table 3.



1 - case, 2 - capsule, 3 - tailer, 4 - purge gas inlet heated pipeline of model breeder element, 5 - purge gas outlet heated pipeline of model breeder element, 6 - model breeder element, 7 - purge gas inlet non-heated pipeline of model multiplying element, 8 - purge gas outlet non-heated pipeline of model multiplying element, 9 - model multiplying element, 10 - gas mixer inlet pipeline in a heater-regulation cavity, 11 - tubular type cooled radiator, 12 - capsule bottom.

Figure 3. Experimental channel device

The channel consists of case (1) and capsule (2) that includes inlet and outlet tritium purge gas and tailer (3). The two heated inlet (4) and outlet (5) purge-gas pipelines in the model breeder element (6), two non-heated inlet (7) and outlet (8) purge-gas pipelines in the model multiplier element (9) and gas mixture inlet pipeline (10) are located in the channel cavity above the capsule. The gas pipes system providing the gas supply in the capsule, to model breeder and multiplier elements and gas return are connected to the RITM-F facility gas system and tritium extraction system.

A design of the channel case provides a cooling of capsule external surface, model breeding and multiplying elements by reactor water. The water inlet is organized through the holes in the case wall above the capsule top. The required coolant mass flow rate is provided through the hole area in the channel tailer. The channel casing has the bending that displaces the channel axis on 60 mm for the shielding from neutron "shooting". The channel casing is fabricated from tube diameter 60x1.5 mm; the tube material is steel (Cr - 18%, Ni - 10%, Mn - 2%, Ti - 0.08%). The channel tailer is fabricated from aluminum alloy.

Table 3. Technical characteristics of ECD and the capsule

Length, m	
experimental channel	7.5
capsule	0.485
model active part	0.3
Diameter, mm	
experimental channel	60
capsule	54
breeding element	19
multiplying element (external/internal)	46/24
Gaseous medium in the capsule	He-Ne-mixture
pressure, MPa	0.1
Tritium purge gas	Ne+(0-3.0)% hydrogen
pressure, MPa	0.10-0.15
Gas paths number	5
heated paths	2
heated paths temperature, °C	120
Nuclear power, kW	
channel part in the core	11.8
capsule	8.0
Radiator type	tubular
tubes number	16
radiator tube size, mm	Diameter 3x0.5
Coolant	water
flow rate, m ³ /s (l/h)	
in the channel	2.1x10 ⁻⁴ (750)
in the radiator	1.5x10 ⁻⁴ (540)
Maximum temperature, °C	
breeder	900
multiplier	500
model gaskets	350

The capsule is intended to arrange the test module BZEM for helium-cooled DEMO blanket with ceramic breeder (DEMO HCBCB) and to create the necessary temperature conditions in model breeding and multiplying elements. The capsule consists of a model, radiator, casing, bottom, tube plate, gas pipeline, two heated and two non-heated pipelines and pipeline to supply the technological gas in thermal regulating cavity. The design elements of capsule casing are fabricated from steel (Cr - 18%, Ni - 10%, Mn - 2%, Ti - 0.08%).

The tubular-type radiator (11) is located in an annulus between the model breeding and multiplying elements. The radiator is fabricated from 16 tubes diameter 3x0.5 mm that are flattened to 2 mm. These tubes are concentric in the breeding and multiplying element gaskets. The coolant inlet in the radiator is carrying out through the tubes cutted in the cylindrical tube plate. The tube plate is a part of the capsule casing. Pipeline lower parts are cutted in the capsule bottom (12). Monitoring of the radiator temperature is performed with two thermocouples.

Six thermocouples are arranged in the capsule internal cavity:

- one in the breeding element center;
- one on the breeding element external surface;
- one on the multiplying element internal surface;
- one in the multiplying element center;
- two on the multiplying element external surface (diametrically opposite)

The lead of thermocouples compensation wires is performed in the upper part of channel casing through the connector.

The purge gas supply and return from breeding element is performed along the heated paths. The paths are tubes (diameter 6x1 mm) and their heating is carrying out with the direct electrical current. The electrical current is feeded through a bus in the middle of each pipeline. Thermal and electrical insulation of path pipelines is performed from glass-ribbon (5 mm in thick). The pipelines edges built in the capsule casing cover are insulated with the mixture of aluminum dioxide and liquid glass. In order to eliminate current flows the channel casing is connected with to stainless steel plate the copper cable ("zero" cable). This plate is welded to the pipelines in places of path connections with auxiliary facilities equipment for experimental device. The path pipelines are fabricated from stainless steel (Cr - 18%, Ni - 10%, Mn - 2%, Ti - 0.08%). The thermocouples are arranged in the heated path pipelines to control technological gas supply/return to breeding element. The thermocouple junctions are located on the pipelines external surfaces under the thermal insulation layer. The thermocouples are arranged on the pipeline outlet from the channel casing. The lead of thermocouples compensation wires is carrying out through the connector that is intended also for lead of thermocouples compensation wires of capsule.

The ECD fastening in the core is executed by the tailer in the core support lattice and arm by M14x1 bolts to a CPS platform. The loading of the ECD on a regular place for realization of research work is executed by personnel with the help of crane.

5. GAS SYSTEM

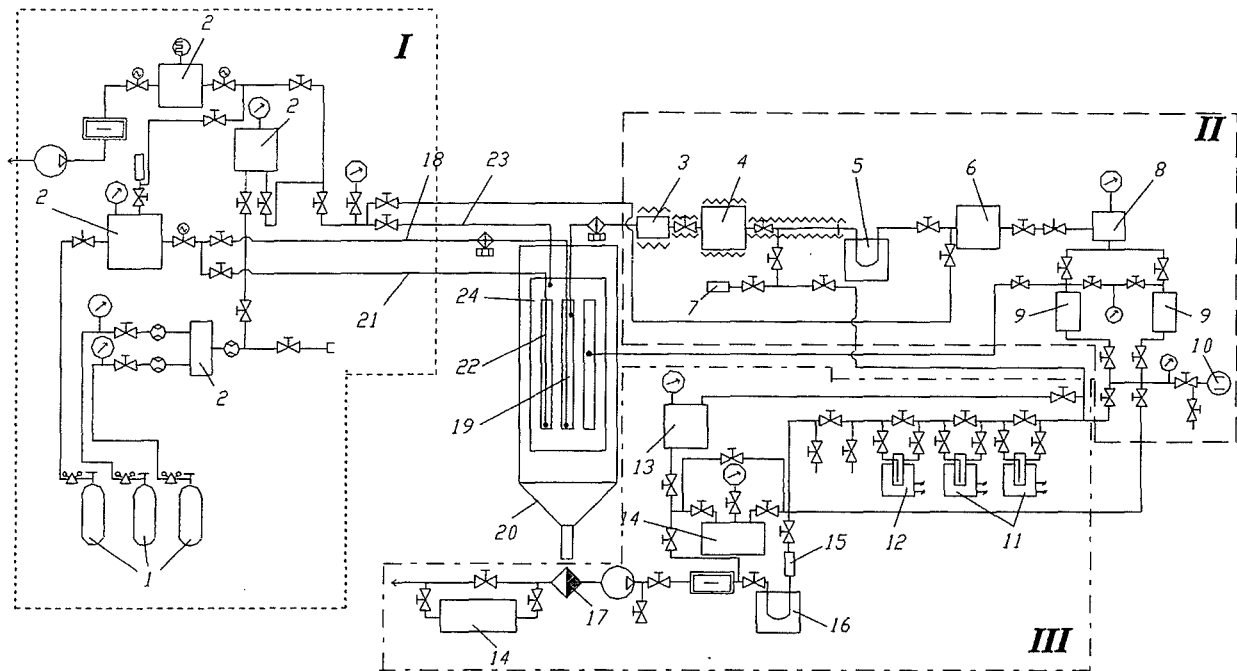
The RITM-F facility gas system should provide permanent circulation of the purge gas of required parameters through the model breeding element to the capsule thermal regulating cavity and monitor extracting gases.

The gas system of RITM-F facility (figure 4) consists of three main parts:

- preparation and bleeding gas section (I). This section consists of gas bottles (1), tanks to create the gas mixtures of the required composition (2), valves and monitoring devices;
- measurement section (II). This section consists of a filter (3), a heated ionization chamber (4), a nitrogen trap (5), a ionization chamber (6), a device for gas sampling (7), a gas collector (8), tanks for tritium purge-gas purification (9), a ionization chamber for tritium measurement (10), valves and pressure monitoring devices;
- section for gas purification from impurities and tritium (III), that consists of titanium apparatus for purge-gas purification from nitrogen and oxygen (11), titanium trap for tritium sorption (12), tank for gas circulation (13), devices to monitor the tritium content (RGB-03) (14), copper catalyst (15), nitrogen trap (16), filter (17), circulation pumps and valves.

In section I (gas preparation and bleeding in model and thermal regulating cavity) the gas flows from bottles (1) to the tanks (2) where the gas mixture is prepared. Then the purge-gas flows through the pipeline (18) to the model breeding element (19). The model is arranged in ECD (20). The pipeline (21) provides the purge-gas supply to the model multiplying element (22). The pipeline (23) is used for gas mixture supply to the thermal regulating cavity of the capsule (24).

In the measurement section (II) there are heated paths for the purge-gas. The purge-gas (Ne+1-3% hydrogen or pure Ne) is permanently supplied from the model breeding element (19) at 0.1 MPa pressure and a constant velocity. The total tritium quantity extracted from the breeding element is measured in the heated ionization chamber (4). Then the gas flows to the nitrogen trap (5) where the tritium water component are separated, and the tritium gas component is measured in a non-heated ionization chamber (6). Furthermore the gas flows to a receiver (8) and gas purification tanks (9). A device for purge-gas sampling (7) is provided in the measurement section of the gas system. The sampling gas is intended to its check composition with chromatograph or mass-spectrometer methods. The measurement of the total collected gas in bottles and its concentration by CRG-6 standard ionization chamber (10) is provided in order to summarize the tritium gas balance. To summarize the tritium balance in water the measurement of sorbed moisture from trap is provided with the scintillation method.



I - section of gas preparation and bleeding in model and thermal regulating cavity, II - measurement section, III - section for gas purification from impurities and tritium

1 - gas balloons, 2 - tanks to created the gas mixes, 3 - filter, 4 - heated ionization chamber, 5 - nitrogen trap, 6 - ionization chamber, 7 - gas sampling device, 8 - gas collector, 9 - tank for purge gas purification, 10 - ionization chamber for tritium measurement, 11 - titanium apparatus for purge gas clearing from a nitrogen and a hydrogen, 12 - titanium trap for tritium sorption, 13 - tank for purge gas circulation, 14 - tritium monitoring devices, 15 - copper catalyst, 16 - nitrogen trap, 17 - filter, 18 - purge gas supply pipeline to the model breeder element, 19 - model breeder element, 20 - ECD, 21 - purge gas supply pipeline to the model multiplier element, 22 - model multiplier element, 23 - purge gas supply pipeline to the heater-regulation cavity, 24 - capsule.

Figure 4. Gas system of the RITM-F facility

In the section III the purge-gas is purified from nitrogen and hydrogen in the titanium apparatus (11), and the tritium sorption takes place in the titanium trap (12). The extent of gas purification from tritium is monitored with RGB-03 radiometer (14). The possibility for tritium after-burn on copper catalyst (15) with its deposition on the nitrogen trap (16) is provided in section III.

The following works on determination of system parameters and various factors that influent on the tritium extraction were performing during the model tests in IVV-2M reactor and after:

- tritium extraction parameters, time of the stationary require, tritium extraction rate in the stationary phase and inventory;
- influence of tritium purge-gas parameters (composition, flow rate, pressure) on the tritium extraction rate;
- a chemical form of the extracting tritium;
- impurities appearing in the irradiated breeding material;
- tritium and helium content in beryllium multiplier;
- tritium from breeding element diffused through the steel.

Measurements of tritium diffused through the steel from breeder material are performed by the gas transfer from the thermal regulating clearance gap to the receiving tank (during the PM) and by the tritium measurement in this clearance by CRG-6 ionization chamber. Measurements of tritium in beryllium were performed at the end of the campaign by the analogue to measurements of tritium diffused through the steel from the breeder material. Liquids collected in the nitrogen traps were analyzed on a tritium content with the scintillation method.

6. CONCLUSION

In the beginning of 1999 starting and adjustment works were conducted on the RITM-F facility in a full volume. Since March 22, 1999 the RF DEMO CHC BTM pebble bed breeding zone model tests were started and were successfully finished in the beginning of 2000. At RF DEMO CHC BTM pebble bed breeding zone model tests on 15 MW reactor nominal power. The following operating characteristics of model also were reached:

- nuclear power of the IVV-2M reactor – 15 MW;
- breeder (lithium orthosilicate) maximum temperature – 900°C;
- multiplier (beryllium) maximum temperature – 210°C;
- temperature of the heated channel - 120°C;
- purge-gas flow rate – 6-8 l/day.

Experiments on the influence of the purge-gas composition on the tritium extraction from breeding material have been performed during the model tests. The following results have been received during the tests:

- a) average tritium production rate - 6 Ci/day;
- b) tritium oxide production rate - 2.5-3 Ci/day,
- c) gaseous tritium production rate - 2.5-3 Ci/day.

Now on the RITM-F facility the testing of breeding zone pellet model with lithium orthosilicate pebble and porosity beryllium are carried out. These tests are planned to complete at the end of 2001.

STATUS OF FABRICATION OF Li_2TiO_3 PEBBLES BY THE EXTRUSION-SPHERONISATION-SINTERING PROCESS

J.D. Lulewicz^a, N. Roux^a, F. Pourchet^b, J.P. Joulin^b

^aCEA- DRT/DECS/SE2M- CE SACLAY- 91191 Gif/sur/Yvette, France

^bCTI- La Resclause, Route de Saint-Privat- 30340 Salindres, France

ABSTRACT

Li_2TiO_3 pebbles are a ceramic breeder material option for the Helium-Cooled Pebble Bed (HCPB) blanket being developed in the E.U. The extrusion-spheronisation-sintering process was selected in order to produce Li_2TiO_3 pebbles fulfilling the HCPB blanket requirements, and developed with the collaboration of the industrial firm CERAMIQUES TECHNIQUES ET INDUSTRIELLES. Adjusting the fabrication process parameters allows varying the pebbles characteristics, i.e., pebbles diameter, pebbles open/closed porosity, pebbles grain size which, in turn, determine the behaviour of the pebbles. Current reference pebbles have a diameter of 1 mm, a density of 90% of the theoretical density, a grain size of 1-2 μm , and an excellent purity. The feasibility of the fabrication by pre-industrial means is demonstrated at the 10 Kg scale which is sufficient to cover the present needs for the tests. A production of 150 Kg/year of Li_2TiO_3 pebbles is achievable with the current facility and no significant difficulty is to be expected for extrapolation of the production to the industrial scale. The advantage of this fabrication process to cover a wide range of characteristics (geometrical, microstructural, and mechanical) is shown. The overall results indicate both excellent prospects for the fabrication of Li_2TiO_3 pebbles and the attractiveness of their properties. In addition, in view of the necessary utilisation in the future of costly ^6Li enriched ceramic pebbles, focus is being placed on the minimisation of production losses as well as on the recycling process of the unburnt ^6Li in the Li_2TiO_3 pebbles after service in a reactor.

1. INTRODUCTION

Li_2TiO_3 pebbles are one of the options of ceramic breeder material for the Helium-Cooled-Pebble-Bed (HCPB) blanket developed in the E.U. The extrusion-spheronisation-sintering process was selected for the fabrication of the pebbles, as it proved to be the most appropriate one to obtain the goal characteristics. The satisfactory performance observed in the first functional tests of the so-fabricated pebbles [1] confirmed the promise and substantiated the validation with pre-industrial means of the steps of the lab-scale process. This work was made with the Ceramiques Techniques et Industrielles (CTI) firm. In agreement with previous studies [2], it was observed in the functional tests that the Li_2TiO_3 pebbles microstructural characteristics (open/closed porosity, grain size, specific surface area) are key parameters. Since this fabrication process easily allows varying the pebbles microstructural characteristics, it is very advantageous to tailor pebbles properties.

2. OPTIMISED FABRICATION OF 1 mm Li_2TiO_3 PEBBLES

The aim of the validation by pre-industrial means of the steps of the lab-scale process was to adapt the parameters at each step of the process to the pre-industrial conditions so as to reproduce lab-scale pebbles characteristics [3]. Simultaneously, strong consideration should be given to simplicity,

economics, and to production yield of the process, and to the capability to recycle ${}^6\text{Li}$, a must in the future.

The different steps of the extrusion-spheronisation-sintering process were described in [3]. It seems that the sintering temperature is a key parameter to adjust the microstructural characteristics of the pebbles, i.e., grain size, density, specific surface area. The objective is to obtain high density (~90% of the theoretical density) pebbles with small grain size (1-2 μm). Such characteristics proved so far to offer a good compromise of the pebbles requisite properties in the functional tests of pebbles and pebble beds. The main characteristics of the Li_2TiO_3 pebbles as a function of the sintering temperature are listed in Table 1. Advantage is taken of adjusting the sintering temperature to tailor the pebbles properties and the pebble beds behaviour. Examples are given in [4] showing the effect of the sintering temperature on important properties such as the high temperature long term annealing behaviour, thermal creep of pebble beds, and tritium release behaviour.

At this stage of the development of the extrusion process for the fabrication of 1 mm Li_2TiO_3 pebbles in the 5-10 kg range it was demonstrated that:

- the process allows to obtain pebbles with high purity and fulfilling the goal characteristics
- the process is relatively simple and unexpensive
- the process is flexible and can be adjusted to a range of pebbles specifications (pebble size, pebble density, pebble grain size).

The current fabrication facility at CTI allows the production of 150 kg/year of Li_2TiO_3 pebbles.

3. INVESTIGATION OF PEBBLE SIZE IN THE RANGE 0.5 mm – 0.7 mm

The current sintered Li_2TiO_3 pebbles have diameters in the range 0.8 mm to 1.2 mm. Investigation was made to determine the lower limit of Li_2TiO_3 pebble diameter achievable with the extrusion process with a view to find out any benefit for the design of the Helium-Cooled-Pebble-Bed blanket. Smaller pebbles can be advantageous to fill better the ceramic breeder space and to increase pebble bed density and thermal conductivity.

The fabrication process parameters are being adjusted in order to obtain Li_2TiO_3 pebbles with a smaller diameter. In a first attempt to decrease the diameter of the green pebbles, a nozzle of 0.8 mm instead of 1 mm was used during the extrusion step and a spheronization plate was re-designed for the spheronization of the smaller granules. The same extrusion machine and cutting system as for the preparation of the current pebbles were used for these trials. The pebbles were sintered at 1100°C and 1140°C, and characterised at CEA. The shape, the size and the microstructure of the smaller Li_2TiO_3 pebbles were observed using scanning electron microscopy. The shape is close to spherical, and the pebble size distribution is 0.7 mm to 1 mm. The microstructure is homogeneous, and grain size is 1 to 4 μm . A comparison of the characteristics of the current Li_2TiO_3 pebbles with the characteristics of the smaller pebbles is displayed in Table 1 showing that open and closed porosity decrease slightly for smaller pebbles and pebble bed density increases significantly. Grain size is very similar for smaller pebbles and current pebbles sintered at 1100°C.

The feasibility to produce small Li_2TiO_3 pebbles in the range 0.7 mm to 1 mm with the extrusion process was shown in this study. Although there is no experimental evidence that perfect sphericity of the pebbles constituting the pebble bed is a must, an attempt will be made to obtain even better sphericity. Further adaptations can be made also to decrease pebble diameter down to 0.5 mm.

4. EVALUATION OF PRODUCTION YIELD AND PRELIMINARY STUDY OF ENHANCEMENT

For economical purpose (high cost of ${}^6\text{Li}$ material to be used in the future), it is required to minimise Li losses throughout the fabrication process of Li_2TiO_3 pebbles. A preliminary (no attention paid to save the materials) value of 50% was calculated for the fabrication yield of 6 Kg of Li_2TiO_3 pebbles produced in 2000. Losses of lithium materials originate from elimination after the cutting step

of the too long granules and from elimination by sieving of the green pebbles which do not meet the size specification.

The objective is to recover the lithium materials separated during the process (granules, green pebbles) and to recycle them after transformation into a Li_2TiO_3 powder having the same characteristics as the initial one. To this end, granules and green pebbles are subjected to calcination, in order to remove binder and plasticiser, and to sieving. A recyclable powder is obtained and can be used directly at the first step of the process, i.e., the preparation of the paste for extrusion. Comparison in Table 2 of the characteristics of the initial powder and of the recyclable powder shows a very good agreement regarding apparent density, specific surface area and mean particle size. Crystal phases are identical.

5. CONCLUSION

The extrusion-spheronisation-sintering process was finalised at the semi-industrial scale for the production of very pure 1 mm Li_2TiO_3 pebbles fulfilling the HCPB blanket requirements. The current facility at CTI allows the production of 150 Kg/year of Li_2TiO_3 pebbles which is sufficient for the present needs. The process can be easily extrapolated to industrial scale as it makes use of conventional techniques of the ceramic industry. Owing to its great flexibility, the process is very suitable to tailor the pebbles properties and the pebble beds behaviour, as show by the results of the the functional tests which are in progress in the European blanket program. Exploring the whole range of pebbles diameters achievable by the extrusion process is currently under study, especially exploring the lower diameter limit since smaller pebbles are likely to ease the blanket filling procedure, and increase pebble bed density and thermal conductivity. In addition, in view of the necessary utilisation in the future of costly ^6Li enriched ceramic pebbles, focus is being placed on the recycling process of the unburnt ^6Li in the Li_2TiO_3 pebbles after service in a reactor, and in parallel minimisation of production losses is to be carried out.

REFERENCES

- [1] N. Roux, Compilation of blanket-relevant properties data and pebble beds, Proceeding of the 9th CBBI, September 2000, Toki, Japan.
- [2] J.D. Lulewicz, N. Roux, G. Piazza, J. Reimann, J. van der Laan, Behaviour of Li_2ZrO_3 and Li_2TiO_3 pebbles relevant their utilization as ceramic breeder for the HCPB blanket, Journal of Nuclear Materials, 283-287 (2000) 1361-1365.
- [3] J.D. Lulewicz, Advances in the pre-industrial fabrication of Li_2TiO_3 pebbles by the extrusion-spheronisation-sintering process, Proceeding of the 9th CBBI, September 2000, Toki, Japan.
- [4] J.D. Lulewicz, N. Roux, The fabrication of Li_2TiO_3 pebbles by extrusion-spheronisation-sintering, a suitable process for tailoring pebbles properties, presented at ICFRM-10, October 2001, Baden-Baden, Germany.

Table 1: Characteristics of the sintered pebbles

Sintering temperature (°C)	Pebble size (mm)	Porosity (%)		Bed density (g/cm ³)	Grain size (µm)	Average crush load (N)
		Open	Closed			
950	0.8 – 1.2	13	4	1.71	0.5 - 1	52
1050	0.8 – 1.2	5	5	1.80	1 - 2	66
1100	0.8 – 1.2	6	5	1.81	1.5 - 5	40
1140	0.8 – 1.2	5	5	1.86	2 - 7	38
1100	0.7 – 1.0	4	5	1.89	1 - 4	32
1140	0.7 – 1.0	2	5	1.96	Over sintered	28

Table 2: Characteristics of the initial and recyclable Li₂TiO₃ powders

	Initial powder	Recyclable powder
X-ray diffraction	Li ₂ TiO ₃ + Li ₄ Ti ₅ O ₁₂	Li ₂ TiO ₃ + Li ₄ Ti ₅ O ₁₂
Specific surface area	4.0 m ² /g	4.2 m ² /g
Mean particle size	0.6 µm	0.58 µm
Apparent density	0.38 kg/l	0.37 kg/l

FT-IR study on hydrogen isotopes in lithium oxide combined with ab-initio analysis of O–H vibration

H. Tanigawa and S. Tanaka

Department of Quantum Engineering and Systems Science, The University of Tokyo

1. Introduction

For establishment of the fusion reactor fuel cycle, it is necessary to understand the tritium release behavior from the blanket materials. Lithium-based ceramics are candidates of the breeder materials. Both irradiation tests in reactors and fundamental studies have been worldwide conducted [1, 2]. The group of the present authors has investigated existing state of hydrogen isotopes on the surface and in the bulk Li_2O using Fourier transform infrared absorption spectroscopy (FT-IR). In a series of the experiments, deuterium was used in order to avoid the high background of O–H in the air. O–D stretching vibrations of surface deuteroyl group were observed using a diffuse reflectance method [3, 4]. Plural peaks were observed under controlled temperature and atmosphere and they were assigned to the heterogeneous surface nature. The bulk –OD was studied for the perfect crystal [5, 6]. Observed multiple peaks were attributed to the O–D presenting as LiOD or that existing as D^+ bonded with an oxygen ion in the Li_2O crystal with or without defects.

In order to explain multiple peaks observed by FT-IR and to clarify the nature of hydrogen isotopes in Li_2O , the quantum chemical calculation has been conducted. As regards the surface –OH, it was shown that O–H stretching vibrations were affected by the chemical species around –OH [7]. In the case of bulk –OH, it was found that oxygen vacancies affected –OH and different configurations resulted in different existing states of hydrogen isotopes [5]. However, it was difficult to estimate the stretching vibrational frequency of O–H because our calculations were limited in the Hartree-Fock (HF) method. In the present paper, O–H stretching vibrational frequency in LiOH crystal was calculated with hybrid (B3LYP) method. The result was compared with that of the FT-IR studies.

2. Calculation details

2.1. Computational methods

It is well known that HF method tends to overestimate vibrational frequencies because it does not take electron correlation effects into consideration. In density functional theory (DFT), some correlation effects are taken into account through the effective exchange-correlation potential. The hybrid method, which mixes HF with DFT approximations, is recently developed and performs well for many properties including vibrational frequencies [8, 9]. B3LYP is one of the most popular functionals [10].

CRYSTAL 98 code was used for the calculations [11]. This code enables us to solve both the Hartree-Fock and Kohn-Sham equations. In addition, mixed schemes such as B3LYP can be treated. In this study, HF and B3LYP methods were used.

2.2. Calculation scheme

For the first step of the study on O–H frequencies, LiOH crystal was considered. In this stage, some difficulties still remain for surface –OH and H^+ in Li_2O crystal because of discontinuity at the surface and the charge of the system, respectively.

In the CRYSTAL code, an infinite system such as crystal environment can be treated by considering series of consecutive cells. LiOH has tetragonal structure and the primitive

cell which contains two LiOH was used for the calculations. Each cell parameters were fixed according to X-ray diffraction data as follows, $a = b = 3.550$, and $c = 4.330 \text{ \AA}$. The shrinking factors of the reciprocal space net were set to 6, where the total energy of the system was considered fully converged. The basis sets for Li, O, and H are 6-1G, 8-411-(1d)G* and 5-11G* contractions, respectively. The information about the basis sets is shown in ref. [12]. The exponents of the two most diffuse shells of all atoms were re-optimized for the present system.

A limited anharmonic analysis was carried out for the O–H stretching vibrational frequency. The following is the procedure of the calculation. The O–H distances were fully optimized at the both HF and B3LYP levels. Around the stable positions, the potential energies were calculated. The corresponding nuclear Schrödinger equations were solved numerically using the program ANHARM [13]. The program gives the vibrational energy levels. From the obtained eigenvalues, the harmonic frequency (ω_e), anharmonicity constant ($\omega_e \chi_e$) and anharmonic frequency (ω_{01}) were calculated. Here, ω_{01} is defined as $\omega_{01} = \omega_e - 2\omega_e \chi_e$.

By taking account of reduced mass, O–D and O–T frequencies could be also estimated from the results of O–H, because the isotope effect in the potential calculation is considered to be negligible.

3. Results and discussion

3.1. Calculated anharmonic frequency

The calculated equilibrium O–H distances were 0.934 and 0.954 Å for HF and B3LYP methods, respectively. Fig. 1 shows the calculated potential curve in B3LYP. In table 1, vibrational frequencies (cm^{-1}) of O–D in LiOD crystal converted from the results of LiOH are shown with the experimental data [14]. The symbol Δ is the percentage difference with respect to the experimental value.

These differences between HF and B3LYP are considered to come from the electron correlation effects. In HF, the correlation effects related to the transfer of an electron from Li to O and to the formation of the O–H bonding are not taken into account. Concerning the vibrational frequency, it is shown that agreement with experimental data is much better in B3LYP than in HF, as reported for other hydroxide materials [9]. There exist several effects neglected in this calculation, for example, the coupling effect between two O–H vibrations in the cell. To consider these effects could give more correct frequencies, however, it is beyond the scope of this paper.

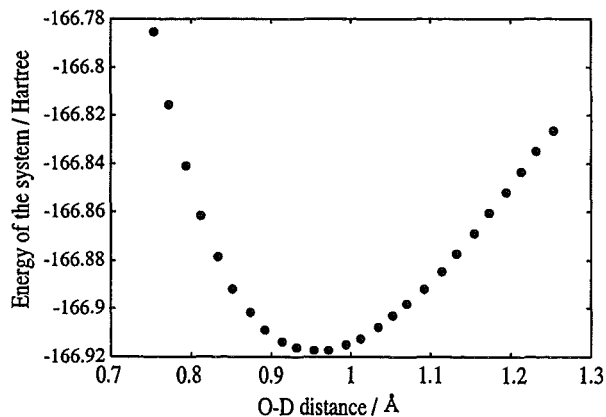


Fig. 1 Total energy curve of LiOH system as a function of O–H distance calculated by B3LYP

Table 1 ω_e , $\omega_e\chi_e$ and ω_{01} for O–D vibration in LiOD calculated by the two methods and comparison with experimental data (cm^{-1})

	ω_e	$\omega_e\chi_e$	ω_{01}	$\Delta(\%)$
HF	3070	38	2994	10
B3LYP	2824	42	2740	1.0
Exp. [14]			2713	

(ω_e : harmonic frequency, $\omega_e\chi_e$: anharmonicity constant, ω_{01} : anharmonic frequency)

3.2. Comparison with IR experiment

Finally, the present results will be compared with those from our previous FT-IR studies. Fig. 2 shows infrared spectra in Li_2O single crystals which were treated by thermal absorption of D_2 and consequent quenching.

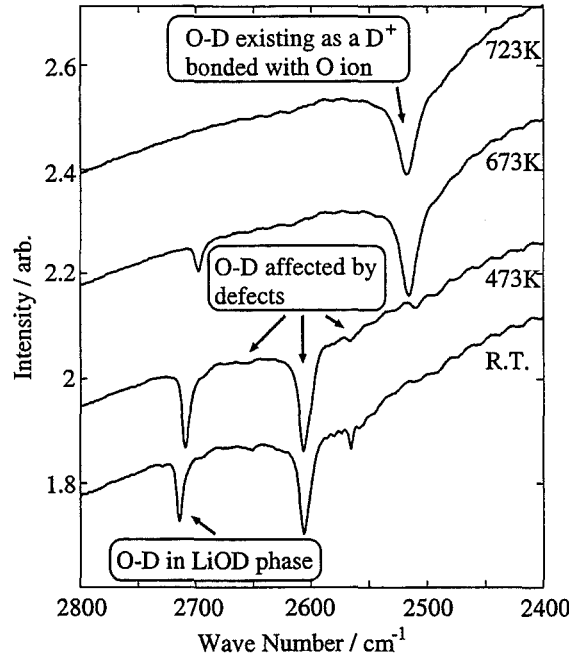


Fig. 2 IR spectra of D_2 absorbed Li_2O single crystal (modified from ref. [6])

In the previous work, the peak observed at 2715cm^{-1} at room temperature was attributed to O–D in LiOD phase. The present calculation supports the assignment. The future direction of the present study will be one that deals with surface –OH or –OH in the crystal. The ab-initio analysis combined with the FT-IR study is a powerful tool to study the behavior of hydrogen isotopes in the ceramic breeder materials.

4. Conclusions

The vibrational frequency of O–H in LiOH crystal was calculated with HF and B3LYP methods. In the case of B3LYP, agreement with experimental data was quite good. The present study affords new approach to analyse infrared absorption spectroscopy of O–H in the ceramic breeder materials.

Acknowledgments

This work has been supported by Theoretical Chemistry Laboratory of Torino University. The authors thank to Profs. R. Dovesi, Ph. Baranek, and G. Mallia for their help and useful discussion.

References

- [1] C. E. Johnson, K. Noda, N. Roux, *J. Nucl. Mater.*, **258-263**, 140(1998).
- [2] J. G. van der Laan, H. Kawamura, N. Roux, D. Yamaki, *J. Nucl. Mater.*, **283-287** 99(2000).
- [3] M. Taniguchi, S. Tanaka, Y. Nose, V. Grishmanov, *Fus. Technol.*, **28** 1284(1995).
- [4] S. Tanaka, M. Taniguchi, *J. Nucl. Mater.*, **248** 101(1997).
- [5] H. Tanigawa, M. Taniguchi, S. Tanaka, *Fus. Technol.*, **34** 872(1998).
- [6] H. Tanigawa, S. Tanaka, *Fus. Eng. Des.*, **51-52** 193(2000).
- [7] M. Taniguchi, S. Tanaka, *Fus. Technol.*, **30** 874(1996).
- [8] B. G. Johnson, P. M. W. Gill, J. A. Pople, *J. Chem. Phys.*, **98** 5612(1993).
- [9] Ph. Baranek, A. Lichanot, R. Orlando, R. Dovesi, *Chem. Phys. Lett.*, **340** 362(2001).
- [10] A. D. Becke, *J. Chem. Phys.*, **98** 5648(1993).
- [11] V. R. Saunders, R. Dovesi, C. Roetti, M. Causà, N. M. Harrison, R. Orlando, C. M. Zicovich-Wilson *CRYSTAL98 User's Manual*, University of Torino, Torino, (1998).
- [12] Information about basis sets are shown in the following web site,
"http://www.ch.unito.it/ifm/teorica/Basis_Sets/mendel.html".
- [13] P. Ugliengo, B. Civalleri, C. M. Zicovich-Wilson, R. Dovesi, *Chem. Phys. Lett.*, **318** 247(2000).
- [14] R. A. Buchanan, E. L. Kinsey, H. H. Caspers, *J. Chem. Phys.*, **36** 2665(1962).

Cellular Automaton Model for Near-Surface Dynamics for Interaction Between Breeder Materials and Sweep-Gas

K.Shimura^a, K.Yamaguchi^b, T.Terai^a and M.Yamawaki^a

^aDepartment of Quantum Engineering and Systems Science, Graduate School of Engineering, The University of Tokyo, 7-3-1 Hongo, Bunkyo-ku, Tokyo 113-8656, Japan

^b Japan Atomic Energy Research Institute, Shirakata 2-4, Tokai-mura, Naka-gun, Ibaraki-ken 319-1195, Japan

Tritium release from the lithium ceramics as a fusion reactor breeder material is strongly affected by the composition of the sweep-gas which influences the surface processes. The typical surface processes which play important roles are adsorption, desorption and interaction between vacancy site and the constituents of the sweep-gas. Among a large number of studies and models, yet it seems to be difficult to model the overall behaviour of those processes due to its complex time-transient nature. In the present work the coarse grained atomic simulation based on the Cellular Automaton (CA) is used to model the dynamics of near-surface interaction between Li_2O surface and sweep-gas.

1. Introduction

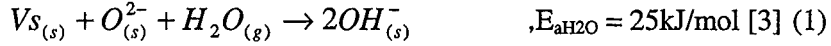
Tritium release from the lithium ceramics as a fusion reactor breeder material is strongly affected by the composition of the sweep-gas which influences the surface processes. The typical surface processes which play important roles are adsorption, desorption and interaction between vacancy site and the constituents of the sweep-gas. Among a large number of studies and models, yet it seems to be difficult to model the overall behaviour of those processes due to its complex time-transient nature. In the present work the coarse grained atomic simulation based on the Cellular Automaton (CA) is used to model the dynamics of near-surface interaction between Li_2O surface and sweep-gas that is assumed to be consisting of a noble gas, hydrogen gas and water vapour. For the purpose of describing such a complex systems, Cellular Automata (CA) are one of the very powerful tools [1][2] that has less restriction on conditioning the model compared with some methods based on differential equation such as Molecular Dynamics (MD). In general, CA are known as discrete mechanical system which is fully discrete in both time and space. The system can be represented by some sets of rules that describe the microscopic interactions between cells. Moreover in CA model, the control space is discretised into cells. And the states of each of those cells are updated according to the states and the corresponding rules in each time interval. Because of these characteristics, complex physical and chemical systems can be described by fairly simple manner. CA is also possible to imply highly non-linear boundary conditions in contrast to the model based on the differential equation. However in present work CA model of adsorption and desorption of hydrogen and water at Li_2O surface is constructed and the validity and its applicability for modelling the tritium release are discussed.

2. Modelling

In this model, (110) surface of Li_2O which is known to be its most stable surface is considered. The ideal top three rows of the surface are shown in Figure 1. O^{2-} ions are located on the O^{2-} lattice sites and empty sites (E_0) are located on the interstitial sites in the O^{2-} sub-lattice, which are arranged regularly among Li^+ ions. The first step of the modelling is to discretise this surface as shown in Figure 2. For

convenience, O^{2-} , Li^+ and E_0 are rearranged in to the flat lattice consisting of square cells and each of those cells contain each of those ions. (110) surface of Li_2O shows an anisotropy that is the longitudinal and lateral length between the adjacent O^{2-} ions are different as illustrated in Figure 1. Thus the size of each square cells of this model is taken as the averaged size. Secondly, a lattice that represents the gaseous phase is considered on top of the surface lattice. The lattice conditions such as cell's size, number of cells and etc. are the same as those for the surface lattice. This lattice reflects the condition of the sweep-gas and desorbed particles. However, the dynamics of adsorption and desorption are implemented as local interactions between those two layers by use of thermally-activated processes.

At first the following adsorption and desorption mechanisms are assumed in this model. For adsorption of H_2O vapour, H_2O is dissociatively adsorbed on pair of V_s and O^{2-} site. This process and its corresponding activation energy is then,



Where V_s represents either E_0 (empty site) or V_0 (oxygen vacancy). Strictly speaking, E_0 and V_0 are energetically different but it is known that there is no significant difference in the energetics between those two [3]. And hence E_0 and V_0 are treated in the same way. Contrary to this, desorption of H_2O is the reverse reaction and is described as recombination process of two OH^- site to produce a V_s and O^{2-} on the surface.



The sweep-gas is considered to be consisting of H_2O vapour and H_2 gas, so the next step is to make clear about H_2 desorption and adsorption mechanism. The adsorption mechanism of H_2 is dissociative and is as follows. One dissociative H atom is adsorbed on an O^{2-} to produce OH^- and another is adsorbed on the site existing between the two adjacent Li^+ [4]. *i.e.*



Conversely desorption is then,



The above processes are now implemented into the CA rules as illustrated in Figure 3. For each time step whole surface and gaseous lattice is scanned through and if and only if the states of cells are listed in the rules then the transition occurs with the corresponding probability P_i $\{i | 1,2,3,4\}$. The probability P_i should reflect thermally-activated processes in order to make the CA model consisting with the chemical model and thus they are as follows.

$$P_1 = \frac{\max(E_{aH_2O}, E_s) - E_{aH_2O}}{E_s - E_{aH_2O}} \tau \nu \exp\left(-\frac{E_s}{RT}\right) \quad (5)$$

$$P_2 = \frac{\max(E_{dH_2O}, E_s) - E_{dH_2O}}{E_s - E_{dH_2O}} \tau \nu \exp\left(-\frac{E_s}{RT}\right) \quad (6)$$

$$P_3 = \frac{\max(E_{aH}, E_s) - E_{aH}}{E_s - E_{aH}} \tau \nu \exp\left(-\frac{E_s}{RT}\right) \quad (7)$$

$$P_4 = \frac{\max(E_{dH}, E_s) - E_{dH}}{E_s - E_{dH}} \tau \nu \exp\left(-\frac{E_s}{RT}\right) \quad (8)$$

Where E_{aH_2O} and E_{dH_2O} are the activation energy for adsorption and desorption energy for H_2O respectively. Similarly to this E_{aH} and E_{dH} are the activation energy for adsorption and desorption energy for H_2 . τ and ν represents time interval and the frequency factor respectively. E_s are the energy of the states that are given by Boltzmann distribution under the assumption of the quasi-equilibrium condition. However the above calculation is sequentially carried out until steady state is observed.

3. Result and discussion

By using the above model, surface concentration of OH^- , O_2^- and V_s are calculated for several conditions of different partial pressure of H_2 and H_2O as shown in Table 1. The result is illustrated in Figure 4 through 6. Moreover, Figure 4 illustrates the case of the partial pressures are taken as $P_{\text{H}_2\text{O}} = 1$ Pa, $P_{\text{H}_2} = 100$ Pa. It is seen that at transition stage, adsorption of H_2 is dominant since increase of OH^- and decrease of O_2^- occurs at similar rate and the increase of V_s shows the desorption of H_2O is simultaneously occurring. Also at steady state, $V_s < \text{O}_2^- < \text{OH}^-$ has been observed because of adsorption of hydrogen is the most dominant, then desorption of hydrogen is second dominant. Lastly the adsorption and desorption of H_2O comes the least dominant. This fact can obviously be seen from the value of the partial pressure and the activation energy of each process. Secondly, the partial pressures are taken as $P_{\text{H}_2\text{O}} = 1000$ Pa, $P_{\text{H}_2} = 1000$ Pa. It is seen from Figure 5, at transition stage, adsorption of H_2 and H_2O are dominant since rapid increase of OH^- . After some point, the effects of desorption of H_2O and H_2 appear as increase of V_s and decrease of O_2^- respectively. Then $V_s < \text{OH}^- < \text{O}_2^-$ has been observed at steady state. The partial pressure of H_2 and H_2O is the same value in this case, and so the dominant processes are adsorption of H_2 and H_2O . Then desorption of H_2O comes next. The least dominant process is then desorption of H_2 due to its high activation energy. Thirdly the partial pressures are taken as $P_{\text{H}_2\text{O}} = 10000$ Pa, $P_{\text{H}_2} = 1$ Pa. Rapid increase of OH^- and decrease of O_2^- and V_s are seen from Figure 6. Very fast decrease of O_2^- and V_s and increase of OH^- shows the adsorption of H_2O is the most dominant in this case. This is obvious since the partial pressure of H_2O is significantly large comparing to that of H_2 . It is also seen that the processes are rapidly reaching to the steady state since the rate of adsorption is so fast that sites are immediately occupied after desorption of H_2O and H_2 .

4. Conclusions

Cellular Automaton (CA) model for adsorption and desorption of H_2 and H_2O on Li_2O (110) surface is developed in this work. Preliminary calculation is made for the surface concentration of V_s , O_2^- and OH^- are carried out for three different cases of partial pressures. Those results show a consistency with the chemical model at steady state. But this model is not yet complete for the transient discussion. However, it is foreseen that inclusion of tritium effect is rather simple in order to estimate the tritium release. Strictly speaking, in order to clarify the validation of the model, it is necessary to compare the result with other model and/or some experimental result. From this point of view it can be said that this model is still under development. But one clear point that has to be stressed here is the present work provides many insights for the capability of CA to model more complex surface processes.

References

- [1] Cellular Automata and Modeling of Complex Physical Systems, edited by P. Manneville, N. Boccara, G.Y. Vichniac, and R. Bidaux, Springer Proceedings in Physics 46, (1989)
- [2] S. Wolfram, Cellular Automata and Complexity, (1994)
- [3] D. Yamaki et al., Key Engineering Materials, 111-112 (1995) 83
- [4] M. Taniguchi et al, Proc. of the 7th International Workshop on Ceramic Breeder Blanket Interaction (CBBI-7), Petten, Netherlands, Sep.14-16, 1998, (1999) 6

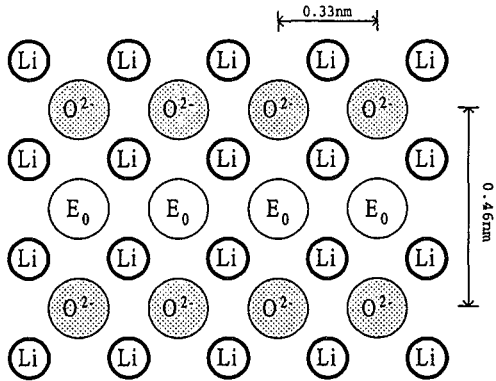


Figure 1: Li_2O (110) surface.

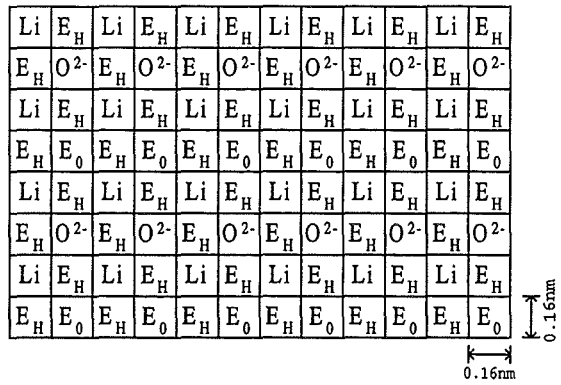


Figure 2: Discretised surface of Li_2O (110).

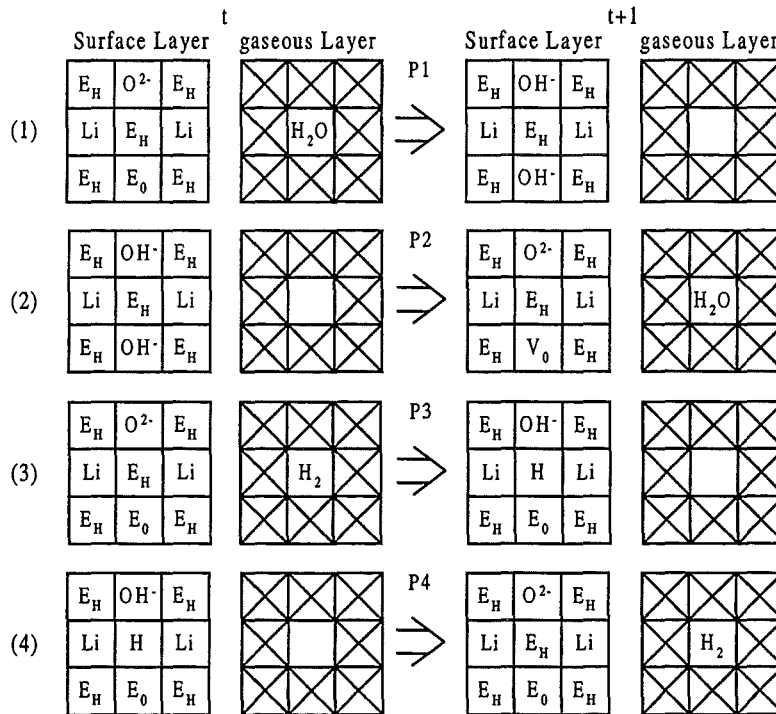


Figure 3: The transition rules of CA for each process. Where t represents the time before the transition, $t+1$ represents the time after the transition and also P1 through P4 represent the transition probabilities.

H_2O partial pressure	H_2 partial pressure	Temperature
1 [Pa]	100 [Pa]	773K
1000 [Pa]	1000 [Pa]	773K
10000 [Pa]	1 [Pa]	773K

Table 1. The calculation conditions for this model.

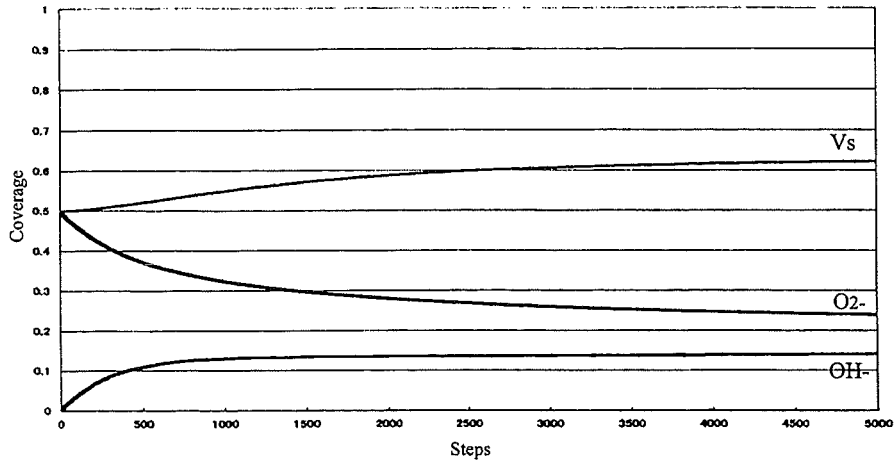


Figure 4: Result of CA calculation for $P_{H_2O} = 1$ Pa, $P_{H_2} = 100$ Pa.

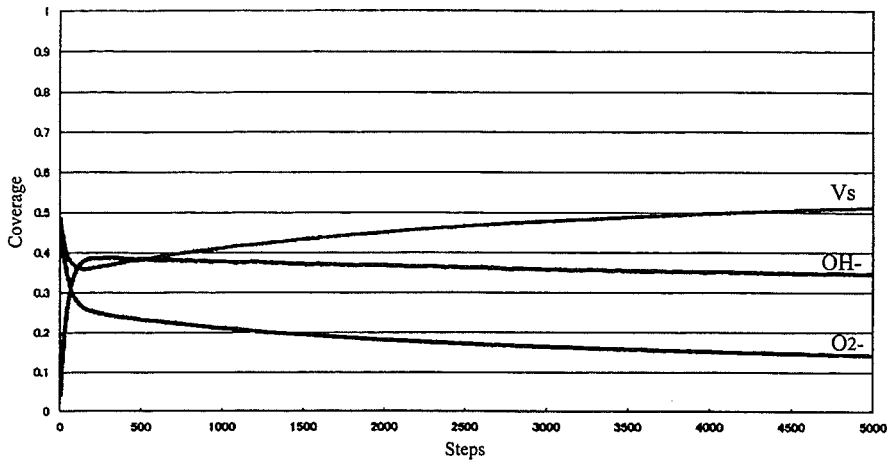


Figure 5: Result of CA calculation for $P_{H_2O} = 1000$ Pa, $P_{H_2} = 1000$ Pa.

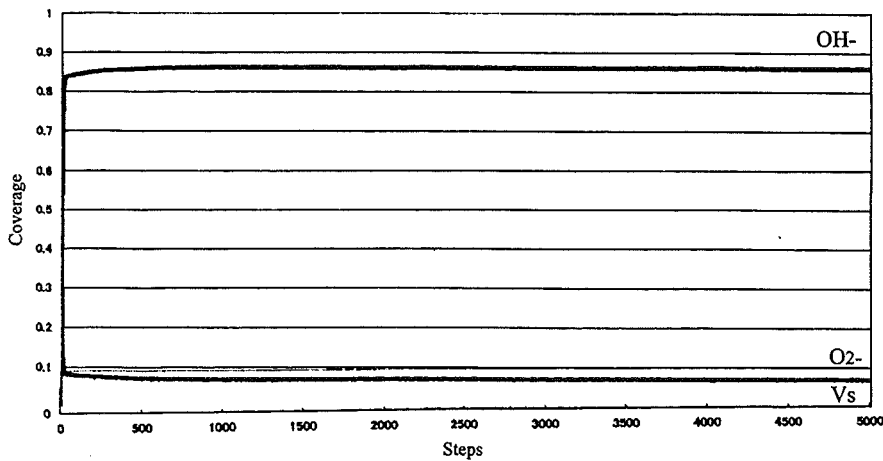


Figure 6: Result of CA calculation for $P_{H_2O} = 10000$ Pa, $P_{H_2} = 1$ Pa.

7

Study on ceramic breeder and related materials by means of work function measurement under irradiation

G. -N. Luo^a, K. Yamaguchi^b, T. Terai^a, and M. Yamawaki^a

^aDepartment of Quantum Engineering and Systems Science, The University of Tokyo

^bDepartment of Materials Science, Tokai Research Establishment, Japan Atomic Energy Research Institute

Ceramic breeder materials, Li_2O , LiAlO_2 and Li_4SiO_4 , under irradiation have been studied using a Kelvin probe that measures work function changes of materials. Surface charging was observed to influence greatly the probe output, which can be explained qualitatively employing a model concerning induction electric field due to external field and free charges on ceramic surface. It is found that the insulating ceramics could not be studied properly with the Kelvin probe. A probable solution is to heat the ceramics, so as to raise their electric conductivities high enough to root out the surface charging. Also briefly discussed is the application of the probe to metals under ion irradiation.

1. INTRODUCTION

Though tritium release from lithium ceramics under irradiation is one of critical issues of current interest, the understanding is still limited about the details of the release processes. In some cases where desorption is the rate-determining step, surface properties of the ceramics may play an important role in the processes [1]. Thus there are practical needs to study the influence of irradiation on the surface states of the ceramics in reactor and in laboratory using various kinds of irradiation sources.

Surface electronic properties of the ceramics were studied in the present authors' group using high temperature Kelvin probe under controlled atmosphere (sweep gases) and at elevated temperatures [2, 3]. Adsorption / desorption of hydrogen and water vapour, and oxygen vacancies formation on the surface / near surface were considered to be responsible for the corresponding work function changes observed in the experiments. The device operates under pressures around 1 atm, and is not suitable to be connected to any irradiation devices, which limits its application in studying the irradiation-induced effects. Thus the effects have been studied using the devices recently developed and very preliminary results have been presented in CBBI-8 [4]. In this paper, the latest development related to this topic is to be reported.

2. MODEL

Kelvin probe measures contact potential difference (*CPD*) between probe tip and sample, which can be expressed as

$$CPD = (\Phi_s - \Phi_p) / e, \quad (1)$$

where the *CPD* is in the units of volts, Φ_s and Φ_p , the work functions (WFs) of the tip and the sample, respectively, all in the units of eV, and e the elementary charge. Currently used probe to measure the *CPD* was named after Lord Kelvin who arranged the tip and the sample as two plates of a parallel plate capacitor that were in contact via an external circuit [5]. The setup was greatly improved by Zisman[6] by introducing vibration to one of electrodes of the capacitor, which made it possible to measure the *CPD* more exactly, quickly, and continuously. Modern Kelvin probes are only variants of the one modified by Zisman, with the use of different ways of vibration and electronics.

As introduced by Harris and Fiasson [7–9], when an insulating sample is seated on a metallic sample holder, as shown in Figure 1, the value of backing voltage V_b in the probe circuit will counteract not only the CPD but also any other potential differences between the probe and the holder. The gap d and insulator thickness t constitute capacitors in series that divide up any voltage applied across them and hence

$$V_b + CPD = Ed + E't, \quad (2)$$

where, as stressed by the authors, the CPD is the contact potential difference between the probe and the holder; E and E' are the fields across gap and insulator, respectively. If free charges of density σ_0 exist on the surface, it will affect the polarization within the insulator, and in turn the field E' . Therefore, the variation of electric displacement across the surface, according to Gauss's law, becomes

$$\epsilon_0 \epsilon E' - \epsilon_0 E = \sigma_0. \quad (3)$$

In case the balance is achieved by adjusting V_b , a zero field will be obtained in the gap, which means $E = 0$. Thus we achieve the following equation

$$-V_b = CPD - \sigma_0 t / \epsilon_0 \epsilon. \quad (4)$$

Eq. (4) clearly indicates that the probe output ($-V_b$) changes with the build-up charges on the surface, which can be classified into the following three cases.

(1) $\sigma_0 = 0$, i.e., no charges build-up, in this case, Eq. (4) becomes

$$-V_b = CPD, \quad (5)$$

which means that the probe output is equal to the CPD between the probe and the holder.

(2) $\sigma_0 > 0$, i.e., positive charges build-up, then

$$-V_b < CPD. \quad (6)$$

Thus the output will decrease with increasing the number of charges.

(3) $\sigma_0 < 0$, i.e., negative charges build-up, we obtain

$$-V_b > CPD. \quad (7)$$

Therefore the probe output will increase with increasing the number of charges.

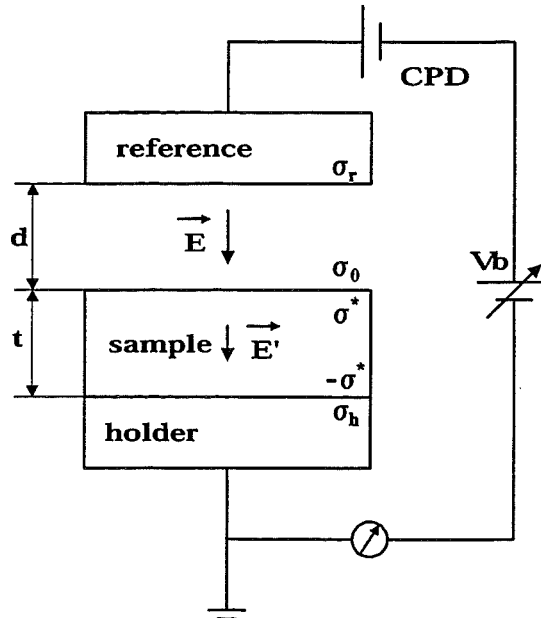


Figure 1. Schematic figure of a Kelvin probe in case where an insulating sample is measured, where σ_r , and σ_h denote charge densities on the reference and the holder, respectively, and σ^* the induced charge density. See the text for other symbols.

3. EXPERIMENTAL

3.1. MeV irradiation

The experiments were done using a device at Heavy Irradiation Facility, Research Center for Nuclear Science and Technology, the University of Tokyo (HIT). The device connected to one of beamlines of the van de Graff accelerator of the facility is shown in Figure 2. Its vacuum chamber was evacuated by a pumping system composed of a turbo molecular pump and a rotary pump. Generally, a sample was mounted on position B, facing a Kelvin probe. During beam adjustment period through an open hole (position D), the probe output was not recorded. Once the adjustment finished, the recording started. The sample was irradiated by moving it to align to the beam line. After irradiation, the sample was moved back to face the probe for work function measurement. Thus the measurement and the irradiation could not be performed at the same time, otherwise the irradiation would damage the probe and the sample would also be blocked by the probe.

Experimental conditions are tabulated in Table 1.

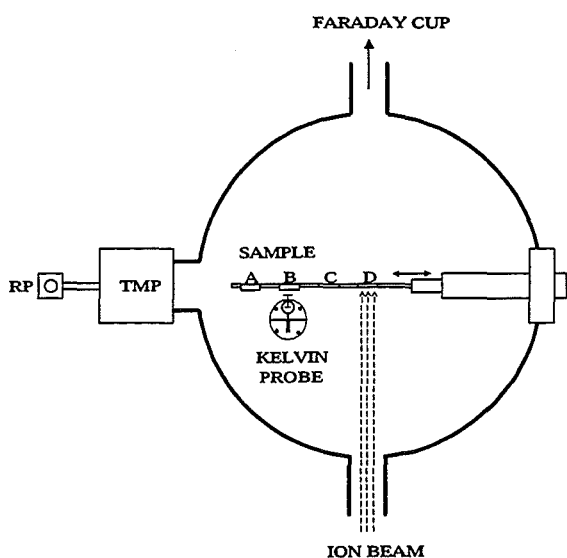


Figure 2. Scheme of the device used for MeV ion irradiation in HIT

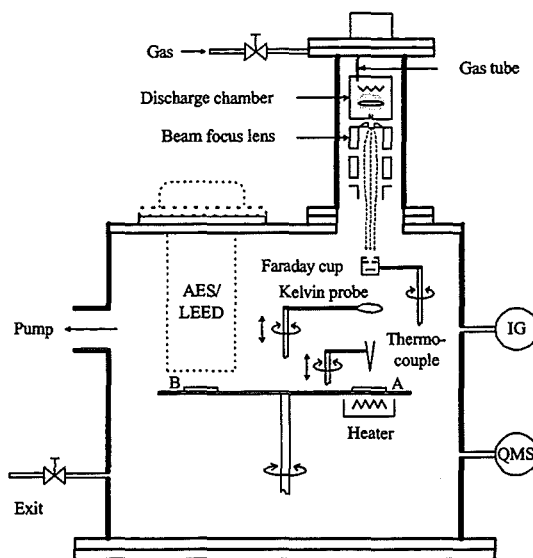


Figure 3. Scheme of the device used for low energy ion irradiation

Table 1. Experimental conditions for lithium ceramics in HIT

Sample	Li ₂ O	LiAlO ₂	Li ₄ SiO ₄
Ion species	He ⁺	He ⁺ , H ⁺	He ⁺ , H ⁺
Ion current (μA)	0.1 (=4 × 10 ¹⁵ ions/m ² /s)	0.1 (He), 0.5 (H)	0.1 (He), 0.5 (H)
Energy (MeV)	1		
Pressure (Pa)	1 × 10 ⁻⁴		
Temperature	Room T		

Note: Suppliers of the samples,
 (1) Li₂O and Li₄SiO₄, Japan Atomic Energy Research Institute;
 (2) LiAlO₂, Mitsubishi Heavy Industry.

3.2. Low energy irradiation

The experiments were performed using a recently built device, in the present authors' lab [10], as shown in Figure 3. The new device has been equipped with the same KP, and a beam source composed of a dc-arc discharge section, and a beam extraction and focusing section. The ion source is capable of producing both positive ion beam and negative electron beam up to 660 eV. The beam flux is measured with a Faraday cup. The probe can be rotated and moved for fine adjustment of the separation between the probe and the sample. Due to the intrinsic configuration of the probe, as mentioned above, the WF measurement could not be made during the irradiation on samples. Once completing each run of irradiation, the probe had to be rotated over the sample and adjusted to the given distance from the sample; then the measurement was started.

The experimental conditions of irradiation of ion / electron beam are tabulated in Table 2. In this experiment, the ion beam was used first, and then the electron beam was applied to investigate the effect induced by charges of different signs.

Table 2. Conditions for irradiation on Li_4SiO_4 in our lab

	He ion beam	Electron beam	Electron beam
Energy (eV)	150	150	250
Flux ($10^{16}/\text{m}^2/\text{s}$)	4	1.4	4
Time (min)	1	1	3
Pressure (Pa)	1×10^{-2} (beam), 1×10^{-6} (base)		
Temperature	Room T		

Note: Sample supplier, Japan Atomic Energy Research Institute.

4. RESULTS AND DISCUSSION

4.1. MeV irradiation

As indicated in Table 1, five experiments were carried out on Li_2O , LiAlO_2 and Li_4SiO_4 samples using 1 MeV H and He ion beams. Due to similarity of the results, herein only the result of the LiAlO_2 sample irradiated by He^+ is to be shown. The result is presented as the probe output versus time sequence, which shows the evolution of the output after each irradiation, as shown in Figure 4, where symbols "s" and "m" in the figure denote the irradiation time in seconds and minutes, respectively, and "beam adj." denotes the period for adjusting the beam to given parameters.

The probe output was recorded immediately after the beam adjustment period, which indicated an increase in the output more than 1 V, followed by a recovery process until the first irradiation run. The subsequent ion irradiations always resulted in drastic decreases in the output even up to -6 V, then very quick recoveries. With increasing the irradiation time, a tendency of reduction of the drastic decrease after irradiation was observed. For low fluences (first several short irradiations), the output seemed to recover to a similar level, while for large fluences, there did not exist such a level, and an increasing maximum of the output in the recovery processes had been easily observed, and the increase in the maximum was nearly 1.5 V at the end of the final irradiation. After passing the maxima, the recovery processes tended to saturate.

The output increase due to the beam adjustment might be attributed to the deposition on the sample surface of the secondary electrons emitted from the areas irradiated by the primary ions. It was this negative charges build-up on the insulating ceramics that affected the electric field around the sample. According to Eq.(7), the probe output should be increased. The subsequent recovery (decrease) then might be the consequence of discharging processes occurring on the surface, which induced a decrease in the second term in Eq. (4), noting that $\sigma_0 < 0$ in this case, while the first term CPD should not vary significantly since there were not significant changes to occur on the surfaces of both the probe tip and the holder during the adjustment period, even during the whole experiment.

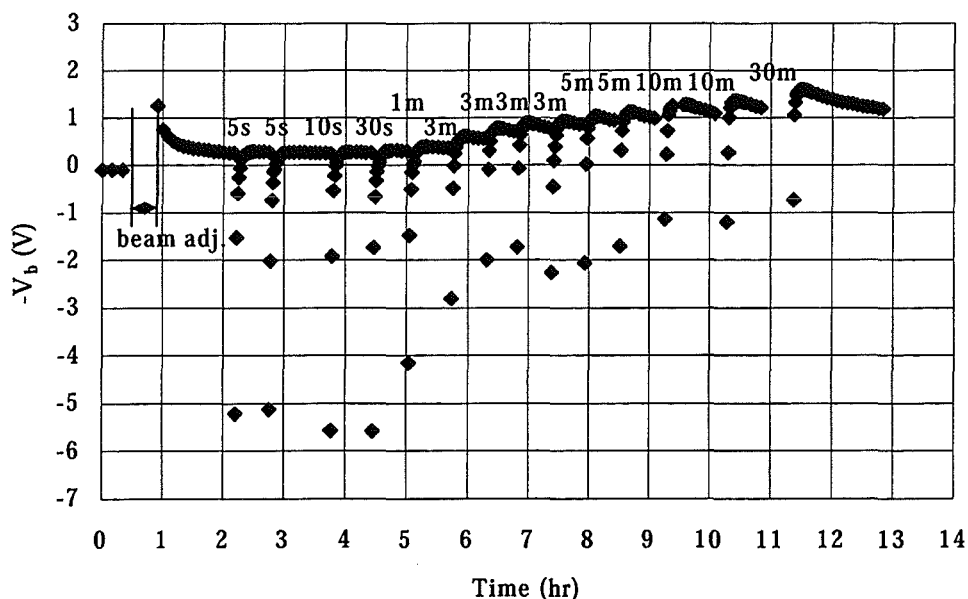


Figure 4. Kelvin probe output as a sequence of time for LiAlO_2 irradiated by He^+ of 1 MeV, $0.1 \mu\text{A}$. See the text for meaning of the symbols.

The first four runs of irradiation labelled 5s, 5s, 10s and 30s resulted in great decreases in the output, and the initial value immediately after stopping each irradiation might be much lower than the recorded one because the recovery processes were fast and it took several seconds to move the sample back to face the probe. Such a decrease could be attributed to the deposition of the positive charges from the ion beam according to Eq. (6). The similar saturation level of the recovery processes might imply a stable status of residual charging-up, and a stable surface state. With increasing irradiation fluence, surface defects developed, and surface properties might change, too. Therefore the decrease in the first recorded output value after each irradiation might stem from the increase in surface electric conductivity that sped up the discharging processes. And the evolution of the output, i.e., recovery – maximum – slow decrease – probable saturation, should be a complicated process, dependent on a combination of some elementary processes, probably including the change in charging status (discharging process), the defects development, the surface processes like adsorption of reactive gas species from the residual gases, which might influence significantly the charging state on the surface.

4.2. Low energy irradiation

As stated in subsection 3.2, only Li_4SiO_4 sample was examined using the low energy ion beam and the electron beams. Again, the result is presented as the probe output versus time sequence, as shown in Figure 5.

The irradiation period indicated as “ion beam” or “e-beam” includes two stages, i.e., adjustment and irradiation, and the irradiation time is listed in Table 2. It can be seen that ion irradiation induced huge decrease in the probe output that was much larger than the measurement range of the probe controller of about ± 14 V. On the contrary, electron beam irradiations led to increases in the output that were much smaller than the decrease induced by the ion beam. Moreover, the increase by the e-beam irradiation of 250 eV, 3 min was not larger than that by the e-beam of 150 eV, 1 min.

According to Eq. (6), positive charges build-up on the surface induced by the ion irradiation caused decrease in the output. In the present case, the huge decrease in the output (out of the measurement range) was very different from what was observed under MeV ion irradiations where the charge build-up on the Li_4SiO_4 samples induced only decreases of several volts, although the total fluences were

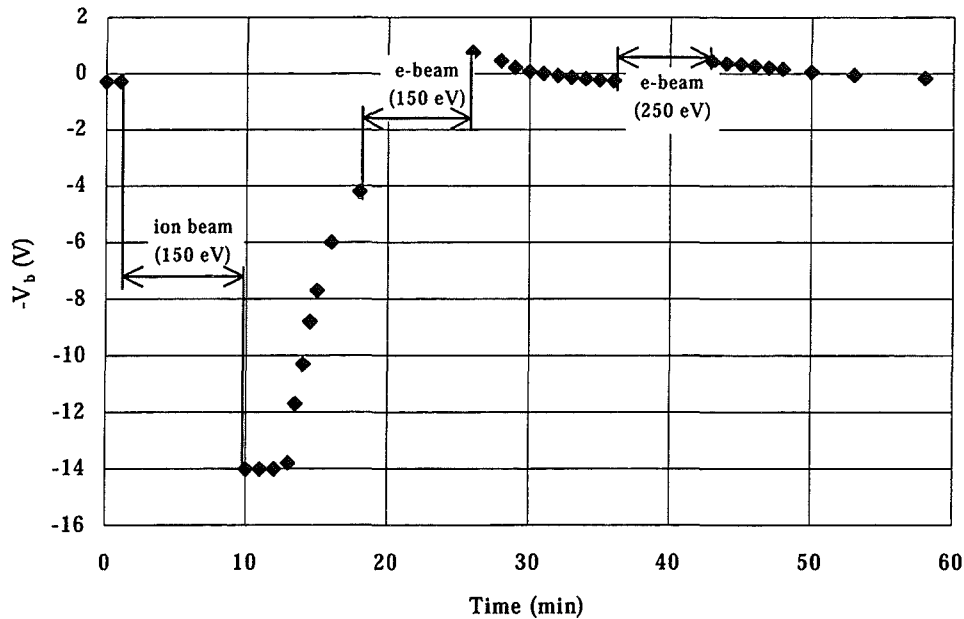


Figure 5. Kelvin probe output as a sequence of time for Li_4SiO_4 irradiated by He^+ and electron of low energies. See Table 2 for details.

comparable. The difference may lie in the different behaviours induced by MeV light ions and low energy ions in insulating materials. As we know, MeV light ions usually generate defects at near surface region via electronic stopping processes, while low energy ions via nuclear processes. However, the correlation between the surface charging on insulators and the stopping processes is still an open question. The subsequent electron beam irradiations led to increases in the output, coincident with the prediction of Eq. (7). The increases of less than 1 V with respect to the value prior to irradiation, were much smaller than the decrease induced by the ion irradiation, which was reasonable because the incident electrons stimulated the emission of secondary electrons from the surface. Net charges accumulated on the surface were the difference between incoming and outgoing electrons. The incident electrons of 250 eV even produced more secondary electrons, thus a smaller change of the probe output could be expected.

4.3. Further discussion

Based on the above results and discussion, the surface charging affected the probe output significantly. In Eq. (4), the probe output is only related to the WFs of the probe tip and the sample holder, and the surface charges. The WF of the sample itself was not involved in. Thus one may draw a conclusion that Kelvin probe is not suitable to the work function measurement of insulators. In our present study on the lithium ceramics, to heat the samples so that their electric conductivity can be raised to a high enough level may be a feasible way, which may cancel the surface charges build-up, and allow the CPD between the probe and the sample to be evaluated. For the purpose, a powerful heater must be incorporated into the system. As stated in a previous paper [11], this heater must not emit thermal electrons during operation. The heater is under construction now.

Though a Kelvin probe cannot be used to measure the work function of an insulator, it does provide possibility to monitor the charges on an insulating surface since its output is so closely related to the surface charge density. In practice, as semiconductor device size continues to shrink, the thinner gate oxides are required. Charging damage to the oxide layer is becoming an increasingly concern for the next few device generations. Recently, some devices have been developed based on Kelvin probe to fulfil the purpose [12–14].

The same devices were also applied to the studies on the metals like Ni and W under ion irradiations [11, 15]. On metals irradiated by MeV H and He ion beams, a WF decrease of about several hundreds of meV was observed, followed by saturation, which might be attributed to the desorption of the topmost weakly bound adsorbates due to the energy transfer at the surface from the absolutely dominant electronic stopping. The desorption led to the decrease of the surface dipole moment towards to bulk, which triggered the decrease of the WF.

As for nickel under 500 eV He ion irradiation, the bombardment induced a WF decrease at first, and then an increase, and saturation with further increasing the fluence. Under low energy regime, the nuclear stopping is dominant, and the induced sputtering plays a key role in the surface change. Low energy irradiation is quite effective to remove the loosely bound adsorbates, thus a WF drop was observed at first. The following irradiation sputtered away gradually the oxide layer naturally formed on Ni surface in air. As a result, the WF increased gradually. The final saturation might be due to the total removal of the oxide and a balance between the sputtering and the adsorption from the residual gases. The result, in an opposite direction, is consistent qualitatively with oxidation processes reported by other research groups [16].

5. SUMMARY

- (1) Due to charges build-up on the sample surface, the output of the Kelvin probe was affected greatly. In the case of positive charges build-up due to the ion irradiation, the output decreased; whereas negative charges build-up due to deposition of the secondary electrons or the electron beam resulted in increases in the output, qualitatively in agreement with the theoretical prediction.
- (2) It has been realized that the acquisition of *CPD* from insulating sample by Kelvin probe is impossible. But to raise the temperature of the sample so as to increase its electric conductivity and to achieve a charge free surface may be a feasible way to apply Kelvin probe to the field, as proved in the use of a high temperature Kelvin probe in the field of oxide ceramics by Suzuki et al. [2, 3].

REFERENCES

- [1] P. C. Bertone, *Journal Nuclear Materials* 151 (1988) 281.
- [2] A. Suzuki, K. Yamaguchi, T. Terai, and M. Yamawaki, *Fusion Engineering and Design* 49-50 (2000) 681.
- [3] A. Suzuki, *Fusion Engineering and Design* 39-40 (1998) 699.
- [4] G. -N. Luo, K. Yamaguchi, T. Terai, and M. Yamawaki, *Proceedings of the 8th CBBI*, October 6 – 8, 1999, Los Angeles, USA.
- [5] Lord Kelvin, *Philosophical Magazine* 46 (1898) 82.
- [6] W. A. Zisman, *Review of Scientific Instruments* 3 (1932) 367 .
- [7] J. Fiasson and L. B. Harris, *Journal of Physics E10* (1977) 1160.
- [8] L.B. Harris and J. Fiasson, *Journal of Physics E17* (1984) 788.
- [9] L.B. Harris and J. Fiasson, *Journal of Physics C18* (1985) 4845.
- [10] G. -N. Luo, K. Yamaguchi, T. Terai, and M. Yamawaki, *Journal of Nuclear Materials* 290-293 (2001) 116.
- [11] G. -N. Luo, K. Yamaguchi, T. Terai, and M. Yamawaki, *Review of Scientific Instruments* 72(5) (2001) 2350.
- [12] M. J. Goekner, S. B. Felch, J. Weeman, and S. Mehta, *Journal of Vacuum Science and Technology A17(4)* (1999) 1501.
- [13] A. M. Hoff, T. C. Esry, and K. Nauka, *Solid State Technology* July (1996) 139.
- [14] Y. Tada and Y. Tomizawa, *Japanese Journal of Applied Physice* 34 (1995) 643.
- [15] G. -N. Luo, K. Yamaguchi, T. Terai, and M. Yamawaki, *Surface Science*, submitted.
- [16] T. D. Pope, S. J. Bushby, K. Griffiths, and P. R. Norton, *Surface Science* 258 (1991) 101

Li₂TiO₃ pebbles tritium release mechanism and kinetics by post-irradiation “Temperature Programmed Desorption” (TPD) spectroscopy.

C. Alvani ^a, P. L. Carconi, St. Casadio ^b, S. Casadio ^a

^aENEA, CR Casaccia, via Anguillarese, 301; 00060 S.M. di Galeria, Rome, Italy

^bK. F. University, Univ. Platz, 5, A 8010, Graz, Austria. C/o ESA/ESRIN, via Galileo Galilei, 00044, Frascati (RM), Italy

The interaction of gaseous environments such as air (with moisture and CO₂ impurities) and the purge gas mixture He + H₂ (1000 vpm) (R-gas) with Li₂TiO₃ pebbles was examined by TPD/TPR methods. Surface “cleaning” processes were stated and the titanate reduction kinetics to Li₂TiO_{3-x} concerning free and grain boundary surfaces were determined by TPR spectra de-convolution-fitting analysis performed by assuming the reaction rate signal as the overlap of independent first-order steps. Formally near all the Ti⁴⁺ on both the grain and grain boundary surfaces around 800 and 950 K respectively was found reduced to Ti³⁺ (i.e x ≈ 1).

Several specimens were shortly irradiated and examined for tritium release by previously annealing them for 1-2 hours at 473K in flowing R-gas and then by heating at the rate β = 5 K/min (TPD method). Specimens with density lower than about 82% TD and nearly full open porosity showed a single broad peak (T_p = 760 ± 20 K) whose first-order deconvolution gave a main contribution of a desorption site-peak characterized by the kinetic rate constant $k = 9.5 \cdot 10^5 \exp(-1.52 \cdot 10^4/T)$ [s⁻¹]. Diffusion control was however found to be more compatible with experimental data for these porous materials. Tritium removal from pebbles with density higher than 90 % TD was found to be limited by diffusion within the grain boundary interface. This transport stage was found to be affected by the above mentioned “reduction” steps, tritium trapped on grain boundaries resulting removable above 900 K where the pebbles reduction occurs.

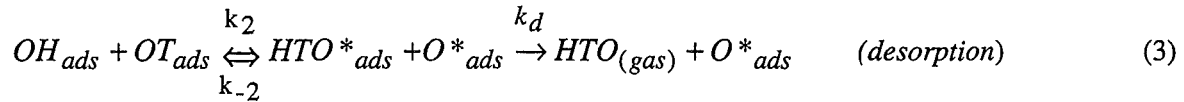
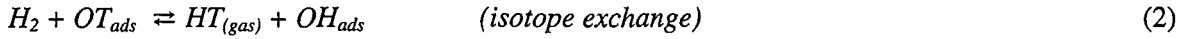
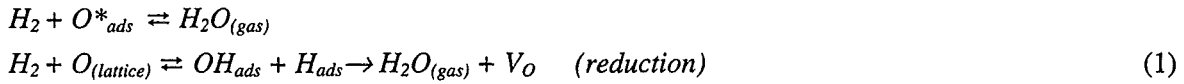
1 - INTRODUCTION

Lithium metatitanate (Li₂TiO₃) pebbles (diam. 0.5-1.5 mm) have been proposed for tritium-breeding in fusion reactor blankets [1,2]. Several years ago they were prepared and tested for tritium release properties [3,4] by post irradiation tests. The results indicated that i) tritium could be easily removed from Li-titanate at temperature as low as 600 K, ii) the method of preparation was found to affect the tritium release, and iii) the addition of H₂ to the helium purge gas did not improve tritium recovery. The last claim (iii) was not confirmed by recent reliable experiments [5], pebbles surface status or material pre-treatments could have influenced the first one (i).

This work deals with the investigation of the effects of impurities (CO₂ and H₂O) adsorbed on the pebbles surface and of H₂ in the purge gas in out-of-pile tritium release rate tests of irradiated Li₂TiO₃ specimens. The main experimental tools employed were the “Temperature Programmed Desorption” (TPD) and “Reaction or Reduction” (TPR) techniques. The objective was to correlate the results to the tritium residence times directly obtained by in-situ irradiation tests [5].

The chemical interaction of Li₂TiO₃ with the purge gas is determined by the presence of 1000 vpm H₂ according to the reactions scheme (1). The tritium removal from Li-oxides as HTO or HT forms during or after irradiation under R-gas purging is sketched by the equations (2-3). According to Fisher’s scheme [6] k₂ is the dissociation rate constant, k₃ the recombination rate constant and k_d the desorption rate constant. k₂ may also be interpreted as mobility rate constant preceding the hydroxides

recombination into activated HTO* complex as precursor of tritiated water desorption under diffusion control.



The reduction steps (1) and their effects on the tritium release process (3) are considered by assuming the isotopic exchange (2) so fast to always assure thermodynamic equilibrium at the material surface, at the designed and constant H₂ partial pressure (i.e. data refer to R-gas environment). Some already reported literature data are also re-elaborated by the TPD-TPR diagnostic criteria.

2. EXPERIMENTAL

2.1. Materials

Several specimens of Li₂TiO₃ pebbles supplied by different laboratories were examined. Most of them were available because we were involved in fabrication, reprocessing and characterization of this kind of pebbles, mainly concerning their chemical interaction with R-gas in the frame of HCPB blanket program. Other specimens were available because of a wider free international cooperation on this kind of study. Preparation routes and characteristics of the specimens have been already published. The involved institutions, the specimen or batches codes, the grain size (gs), the % of theoretical density (TD) and the related references are recalled in Table 1.

Table 1 – Main characteristics of the considered lithium titanate specimens in this work

Institute	Specimen batch code	gs (μm) min.-max. */from SA sph.eq.	Density (% TD)	Pebbles diam. Ø mm	References
AECL	S. 1673K	40 – 140	85.4	1.2	[3]
CEA	CTI30C7	1-2.5	92		[6]
ENEA	FN1	10-30 */ 20	56	1.56	[7, 8, 9, 10]
	FN2	10-30 */ 19	70	0.87	
	FN4-2/FN5	5 - 80	92	0.8	
	FN4-3/FN5	5 - 80	92	2.0	
CEA	ref 424	0.5 – 1 */ 2.5	81	pellets	[15, 14]
ECN	pebbles	5 - 10	74 - 79	0.5 – 1.0	[14]
CCHEN	RS11/1300	3 – 4 */ 21	66.7	2.2 ± 0.2	[17]

The most used preparation route started from Li₂TiO₃ powders mixed with binders and plasticizers. Pebbles forming was performed by: i) the extrusion-cutting spheronization sintering (CEA-(CTI series) [6] and AECL [3]) and ii) agglomeration-spheronization-sintering (ENEA (FN series) and CCHEN-(C) [7,8]). The specimens were different for ceramic grade quality of the precursors and for forming + sintering temperatures. The “agglomeration” process with fine powders gave a density gradient inside the pebbles which resulted very compact at the surface but quite porous inside (FN4-

FN5. Such a gradient was not observed for low density pebbles prepared by powders with larger grains (FN1) [8] and RS11/1300. In particular CTI30C7 (a "reference" material for HCPB blanket) and FN1 specimens were examined for their interaction with purge R-gas [6] since they had the highest and the lowest density, very different grain size and microstructure but similar geometric form, phase composition and Surface Area (SA $\sim 0.1 \div 0.2 \text{ m}^2/\text{g}$). The extent of the grain boundary interface (GBS) of the CEA specimen resulted to lie in the $0.6 - 1.6 \text{ m}^2/\text{g}$ range by SEM analysis, an order of magnitude higher than that observed for the ENEA specimen ($0.06 - 0.2 \text{ m}^2/\text{g}$) [9].

2.2 - Instruments

The equipment used for studying solid-gas chemical interactions (Micromeritics TPD/TPR 2000 apparatus as modified and implemented in our lab) and tritium release properties (CREATE apparatus) were already described in details elsewhere [9-10]. TPR-TPD runs were performed by heating at constant rate ($\beta = dT/dt$) the specimens (200 mg) held under purge R-gas flow (rate range $F = 20-100 \text{ cm}^3/\text{min}$). The initial temperature T_0 was generally room temperature (r.t).

In particular the chemical interaction of Li_2TiO_3 with the H_2 of the R-gas was performed by two complementary TPR tests. A run was devoted to the measurement of H_2 consumed by the reaction, in this case the R-gas was simulated by the Ar + 0.1% H_2 mixture in which the H_2 concentration (P_{H_2}) evolution could be well analyzed on line by the difference between the gas thermal conductivity detected upstream and downstream the reaction pot (TCD detectors in differential analysis). The other run was performed directly with the R-gas in which the H_2O concentration ($P_{\text{H}_2\text{O}}$) evolution could be measured with high TCD sensibility. In every case and in each run the TCD signal was calibrated for quantitative analysis of H_2O and H_2 species in the carrier gas (He or Ar).

The short irradiations and out of pile tritium release tests consisted in inserting about 0.2 g of each specimen in the TRIGA reactor "lazy Susan" rotating device (nominal neutron flux $\sim 2 \times 10^{12} \text{ n/cm}^2/\text{s}$, irradiation time ~ 30 hours). The amount of tritium generated and implanted into the pebbles (by the nuclear reaction ${}^6\text{Li}(n,\alpha)\text{T}$) ranged from 30 to 60 MBq; its removal rate by R-gas purge was measured by the CREATE device operating in TPD mode; heating procedure was: (i) fast heating up at 473 K, soaking at this temperature for about two hours (isothermal step removing adsorbed moisture and CO_2), then (ii) heating with $\beta = 5 \text{ K/min}$ up to 1073 K. An analysis of the IRF (Instrument Response Function) was carried out to evaluate the signal (peak) distortions. A pulse of tritium (half peak wide 1 min) was injected in the apparatus (by letting fall small activated Li_2TiO_3 fragments in the specimen chamber held at 1123 K) while R-gas was flowing. The shape of the peak function was found conserved when convoluted with IRF.

A TPD/TPR spectrum deconvolution best-fitting procedure (by IDL-5.0 system for Windows) was developed for first-order and second-order rate overlapped steps by assuming them non-interacting, that is a procedure similar to that applied by Kopasz on Li_2TiO_3 pebbles [4] and Fisher on LiAlO_2 pellets [17].

3 – RESULTS AND DISCUSSION

3.1 – Air interaction with Li_2TiO_3 pebbles

"As received" pebbles were generally found contaminated by H_2O and CO_2 due to air exposure [9,10]. "Cleaned" Li_2TiO_3 pebble batches catch water and carbon dioxide from the air at room temperature as a function of exposure time as reported in Figure 1 for two typical specimens. Most of this adsorbed moisture was found to be removed at 480 K, this temperature corresponding to a peak of $P_{\text{H}_2\text{O}} \sim 1000 \text{ vpm}$ in our experimental chemical TPD runs (This alteration of the chemistry of both the pebbles surface and purge gas produced important effects on tritium release rate tests for "as received" specimens [9]). The remaining chemisorbed or dissociated H_2O was removed by higher temperature desorption steps as shown by shoulder peaks between 570 and 870 K in pure He sweeping, reproducing those obtained by Kopasz et al. for tritium removal in He [4]. The total amount of CO_2 adsorbed was found to be close to that of moisture (see Figure 1) and its desorption was found to accompany the "drying" process. In other words de-hydroxylation of the specimens could be described

by the desorption-decomposition of the adsorbed carbonic acid or “bicarbonates” from the specimen surfaces.

In practice this maximum $\text{H}_2\text{O} + \text{CO}_2$ content resulted to be lower than 0.02 % by weight in pebbles stored in free air environment. Their removal by annealing in He or R-gas at 473 K for few hours was significant but not complete.

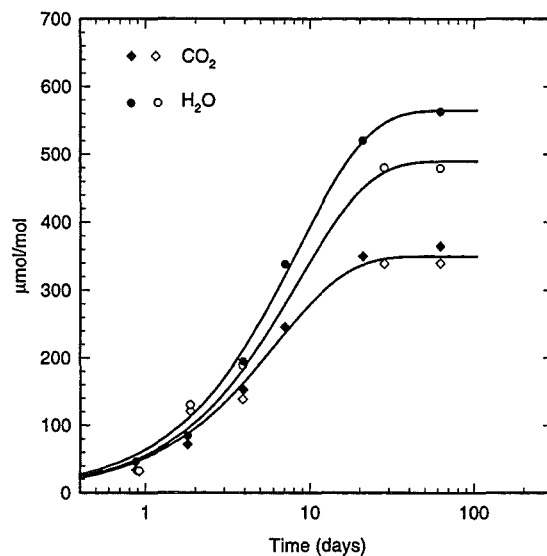


Fig.1: Moisture and carbon dioxide uptake on Li_2TiO_3 pebbles CTI30C7 (open points) and FN1 (full points) in air at room temperature as function of exposure time.

3.2 –Hydrogen reaction with Li_2TiO_3 pebbles by TPR tests

When heated-up above 873 K in R-gas, lithium titanate was found to generate (and release) water [9,10]. This phenomenon was not observed to occur in pure helium gas stream, since H_2O generation was due to H_2 reaction with reducible oxygen containing impurities or with “active O-sites” of Li_2TiO_3 lattice with consequent O-vacancies generation following the scheme (1).

Some build-up of the intermediate hydroxide ions during the run was observed to occur (Figure 2) by the difference between the peaks corresponding to H_2 consumption and H_2O generation (accompanied by a small temperature shift, Table 2) that was remarkable for the CTI30C7 specimen. The elimination of water by the step (1) reduced the pebbles to $\text{Li}_2\text{TiO}_{3-x}$ and induced color change from white to black. We observed a fast re-oxidation of these black pebbles as exposed to $\text{He} + \text{O}_2$ mixture at 1073 K. During the first reduction-oxidation cycle the generated H_2O was not found to be balanced by the O_2 consumed for re-oxidation, while a perfect balance was recorded for the successive and quite reproducible red-ox cycles. We related this behavior to the elimination of reducible volatile impurities during the first red-ox cycle, while the successive ones involved only O-vacancy generation and annihilation. So the application of at least one reduction-oxidation cycle was considered to “clean” the specimens surface.

Figure 2 reports the “calibrated” TPR reaction rates evolution in terms of H_2 consumed and H_2O generated when “as cleaned” specimens (table 1) were exposed to hydrogen (in $\text{Ar}+0.1\%\text{H}_2$ mixture and R-gas respectively) during heating at the rate $\beta = 10$ K/min. The elaboration of the TPR spectra by the current theory of heterogeneous reaction kinetics [11] was difficult (example in Figure 3) because the reaction was not yet complete at the final temperature $T_f = 1073$ K. Taking T_f constant more than two days were necessary to complete the “bulk” reduction of the specimen to the composition formula $\text{Li}_2\text{TiO}_{3-x}$ with $x \cong 0.01$ [9]. The main two steps that precede the bulk reduction were analyzed by continuing to express the reaction rate (v_r , eq.(4)) in term of variation with time of the fractional reactants conversion x (as mole fraction $0 \leq x \leq 1$)

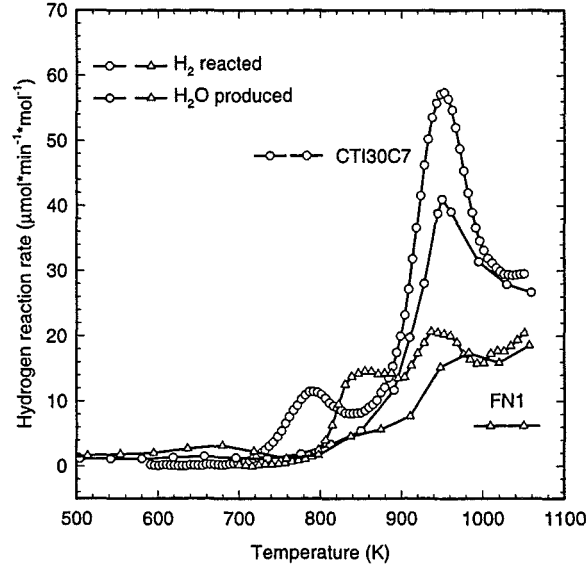


Fig.2: Hydrogen interaction with Li_2TiO_3 pebbles CTI30C7 and FN1 as function of temperature with $\beta=10$ K/min.

$$v_r = \frac{dx}{dt} = \beta \frac{dx}{dT} = \beta \sum_i g_i \frac{d\alpha_i}{dT} \quad (i = A, B, C, \dots) \quad (4)$$

and by assuming the individual (i) reaction rate steps (fractional conversion $0 \leq \alpha_i \leq 1$) having the weight factors g_i and being represented by Arrhenius type relations (5)

$$\frac{d\alpha_i}{dt} = \beta \frac{d\alpha_i}{dT} = \alpha_i A_i \exp\left(\frac{-E_i}{RT}\right) \quad (5)$$

The rate of each step will reach a maximum value for $dv_r/dT = 0$, i.e. for

$$\frac{d^2\alpha_i}{dT^2} = -\frac{\alpha_i A_i E_i}{\beta RT^2} \exp\left(\frac{-E_i}{RT}\right) + \frac{A_i}{\beta} \exp\left(\frac{-E_i}{RT}\right) \frac{d\alpha_i}{dT} = 0 \quad (6)$$

by the equations (6) and (5), the temperature $T_{p,i}$ for which we have the maximum reaction rate constant $k_{m,i}$ of the step i is given by the relationship (7)

$$\frac{E_i}{RT_{p,i}^2} = \frac{A_i}{\beta} \exp\left(\frac{-E_i}{RT_{p,i}}\right) \quad (7)$$

Equation (7) cannot be manipulated to give a single $(E_i; A_i)$ couple of kinetic parameters, although it is commonly used to get a first evaluation of E_i by the slope of its log-Arrhenius plots when T_p values are measured at various heating rates β (" β -variation method"). This data elaboration could be better performed by the peak shape analysis fitting theoretical formula, that is in principle feasible only for a

single reaction step. For processes involving polycrystals the TPR/TPD spectra have to be deconvoluted in the single contributions. Figure 3 reports an example of deconvolution and fitting of our code, and the parameters reported in table 2 were found to characterize the first two steps (i=A and B) of the process (1) in R-gas (i.e. at $P_{H_2} = 1000$ vpm at total pressure ≈ 1 atm). The beginning of contribution C (whose peak could be observed for temperature out of the range here explored) concerns the Li_2TiO_3 pebbles bulk reduction whose kinetics was already examined by isothermal annealing desorption performed at 1173 K [9].

In surface science the surface concentration of each species Γ_i is related to its “coverage” $\theta_i = \Gamma_i/\Gamma_{i,max}$ ($\Gamma_{i,max}$ is a sort of saturation value, $0 \leq \theta_i \leq 1$). The treatment of the reaction processes in term of surface coverages is formally identical to that exposed for the α 's, the elaboration within the frame of first order kinetics is the same (constant factors disappear in the “normalization” procedure).

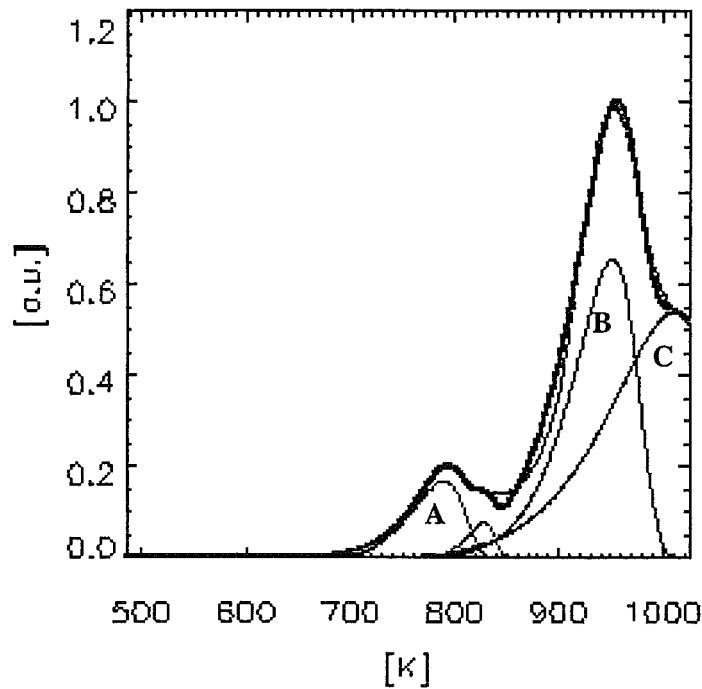


Figure 3: Plot of the deconvolution-fitting elaboration of the H_2 consumed for CTI30C7 specimen during heating at rate $\beta = 10$ K/min, experiment reported in Fig.2, parameters for the A and B peaks reported in Table 2.

Table 2 – Kinetic parameters for the reaction (assumed of first order) of R-gas with Li_2TiO_3 pebbles.

pebble bed specimen	step	T_{pA} [K] (by H_2 consumed)	T_{pB} [K] (by H_2O generated)	E_A [kJ/mol]	E_B [kJ/mol]	A_A [s^{-1}]	A_B [s^{-1}]	g_A [%]	g_B [%]
CTI30C7	A	789	not obs.	291	---	$1.8 \cdot 10^{17}$	---	9	---
CTI30C7	B	951	955	346	299	$8.1 \cdot 10^{16}$	$1.6 \cdot 10^{14}$	44	34
FN1	A	840	840	278	294	$1.6 \cdot 10^{15}$	$1.6 \cdot 10^{16}$	24	6
FN1	B	951	991	203	193	$8.2 \cdot 10^9$	$6.4 \cdot 10^8$	73	70

The extent of reaction rates shown in Figure 2 and kinetic parameters reported in Table 2 suggest that steps A for the two very different specimens are proportional to their SA (which was comparable)

while steps B are proportional to their grain boundary area (GBS). We may consider the A steps to occur on the free surfaces of the specimens with $\Gamma_{\max, \text{surf}} \approx 10\text{-}15 \mu\text{mol/m}^2$ while the peaks B could result from the reaction (2) occurring at grain boundaries at a comparable $\Gamma_{\max, \text{gb}} \approx 10\text{-}20 \mu\text{mol/m}^2$ for both the specimens. This rough estimation implies that near all the titanium on the free surface and on grain boundary interface was reduced to Ti^{3+} after completion of steps A and B.

3.3 – Post-irradiation tritium release by TPD tests

Theory and modeling of gas desorption from surface of specimens when annealed by heating ramps is well developed [12, a “classical” paper], algorithms being similar to those developed for reaction kinetics study [11], although the related parameters have different meanings. The most commonly applied procedures in the TPD signal diagnostics (thermal desorption analysis) have been reviewed and compared by Jong and Niemantsverdriet [13]. According to these authors the “heating rate (β) variation” method (based on the exploiting of the best fitting of the experimental couple β/T_p^2 versus $1/T_p$ with eq.7) is particularly attractive when a number of spectra corresponding to the same initial coverage are recorded at different β 's. For various kind of Li_2TiO_3 pebbles and pellets “ β -variation” data and analysis were reported by several authors [3, 14, 15] by assuming the desorption rate was following Arrhenius type law $k_d = A \exp(-E_a/RT)$. Most of these data are plotted in Figure 4 where values obtained at a single β (5 K/min in this work) are also reported. In spite of so much different specimens and laboratories the log-plot shows a rough agreement among them, E_a ranging from 35 to 55 kJ/mol. By the equation (7) the couples E_a and A values were inserted in equation (7) to calculate the desorption rate constants and time constants (Table 3) which had to be consistent with isothermal annealing tests [3, 4, 14] whose roughly estimated time constants are reported in the last column of Table 4.

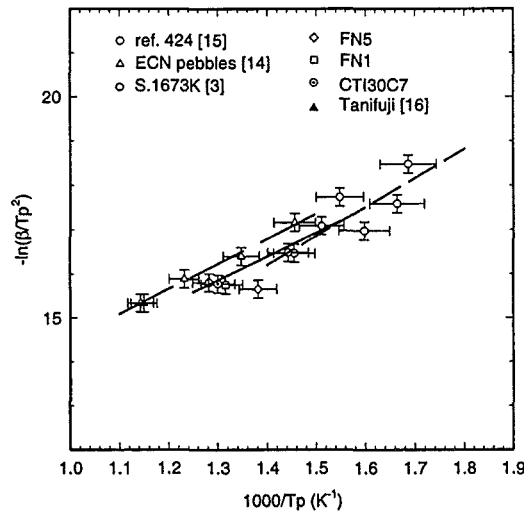


Fig.4: β -variation method (parameters fitting the equation 7 in table 3) applied to different Li_2TiO_3 materials.

Table 3 – Kinetic parameters for TPD tritium desorption from Li_2TiO_3 by the “ β -variation” method by best fitting the data with equation (7).

Specimen type	Activ. energy: E_a (kJ/mol)	Pre-exponential factor: A (s^{-1})	Rate const. at 623K k_d (s^{-1}) (eq. A-4)	Time const. at 623K τ_{623} (hours)
ref 424 pellets [15]	54 (35)	5.47	$1.6 \cdot 10^{-4}$	1.7
S. 1673K [3]	44 (55-60)	0.73	$1.35 \cdot 10^{-4}$	2.0
ECN pebbles [14]	47	0.8	$0.9 \cdot 10^{-4}$	3.1

Really the “ β -variation” method was considered to be “moderately accurate” [13] for the evaluation of E_a even when desorption from a single type of surface site is considered. Surfaces of complex polycrystals are always characterized by a set of desorption defect-sites and the relative TPD spectrum de-convolution is affordable if they are reciprocally **independent** sites, so that the overall signal results from the overlapping of the single contributes, as eq.4 suggests. However Kopasz recognized that this condition did not hold since the de-convoluted peaks population evidently changed by shifting β from 2 to 5 K/min in the TPD spectrum analysis of tritium desorption in He [4]. For $\beta = 5$ K/min we observed a single broad peak for almost all the investigated materials with density below 82% of TD. This peak was assumed to result from the overlapping of first order rate single peaks. Elaboration of the dominant peak allowed to determine the kinetic parameters reported in Table 4. Desorption time constant values ($k_d = A \exp(-E_a/RT)$) are an order of magnitude higher than those of Table 3. Deconvolution-fitting by assuming second order reaction steps give simpler results with E_a values closer to those of the “ β -variation” method (see for example Fig.s 6,7) but it is difficult to get characteristic rates and time constants if the initial tritium and protium concentration in the material are not well known. It is important to note that in any case the shape analysis gives kinetic parameters for the dominant peak of the peak-clusters corresponding to rate constants in rough agreement with other isothermal annealing tests (performed at temperatures $< T_p$), (Table 4). Mean values characterizing this main peak whatever the specimen of Table 4 are $T_p = 760 \pm 20$ K, $E_a = 126 \pm 5$ kJ/mol, and $A = 9.8 \cdot 10^5 \text{ s}^{-1}$, and they give the temperature $T_{\tau=1 \text{ day}} = 603 \pm 20$ K for “one day” tritium retention time, a value in agreement with that measured by in-situ irradiation tests for porous fine grained Li_2TiO_3 pellets (CEA, 82% TD) [5].

Table 4 – First order kinetic parameters of the main peak best fitting the spectrum deconvolution of the post irradiation TPD tritium desorption performed at $\beta = 5$ K/min on some pebbles-specimens

Porous pebbles	T_p (K)	g (%)	E_a (kJ/mol)	A (s^{-1})	k_d (s^{-1}) at 623 K	τ_{623} (hours)	τ_{623} calc. by (9) + (A-7)	τ by isothermal annealing tests
S 1673K	778	47	122	$3.5 \cdot 10^5$	$2.0 \cdot 10^{-5}$	14	20	$\tau_{573} \approx 17$ h [3]
S 1673K	789	49	115	$1.0 \cdot 10^5$	$2.3 \cdot 10^{-5}$	12	20	$\tau_{573} \approx 17$ h [3]
FN1	763	49	130	$2.0 \cdot 10^6$	$2.5 \cdot 10^{-5}$	11	2.2	$\tau_{673} \approx 1$ h [17]
FN1 red.	782	33	176	$1.6 \cdot 10^6$	$2.7 \cdot 10^{-5}$	10.3	2.2	
FN2	720	42	135	$9.0 \cdot 10^6$	$4.3 \cdot 10^{-5}$	7	2.2	$\tau_{673} \approx 1$ h [17]
RS11/1300	786	47	127.5	$8.9 \cdot 10^5$	$1.8 \cdot 10^{-5}$	15	4.3	$\tau_{573} \approx 2$ h [17]
Dense pebbles								*) in-situ tests
FN4-2/FN5	780	47	131	$1.2 \cdot 10^6$	$1.3 \cdot 10^{-5}$	22	16	* $\tau_{623} > 1$ day [5]
FN4-3/FN5	770	47	127.5	$9.8 \cdot 10^5$	$1.8 \cdot 10^{-5}$	15	16	* $\tau_{623} > 1$ day [5]
CTI30C7	770	33	117	$1.9 \cdot 10^5$	$2.8 \cdot 10^{-5}$	10	0.02	* $\tau_{623} > 1$ day [5]

It must be recalled in fact that this kind of time constants (τ) have nothing to do with the classical tritium retention times ($*\tau$) or with pebbles tritium inventory as measured by in-situ irradiation tests. They almost characterize the desorption steps (sites) occurring at temperatures “below” the measured T_p . Miller [3] was the first to show how a large fraction of the tritium implanted in Li-titanate pebbles could be removed by isothermal annealing at 873 K with a time constant ($\tau_{873} \sim 10$ h) much larger than that measured at 673 K ($\tau_{673} \sim 2$ h).

In the Appendix is briefly recalled how the material grain size (or the equivalent average radius $a = gs/2$) affects the desorption (A-4) and diffusion (A-5, A-6, A-7) constant rates characterizing tritium release from porous Li-ceramics with fully open porosity. In particular equation (8) (A-6 in Appendix) relates T_p with Q_a , β and a when the gas release rate is controlled by the thermally activated diffusion [12, 13, 19].

$$\frac{Q_a}{RT_p^2} \cong \frac{\pi^2 D_o \exp(-Q_a / RT_p)}{\beta a^2} \quad (8)$$

Bulk diffusion coefficients (D) for tritium in irradiated Li₂TiO₃ single crystals were reported by Tanifuji et al [16] between 625 and 1373 K and they were best fitted by the equation (9)

$$D[\text{cm}^2/\text{s}] = 0.1 \exp(-104[\text{kJ/mol}]/RT) \quad (9)$$

For porous specimen with interconnected porosity the bulk diffusion path should be close to grain radius *a*. Values which satisfy eq.s (8) and (9) are plotted as solid line in Figure 4 for $\beta = 5$ K/min. In this Figure the measured (*a*; *T_p*) data-points for the various specimens are also reported.

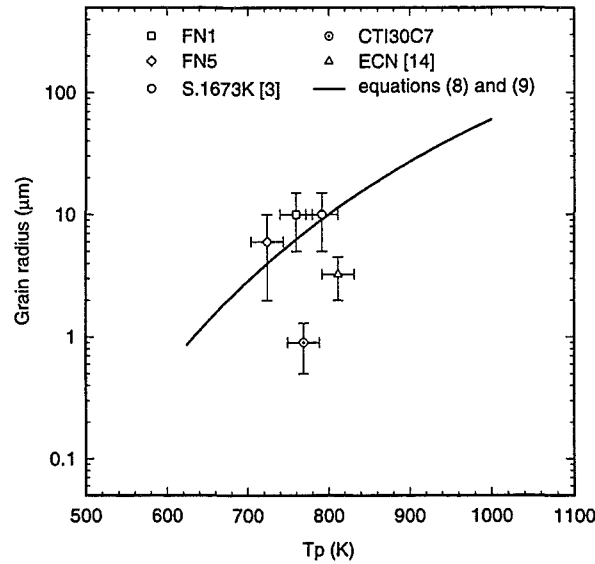


Fig 5: Grain radius (*a*) vs. peak temperature (*T_p*) of tritium release TPD spectra ($\beta = 5$ K/min) of some pebbles-specimens as compared to the equation (8) as evaluated by the Tanifuji's equation (9).

This Figure and the diffusion time constant τ_{623} evaluated by the equation (A-7) of the Appendix (8th column of Table 4) for $T = 623$ K seems to be good enough for porous specimen with $2 \mu\text{m} \leq a \leq 40 \mu\text{m}$ corresponding to $625 \leq T_p \leq 978$ K respectively to retain tritium release TPD spectra determined by the diffusion control.

For fine grains near fully dense pebbles an alternative effective diffusion path must be considered. Density play a role above the "percolation" transition from fully open to closed porosity occurring around 85 % of TD. Conservation of fine microstructure by increasing density lead to an increase of the grain boundary interface, and these kind of dense with fine grains pebbles showed in fact TPD spectra with evident "shoulder" contributing peaks at in the high temperature zone [20]. This phenomenon was very well demonstrated to occur for Li₂O ceramics [21]. However heavy thermal annealing or/and irradiation could put in better evidence this phenomenology also for Li-metatitanate pebbles. Well detectable high energy tritium trapping were in fact observed to occur in reduction-annealed CTI30C7 as irradiated at near room temperature [9]. The deconvolution analysis of those TPD spectra is reported in Figure 6.

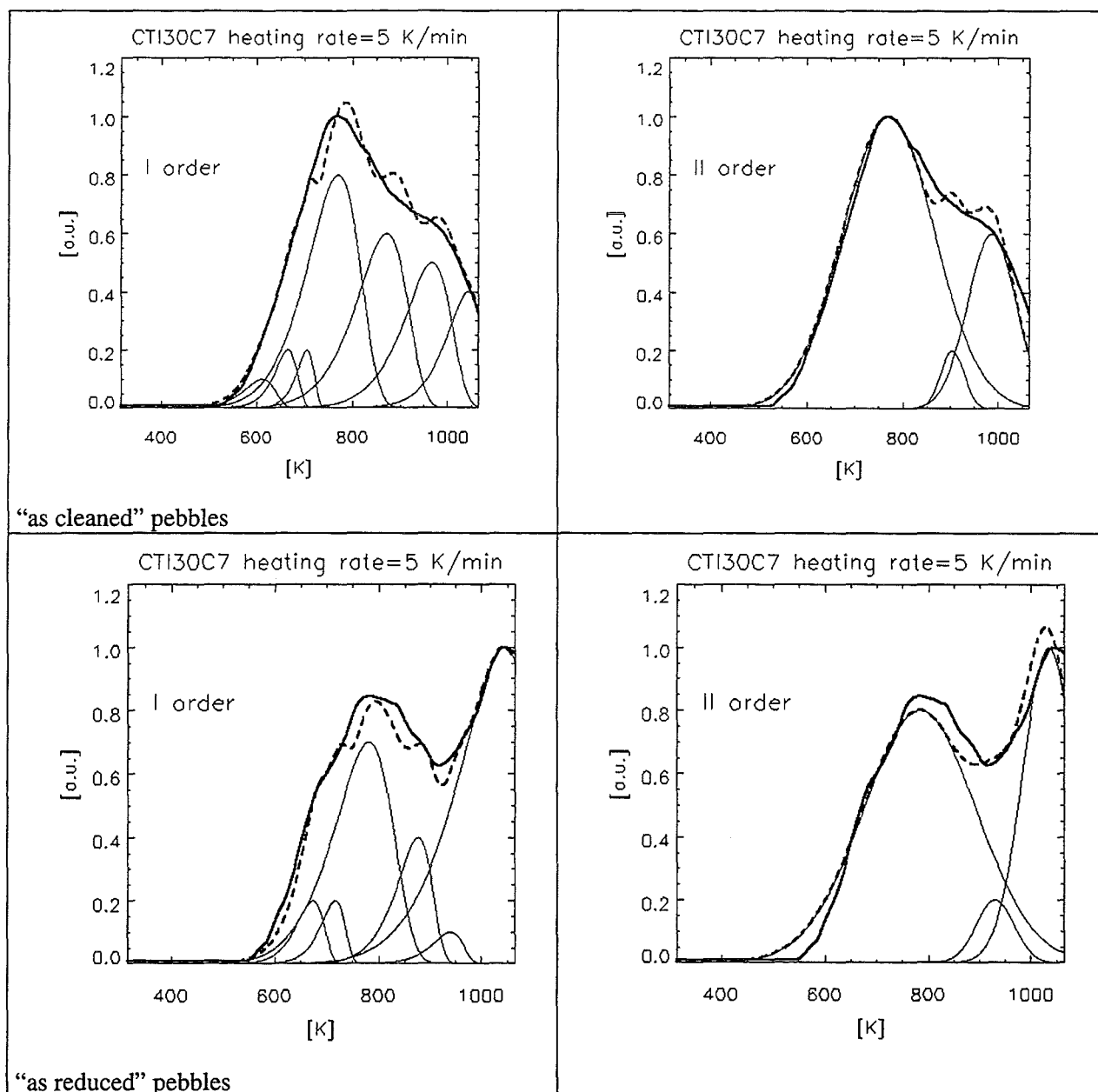


Figure 6: Deconvolution-fitting images of the TPD spectra obtained for the CTI30C7 pebbles reported in the Figure 2 of reference [9].

It is interesting to note how the difference between the spectra determined by the different pre-treatments play a role in changing the sites (peaks) population while their shape and position is conserved. Pebbles with large grains (small grain boundary interface area) were not found to show this kind of tritium trapping [9].

A pebble specimen with properties similar to CTI30C7 was irradiated in EXOTIC-8/1 at 1.9 Li-burnup at about 773 K. When tested by TPD by $\beta = 5$ K/min a peak with T_p above 1000 K was observed with characteristics close to those characterizing the last one of Figure 6 obtained in quite different conditions. Quantitative analysis on these spectra is not easy or even not allowed. However it is interesting to relate their high temperature part in which the “reduction” process of the specimen surface and grain boundary interface should occur (Figure 2, A and B peaks) simultaneously. By one side the presence of H_2 in the purge gas seems to help tritium removal from the high energetic trapping site by generating oxygen vacancies (or Ti^{3+} species). By the other side this “reduction” process seems

to increase the room temperature tritium trapping in short Li_2TiO_3 irradiation tests. Since the first case is expected to occur in real operating conditions of breeding blankets (as well as in “in-situ” tritium extraction tests) we may conclude that H_2 addition to the He purge should increase the tritium removal rate from lithium titanate pebbles. Grain boundary plays in any case a big role on the tritium transport phenomena for this breeder material.

4. CONCLUSIONS

The TPR/TPD methods were applied to examine the chemical interaction of R-gas purge and the tritium release kinetics for Li_2TiO_3 pebbles. It was not possible to develop a complete quantitative elaboration of the experiments because the complex microstructure of the materials (available theory and diagnostic criteria refer to ideal systems), bad control of initial conditions (coverages) and limited variation of the “perturbing mode” (as heating rate β parameter) imposed to the specimens. However it was possible to examine the main characteristics of the chemical interactions of the R-purge gas with the surface and the grain boundary interface preceding the bulk reduction observed to occur at 1173 K for these materials [9]. These processes were found to be related to the irradiation behavior of fine grains dense pebbles, they explain a positive role of H_2 addition to the purge for remove the tritium from the most energetic chemisorbing sites. On the same time the generated O-vacancies by the reduction step at the material grain boundaries were found to trap most of the tritium generated in low temperature irradiation tests, and this fact could explain the negative role of H_2 observed in the very first post-irradiation thermal-desorption rate measurements [3, 4].

These reduction processes are not acting at temperatures below 800 K. TPD diagnostics in this zone is roughly satisfying for porous pebbles with homogeneous grain size distribution. Diffusion control for tritium removal rate was roughly fitting the data. Deconvolution-fitting based on simple overlapping of first-order rate single steps gave reasonable values for the main contributors to the kinetics of the process.

Considering as determining second order rate steps for tritium desorption gave simpler deconvolution patterns with activation energies fitting better those observed by in-situ tests [5], and this is in agreement with a diffusion rate control. A mixed overall diffusion-desorption rate should in fact emphasize the role of the “recombination” step in the scheme (3) which is a second-order process and the use of the Lyndeman equation type (eq. (A-8) in Appendix) must be considered in TPD modelling. However in this case the experimental control of the initial conditions should be assured that was not the case in the present work.

REFERENCES

- [1] S. Malang, “Limitations on blanket performance, Fusion Engineering and Design” 46 (1999) 193-206
- [2] M. Ferrari et al. “ITER reference breeding blanket design”, Fusion Engineering and Design 46 (1999) 177
- [3] J.M. Miller, H.B. Hamilton and J.D. Sullivan, “Testing of lithium titanate as an alternative blanket material”, J. Nucl. Mater. 212-215 (1994) 877-880.
- [4] J.P. Kopasz, J.M. Miller and C.E. Johnson, “Tritium release from lithium titanate, a low-activation tritium breeding material”, J. Nucl. Mater. 212-215 (1994) 927-931
- [5] J. G. van der Laan et al., “Irradiation performance and tritium release characteristics of solid breeder materials – an update on results from EXOTIC-8”, Proceeding of the CBBI-8 (A. Ying editor), Oct. 6-8, 1999, Colorado Springs, Colorado, USA, pp 81-88. Proc. of the 7th International Workshop on Ceramic Breeder Blanket Interactions (CBBI-7), editor: J.G. van der Laan (NRG, ex ECN), Petten, The Netherlands, 14-16 September 1998, pp 4-9 to 4-20.
- [6] A.K. Fisher, “Processies for desorption from LiAlO_2 treated with H_2 as studied by temperature programmed desorption”, Fusion Technology 19 (1991) 1012-1017

- [7] C. Alvani et al. Fabrication of Li_2TiO_3 pebbles by a sol-gel (wet) route, ENEA internal doc.INN/NUMA/MATAV(99)1.
- [8] C. Alvani et al., "Lithium titanate pebbles reprocessing by wet chemistry", *J. Nucl. Mater.* 289 (2001) 303-307
- [9] C. Alvani, P.L. Carconi, S. Casadio and N. Roux, "Effects of pre-treatments of Li_2TiO_3 pebbles on the release of tritium generated during short irradiations"; *Fusion Engineering & Design* XX (2001) YY.
- [10] C. Alvani, P.L. Carconi, S. Casadio, F. Pierdominici, "Effect of Li_2TiO_3 pebbles characteristics on tritium release properties by out-of-pile TPD under $\text{He} + \text{H}_2$ (0.1%) gas purging", *Proc. of the 7th International Workshop on Ceramic Breeder Blanket Interactions (CBBI-7)*, editor: J.G. van der Laan (NRG, ex ECN), Petten, The Netherlands, 14-16 September 1998, pp 4-69/80
- [11] R.K. Agrawal, "Analysis of non isothermal reaction kinetics". "Part 1. Simple reactions", *Thermochemica Acta*, 203 (1992) 93-110, and "Part 2. Complex reactions". *Thermochemica Acta*, 203 (1992) 111-125
- [12] R.J. Cvetanovic, Y. Amenomiya, "Application of a Temperature-Programmed Desorption Technique to Catalysis Studies", *Advanced Catalysis*, 17 (1967) 103-149; and *Catal. Rev.* 6(1) (1972) 21-49
- [13] A.M. de Jong and J.W. Niemantsverdriet, "Thermal desorption analysis: comparative test of ten commonly applied procedures", *Surf. Sci.* 233 (1990) 355-365
- [14] J.G. van der Laan and R.P. Muis, "Properties of lithium metatitanate pebbles produced by a wet process", *J. Nucl. Mater.* 271&272 (1999) 401-404
- [15] J. Mougin, B. Rasneur, N. Roux, "Tritium and Helium release from Li_2TiO_3 comparison with Li_2ZrO_3 ", *Proceedings of International Workshop on Ceramic Breeder Blanket Interaction (CBBI)*, Editor: C.E. Johnson (ANL), UCLA, June 22-24, 1994, pp 227-235
- [16] T. Tanifuji, D. Yamaki, S. Nasu and K. Noda, "Tritium release behavior from neutron-irradiated Li_2TiO_3 single crystal", *J. Nucl. Mater.* 258-263 (1998) 543-548
- [17] L. Pena, S. Lagos, R. Rebecca, J. Jimenez, "Effect of pebble size and microstructure on tritium release by isothermal annealing", *Proc. of the 7th International Workshop on Ceramic Breeder Blanket Interactions (CBBI-7)*, editor: J.G. van der Laan (NRG, ex ECN), Petten, The Netherlands, 14-16 September 1998, pp 4-21/32.
- [18] A.K. Fischer, "Temperature programmed desorption from LiAlO_2 treated with H_2 ", *J. Nucl. Mat.* 191-194 (1992) 235-239
- [19] P. Basu, J.T. Yates, *Surface Science* 177 (1986) 291-313
- [20] C. Alvani, P.L. Carconi, S. Casadio, F. Pierdominici, "Effect of Li_2TiO_3 pebbles characteristics on tritium release properties by out-of-pile TPD under $\text{He}+\text{H}_2$ (0.1%) gas purging", *Proc. of the 7th International Workshop on Ceramic Breeder Blanket Interactions (CBBI-7)*, editor: J.G. van der Laan (NRG, ex ECN), Petten, The Netherlands, 14-16 September 1998, pp 4-69/80.
- [21] T. Tanifuji, D. Yamaki, T. Takahashi, A. Iwamoto, "Tritium release from neutron irradiated Li_2O sintered pellets", *J. Nucl. Mat.* 283-287 (2000) 1319-1423
- [22] D.R. Olander, P. Van Uffelen, "On the role of grain boundary diffusion in fission gas release", *J. Nucl. Mater.* 288 (2001) 137-147

APPENDIX

tritium desorption TPD spectrum analysis

Tritium and helium generated by the fission ${}^6\text{Li}(n,\alpha)\text{T}$ in polycrystalline specimens during irradiation are trapped as defects or from the defects of the materials whose annihilation will produce their desorption. An oversimplified reaction scheme of the tritium removal mechanism from these Li-oxides defects neglects (because "fast") inter-grain and intra-grain diffusion and assumes surface desorption rate control. The average (in space) overall concentration C of tritium generated at the rate q [g.atoms.cm³.s⁻¹] inside a specimen of volume V [cm³] during irradiation is given by the mass balance equation

$$V q dt - V dC = h(C-C^*)S dt = F P_T dt \quad (\text{A-1})$$

where C^* is the tritium concentration on the breeder material surface exposed to the purge gas flowing at the rate F , and P_T is the tritium concentration in the purge gas, h the mass transfer rate coefficient, S specimen surface and t the time. For spherical particles of radius a ($S/V = 3/a$) and for post irradiation annealing step ($q = 0$) (A-1) reduces to

$$\frac{F P_T}{V} = \frac{dC}{dt} = -\frac{3h}{a}(C - C^*) \cong -k_d(C - C^*) \quad (\text{A-2})$$

whose integration (under isothermal conditions) with the limit $C(t \rightarrow \infty) = C^*$ leads to

$$\frac{C - C^*}{C_i - C^*} = \alpha(t) = 1 - \exp(-k_d t) \quad (\text{A-3})$$

where $\alpha(t)$ is the fractional tritium release, the product $V(C_i - C^*)$ representing the total removable tritium during the desorption annealing step. For a thermally activated desorption process, the eq.(12) holds with the pre-exponential factor A including the microstructural grain radius parameter a and where the time constant τ represent the tritium residence time (63% of the steady state value) in the specimen.

$$\frac{1}{\tau} = k_d = \frac{3h}{a} = A \exp(-E_d / RT) \text{ [s}^{-1}\text{]} \quad (\text{A-4})$$

In a first approximation equation (A-4) may hold for each site, and under linear heating rate the temperature derivative of α_i assumes the form (3) and the maximum tritium desorption rate from each site (i) during the heating ramp will occur at the temperature $T_{m,i}$ following the eq.s (5-7).

By evaluating A_i and $E_{d,i}$ from the correlation (7) (or by the integral TPD spectra analysis) it is in principle possible (eq. A-4) to get the τ value at the needed temperature by an appropriate coupling (see eq.4 for example) of the single contributes [13]. The above described step-wise desorption consider fast the diffusion toward the recombination desorption sites once tritium is debonded from a defect.

The case for which tritium diffusion inside the grains becomes rate controlling presents mathematical complexity in TPD theory. Since the diffusion coefficients (D) are in general a thermally activated process

$$D = D_o \exp\left(\frac{-Q_d}{RT}\right) \quad (\text{A-5})$$

approximate procedures [12, 13,14] give the relationship (A-6) characterizing the peak maximum D_m - T_p couple of values

$$\frac{E_a}{RT_p^2} \approx \frac{\pi^2 D_m}{\beta a^2} \cong \frac{\pi^2 D_o \exp(-Q_a / RT_p)}{\beta a^2} \quad (\text{A-6})$$

Here a is the typical diffusion path. Its lowest limit may be attributed grain radius ($a \sim (g.s.)/2$) of the material of the pebbles. Also in this case the D_o , Q_a couple from (A-6) gives D by (A-5) and the tritium retention time by the relationship (A-7) characterizing diffusion rate control

$$\tau \cong \frac{\pi^2 D}{a^2} \quad (\text{A-7})$$

Since both the desorption control (through pre-exp parameter A_i) and diffusion control of the tritium release rate depend on grain size, specimens with a complex grain size distribution will give a complex TPD spectrum which is convoluted to that due to the energetically different defect sites. Much more complex is the case in which diffusion acts while desorption occurs, which should be often the case. In that case, by assuming acting the thermodynamic equilibrium the isotopic exchange (2), the reaction rate of (1) results [6]

$$r_d = -\frac{d\theta}{dt} = \frac{k_d k_2 \theta_1^2}{k_{-2} \theta_1 + k_d} \quad (\text{A-8})$$

where θ_1 and θ are the dissociated hydroxide and undissociated water surface coverage respectively. For $k_{-2} \gg k_d$ the desorption rate remains within the frame of first order reaction rates. On the other end ($k_d \gg k_{-2}$) we have a second order reaction rate which is controlled by k_2 , that is the case of pure diffusion control of the desorption process.

Li₂TiO₃ pebbles reprocessing, recovery of ⁶Li as Li₂CO₃

C. Alvani, S. Casadio, V. Contini, A. Di Bartolomeo, J.D. Lulewicz^a and N. Roux^a

C.R. ENEA Casaccia, via Anguillarese Km 3.01 00060 ROMA (Italy)

a : C.E.A.- C.E. Saclay, 91191- GIF sur Yvette Cedex (France)

A process for obtaining Li₂CO₃ from Li₂TiO₃ powder by wet chemistry was developed. This is considered useful in view of the recovery of ⁶Li isotope from a lithium titanate breeder burned up to its end of life in a fusion reactor. The process was optimized with respect to the chemical attack of titanate and the precipitation of carbonate from aqueous solutions to get a powder, with the chemical and morphological characteristics, suitable for its re-exploitation in the fabrication of Li₂TiO₃ pebbles. Reprocessing was also planned to adjust the ⁶Li concentration to the desired value and to obtain homogeneous distribution in the powder batch. Further development concerning reprocessing of sintered Li₂TiO₃ pebbles is in progress exploiting the results obtained with lithium titanate powders

1 - INTRODUCTION

Lithium titanate is one of the most promising candidate for tritium breeding [1]. The temperature of tritium release from polycrystalline Li₂TiO₃ ceramic pellets and pebbles was found lower than from many other Li-ceramics [2,3]. This material shows also good chemical stability to the air environment and acceptable mechanical strength [4], a review of the preparation, properties, irradiation performance and tritium release of lithium containing ceramics has been published [5],[6]. Beyond the chemical and physical characteristics of a Li-based ceramic breeder, its ⁶Li enrichment must be taken into account too. Neutronics analyses indicate, for Li₂TiO₃ pebbles with a mass density of 90% TD, a ⁶Li enrichment of 55-65 at% and a maximum burn-up of 14.6 at% for the HCPB Demo blanket [7].

The objectives of this activity were to investigate about the feasibility of reprocessing Li₂TiO₃ pebbles, at their "end-of-life" and still containing 40-50 at% of ⁶Li, in order to: i) recover ⁶Li isotope as Li₂CO₃ with the suitable chemical and morphological characteristics, requested for the reference fabrication route (extrusion) of Li₂TiO₃ pebbles [4] and reported in table 1, and ii) increase the depleted ⁶Li concentration, to the value foreseen for this type of ceramic breeder, assuring moreover a fully homogeneous distribution of ⁶Li isotopes.

Table 1 : Some characteristics of the requested Li₂CO₃ powder.

Bed apparent density	0.45 g/cc
Specific surface area	1-1.5 m ² /g
⁶ Li conc.	55-65 at%
Main impurities (ppm):	
Al	20
Ca	35
Fe	9
K	30
S	10
Si	20
Zr	10

2 - EXPERIMENTAL

Lithium titanate powder, obtained by solid state reaction between lithium carbonate and titania, was used for a preliminary set-up of the preparation procedure. This was planned for two principal steps:

- A) attack of the Li_2TiO_3 by wet chemistry, to separate completely Li from titanium and obtain a lithium solution,
- B) recovery of Li as Li_2CO_3 including, in this last step, the above mentioned objective (ii) taking into account the chemical characteristics of the produced Li-solution from step (A).

2.1 - A : Lithium separation from Li_2TiO_3

Two chemical methods were tested, the first (A-1) was based on our previous experience [8] on producing reprocessed lithium titanate powders by using H_2O_2 to dissolve Li_2TiO_3 ; within the second (A-2), lithium was leached from titanate by using an HNO_3 solution.

2.1.1 - Li_2TiO_3 attack by H_2O_2 (A-1)

The dissolution of lithium titanate in hydrogen peroxide produced a clear yellow solution of Li-Ti-peroxo-complex through the following reaction that can be schematically inferred:



The reaction was carried out at the following experimental conditions:

- 20°C with a cooling system for 24 hours,
- [Li] concentration = 0.91 Mol/L,
- H_2O_2 concentration 12 w%.

$\text{Li}_4\text{Ti}_5\text{O}_{12}$ and traces of TiO_2 , already present in the starting material, remained as insoluble phases and were identified by X-ray diffraction measurements (fig 1) performed on the filtered material just after reaction (1).

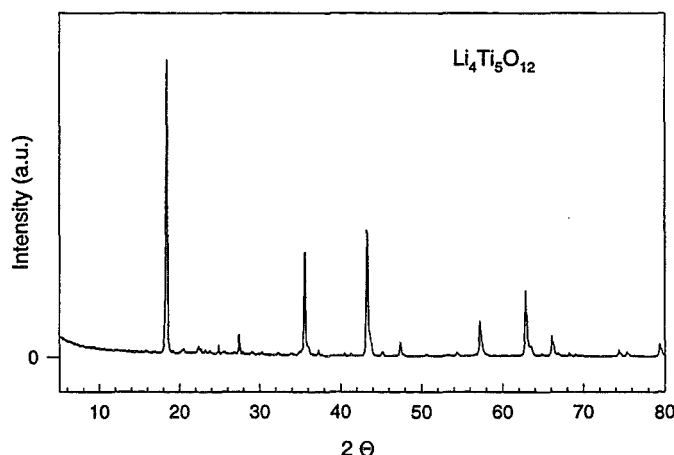


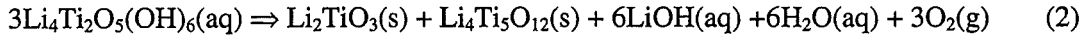
Fig. 1 : X ray diffraction pattern ($\text{Cu K}\alpha$) of the insoluble residue (about 4 w% of the starting powder) obtained after dissolving Li_2TiO_3 in H_2O_2 at low temperature x 24 hours. The principal phase is $\text{Li}_4\text{Ti}_5\text{O}_{12}$, traces of TiO_2 are also present.

The yellow peroxo-complex solution was not stable and could be easily decomposed, with oxygen evolution and pH increase, into a Li-containing solution and a solid phase. This "condensation",

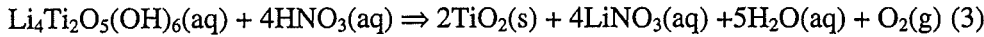
carried out at 80°C for two hours, produced different species depending on the final pH that was varied by adding different amounts of HNO₃.

From XRD analysis, on the dried and calcined solids, the following reaction could be inferred:

1) at pH>12, without acid addition, only 50% of total Li could be transferred into the liquid phase:



2) at pH<2 with a ratio [HNO₃]/[Li] ≈ 1.26, lithium was quantitatively recovered into the acid solution:



The XRD patterns of the solid products of the above reactions (2) and(3) are shown in fig. 2 while a rough quantitative analysis at intermediate pH values is reported in table 2.

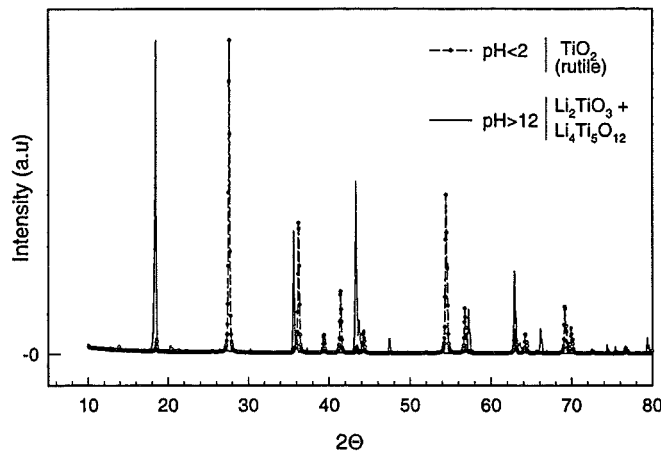


Fig. 2: X ray diffraction patterns (Cu Kα) of the solid phases, dried and calcined at 800°C, produced by the reactions (2) and (3).

Table 2: Quantitative evaluation of the solid phases produced by decomposition of the Li-Ti-peroxo-complex solution as a function of the final pH.

pH	Li ₂ TiO ₃	Li ₄ Ti ₅ O ₁₂	TiO ₂ (rutile+anatase)
>12	50%	50%	traces
7	-	70%	30%
6	-	50%	50%
3	-	15%	85%
<2	-	traces	≈ 100%

2.1.2 - Li₂TiO₃ attack by HNO₃ (A-2)

The experimental activity within the chemical attack by nitric acid, firstly abandoned, was resumed owing to the following considerations: I) the use of HNO₃ was found unavoidable, in the above described procedure, for a complete separation of lithium from titanate, II) this type of ceramic breeder will probably contain, at its end of life, a certain amount of Li₄Ti₅O₁₂ insoluble in H₂O₂. Some considerations about the amount of this last phase are reported in appendix 1.

Experiments were performed in order to minimize the amount of HNO₃ necessary for a complete Li extraction according to the following foreseen reaction:



Temperature and time were optimized in order to be compatible with a practical application of the process. The best results were obtained by leaching at the following conditions:

- boiling point under reflux for 6 hours,
- [Li] concentration = 0.91 Mol/l
- [HNO₃] concentration = 1.15 Mol/l like in the reaction (3).

According to the procedure A-1, the resulting solid phase was dried and calcined at 800°C. The X ray diffraction pattern, reported in fig. 3, showed the characteristic peaks of a TiO₂ rutile and anatase mixture without the presence of Li-containing phases. Therefore it was concluded that lithium was extracted also from Li₄Ti₅O₁₂ already contained in the starting material. This feature of the process will be in any case investigated by using pure Li₄Ti₅O₁₂ as raw material and will be the object of future activity.

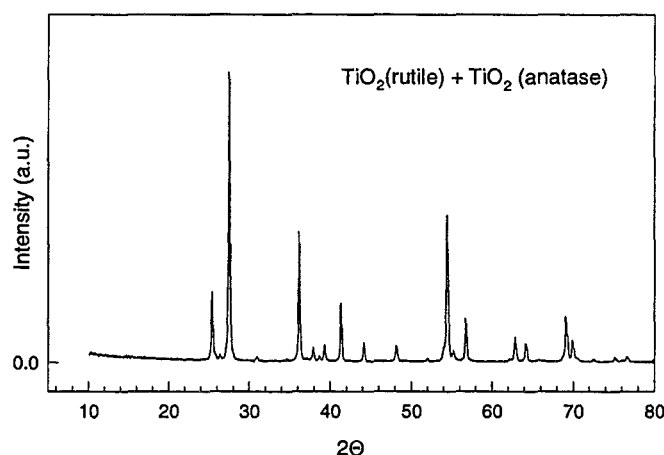


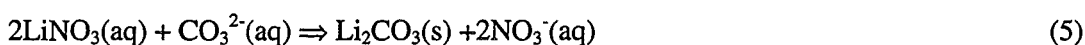
Fig. 3: X ray diffraction pattern (Cu,K α) of the calcined solid obtained after leaching Li₂TiO₃ in HNO₃. No Li-containing phases were detectable.

2.2 - B : Lithium recovery as Li₂CO₃

Lithium nitrate solutions were obtained from the above described procedures, moreover an excess of HNO₃ was necessary to assure a complete Li-Ti separation.

Thermal decomposition of lithium nitrate from the dried solutions and subsequent reaction with CO₂ of the formed oxide, was excluded due to problems arising in the control of the final morphology of the powder.

Therefore, owing to the quite low water solubility of Li₂CO₃, the final reprocessing step was addressed optimizing the precipitation of lithium by means of a carbonating agent in aqueous solutions as reported schematically:



Since this reaction is possible only at high pH, addition of an excess of a strong base was necessary to neutralize the nitric acid and to rise the pH up to values >12. Good results were obtained by adding LiOH*H₂O.

The addition of lithium hydroxide, to adjust the pH at this step of the procedure, can be considered useful, in a real reprocessing, to increase the depleted ${}^6\text{Li}$ concentration assuring moreover a fully homogeneous distribution (objective ii) since the precipitation of carbonate occurs in an homogeneous solution with the already adjusted ${}^6\text{Li}$ concentration. Therefore a lithium hydroxide containing the proper amount of ${}^6\text{Li}$ should be considered for a future application of this type of reprocessing. The amount added in this work corresponded to a ${}^6\text{Li}$ increase from 45at% to 60at% provided $\text{LiOH}\cdot\text{H}_2\text{O}$ at 95at% of ${}^6\text{Li}$ was used. Detailed stoichiometric evaluation are reported in appendix 1.

Carbon dioxide, $(\text{NH}_4)_2\text{CO}_3$ and Na_2CO_3 were tested as carbonating agents; the concentrations and temperature were optimized to give an acceptable yield together with the requested morphological characteristics of the final product. The best results were reached by using Na_2CO_3 as precipitating agent on solutions coming from both A-1 and A-2 chemical attacks. The following experimental conditions were found to be the most suitable:

- 80°C with stirring,
- $[\text{LiNO}_3]$ concentration = 1.82 Mol/L,
- $[\text{LiOH}]$ concentration = 0.78 Mol/L,
- a molar ratio $[\text{Na}_2\text{CO}_3]/[\text{total Li}]=0.52$

In order to test the reproducibility of the procedures, several small batches of Li_2TiO_3 were reprocessed and characterized. Some characteristics of the obtained Li_2CO_3 powders are reported in table 3, together with the total and recovered Li related yields.

Figure 4 shows the X ray diffraction pattern of the final powder which was identified as monoclinic Li_2CO_3 according to the standard ASTM JCPDS-831454.

Table 3: Some characteristics of procedures and obtained Li_2CO_3 powders.

Property	Requested	Type of chemical attack	
		A-1	A-2
Total yield (%)	-	70 ± 5	75 ± 5
Recovered Li (%)	-	62 ± 5	70 ± 5
BET surface area (m^2/g)	$1 \div 1.5$	2.3 ± 0.1	2.8 ± 0.1
Bed apparent density (g/cc)	0.45	0.41 ± 0.02	0.39 ± 0.02
True density by He picnometry (g/cc)	-	2.08 ± 0.01	2.09 ± 0.01

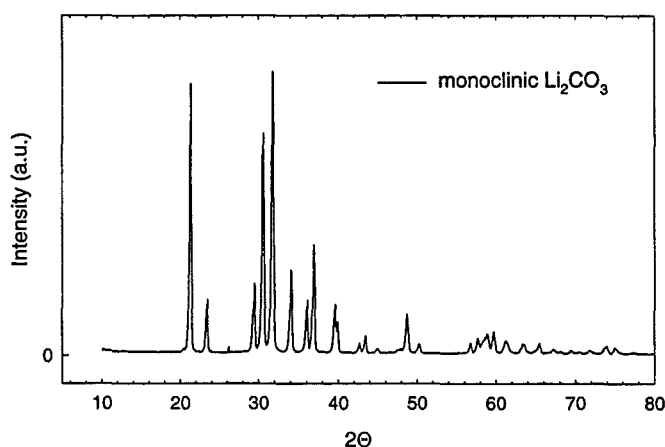


Fig. 4 : X ray diffraction pattern of monoclinic Li_2CO_3 obtained from reprocessing of Li_2TiO_3 .

3 - CONCLUSIONS AND FUTURE WORK

The set-up of the parameters suitable for recovery of lithium carbonate from titanate was performed following the schematic flow-sheet reported in appendix 2. The activity was successfully addressed towards a quantitative separation of lithium from titanium oxide together with the recovery of a final product with the morphological characteristics very close to the requested ones. At this point of the reprocessing development the following considerations can be done:

- Differences on the yields obtained using A-1 and A-2 procedure can be attributed to the inability of H_2O_2 to dissolve the titanium rich phase $Li_4Ti_5O_{12}$ already contained in the raw material. In any case the evaluation of lithium extraction by the A-2 procedure from $Li_4Ti_5O_{12}$ will be the object of future activity.
- Efforts should be done in order to increase the efficiency of the precipitation step. Some problems probably arise from an increase of the Li_2CO_3 solubility due to a decrease of the activity coefficient in solutions at high ionic strength (the so called "salting-in" effect).
- Following measurements of the impurity content (especially Na) in the final product, possibly a further purification step should be planned.
- In order to simulate a real reprocessing of Li_2TiO_3 breeder, the efficiency of the set up procedures will have to be confirmed by using small batches of sintered pebbles. Taking into account that the reactivity of such samples will be almost certainly lower with respect to the up to now used powders, some variation of the process parameters will be probably necessary and will be extensively investigated trying to avoid a troublesome preliminary pebbles milling step. In addition within this activity a choice between the A-1 and A-2 processes will be done.
- The final experimental activity will be carried out with the production of a larger Li_2CO_3 batch suitable for the already mentioned reference fabrication route of Li_2TiO_3 pebbles.

REFERENCES

- [1] C.E. Johnson, G.W. Hollemberg, N. Roux, H. Watanabe, Fusion Eng. Des. 8 (1989) 145.
- [2] J.M. Miller, H.B. Hamilton, J.D. Sullivan, "Testing of Lithium Titanate as an alternative Blanket Material.", J. Nucl. Mater. 212-215 (1994) 877-880.
- [3] P. Kopasz, J.M. Miller, C.E. Johnson, "Tritium Release from Lithium Titanate, a Low-activation Tritium breeding Material.", J. Nucl. Mater. 212-215 (1994) 927-931
- [4] J.D. Lulewicz, N. Roux, "Optimization of Li_2ZrO_3 and Li_2TiO_3 pebbles.", CEA internal document CEREM/LECMA DT 98/94 (1998).
- [5] C.E. Johnson, K. Noda, N. Roux, J. Nucl. Mater. 258-263(1998)140-148.
- [6] K. Tsuchiya, H. Kawamura, "Development of Wet Process with Substitution Reaction for the Mass Production of Li_2TiO_3 pebbles." J. Nucl. Mater. 283-287 (2000) 1380-1384.
- [7] U. Fischer, P. Norajitra, "Neutronics and Thermal-mechanical Analyses for Design Variants of the EU Helium-cooled Pebble Bed Demo Blanket." Proc. of the 20th Symp. On Fus. Techn., Marseille, France 7-11 Sept. 1998, pg 1149-1152.
- [8] C. Alvani, P.L. Carconi, S. Casadio, V. Contini, A. Di Bartolomeo, F. Pierdominici, A. Deptula, S. Lagos, and C.A. Nannetti " Lithium Titanate Pebbles Reprocessing by Wet Chemistry", J. Nucl. Mater 289 (2001) 303-307.

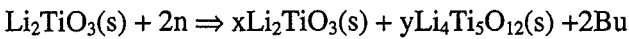
APPENDIX 1

Stoichiometric considerations

If we define the burn-up (Bu) as the atomic fraction of total lithium that will generate tritium, Bu will be the unique parameter necessary to calculate the amount of ${}^6\text{Li}$, to be added to the recovered lithium, to adjust its concentration. Since the procedure for the Li-Ti separation (step A) can be dependent from the chemical features of the burned breeder, some considerations about the possible composition, at its end of life, may be useful.

We assume that the irradiated lithium titanate will be out of pile annealed at high temperature, in order to extract the residual tritium. In these conditions we can consider, according to the $\text{Li}_2\text{O-TiO}_2$ phase diagram and after a limited burn-up (Bu), $\text{Li}_4\text{Ti}_5\text{O}_{12}$ in thermodynamic equilibrium with the unburned Li_2TiO_3 .

Therefore the total (in-pile + out of-pile) tritium production from neutron irradiation can be formally represented by the following equation:



Lithium mass balance imposes : $\begin{cases} 2x + 4y + 2\text{Bu} = 2 \\ \text{and the titanium mass balance : } x + 5y = 1 \end{cases}$

The solution pair (x,y) of the system of these equation, expressed as mol% of each phase, is grafically reported in fig 1A, for a burn-up up to 0.6.

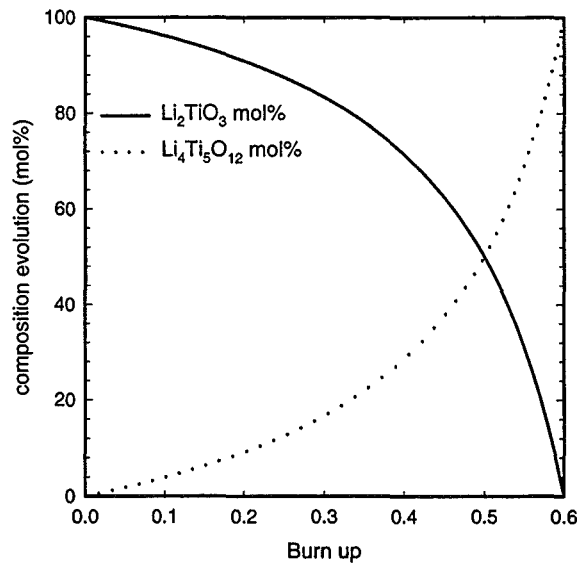


Fig. 1A Evolution of Li_2TiO_3 breeder composition as a function of burn-up. The low lithium content $\text{Li}_4\text{Ti}_5\text{O}_{12}$ phase is assumed to be in thermodynamic equilibrium with Li_2TiO_3 .

As suggested in ref [7], starting with stoichiometric Li_2TiO_3 90%TD, and a ${}^6\text{Li}$ enrichment of 60at%, the breeder material will undergo, at its end of life, to a burn-up of about 0.15 (or 15at%), resulting in a final composition of 93.75 mol% of Li_2TiO_3 and 6.25 mol% of $\text{Li}_4\text{Ti}_5\text{O}_{12}$, with a ${}^6\text{Li}$ concentration of 45at%.

To a practical point of view we can calculate (fig. 2A) the amount of ${}^6\text{Li}$ enriched $\text{LiOH}\cdot\text{H}_2\text{O}$ to be added to the total lithium recovered, for example from 100g of reprocessed breeder, to restore the ${}^6\text{Li}$ concentration at 60at%.

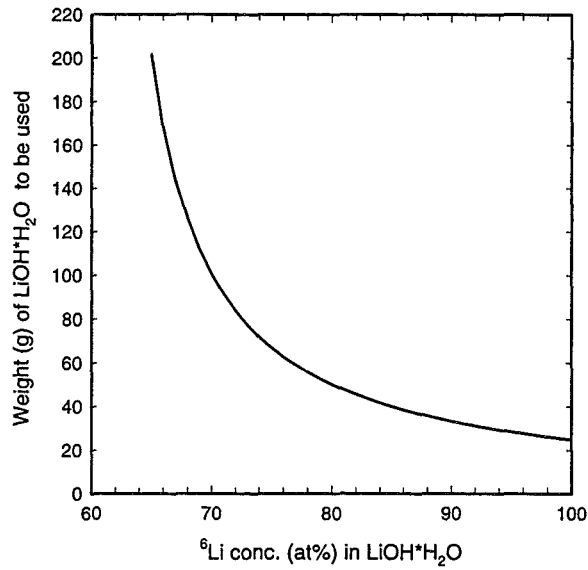


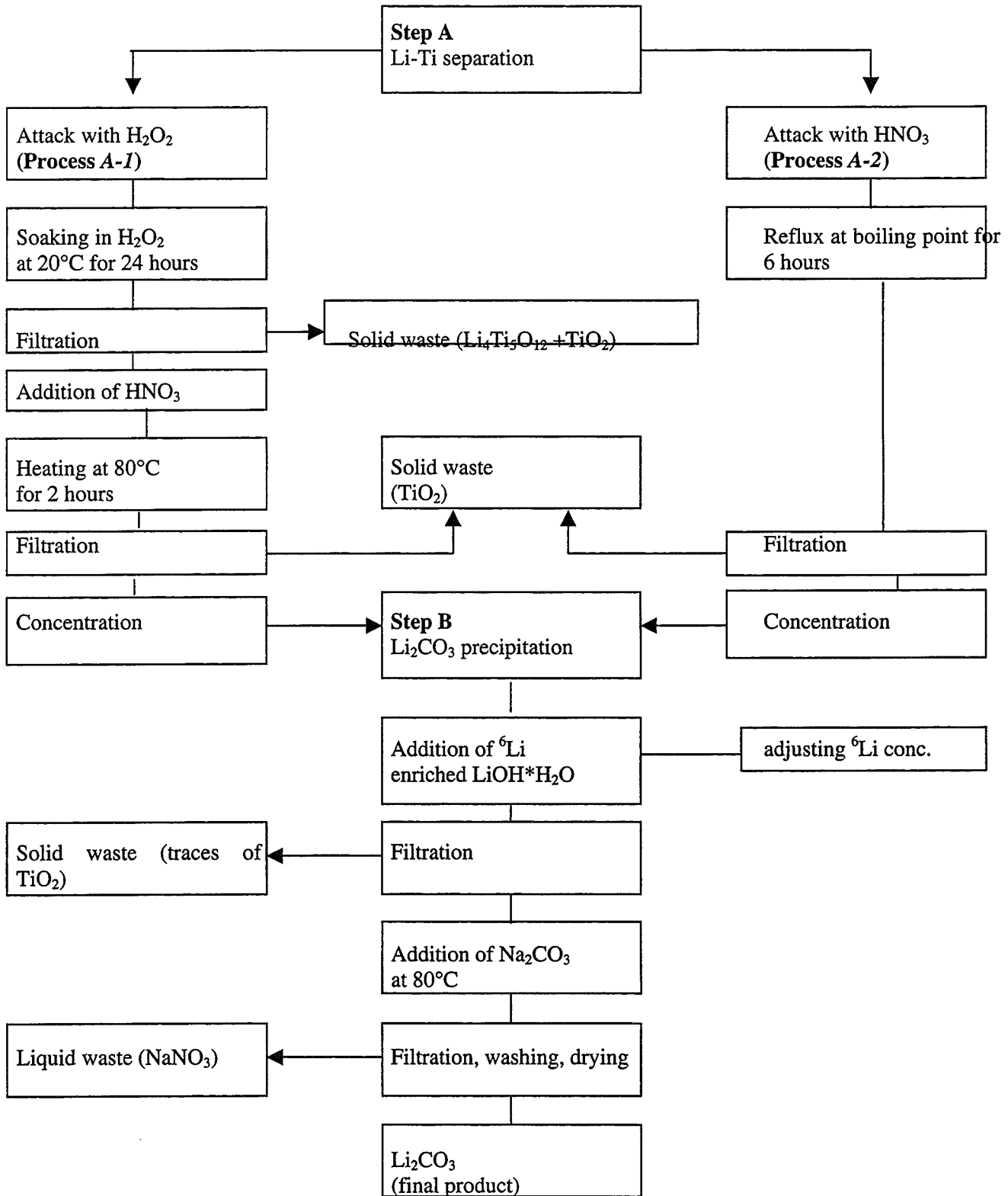
Fig. 2A : Quantity of LiOH·H₂O as function of its ⁶Li concentration to be used with reprocessing 100g of breeder (⁶Li 45at%) to restore ⁶Li concentration to 60at%.

As consequence of the above considerations it can be remarked that the amount of LiOH·H₂O, ⁶Li enriched at 95at% corresponds to that used for the optimization of the Li₂CO₃ precipitation in the step **B** of the experimental procedure.

LiOH·H₂O with 95at% of ⁶Li seems therefore the most suitable additive that could be used to match all the objectives foreseen in this type of reprocessing.

APPENDIX 2

Reprocessing flow sheet



Progress on pebble bed experimental activity for the HE-FUS3 mock-ups

G. Dell'Orco^a, L. Sansone^a, M. Simoncini^a and D. Zito^b

^aENEA Brasimone, PO Box 1, 40032 Camugnano (Bo) Italy

^bDipartimento Ingegneria Nucleare - Università di Palermo, V.le delle Scienze, 90128 Palermo, Italy

The EU Long Term for DEMO Programme foresees the qualification of the reference design of the Helium Cooled Pebble Bed (HCPB) - Test Blanket Module (TBM) to be tested in ITER Reactor. In this frame, FZK and ENEA have launched many experimental activities for the evaluation of the interactions between the Tritium breeder and neutron multiplier pebble beds and the steel containment walls. Main aim of these activities is the measuring the pebble bed effective thermal conductivity, the wall heat transfer coefficient as well as their dependency from the mechanical constraints. The paper presents the progress of the testing activity and results of the tests on two mock-up, called Tazza and Helichetta, carried out on the HE-FUS3 facility at ENEA Brasimone.

1. INTRODUCTION

ENEA has started a design of an experimental activity conceiving two mock-ups, called HELICA and HEXCALIBER, reproducing a small and a medium portion of the a TBM module with some adaptation for the experimental requirements. The test programme, to be carried-out in the ENEA HEFUS3 facility, will be mainly focused on the thermal-mechanical characterization of the beryllium multiplier and the selected Lithiate ceramics breeder, both in form of pebble beds. In 2000 ENEA has preliminarily launched an experimental activities on two mock-ups called Tazza and Helichetta. Tazza reproduces a cylindrical cell whilst Helichetta is a prismatic cell with an axial toroidal radial heating plate and two lateral cooling plates. The main aim of the experimental campaigns is the thermo mechanical characterization on Li_4SiO_4 , Li_2TiO_3 pebble beds at the design reference temperatures and with different mechanical boundary conditions. During the tests the pebble bed thermal conductivity, its variation during the thermal tests, the cooling plates deformations and the radial pressure loads are measured.

2. TESTS ON TAZZA MOCK-UP

2.1. Test objective

Tazza mock-up reproduces a simple cylindrical pebble bed cell with 40 mm in diameter and 160 mm in height, Figs. 1-2. This geometry was firstly used for the simulation and the preliminary assessment of the filling procedure of the polydispersed and binary Li_4SiO_4 (0.25-0.63 mm in diameter), Li_2TiO_3 (0.8-1.2 mm in diameter), Fig 3-4, and Beryllium pebble beds based on the Ultra Sound shaking method.

The filling method consists in the following actions:

- 1) The mock-up is filled with a quantity of pebbles (the large ones, in the case of binary beds) determined by the wanted height and the expected packing factor of the bed;
- 2) The mock-up is put in an ultra sound bath for a time from 6 to 20 minutes;
- 3) In the case of binary beds, a can (item #9, fig. 1) is slid into the test section, over the bed;
- 4) The "small" pebbles are poured into the can, which is blocked over the matrix of large pebbles by a plug (item #2);.
- 5) The mock-up is then sinked into the bath for 5-10 minutes of additional US shacking.

The mechanical properties of these pebbles were also measured by Uniaxial Compressive Tests (UCT) performed at room temperature on bed at different heights (20, 35, 50 and 100 mm). The load was applied by a cylindrical piston which can slide along the internal surface of the mock-up. The instrumentation consisted of a load cell at the bottom of the mock-up and a displacement transducer (LVDT) which measures the vertical displacement of the piston, Fig. 2.

2.2. Test results

A new filling method for binary or polydispersed beds was assessed by these experiments testing about 50 different beds. Very high packing factors were achieved by using an Ultra Sound bath for the pebble compaction. During the Uniaxial Compressive Tests (UCT), the load in the axial direction and the displacements of the piston were measured in order to obtain the pressure-strain characteristics, Fig. 5. These results were elaborated to obtain the Uniaxial Deformation Module (UDM), defined as the apparent Young's Module of the pebble bed. In Fig. 6, the ratio between the UDM and the Young modulus of the full dense material is reported versus the Packing Factors (PF) of the bed, [1]. The test results showed that the polydispersed beds behave more like a monosize bed than like a binary bed. Furthermore, the roughness of the pebbles seems to have a sensible influence on the PF whilst the higher PF the higher the UDM. The height of the bed seems to have a strong influence on the UDM. This is due to the fact that when the load is imposed from the top, the friction forces among the pebbles and between the pebbles and the containment walls dissipate it through the height of bed, thus giving a pressure field decreasing with the height of the bed. Therefore, the mean pressure in the bed is lower than would be in a full dense material in the same conditions of imposed stress, the strain is consequently lower than would be with an homogeneous pressure field, which is the condition for a correct calculation of the Young Modulus. As a result, the calculation for the UDM for higher beds gives higher numbers than for lower beds, Figs. 5-8.

On the basis of the TAZZA experimental results, the Department of Nuclear Engineering of the University of Palermo carried out the theoretical modelling of the TAZZA mock-up and its pebble bed using the Porous Elasticity and the Modified Drucker-Prager models modified to take into account the specific properties of the pebble bed with a particular reference to the effective elastic modulus on the pebble bed height [2].

3. TESTS ON HELICHETTA MOCK-UP

3.1. Test objective

At beginning of 2001, a new thermal test campaign on breeder pebble beds was conceived aiming at discriminating if the mechanical pre-cycling of the pebbles is necessary and if the load control on the rear zone of the pebble cell has some influence on the thermal parameter in a prismatic geometry. For such purpose, an AISI 316L steel mock-up, called HELICHETTA, reproducing a single breeder pebble bed cell, was exclusively designed by ENEA, Fig. 9. The tests, carried-out on both the reference breeder Li_4SiO_4 and Li_2TiO_3 pebbles, aim at investigating the influence of the pebble pressure pre-loading, both during the filling, at room temperature, and during the thermal tests, and the relevance of the cell orientation (horizontal and vertical) on the thermal behaviour as far as the pebble temperatures, their conductivities and the cell deformations are concerned. During the first half of 2001, this small test section was manufactured using available components (CP's, frame, heater etc.). It reproduces two symmetric prismatic breeder cell divided by an axial electrical resistor. The main dimensions of the breeder cells are 485 mm in length, 100 mm in width and 10 mm in bed thickness. The cells are laterally closed by two helium CP and stiffed by a proper steel frame, Fig.10. The temperature field in the mock-up was measured by a total of 51 thermocouples, 24 inside the pebble bed, 15 on the resistor walls and 12 on the CP walls. The pebble bed could be compressed on a single end by an end plug loaded by a Schnorr spring system, Fig. 11. The effect of the pressure on the pebble is measured by a load cell located in correspondence of the plug. The CP lateral deformation is measured by 6 displacement transducer (3 for each side), Fig.10. The vertical displacement of the plug and its spring system 2 is measured by 2 more transducers. The tests on Helichetta were carried-out on the HEFUS-3 facility at ENEA Brasimone.

3.2. Test results

In order to evaluate the temperature/stress/strain mock-up behaviours during the tests, theoretical FEM calculation will be performed using ANSYS code by ENEA and ABAQUS by University of Palermo. The mock-up nodalization and some preliminary calculation for testing the Drucker-Prager pebble model were carried-out. The temperature field at highest heat flux of the resistor is reported in Fig. 12. The stress-strain results at the lowest heat flux of the resistor but with at the highest lateral pressure load on the pebble are reported in Fig. 13-14. The test campaign was performed on both the reference breeder Li_4SiO_4 and Li_2TiO_3 pebbles for a total of 60 tests as the following test matrix:

- two cell orientation : horizontal (toro-radial layer) and vertical (poloidal-radial layer);
- three pressure load on a lateral end : 0.5 , 2.0, 4.0 (MPa);
- five heat flux step to the resistor : 4.7, 9.3, 14.0, 18.7, 23.4, 27.0 (kW/m^2).

The measured Li_4SiO_4 and Li_2TiO_3 pebble packing factor was respectively 0.65 and 0.64. The Figs. 15 16 show the temperature increasing inside the test cell during the tests of both the breeders at the highest heat flux imposed to the electrical resistor. The Figs. 17-18 show the calculated thermal conductivities versus the average bed temperatures for both the breeders. The Figs. 19-20 show respectively the measured CP deformation versus the average bed temperatures for both the breeders. The Figs. 21-21 show the measured thermal expansion of the bed versus the average bed temperatures for both the breeders during a complete ramp-up and down cycle.

4. CONCLUSIONS

The test on TAZZA confirmed that the filling procedure is fundamental to assure the value and the quality of the PF and its stability during the reactor operation. The main results of the optimised filling method, used for both dispersed and binary beds, are: i) minimisation of the residual strain after the cyclical pre-loading; ii) repeatability of the UDM behaviours; iii) absence of the binary pebble swimming /demixing effects. Further experimental results are: i) the PF of the polydispersed beds is similar to the PF of the monodispersed beds; ii) the PF increases with the spread of the diameters and seems to decrease with the roughness of pebbles; iii) the UDM is dependent from strain history and the stress state; it increases with the PF, the regularity of the pebble geometry and the height of the bed; iv) the superficial electrical charges (in the case of beryllium) seems to affect the PF but not the final stiffness of the bed.

The HELICHETTA campaign is still in progress; the data elaboration of the preliminary HELICHETTA test results are in progress. The calculations of the pebble bed thermal conductivities shows a good agreement with previous FZK experiments obtained in air, Figs 17-18.

The preliminary conclusions on the pebble thermal deformations, when the beds are contained in AISI 316 box, are: i) pebble beds exhibit a "normal" thermal expansion versus temperature (bed heights tend to increase and CP walls tend to increase the bending when the temperature increases); ii) the displacements of the bed are quite large: up to 0,2 mm towards the CP, Figs 19-20, and ranging from 0,5 to 1 mm for Metatitanate and up to 1,5 mm for silicate towards the plug, Figs 20-21; iii) following the amplitude of the displacement towards the plug, the Schnorr spring system seems to prevent larger stresses to the containment structure; in the next experiments, the value of the stresses arising without Schnorr springs will be investigated. Further elaborations are in progress in order to complete the previous conclusions. Further tests will be carried out, by the end of 2001, using a controlled purge flow, aiming at a better estimation of the wall deformation influence on the heat transfer mechanism across the pebbles, and a fixed plug, to investigate the real influence of the Schnorr spring system. Creep tests on pebble at higher temperature ($> 800\text{ }^\circ\text{C}$) will be also performed.

REFERENCES

- [1] G. Dell'Orco, M. Simoncini, D. Zito, G. Vella, "Optimisation of the filling for the improvement of the performance of reference ITER/DEMO ceramic and beryllium pebble beds", 14th Topical Meeting on the Technology for Fusion Energy, October 15-19 2000, Park City Utah
- [2] G. Dell'Orco, G. Vella et al., "TAZZA mock-up pebble beds - Experimental and theoretical investigations, presented to CCBI-10

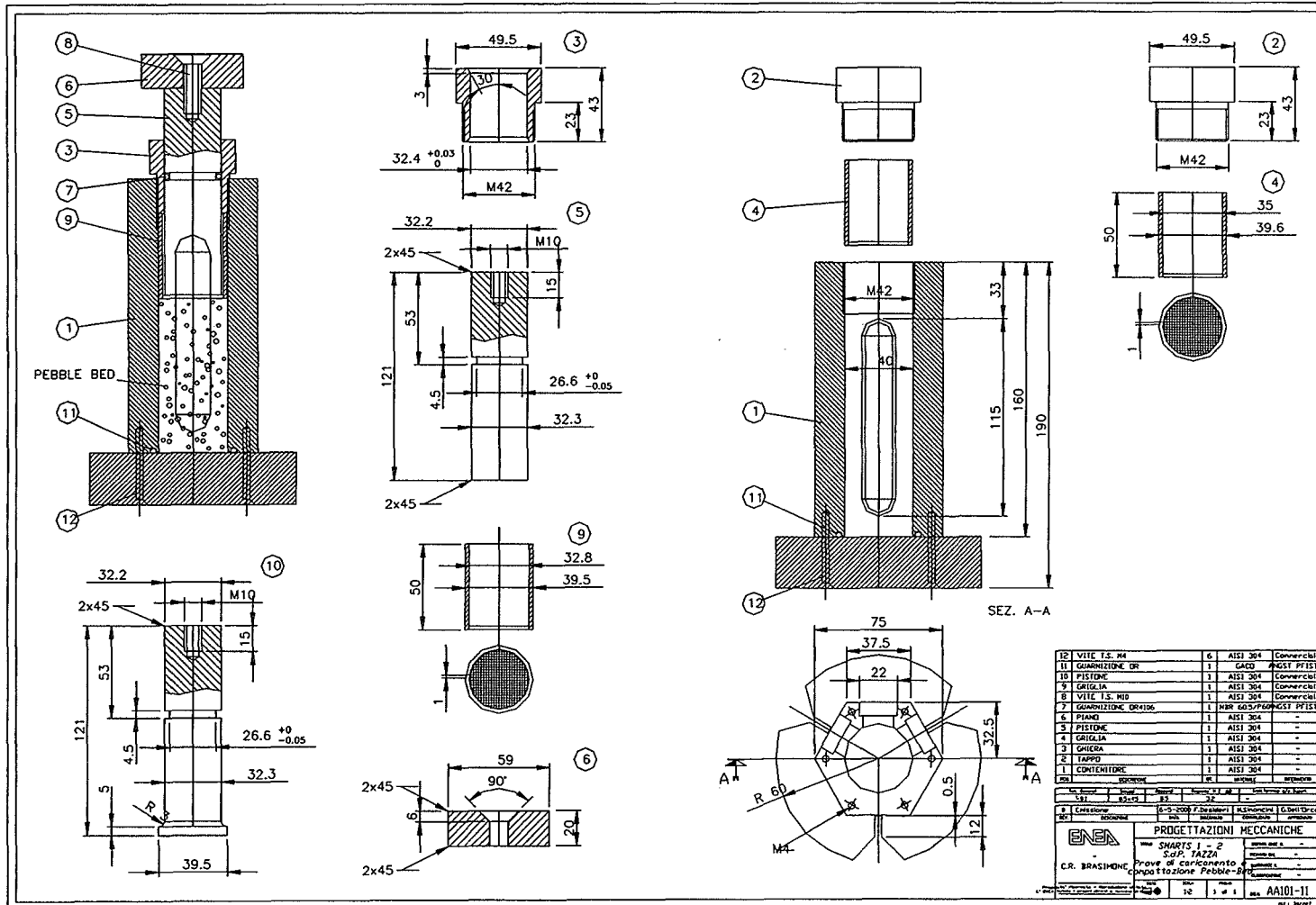


Figure 1 : TAZZA test section

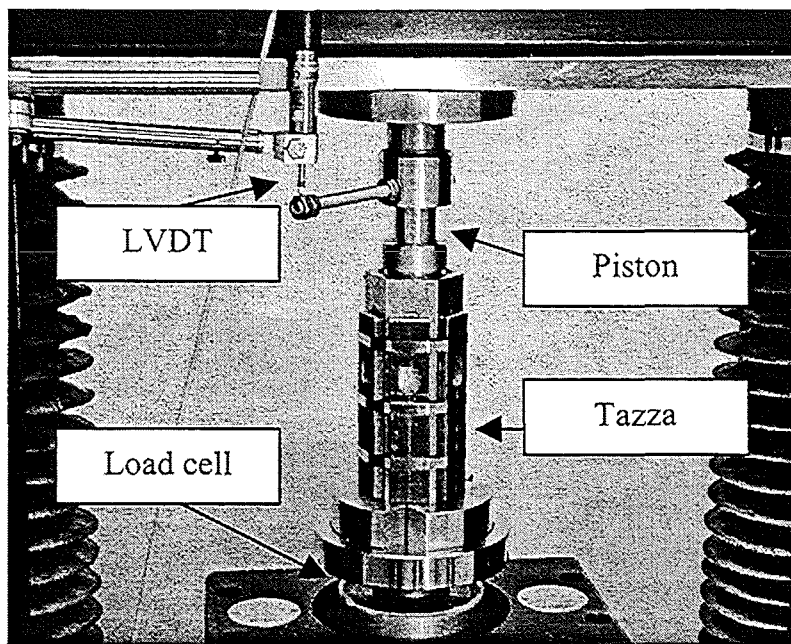


Figure 2 : TAZZA test section and compression device

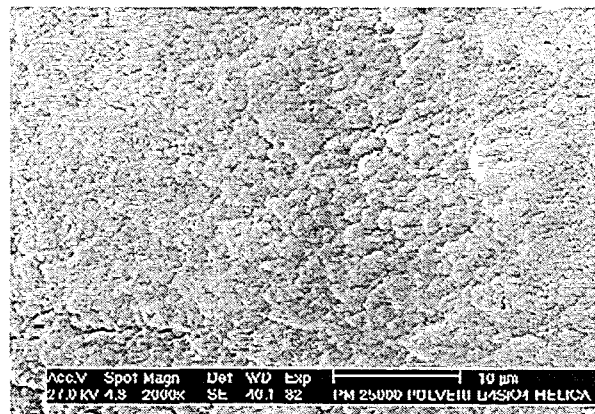
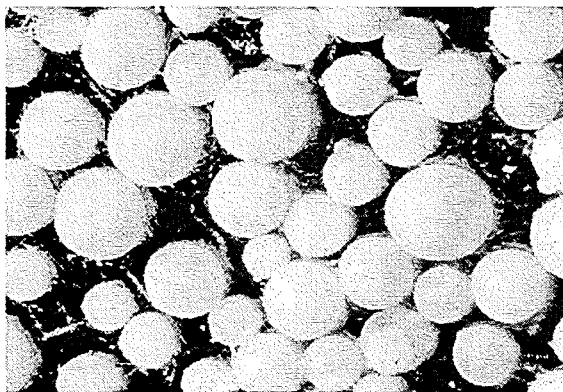


Fig 3 – Optic microscope (left) and SEM (right) images of Li_4SiO_4 pebbles

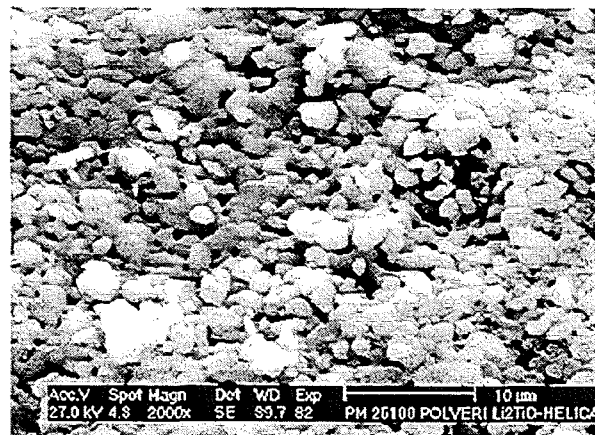
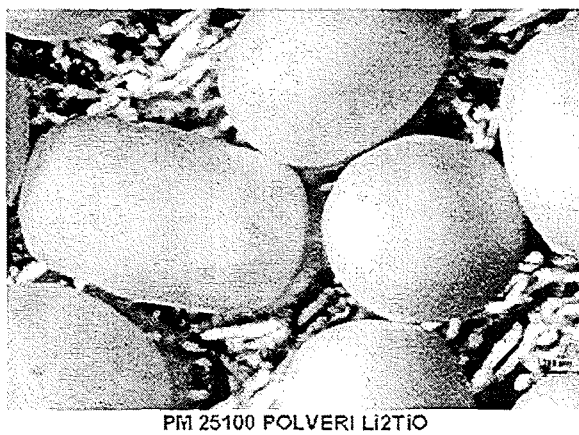


Fig 4 – Optic microscope (left) and SEM (right) images of Li_2TiO_3 pebbles

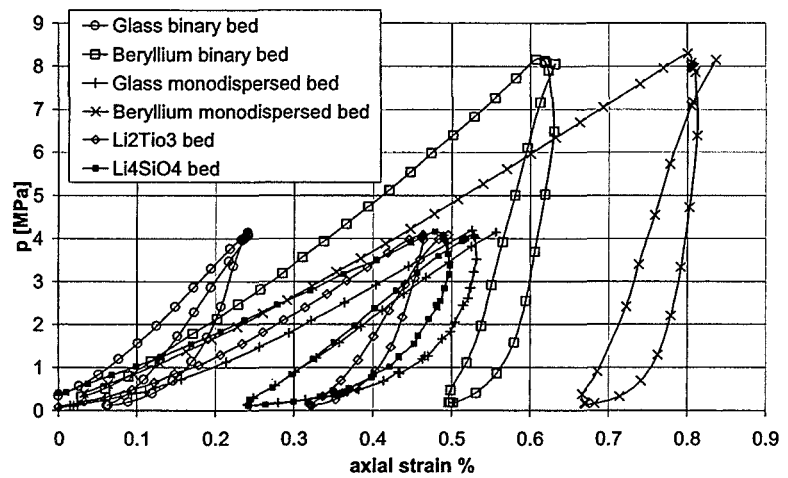


Figure 5 : Pressure-strain cycles on TAZZA mock-up

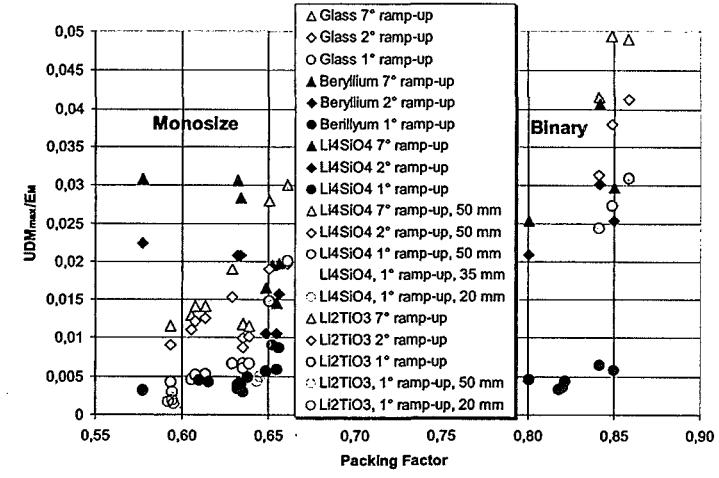


Figure 6 : Relative UDM results on TAZZA mock-up

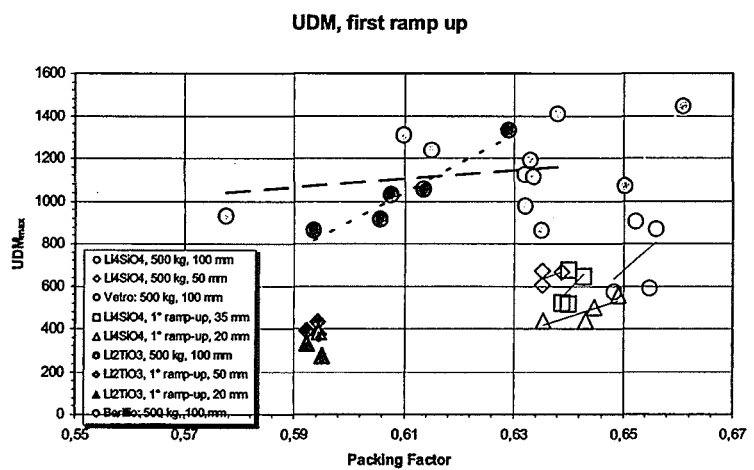


Figure 7: TAZZA mock-up. First ramp up

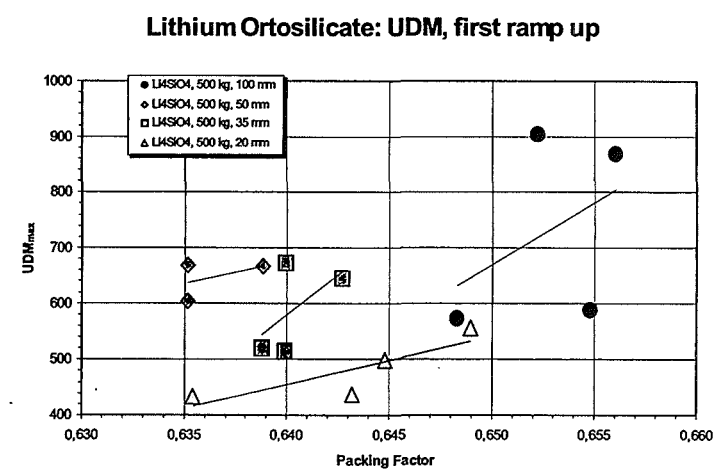


Figure 8 : TAZZA mock-up. Lithium Metatitanate, first ramp-up

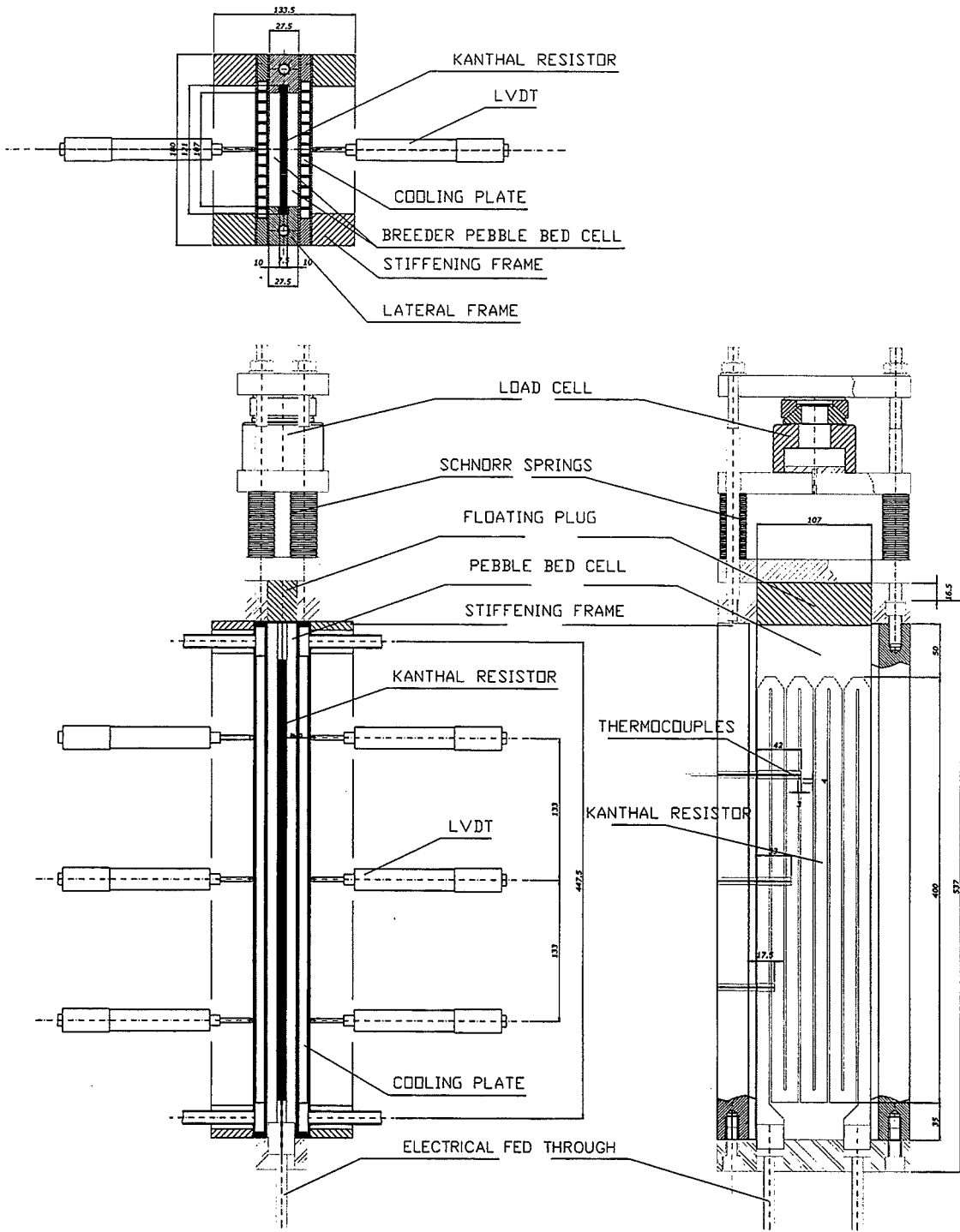


Figure 9 : HELICHETTA scheme

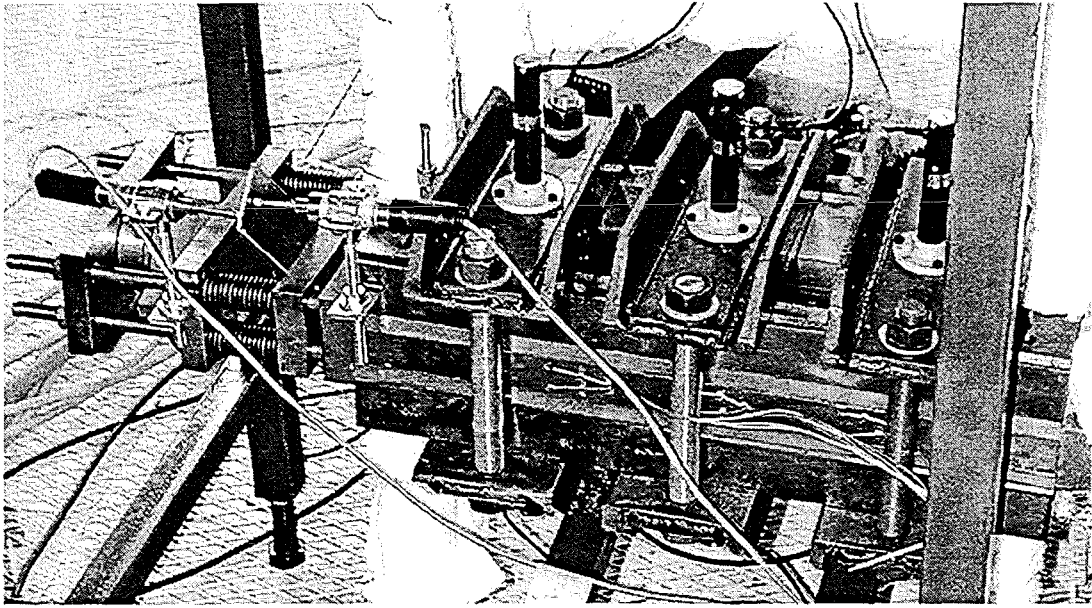


Figure 10 : HELICHETTA during tests

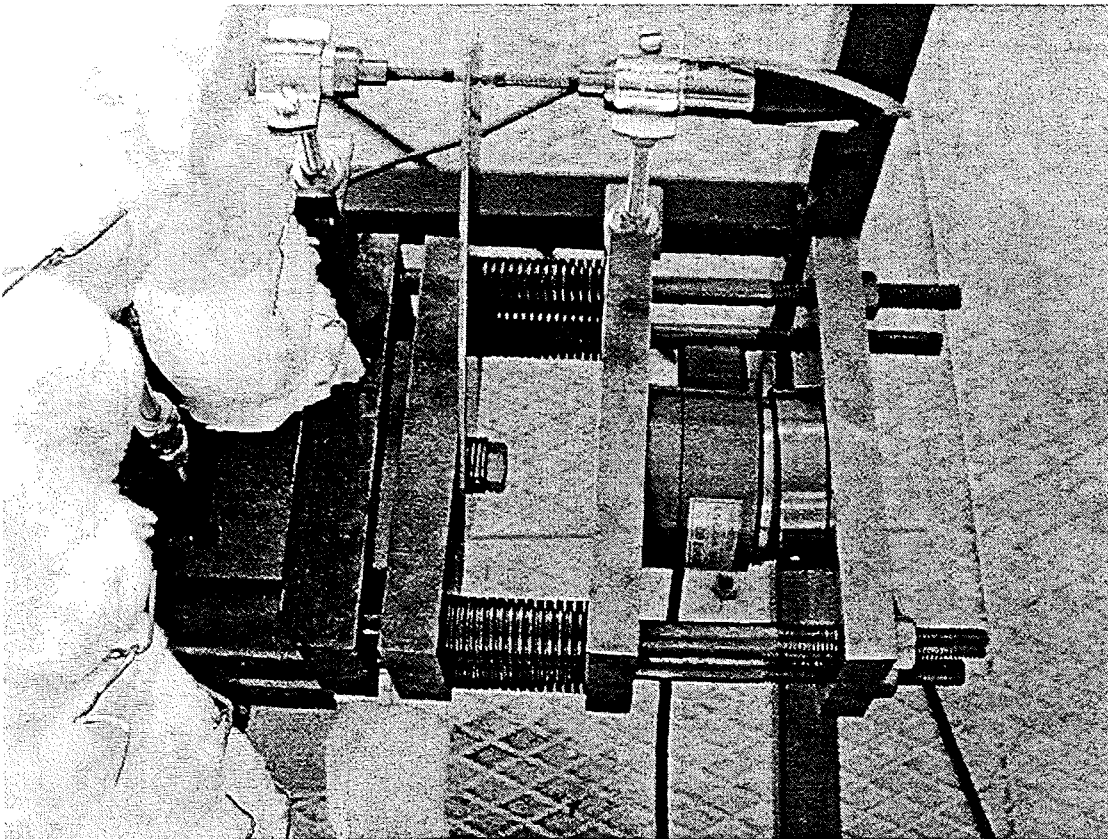
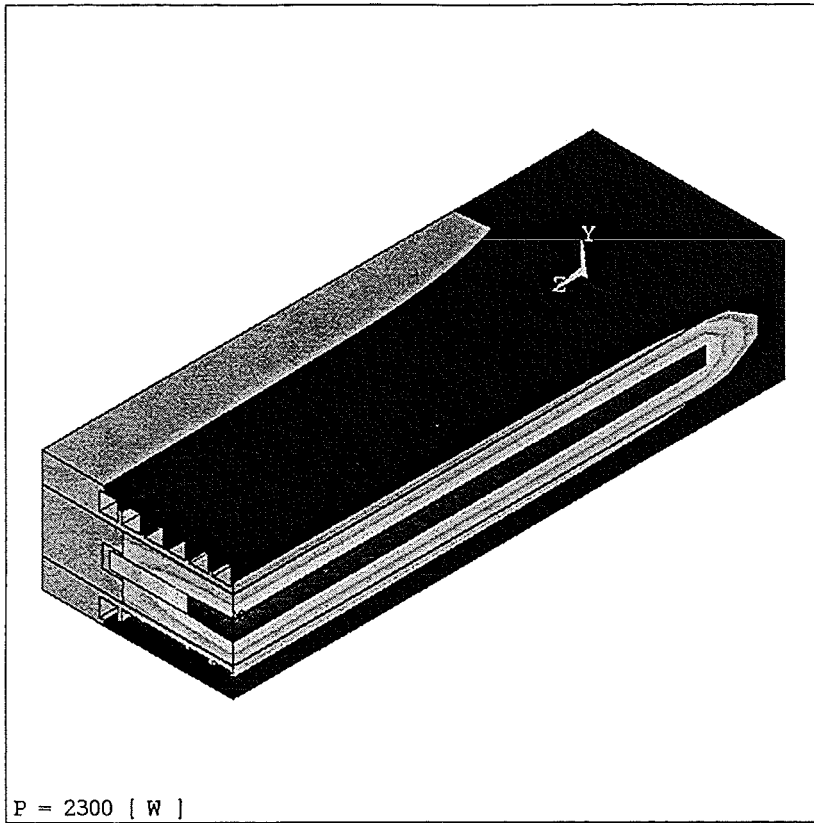


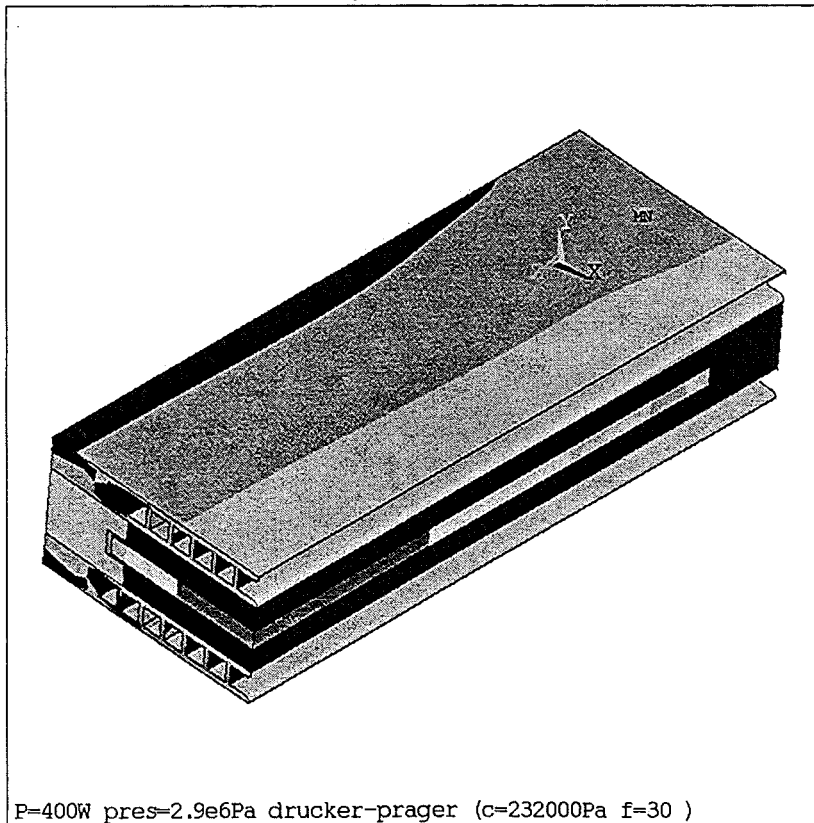
Figure 11 : HELICHETTA lateral end (particular)



ANSYS 5.6.1
 OCT 19 2001
 15:53:38
 PLOT NO. 2
 NODAL SOLUTION
 STEP=1
 SUB =3
 TIME=1
 TEMP (AVG)
 RSYS=0
 PowerGraphics
 EFACET=1
 AVRES=Mat
 SMN =348.971
 SMX =730.663

348.971
391.382
433.792
476.202
518.612
561.022
603.433
645.843
688.253
730.663

Figure 12 : ANSYS temperature results



ANSYS 5.6.1
 OCT 19 2001
 14:19:16
 PLOT NO. 4
 NODAL SOLUTION
 STEP=1
 SUB =9
 TIME=1
 SEQV (AVG)
 PowerGraphics
 EFACET=1
 AVRES=Mat
 DMX =.003256
 SMN =631075
 SMX =.612E+09

631075
.685E+08
.136E+09
.204E+09
.272E+09
.340E+09
.408E+09
.476E+09
.544E+09
.612E+09

Figure 13 : ANSYS stress results

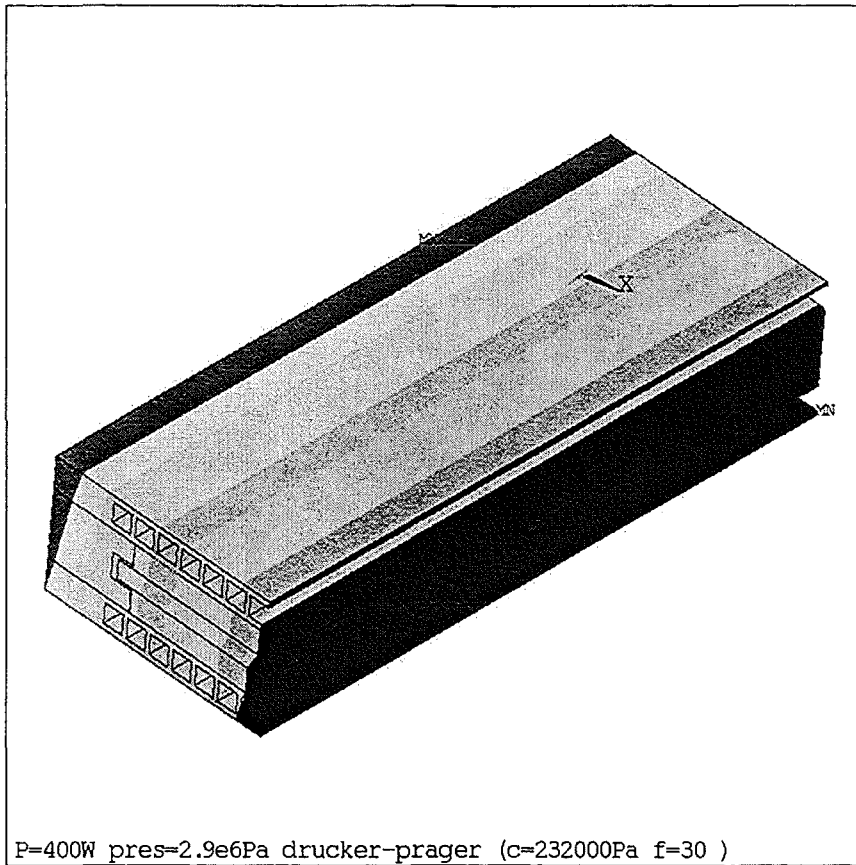


Figure 14 : ANSYS displacement results

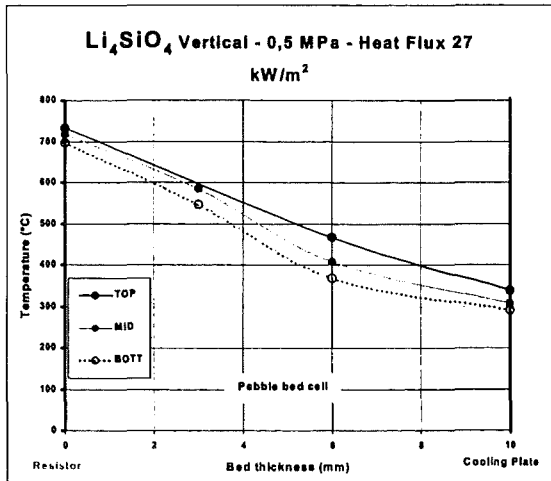


Figure 15 : Temperature distribution across the pebble bed (Ortosilicate)

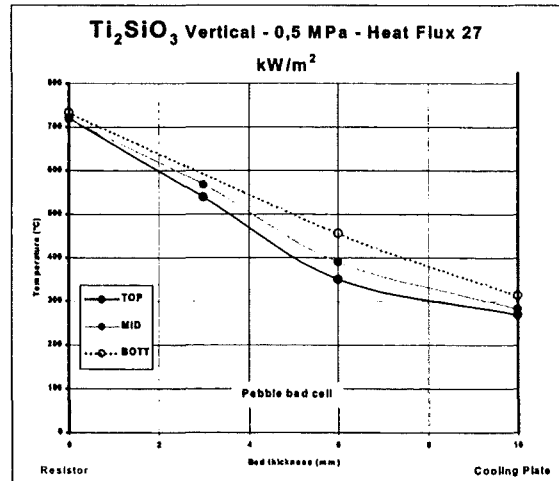


Figure 16 : Temperature distribution across the pebble bed (Metatitanate)

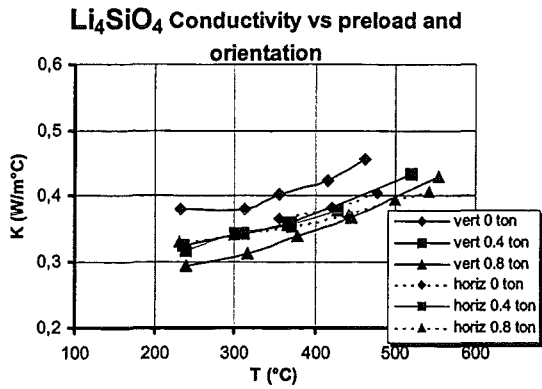


Figure 17

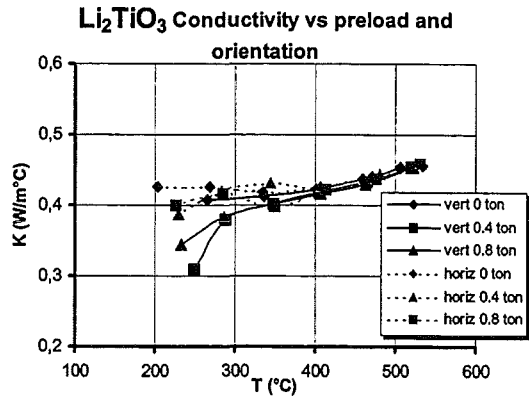


Figure 18

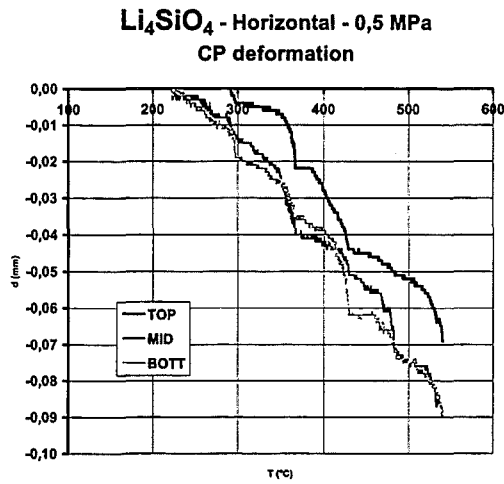


Figure 19

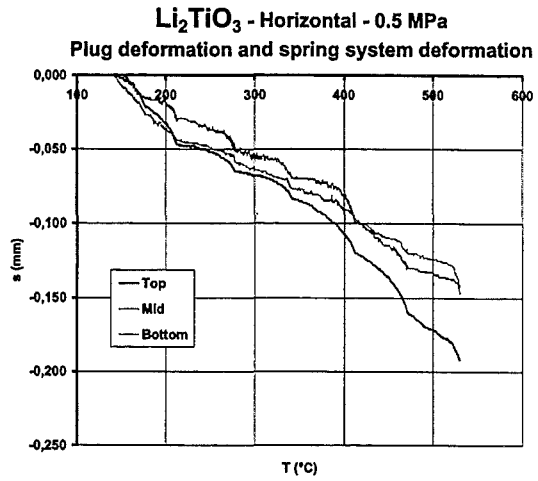


Figure 20

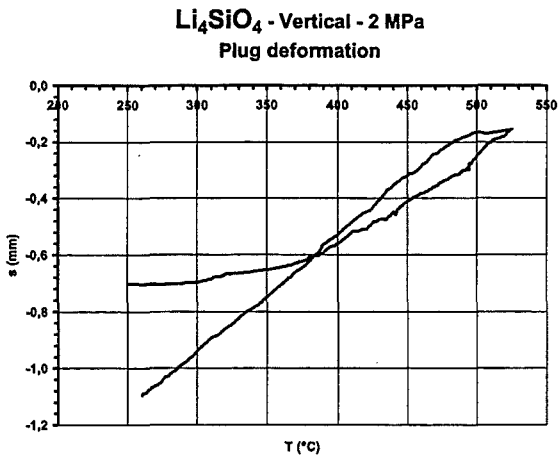


Figure 21

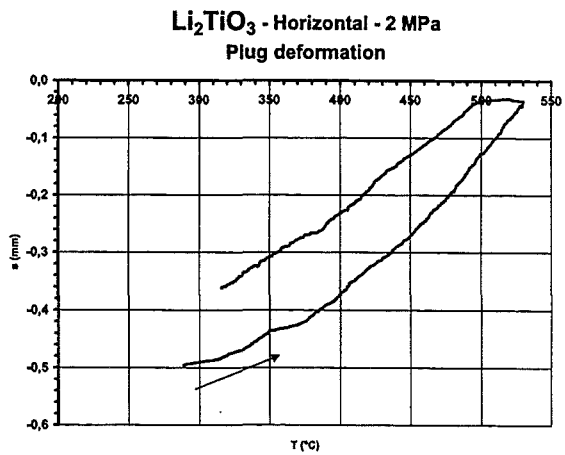


Figure 22

Helium as a temperature moderator in batch irradiation of Li_2TiO_3 pebbles

Ricardo E. Avila (ravila@cchen.cl), Luis A. Peña, Luis Padilla-Campos and Juan C. Jiménez

Departamento de Investigación y Desarrollo,
Comisión Chilena de Energía Nuclear,
Cas. 188-D, Santiago, Chile

The release of tritium in batch experiments is being conducted, with emphasis on the low-temperature regime (below 400 °C), because of the relevance of this range in temperature cycling of future fusion reactors. Initial studies are presented which indicate that Li_2TiO_3 pebbles irradiated in vacuum, at a neutron flux of approximately $3 \cdot 10^{13}/\text{cm}^2/\text{s}$ will release most of the tritium generated to the closed capsule, presumably by irradiation heating. This has been avoided by filling the capsule with He before irradiation, and supporting it in graphite. The temperature programmed desorption experiments reveal a low-temperature (100 to 250 °C) tritium release regime, interpreted to correspond to oxidized tritium which was adsorbed back in the ceramic after being released during irradiation. Then, another wide desorption band occurs in the 370 to 600 °C range, interpreted to correspond to the true tritium inventory resulting from the low-temperature irradiation. The preliminary analysis of the TPD curves fits a second order desorption model, with an average activation energy of 23.1 ± 2 kcal/mol, and an attempt-to-escape frequency of the order of $3 \cdot 10^{15} \text{ s}^{-1}$.

1. INTRODUCTION

The release of tritium (T) from a neutron irradiated lithium ceramic is a major concern towards the operation of fusion reactors, as it determines the tritium inventory within the ceramic during and after operation. This topic has been the object of various studies, mainly, by means of in-core, continuous cycle irradiation-release experiments, and by sealed capsule irradiation, followed by out-of-pile release under controlled temperature and purge gas conditions (batch experiments). The present work has been conducted in the second fashion.

The standard procedure at the La Reina reactor (RECH-1) for the batch release experiments used quartz ampoules, containing some 300 mg of ceramic pebbles. The ampoules were evacuated prior to sealing, and held in loose aluminum foil within an aluminum capsule during irradiation. From prior experience in irradiation at RECH-1, it was observed that a 60 g capsule, vented at 100 sccpm and cooled through Ar gap gas would reach up to 550 °C at a neutron flux of $3 \cdot 10^{13}/\text{cm}^2/\text{s}$. Thus, it was suspected that the ceramic within the ampoules for batch experiments could reach similar temperatures, which would allow for release of the generated tritium to the atmosphere of the capsule. Then, the tritium release experiments would be meaningful only above the highest temperature attained by the ceramic during irradiation.

To explore these considerations, the heat transport out of the ampoules has been, either, minimized by evacuating the ampoule and holding it in alumina within the canister, or maximized by back filling it with helium and fitting it to a graphite holder (thermal conductivities of quartz, alumina and graphite: approximately 1, 3.1 and 171 W/m/K, respectively).

An alternative approach has been used by Johnson *et al.*¹, who placed the ceramic pebbles in polyethylene capsules to act as a sensor for temperature excursions, and discarded capsules which were deformed during irradiation.

2. THE EXPERIMENTS

The tritium generation-release experiments were performed with Li_2TiO_3 pebbles prepared in our laboratories^{2,3}. Each ampoule contained ceramic pebbles in the 300 to 600 mg range. The ampoules are prepared out of a quartz tube, of 4 mm internal diameter and 1 mm thickness. After putting the ceramic pebbles, the quartz ampoules were evacuated to a pressure below 2×10^{-7} mbar, and either sealed, or back-filled with He at a pressure near 1 atm, before sealing.

The ampoules were carried in aluminum canisters, either wrapped in aluminum foil or supported in either alumina or graphite. The irradiations were performed in a side gap of the RECH-1 reactor core, at nominal thermal neutron flux between 2 and $3.4 \cdot 10^{13}/\text{cm}^2/\text{s}$ for periods in the 20-24 h range.

The tritium release facilities have been described previously. Provision is made for breaking the quartz ampoule, and dropping its contents into an oven. Then, a He / 0.1% H mixture was used as sweep gas, which flows through an ionization chamber (IC-1), ethylene glycol bubbler, a second ionization chamber (IC-2), a copper-oxide bed and a second set of bubblers with ethylene glycol as a tritium getter.

The temperature programmed desorption (TPD) process has consisted of breaking the quartz ampoule and dropping the irradiated ceramic into the oven at 20 °C, that temperature is held for 30 min, before heating at rates of 1, 2.5 or 5 °C/min up to 735 °C. A 30 min. isotherm follows, before uncontrolled cooling. A microcomputer provides for the continuous monitoring of the oven temperature, and the current through the 2 ionization chambers.

3. RESULTS AND DISCUSSION

3.1. Summary observations

As relates to exploring the release of T to the interior of the ampoule during irradiation, our summary observations are:

1. The He-filled ampoules, fit to graphite holders, expected to remain at the lowest temperature during irradiation, display the lowest T release upon breaking. Essentially all of the T released appears in a single, broad peak, in the 370 to 600 °C range, as shown in Fig. 1, where the current has been normalized per n fluence, ceramic weight and sweep rate.

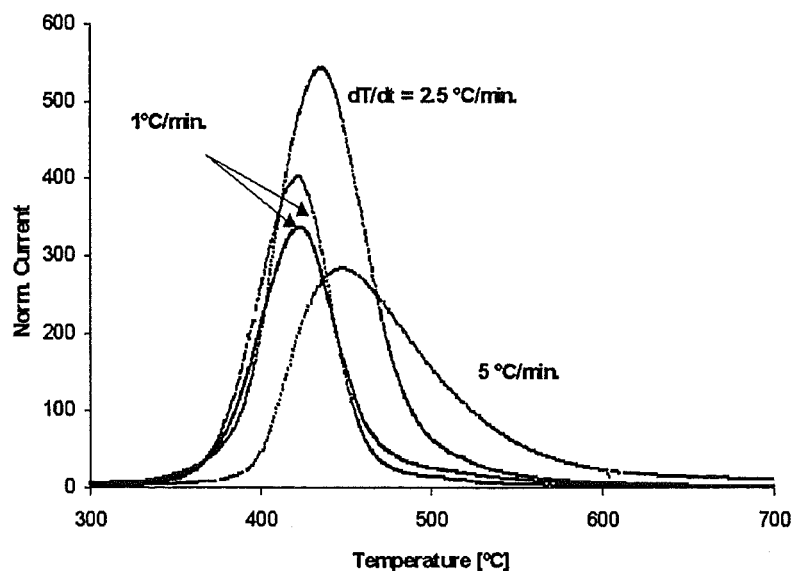


Fig. 1 Normalized IC-1 current at various heating rates, from ampoules backfilled with He and supported in graphite.

- At the other extreme, the ampoules irradiated after evacuation and fit to alumina holders, release T, first upon breaking, then in the 100 to 250 °C range (low temperature peak), and finally, a slight increase which peaks at ~700 °C.

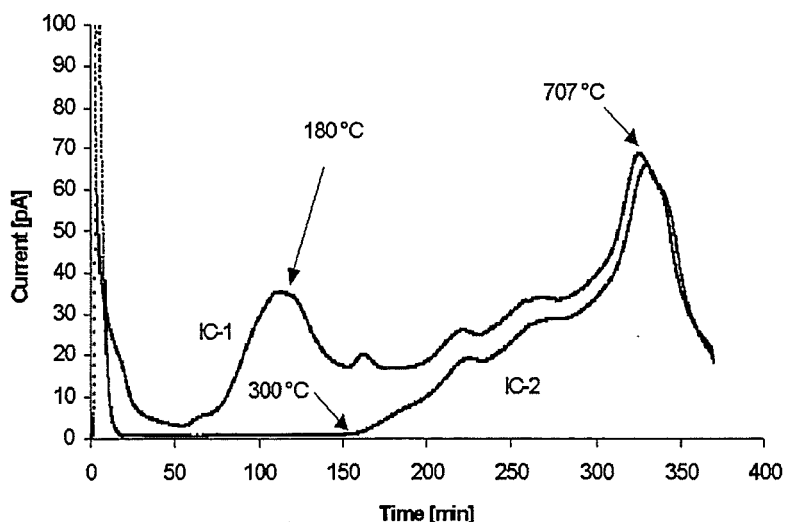


Fig. 2 Tritium release, at 2.5 °C/min., from an ampoule irradiated after evacuation and supported in alumina.

3.2. The non-temperature-moderated samples

The T activity released upon breaking the ampoule consists initially of molecular hydrogen (HT, or T₂) and, later, of water, as evidenced by the integrated signals from the ionization chambers IC-1, prior to, and following, IC-2, water trapping at the ethylene-glycol bubblers, as shown in Fig. 3. There, by the first 4 minutes, approximately one half of the tritium that will be released at room temperature has evolved, and has been detected by both ionization chambers. Later, over the next 30 min., the rest will evolve as water vapor. Upon heating, any T released appears in the oxidized form, up the neighborhood of 300 °C. From there on, the molecular hydrogen form reappears up to the maximum temperature measured (735 °C). In other samples, all of the initial release is in the form of molecular hydrogen.

As seen in Fig. 2, the low-temperature peak appears clearly in IC-1 and it is nearly absent in IC-2, suggesting that it consists essentially of the oxidized form.

Our interpretation is that He introduced in the quartz ampoules and a graphite support are effective heat transport media from the Li₂TiO₃ pebbles during in-core irradiation. The opposite occurs in evacuated ampoules, held in alumina. The significant T release upon breaking the ampoule, and the moderate increase in T release rate in the 500 – 700 °C range suggests that the ceramic pebbles, in the latter conditions, heat to the neighborhood of 500 °C during irradiation. As exemplified in Fig. 2, the T released during irradiation is interpreted to adsorb back as molecular species on the surface of the pebbles upon cooling after irradiation, to desorb, during the TPD experiment, in oxidized form. The latter is implied by the notoriously larger signal from IC-1 than that from IC-2, in the low temperature peak.

This clear cut picture is not always present, a tight reproducibility of the release curves has not been possible; so, the analysis presented must be considered of qualitative character. As an example, in one case, a capsule evacuated before irradiation led to a TPD release curve just as in the case of the He-filled capsules. This may have resulted from a faulty evacuation operation which would have let air back into the capsule during sealing. Also, the total T release registered from evacuated capsules is much less than that from the temperature-moderated ones; suggesting that the ionization chambers are not responding fully to the initial release upon ampoule breaking.

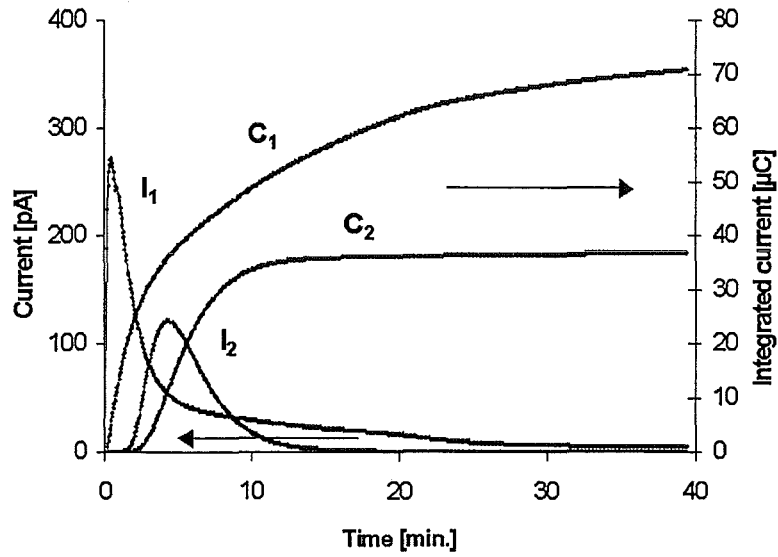


Fig. 3 Initial detail from Fig. 2: T release upon breaking the ampoule, at 20 °C. I_1 , I_2 , and C_1 , C_2 are the current and time integral of the current from IC-1, and IC-2, respectively. Approximately equal amounts of activity appear as water and as molecular hydrogen

3.3. Analysis of TPD curves

The temperature programmed desorption (TPD) curves have been analyzed using the approach of Cabrera⁴ to the Redhead⁵ model.

The desorption rate constant obeys an Arrhenius-type law:

$$K_d = v_d \exp(-E_a/RT), \quad (1)$$

where v_d is interpreted as the attempt-to-escape frequency and E_a is the activation energy. Cabrera shows that, at any point along the desorption curve,

$$K_d = \frac{A_o^{n-1} - \beta f(T)}{[A_o - A(T)]^n} \quad (2)$$

where $f(T)$ is the value of the normalized desorption curve at temperature T , $A(T)$ is the area under the curve up to that temperature, A_o is total area under the curve, n is the order of the desorption model, and β is the heat rate.

Thus, the value of E_a and v_d can be determined from a plot of

$$\ln \left(\frac{A_o^{n-1} - \beta f(T)}{[A_o - A(T)]^n} \right) \text{ versus } 1/T. \quad (3)$$

The kinetics fits a second order desorption model, with activation energy and attempt-to-escape frequency as shown in Table 1. There is a close spread of the expression (3) for the TPD curves taken at 1, 2.5 and 5 °C/min., as shown in Fig. 4. However, a reproducible deviation from the straight line suggest that a more complex analysis may be attempted. Such analysis should include a closer examination of the response of the ionization chambers, which could be keeping some memory, especially in the high-temperature edge of the release peak.

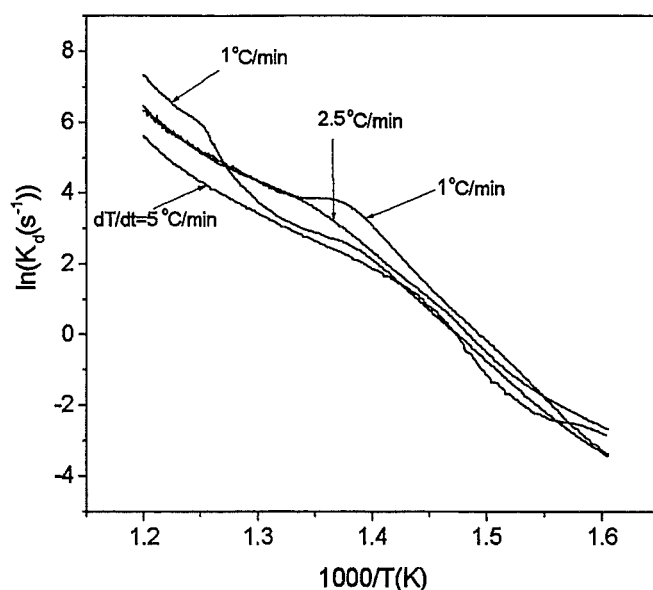


Fig. 4 Redhead analysis of the TPD release curves, from ampoules irradiated after evacuation and supported in graphite (Fig. 1), within a second order desorption model.

Table 1. Modeling TPD curves.

Heat rate [°C/min]	T_m [°C]	E_a [kcal/mol]	ν [$10^{14} s^{-1}$]	R
1(a)	423	25.1	101	0.995
1(b)	421	23.0	8.06	0.995
2.5	437	22.9	61.5	0.982
5	450	21.3	0.24	0.991

The average activation energy is 23.1 ± 2.0 kcal/mol (1.0 ± 0.1 eV/molecule), with an attempt-to-escape frequency of the order of $3 \cdot 10^{15} s^{-1}$. The second order nature of the fit, and the large value of the activation energy suggest that the desorption is limited by the recombination process (surface diffusion) required to form the molecular T_2 or HT species. Once formed, the molecule would desorb with a much lower activation energy. These results are consistent with the findings of Renoult *et al.*⁶, who report an activation energy of 31 kcal/mol, and suggest that the dominant desorbing species is HT. A similar value of the activation energy, 25 kcal/mol, is reported⁷ for tritium diffusion in crystalline Li_2TiO_3 . However, the overall shape of our TPD curves, and, consequently, the present analysis are in contrast with the results of Kopasz *et al.*⁸ These authors suggest that the dominant desorbing species is TOH, and show the need for 5 desorption peaks, assuming first order kinetics, or 4 peaks, assuming second order kinetics, to fully fit their experimental results. The corresponding activation energies are in the range of 10 to 29 kcal/mol.

4. CONCLUSIONS

Helium introduced in the quartz ampoules and a graphite support are effective heat transport media out of Li_2TiO_3 pebbles during in-core irradiation. The opposite occurs in evacuated ampoules, held in alumina. In this case, most of the tritium generated is released during irradiation and adsorbs back as molecular species on the surface of the pebbles, to desorb, upon heating, in oxidized form.

The preliminary analysis of the TPD curves fits a second order desorption model, with an average activation energy of 23.1 ± 2.0 kcal/mol (1.0 ± 0.1 eV/molecule), and an attempt-to-escape frequency of the order of $3 \cdot 10^{15}$ s⁻¹. This results suggest the desorption of T is limited by the recombination process to form molecular species.

5. ACKNOWLEDGMENTS

This work has benefited from the expert advise of Dr. Carl E. Johnson, of the *Argonne National Laboratory*, Argonne, IL, USA, under the auspices of the IAEA, as well as from support for personnel training and equipment from this agency. FONDECYT grant N°1990213 has supported the work of one the authors (LPC).

REFERENCES

- ¹ Carl E. Johnson, private communication.
- ² C. Alvani, P. Ccarconi, S.Casadio, V. Contini, A. Dibartolomeo, F. Pierdominici, A. Deputula, S. Lagos, C. Nannetti, *Journal of Nuclear Materials*, **289** (2001) 303, *Lithium titanate pebbles reprocessing by wet chemistry*.
- ³ S. Lagos and R. Becerra, *Nucleotecnica*, **34** (2000) 21, *Desinfection of lithium titanate spheres*.
- ⁴ A.L. Cabrera, *J.Chem.Phys.*, **93**, (1990), 2854, *Kinetic parameters obtained from area integration of single peak thermal desorption spectra*.
- ⁵ P.A. Redhead, *Vacuum* **12**, (1962), 203.
- ⁶ O. Renoult, L.P. Boilot, J.P. Korb and M. Boncoeur, *J.Nucl.Mater.*, **223**, (1995) 126. *Lithium so-gel ceramics for tritium breeding applications*.
- ⁷ T. Tanifuji, D. Yamaki, S. Nasu and K. Noda, *J. Nucl. Mater.*, **258-263** (1998) 543. *Tritium release behavior neutron-irradiated Li_2TiO_3 single crystal*.
- ⁸ J.P. Kopasz, J.M. Miller and C.E. Johnson, *J. Nucl. Mater.*, **212-215** (1994) 927, *Tritium release from lithium titanate, low-activation tritium breeding material*.

Numerical Simulation of Ceramic Breeder Pebble Bed Thermal Creep Behavior

Alice Ying, Hulin Huang, Mohamed Abdou

Mechanical & Aerospace Engineering Department, UCLA, Los Angeles, CA 90095
Tel: (310) 206-8815

The evolution of ceramic breeder pebble bed thermal creep deformation subjected to an external load and a differential thermal stress was studied using a modified discrete numerical code previously developed for the pebble bed thermomechanical evaluation. The rate change of creep deformation was modeled at the particle contact based on a diffusion creep mechanism. Numerical results of strain histories have compared reasonably well with those of experimentally observed data at 740 °C using activation energy of 180 KJ/mole. Calculations also show that, at this activation energy level, a particle bed at an elevated temperature of 800 °C may cause undesired local sintering at a later time when it is subjected to an external load of 6.3 MPa. Thus, by tracking the stress histories inside a breeder pebble bed the numerical simulation provides an indication of whether the bed may encounter an undesired condition under a typical operating condition.

1. Introduction

Characterization of the elastic and creep properties of ceramic breeder pebble beds under thermomechanical loads is necessary to ensure that the integrity of beds does not become the blanket lifetime limiting factor. Previous experimental results of ceramic breeder Li_4SiO_4 pebble bed thermomechanical tests at temperatures above ~ 650 °C ($\sim 0.5 T_m$) have shown that deformation and/or thermal creep increases as a function of time when the bed is subjected to an externally applied constant pressure [Reimann 1]. These creep rate results have been correlated as a function of temperature and pressure. Contrary to being linearly proportional to stress, which characterizes diffusion creep for a sintered porous form [Zimmermann 2], the creep observed in pebble bed configurations shows a stress exponent factor of less than 1. This might indicate that some of the applied stress caused initial particle relocation and bed rearrangement during thermal creep (this is highly possible since the pebble bed was brought to a high temperature state before a uni-axial stress was imposed), and therefore, led to a lower stress exponent factor.

As known, creep deformation depends on many factors including fabrication, material properties, and operating conditions. Depending on the mechanism involved, the creep rate can be a strong function of grain size, porosity fraction, stresses, temperature, and so forth [Goretta 3, Frost 4, Onaka 5]. Changes in creep mechanisms are entirely possible with stress relaxation, while it is quite unlikely to deform via the same predominant mechanism at all times during the operation. Despite the complexities involved in the processes, predictions of ceramic breeder pebble bed creep deformations are important and are needed to ensure proper designs and operations. In this current work, experimental observations of creep strains was modeled based on a diffusion creep deformation according to there being a small amount of stress. The objective was to develop an

understanding of the effects of applied stress on the deformation characteristics of pebble bed structures at elevated temperatures, while defining operating regimes where pebble bed integrity may be jeopardized. While the present effort does not intend to lead to fully developed understanding and modeling of creep behavior, it does point out the areas where data is missing. In addition, although the irradiation effect is not considered in this paper, the goal is to develop a tool for the beginning of life thermomechanics performance prediction for design scoping.

Numerical simulations were used to trace the evolution of contact characteristics and forces as deformation proceeds. A previously developed 3-D discrete numerical thermomechanics code [Lu 6] provided initial bed and contact conditions, while a micro-constitutive equation was used to determine the development of creep strain at the contact with time. In the following sections, the simplifications of the basic set of equations describing diffusion creep are outlined and numerical results are presented.

2. Phenomenology of Strain Deformation

The deformation mechanism of a packed bed at elevated temperatures prior to the occurrence of significant amounts of sintering can involve particle rearrangement, and surface and boundary diffusions. In this paper, the process of elastic plus diffusion deformation is adopted to model the evolution of the bed deformation. Two problems are considered. The first assumes that the source of the deformation originates from the thermal stress caused by the differential thermal expansion, a case in which stress relaxation leads to a reduced strain rate as time progresses. The second involves a bed subjected to an externally applied constant force in which the strain increases as time proceeds yet the strain rate also decreases.

As pressure is applied, it causes localized deformation at the contacts, resulting in work (strain) hardening. This work hardening is reflected through the increase of bed stiffness while the distance between particle decreases. The effect of heating is to provide thermal energy to initiate interparticle mass transport. When heated to temperatures in excess of approximately half of the absolute melting temperature, the pebbles are expected to bond together. Bonding may take place as the neck grows at the point of particle contact. However, this is an undesirable situation for a pebble bed blanket design configuration. Thus, if the model indicates that a sintering process becomes possible because there is too much force exerted on the particles, engineering solutions has to be built in to prevent this. In this sense, the numerical simulation is a useful and economical tool to help identify whether a design would involve an unfavorable thermomechanical state at the earlier stage of the operation.

At high temperatures and low stresses (or before a large deformation has occurred), deformation of materials proceeds by mutually accommodating grain-boundary sliding and transport of matter. In a deformation based on the Coble creep process, where the transport of matter occurs by grain-boundary diffusion, the strain rate is given as [Coble 7],

$$\frac{d\varepsilon}{dt} = \frac{42\delta D_b \Omega \sigma}{\kappa T d^3} = \frac{42\bar{D}_b \sigma}{d^3} \quad [1]$$

where $\delta D_b (= \delta D_{b_0} \exp(-Q/RT))$ where Q is the activation energy and R is gas constant) is grain boundary diffusion coefficient, $\Omega (= 8.329 \times 10^{-29} \text{ l/m}^3)$ is the atomic volume, κ is the Boltzmanns constant, T is the absolute temperature, d is the particle size, and σ is the effective

stress. In a multi-component system, the diffusion coefficient is calculated through a weighted mean of the diffusivities of the component [Frost 4].

3. Numerical Simulation

The methodology of Svoboda and Riedel [Svoboda 8] of energy rate extremization is applied to solve the problem of a packed bed subject to free and pressure assisted thermal creep deformation. The theory recalls that the sum of the rate of change of the free energy of the system and the rate of energy dissipation has a minimum value with respect to mass flux and surface areas, and that leads to the appropriate governing equations for the mass transport problem on the actual free surface and grain boundary. The rate of change of particle contact radius (\dot{x}) and instant contact distance (ℓ) at the earlier stage of deformation (or small deformation) are given below (details can be found in [Parhami 9]):

$$\dot{x} = \frac{4\bar{D}_b(2\gamma_s - \gamma_b)}{xt^2} - \frac{4\bar{D}_bF}{\pi x^3 t} \quad [2]$$

$$\ell = \frac{1}{x^2} \left[\frac{V_o}{\pi} - \frac{2}{3}(a^3 + b^3) + \frac{x^4}{4} \left(\frac{1}{a} + \frac{1}{b} \right) \right] \quad [3]$$

Where γ_s and γ_b are the surface and grain boundary energies per unit area respectively, \bar{D}_b is defined in Eq. 1, F is the applied force, a and b are particle radii, x is the contact radius at time t , and V_o is the initial half particle volume of the contact. The second term at the left-hand side of Eq. 3 resembles the Coble's creep deformation.

Few papers have been published in the area of creep deformation with regard to ceramic breeder particularly for a pebble bed configuration. Due to the lack of data, the calculations assume that the potential for matter transport due to the surface and boundary energy is negligible when compared with that caused by the applied and induced stresses. Furthermore, considering that the α -phase of lithiumsilicate has the orthorhombic structure, the pre-exponential constant of the boundary diffusion coefficient ($\delta D_{bo=1 \times 10^{-10}}$) takes the same value assumed for Mg_2SiO_4 , while an activation energy (Q) of 180 KJ/mole experimentally obtained for Li_4SiO_4 sintered porous material is used [Zimmermann 2]. The aforementioned rate change equations are implemented into a previously developed 3-D discrete numerical thermomechanics code to determine the development of creep strain with time. Note that, in this first attempt, particles with spherical shape are used and the shape of the particle remains unchanged during the analysis. During simulation, for each time step, the model takes into account that the contact radius increases as a result of diffusion creep, while the bed hardening is determined by the magnitude of the overlap. The amount of particle relocation is reduced as a result of bed stiffness.

4. Numerical Results

Numerical results of strain histories for temperatures of 740 °C and 800 °C under an applied external stress of 6.3 MPa are shown in Figure 1 and compared with the experimental results of [Reimann 1]. Here, the strain is defined as the calculated change of the container plate location.

Numerically, an equilibrium pebble bed configuration at zero applied pressure is obtained first. A subsequent applied pressure of 6.3 MPa causes particles to shift and rearrange, and produce an initial jump in the strain. The stress-induced thermal creep developed at the particle contacts causes further strain increase. Since the pressure is maintained through the cause of the evaluation, the creep increases continuously, although the creep rate drops due to a gradual increase of the contact area, which then reduces the deformation rate. It is also noted that experimentally there is a large increase in strain when the temperature increases from 740 °C to 800 °C. This significant amount of increase in the strain is not captured by the model although the model compares reasonably well with the data obtained at 740 °C. The difference between the calculated and experimental values arises from many factors including model assumption and the lack of physical and material property data. An example of the evolution of particle contacts is illustrated in Figure 2, which shows how the contact area grows as particles approach each other due to the increase of creep. As creep proceeds, the particle center location is adjusted according to:

$$\Delta(X, Y, Z) = \sum_c^{i=x,y,z} \Delta \ell_c^i \quad [4]$$

where $\Delta \ell_c$ is the overlapping distance at contact c . As the result of the creep, particle A (as shown in Figure 2) shifts slightly toward the upper-left corner. The decrease in creep as time proceeds can also be elucidated by the drop of the average stresses exerted on the particles. The average stress exerted on the particles decreases by one order of magnitude as time increases to 2000 minutes (as shown in Figure 3). The potential occurrence of sintering or particle bonding caused by the stress as time proceeds is illustrated in Figure 4, where particles with necks that have grown beyond 0.9 particle diameter are plotted at different time intervals. It is suppressing to see that about one-third of the particles having a contact radius approaching one particle radius at time = 2000 minutes, while it is about 1% at time equal to 10 minutes. The stress evolutions are also simulated for stress generated from a thermally induced breeder-structure interaction. The average stress exerted on the wall as a function of time is shown in Figure 5. The average stress drops from 18.75 MPa to less than 6.3 MPa at around 1000 minutes and to less than 1 MPa at around 2000 minutes after the initiation of creep due to the increase of the contact area caused by creep. This appears to be desirable since the goal is for the stress to be reduced to a significantly lower value at a relatively short period of time after the development of the creep. This should prevent further creep deformation and an undesirable sintering formation.

5. Summary and Discussions

In this paper, strain evolutions of a ceramic breeder pebble bed subjected to a thermal differential stress as well as an externally applied stress were numerically studied. The experimentally observed strain and strain rate as a function of time were reasonably well described by numerical results based on a diffusion creep mechanism. It is believed such a simulation is useful and provides indications as to whether an undesirable sintering condition may or may not occur under the operating conditions by tracking the stress evolution of the bed. However, it should be stated that the experimental data, phenomenological description, and numerical modeling of the strain response of pebble beds are yet to emerge to illuminate what processes are involved. Continued study of mechanistic details of pebble bed thermal creep with respect to the contributions from elastic, plastic and diffusion flow, and interfacial sliding, as functions of stress, temperature, and time during creep is needed.

Acknowledgement

This work was performed under U. S. Department of Energy Contract DE-FG03-ER52123.

References

- [1] J. Reimann, E. Arbogast, M. Behnke, S. Muller, K. Thomauske, *Fusion Engineering and Design*, 49-50 (2000) 643.
- [2] H. Zimmermann, *Fabrication and Properties of Lithium Ceramics II* edited by G. W. Hollenberg and I. J. Hastings, *Advances in Ceramics*, vol. 27 (1989) 161.
- [3] K.C. Goretta, D.S. Applegate, R. B. Poeppel, M. C. Billone and J. L. Routbort, *J. Nucl. Mater.* 148 (1987) 166.
- [4] H. J. Frost and M. F. Ashby, *Deformation-Mechanism Maps* (Pergamon Press, Oxford, 1982)
- [5] S. Onaka, J. H. Huang, K. Wakashima, T. Mori, *Mechanics of Materials*, 31 (1999) 717.
- [6] Z. Lu, *Numerical Modeling and Experimental Measurement of the Thermal and Mechanical Properties of Packed Beds*, Ph. D. Thesis, 2000
- [7] R.L. Coble, *J. of the American Ceramic Society*, 41 (1958) 55.
- [8] Svoboda, J. and Riedel, H., *Acta Metallurgica et Materialia*, 43 (1995) 1.
- [9] F. Parhami, R. M. McMeeking, A.C. F. Cocks, Z. Suo, *Mechanics of Materials*, vol. 31, (1999) 43.

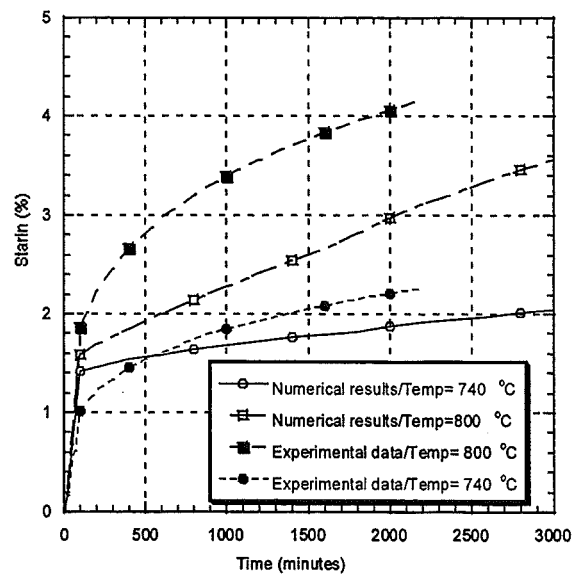


Figure 1. Comparison of strain as a function of time for two different temperatures. Numerically, initial strain is caused by the particle rearrangement subjected to an external load.

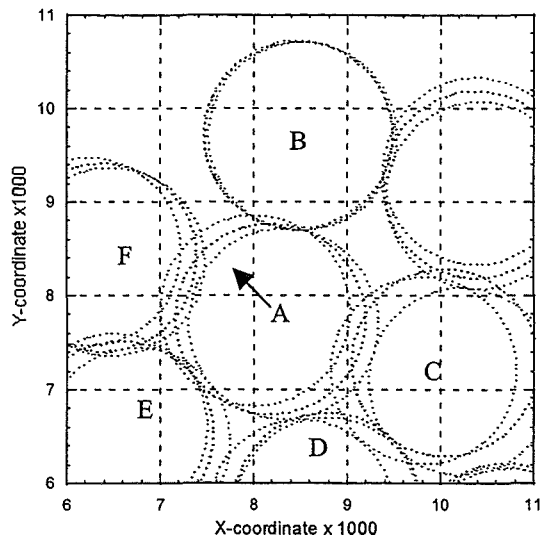


Figure 2. Particle contact evolutions. As creep proceeds, the contact area increases; total particles simulated: 6760. Particle A shifts slightly toward the upper-left corner due to the compression caused by creep.

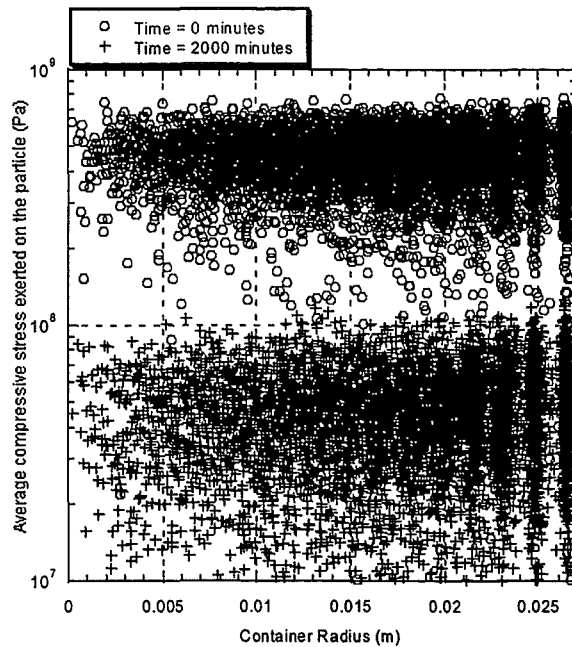


Figure 3. Average stress exerted on the particles at initial time and at time 2000 minutes. The average stress drops about one order of magnitude for most of the particles (each symbols represents a particle).

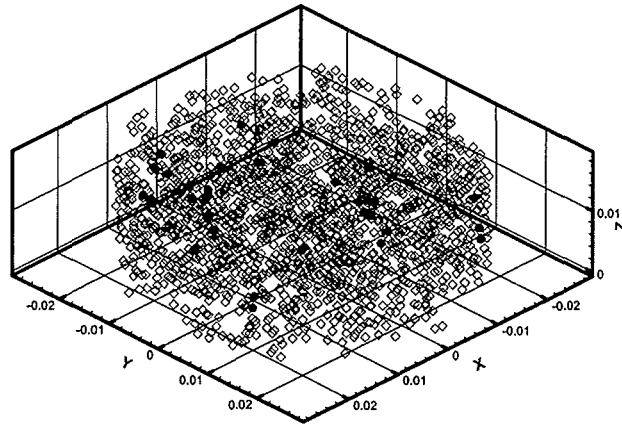


Figure 4. Particles with contact radius growth beyond 0.9 particle radius at time =10 minutes (solid circle) and time =2000 minutes (open diamond).

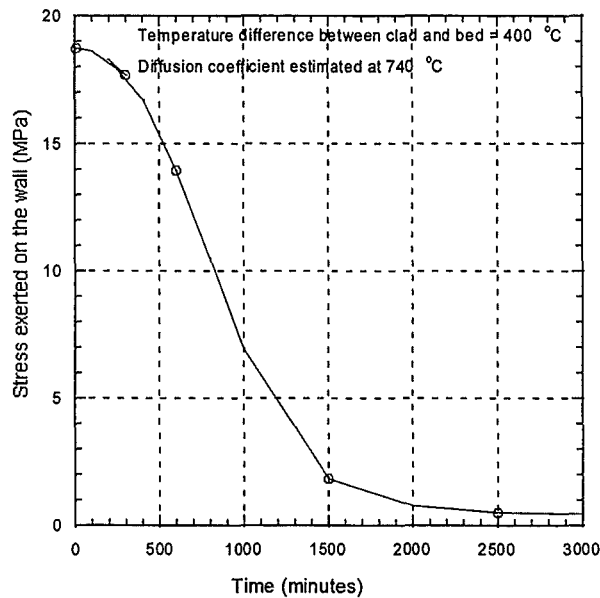


Figure 5 Average differential thermal stress exerted on the wall as a function of time. Stress is reduced due to thermal creep.

Fabrication Tests of Li_2TiO_3 Pebbles by Direct Wet Process

K. Tsuchiya¹, M. Uchida², H. Kawamura¹, S. Casadio³ and C. Alvani³

1 : JAERI, Oarai, Higashi-ibaraki, Ibaraki, 311-1394, Japan

2 : NGK INSULATORS, LTD., Suda, Mizuho, Nagoya, Aichi, 467-8530, Japan

3 : C. R. Casaccia, Via Anguillarese, 301, 00060 Rome, Italy

Lithium titanate (Li_2TiO_3) pebbles are considered to be the candidate material of the tritium breeders for fusion reactor from a point of good tritium recovery, chemical stability, etc. The direct wet process that Li_2TiO_3 pebbles were fabricated from the Li_2TiO_3 solution directly was proposed. In this study, pebble fabrication tests by the direct wet process were performed. The results from the preliminary test were as follows: 1) 100% Li_2TiO_3 powder could be dissolved when the holding time at more than 60°C was longer. 2) Good gel shape was maintained by dropping the Li_2TiO_3 condensed solution liquid in acetone. 3) Adjustment of a solution influenced the cracking rate of the Li_2TiO_3 pebble surface. Additionally, the solvent exchange was effective to decrease the crack of Li_2TiO_3 pebble surface and to improve the density of Li_2TiO_3 pebbles. It was clear that Li_2TiO_3 pebbles could be fabricated by the direct wet process and the pebbles with 5 μm grain and uniform structure were obtained.

1. INTRODUCTION

Lithium titanate (Li_2TiO_3) has attracted the attention of many researchers from a point of easy tritium recovery at low temperature, high chemical stability, etc. [1-2]. The application of small Li_2TiO_3 pebbles was proposed in the Japanese design of a fusion reactor blanket in order to reduce thermal stress, etc. [3-6]. The wet process and sol-gel methods [7-8] are most advantageous from the viewpoint of mass production, reprocessing lithium-bearing solution (see Fig. 1) and so on. In a previous paper, the Li_2TiO_3 pebbles were fabricated successfully by the indirect wet process [9-10]. However, there was a disadvantage on reprocessing from used breeder pebbles because Li_2CO_3 had to be recovered from the Li_2TiO_3 solution for the preparation treatment of this process. On the other hand, a technique of Li_2TiO_3 pebble fabrication that can dissolve the used Li_2TiO_3 pebbles directly, was proposed by C. Alvani, et al. (see Fig. 2) [11]. In this method, the used Li_2TiO_3 pebbles were directly dissolved, but the fabrication of Li_2TiO_3 pebbles was not successful using this solution.

In this study, fabrication tests of Li_2TiO_3 pebbles by the direct wet process were performed as a part of cooperative program on nuclear technology of fusion reactors in IEA (Task F).

1. EXPERIMENT

2.1. Materials

Li_2TiO_3 powder, fabricated by Soekawa Chemical Co. Ltd., was prepared with a purity of 99.9% as the starting material. The particle size of the Li_2TiO_3 powder was in the range of 0.2-2.3 μm and 0.63 μm on average. Silicon (Si) was the highest impurity detected in Li_2TiO_3 powder. Crystal structure of this powder was measured by X-ray diffractometry (XRD) and Li_2TiO_3 was the main component detected.

2.2. Parameter survey tests

The direct wet process mainly consists of four processes: dissolution process of Li_2TiO_3 powder, generation process of gel-spheres, drying process of gel-spheres and sintering process. At first, the

parameter survey tests were carried out in each process and optimum condition for fabrication of Li_2TiO_3 pebbles were examined.

- 1) In the dissolution process of Li_2TiO_3 powder, the solvent for dissolving the Li_2TiO_3 powder was decided. The solvents such as hydrogen peroxide (H_2O_2), citric acid ($\text{C}_6\text{H}_8\text{O}_7$) and/or other acids were selected.
- 2) In the generation process of gel-spheres, the gelation solvent for fabrication of gel-spheres was selected. The degassing was performed to eliminate gas (oxygen or hydrogen peroxide) dissolved in the Li_2TiO_3 solution. The Li_2TiO_3 solution was enriched by heating and a viscosity was increased by evaporating a water component in the solution.
- 3) In the drying process of gel-spheres, the drying temperature and time were selected. Additionally, solvent exchange was performed for decreasing the crack of spheres as required.
- 4) In the sintering process, the spheres were sintered in air, and Li_2TiO_3 pebbles with high density were fabricated.

The flow chart of fabrication process of Li_2TiO_3 pebbles by the direct wet process is shown in Fig.3.

3. RESULTS AND DISCUSSION

3.1. Dissolution tests

The first examination was conducted in order to select the solvent for dissolving the Li_2TiO_3 powder in the dissolution process. The dissolving was performed in a water bath controlled under 20°C with stirring. Result of dissolving test is shown in Table 1. Li_2TiO_3 powder was not dissolved in HNO_3 , HCl and H_2SO_4 (Run No.D-1 to D-3 in Table 1). In ref. [11], 30%- H_2O_2 can dissolve completely Li_2TiO_3 powder. In this examination, Li_2TiO_3 powder was almost dissolved in 30%- H_2O_2 . The dissolving time was over 4 h in the case of solid/liquid ratio of $2\text{ g} : 25\text{ cm}^3$. However, the reaction was highly exothermic and foamed (Run No.D-4). Therefore, Li_2TiO_3 powder was dissolved in the solvent mixed 30%- H_2O_2 and 5g- $\text{C}_6\text{H}_8\text{O}_7$. In this case, the Li_2TiO_3 powder was almost dissolved in the solvent. The reaction was not exothermic and foamed (Run No.D-8). Additionally, the dissolution of Li_2TiO_3 powder in 30%- $\text{H}_2\text{O}_2 + \text{C}_6\text{H}_8\text{O}_7$ added for pH adjustment was performed and the Li_2TiO_3 powder was dissolved when pH was 6.

The second examination was conducted in order to select the condition for dissolving the Li_2TiO_3 powder in the improvement test. The dissolving was performed in a water bath controlled under 60°C with stirring. Improvement of dissolution process is shown in Table 2. In this examination, Li_2TiO_3 powder was almost dissolved in 30%- H_2O_2 .

3.2. Preliminary tests

The first examination was conducted in order to decide the condition in the generation process of gel-spheres. The Li_2TiO_3 solution was prepared by dissolving Li_2TiO_3 powder with 30%- H_2O_2 or 30%- $\text{H}_2\text{O}_2 + \text{C}_6\text{H}_8\text{O}_7$. Acetone and acetic acid were used as the gelation solvent. At first, the kind of gelation solvent and the effect of addition of PVA were evaluated for gelling of Li_2TiO_3 solution. Acetone was selected as the best gelation solvent and the addition of PVA was not a good method because PVA was not able to be homogeneously mixed in Li_2TiO_3 solution. In the next step, the degassing was performed to eliminate gas (oxygen or hydrogen peroxide) dissolved in the Li_2TiO_3 solution. The temperature and time of degassing were 60°C and 5 h, respectively. On the other hand, the Li_2TiO_3 solution was set in a water bath controlled in a temperature range of 40°C and was stirred. A viscosity of Li_2TiO_3 solution was increased by evaporating a water component. The condensed solution was obtained for about 20 h in the case of the starting solution of 25 cm^3 (solid/liquid ratio of $2\text{ g} : 25\text{ cm}^3$). The solution was dropped into acetone of 2000 cm^3 . The droplet became gradually a gel state in acetone and gel-spheres were generated for over one night. The good gel-spheres with 1-2mm diameter were obtained in this method.

The second examination was conducted in order to decide the condition for decreasing the crack of spheres in the drying process of gel-spheres. The dried gel-spheres were sintered in an electric furnace at 1100°C for 4 h. The pebbles were observed by the SEM and cracks were generated on the surface of the pebbles. Therefore, the gel-spheres were picked up from acetone, and the gel-spheres were immersed into an exchanging solvent with a surface tension larger than that of acetone. A mix liquid

solution of acetone and propylene (mix volume ratio of 9:1) was selected as the exchanging solvent. After the solvent exchanging, the drying of gel-spheres was carried out and the dried gel-spheres were sintered in an electric furnace at 1100°C for 4 h. The cracks were not generated in the pebbles and the pebbles had a spherical shape. From the result, it is possible to induce a self-shrinkage of the gel-spheres utilizing the surface tension of the solvent by the solvent exchanging. The summary of preliminary tests is shown in Table 3.

3.3. improvement tests

The first examination was conducted in order to decide the condition in the generation process of gel-spheres. The Li_2TiO_3 solution was prepared by dissolving Li_2TiO_3 powder with 30%- H_2O_2 . Acetone and acetic acid were used as the gelation solvent. At first, the degassing was performed to eliminate gas (oxygen or hydrogen peroxide) dissolved in the Li_2TiO_3 solution. In the next step, the Li_2TiO_3 solution was set on the hot plate and evaporation and enrichment of the Li_2TiO_3 solution was carried out. A viscosity of Li_2TiO_3 solution was increased by evaporating a water component. The content of Li_2TiO_3 powder in the condensed solution was 14wt% in the first run. The content of Li_2TiO_3 powder were 19wt% and 23wt% in the second process and the third process, respectively. The droplet became gradually a gel state in acetone and the good gel-spheres with 1-2mm diameter were obtained in this method.

In the sintering process including the calcination, the dried gel-spheres were sintered in air. The gel-spheres were calcinated at 600°C for 2 h. After the calcination, the gel-spheres were sintered at 1000°C for 4 h. The summary of improvement tests is shown in Table 4.

4. CONCLUSIONS

The parameter survey was performed to determine each process of direct wet process and the results were as follows:

- 1) 100% Li_2TiO_3 powder could be dissolved when the holding time at more than 60°C was longer. Additionally, deposit in Li_2TiO_3 solution liquid was decreased by applying $\text{C}_6\text{H}_8\text{O}_7$ as solvent.
- 2) Good gel shape was maintained by dropping the Li_2TiO_3 condensed solution liquid in acetone.
- 3) Adjustment of a solution influenced the cracking rate of the Li_2TiO_3 pebble surface. Additionally, the solvent exchange was effective to decrease the crack of Li_2TiO_3 pebble surface and to improve the density of Li_2TiO_3 pebbles.

The future works will be to improve density by the optimization of the process parameter and to control shape by adjusting the viscosity of solution, for mass production by direct wet process.

REFERENCES

- [1] J.M. Miller, H.B. Hamilton, J.D. Sullivan, *J. Nucl. Mater.*, 212-215(1994)877-880.
- [2] N. Roux, J. Avon, A. Floreancig, J. Mougin, B. Rasneur, S. Ravel, *J. Nucl. Mater.*, 233-237(1996)1431-1435.
- [3] M. Dalle Donne, U. Fischer, M. Kühle, G. Schumacher, G. Sordon, E. Bojaritra, H. Reiser, D. Baschek, E. Bogusch, *Fusion Eng. Des.*, 8(1989)115.
- [4] N. Asami, K. Nagashima, et al., *Ceram. Trans.*, 27(1991)17.
- [5] P. Gierszewski, M.D. Donne, H. Kawamura, M. Tillack, *Fusion Eng. Des.*, 27(1995)167.
- [6] K. Tsuchiya, H. Kawamura, M. Nakamichi, H. Imaizumi, M. Saito, T. Kanzawa, M. Nagakura, *J. Nucl. Mater.*, 219(1995)240.
- [7] K. Tsuchiya, K. Watarumi, S. Saito, K. Fuchinoue, T. Furuya, H. Kawamura, *Proc. 5th International Workshop on Ceramic Breeder Blanket Interactions*, 1996, pp.191-199.
- [8] R.P. Muis, J.G. Laan, *Proc. 5th International Workshop on Ceramic Breeder Blanket Interactions*, 1996, pp.201-205.
- [9] K. Tsuchiya, H. Kawamura, K. Fuchinoue, H. Sawada, K. Watarumi, *J. Nucl. Mater.*, 258-263(1998)1985.
- [10] K. Tsuchiya, H. Kawamura, *J. Nucl. Mater.*, 283-287(2000)1380.

- [11] C. Alvani, S. Casadio, V. Contini, P. Bruno, E. Marmo, S. Lagos, *Presented at 7th International Workshop on Ceramic Breeder Blanket Interactions*, 1998, Petten, the Netherlands.

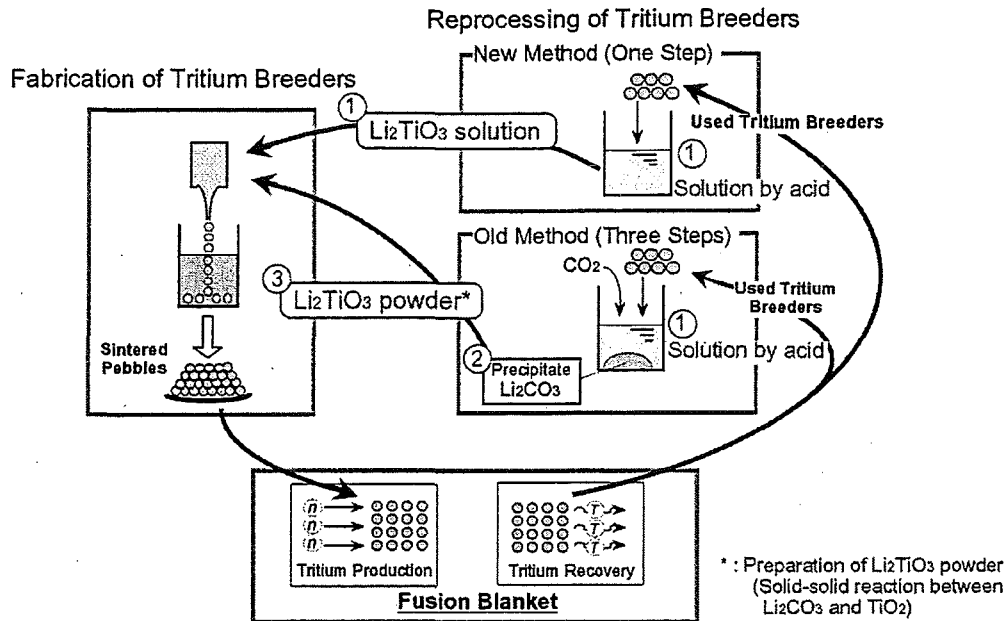


Figure 1 : Concept of lithium reprocessing.
(Comparison between old and new methods on pebble fabrication).

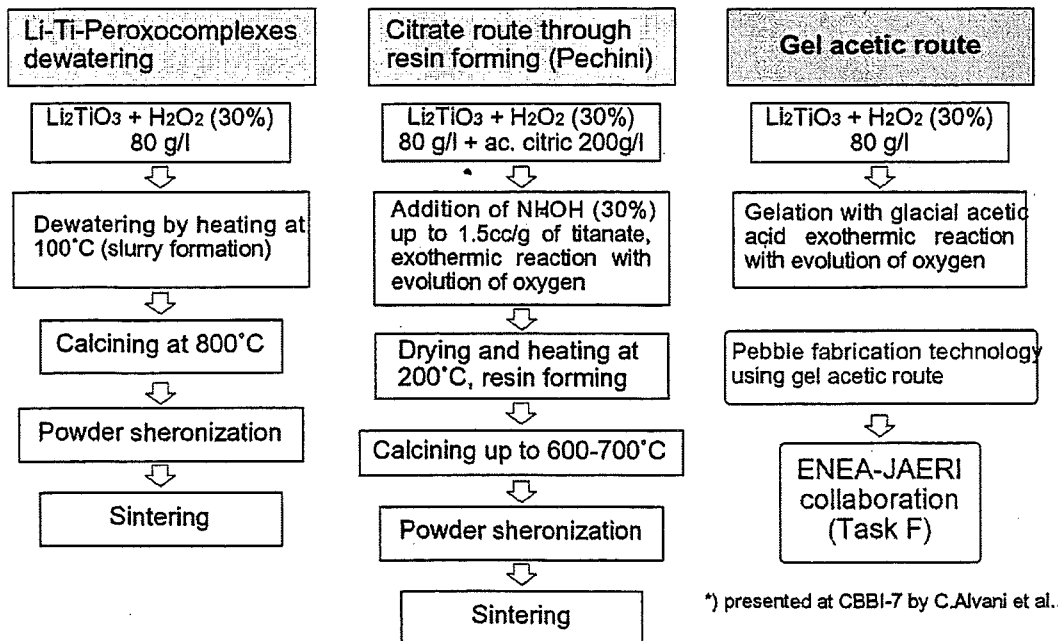


Figure 2 : Schematic flow sheets based on Li-Ti-peroxocomplexes in ENEA.

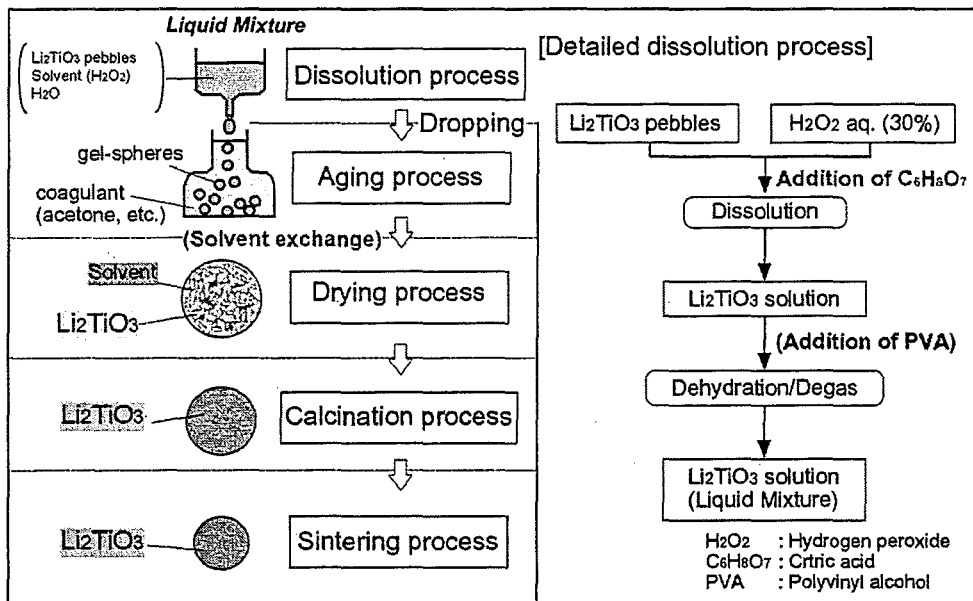


Figure 3 : Flow chart of fabrication process of Li_2TiO_3 pebbles by the direct wet process

Table 1: Result of dissolving test.

Run No.	Solvent	Color of solution	Rate of dissolution	Remarks
D-1	HNO_3	White*1	few	-
D-2	HCl	White*1	few	-
D-3	H_2SO_4	White*1	few	-
D-4	H_2O_2	yellow	much	heat and bubbles
D-5	$\text{H}_2\text{O}_2 + \text{HNO}_3$	reddish-brown	few	-
D-6	$\text{H}_2\text{O}_2 + \text{HCl}$	reddish-brown	few	-
D-7	$\text{H}_2\text{O}_2 + \text{H}_2\text{SO}_4$	reddish-brown	few	-
D-8	$\text{H}_2\text{O}_2 + \text{C}_6\text{H}_8\text{O}_7$	reddish-orange	much	-

*1 : Solution became muddy white.

Table 2: Improvement of dissolution process.

[Condition] Heating : 60°C, Cooling : 0°C

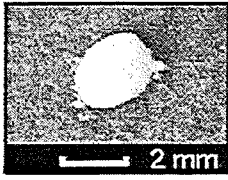
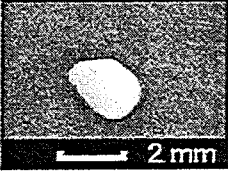
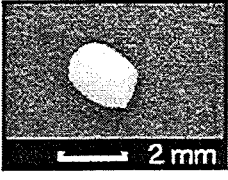
Run No.	Content	Holding time at more than 60°C	Rate of Dissolution	Remarks
ID-1	Li ₂ TiO ₃ : 0.8g H ₂ O ₂ : 50cm ³	3 h	94%	Max. Temp. of Reaction was 90°C.
ID-2	Li ₂ TiO ₃ : 2g H ₂ O ₂ : 50cm ³	4 h	98%	Max. Temp. of Reaction was 81°C.
ID-3	Li ₂ TiO ₃ : 4g H ₂ O ₂ : 50cm ³	5 h	97%	Max. Temp. of Reaction was 85°C.

Table 3: Summary of preliminary tests.

Test Run	Dissolution Condition		Solvent Exchange	Calcination Condition	Sintering Condition	Crack (sintered pebbles)
	Regulation	Remarks				
1st Run	Li ₂ TiO ₃ : 2g H ₂ O ₂ : 25cm ³ (optimum condition)	Decision of solvent - H ₂ O ₂ , H ₂ SO ₄ , HCl, HNO ₃	—	—	—	—
2nd Run (ENEA condition)	Li ₂ TiO ₃ : 2g H ₂ O ₂ : 25cm ³	Decision of coagulant - Acetone, glacial acid (C ₂ H ₄ O ₂ : no gelation)	—	—	—	—
3rd Run	Li ₂ TiO ₃ : 2g H ₂ O ₂ : 25cm ³ C ₆ H ₈ O ₇ : 5g	Coagulant : Acetone	—	600°C 2 h	1100°C 1 h	heavy crack
4th Run	Li ₂ TiO ₃ : 2g H ₂ O ₂ : 25cm ³ C ₆ H ₈ O ₇ : 5g	Coagulant : Acetone (addition of PVA)	—	600°C 2 h	1100°C 1 h	heavy crack
5th Run	Li ₂ TiO ₃ : 2g H ₂ O ₂ : 25cm ³ C ₆ H ₈ O ₇ : 5g	Coagulant : Acetone (addition of degas process)	—	600°C 2 h	1100°C 1 h	heavy crack
6th Run	Li ₂ TiO ₃ : 2g H ₂ O ₂ : 25cm ³ C ₆ H ₈ O ₇ : 5g	Coagulant : Acetone (addition of degas process)	○	600°C 2 h	1100°C 4 h	light crack

Table 4: Summary of improvement tests.

Dropping Condition : RT in acetone

Run No.	Content of Li_2TiO_3	Shape of Spheres	Surface of Li_2TiO_3 Pebbles ¹⁾
1st Run	14wt%		no crack
2nd Run	19wt%		no crack
3rd Run	23wt%		no crack

1) Sintering condition : 1000°C x 4h

Key Issues for the ‘HICU’ Project - A High Fluence Irradiation of Ceramic Breeder Pebble Beds”

J.G. van der Laan^a, R. Conrad^b, J.H. Fokkens^a, H.E. Hofmans^a, J. Hooijmans^c,
H. Kawamura^d, J.D. Lulewicz^e, A.J. Magielsen^a, S. Malang^c, M.A.G. Ooijevaar^a,
G. Piazza, B.J. Pijlgroms^a, N. Roux^d, M.P. Stijkel^a, A.Y. Ying^f

^a NRG, P.O. Box 25, 1755 ZG Petten, The Netherlands

^b JRC, Institute for Energy, Petten, The Netherlands

^c ECN, Petten The Netherlands,

^d JAERI, Oarai, Japan

^e CEA Saclay, France

^f FZK, Karlsruhe, Germany

^g UCLA, Los Angeles, USA

The HICU project concerns the investigation of the impact of neutron spectrum and the influence of constraint conditions on the thermo-mechanical behavior of breeder pebble-beds in a high fluence irradiation. The project is part of the EU technology programme for development of the Helium Cooled Pebble-Bed blanket concept, and performed in collaboration with Japanese and US partners in the IEA framework.

The target dose of the HICU experiment is to accumulate 20 dpa in Li_4SiO_4 and Li_2TiO_3 in about two calendar years. Lithium isotope compositions and spectrum tailoring measures are chosen so as to obtain burn-ups and dpa/burnup-ratios, that are DEMO relevant.

The status of the ‘HICU’ project by Fall 2001 is presented. Main critical issues concern the specimen size and geometry, and the choice of materials for cladding and instrumentation. Results of compatibility tests are presented.

1.INTRODUCTION

In the framework of developing the Helium Cooled Pebble-Bed (HCPB) blanket, the EU decided in 1999 to proceed with "the investigation of a) the impact of neutron spectrum and b) the influence of constraint conditions on the thermo-mechanical behavior of breeder pebble-beds in a high fluence irradiation" [1,2]. The irradiation will be performed in the High Flux Reactor (HFR) at Petten, The Netherlands, and was aimed to start in 2001. The project is called HICU, an acronym for "*High neutron flu-ence Ir-ra-di-a-tion of peb-ble staCks for fUision*".

Within the framework of the IEA agreement, Annex on Fusion Nuclear Technology, Japanese and US partners are involved to profit from materials exchange and knowledge sharing. This task has been adopted as subtask G within the IEA agreement on Fusion Nuclear Technology.

The fast neutron fluence rate in the HICU experiment should allow to obtain a target dose of 20 dpa in Li_4SiO_4 (OSi) and Li_2TiO_3 (MTi) in about two calendar years. Lithium isotope compositions and spectrum tailoring measures are chosen so as to obtain in one set of capsules DEMO relevant

dpa/burnup-ratios (~6 dpa/%) as well as - in an other set of capsules using higher ${}^6\text{Li}$ -enrichment - DEMO relevant burn-ups (10-15 %).

Main critical issues for the HICU project concern the shielding, the specimen size and geometry, and the choice of materials for cladding and instrumentation. Results of compatibility tests are presented. The HICU project status of September 2001 is summarized.

2.DESIGN EVOLUTIONS

2.1.Nuclear characteristics

The nuclear analyses, performed since summer 2000, have concentrated on the Cd-burn rates [3,4]. It is concluded that at least 2 mm Cd is needed to maintain a constant dpa/burn-up ratio for the 'reference' case. An additional Hf-layer would delay burn-through. The FISPACT code showed some deficiencies for Cd burn-up calculations, for which solutions have been proposed to the UKAEA, the responsible association within EFDA. Figure 1 shows a summary of calculated dpa and lithium burn-ups for various experimental options and the HCPB DEMO Blanket, based on a OSi breeder pebble-bed. The curves 'DEMO 1 FPY' and 'DEMO 20.000 hours' represent the dpa and burn-up for various distances from the First Wall [2]. The highest burn-up location is about 10 mm from the blanket front. The line crossing these points represents the dpa and burn-up accumulation with time. Curves '7.5%+1Cd' and '7.5%+2Cd/.5Hf' are the calculated cases for an OSi bed with natural ${}^6\text{Li}$ abundance. The bigger dots correspond to values achieved approximately in 1, 2 and 3 years respectively. The curves '20%..' are for OSi beds with 20% enrichment in ${}^6\text{Li}$. The curve 'EXOTIC-7/8' indicates the area of irradiation experiments performed in the past 10 years on various OSi and MTi pebbles. The curve '0.75% Unsh', shows the calculated dpa and burn-up for depleted material, which is considered to provide insight in neutron damage effects rather than Li transmutation.

For the specimen arrangement in the envisaged HFR position the n,α heating is about 20 and 45 W/cc for the Cd shielded OSi7.5% and OSi20% respectively.

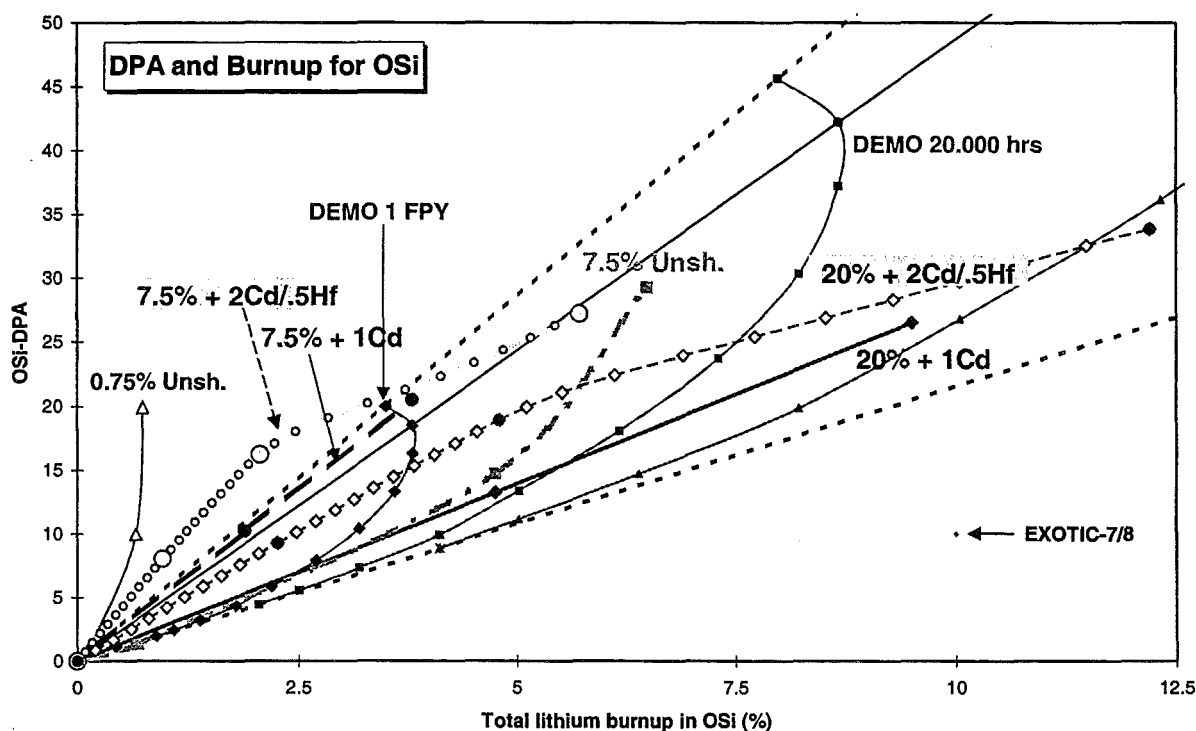


Figure 1: Calculated dpa and lithium burn-up for typical experimental options in the HICU irradiation experiment and the HCPB DEMO blanket.

2.2. Thermo-mechanics

The high expansion coefficient and the low melting point of Cadmium complicate the engineering design of the experiment. The Cadmium shield and its claddings could be considered as independent from the containment tube. In such case the inner space for specimens is only about 22 mm. This would allow locating a maximum of 3 pebble-stacks of 9mm outer diameter in one cross section.

Detailed thermal analyses are ongoing for various arrangements of cylindrical specimens: the high constraint plus high temperature specimens require a structure retaining strength at T=600-650°C. The low constraint plus high temperature specimens require a structure operating at T=750-800°C.

For any case the compatibility of the pebbles with the structure is problematic. Furthermore, since central temperature measurements are required the thermocouple cladding needs to be breeder-compatible. In section 3.1 results of compatibility tests are discussed.

The design of the pebble-stacks shows that they are too small for the present tools for thermo-mechanical analysis of pebble-beds. In particular the ratio of pebble size to stack diameter is large, and larger pebble-wall contact areas increase e.g. wall friction. This prevents a straightforward analysis of stresses during irradiation, and the determination of pebble swelling and the effects on heat transfer. This required pre-testing of specimens representing key features of the HICU pebble-stacks, see section 3.2.

3. PRETESTING

3.1. Compatibility

The compatibility requirements for HICU specimens are two-fold:

1. The formation of a reaction layer on the structure (clad) can be tolerated for the constrained specimens to a limited extent only. For the low constrained specimens the clad should not degrade to the extent that it loses its 'holder' function.
2. The chemical reactions at the pebble-wall interfaces and the diffusion of elements should not influence the key pebble properties under investigation.

High temperature (800°C) tests have been performed with OSi and MTi pebbles in contact with Eurofer-97, AISI 321, INC718, or 15-15Ti in a purged He+H₂ environment. A summary is given in table 1, while figures 2a-d give some typical micrographs of interactions.

Table 1: Summary of compatibility tests performed in helium + 0.1%hydrogen purge for (crushed) MTi and OSi pebbles with some structural materials. Serious interactions are indicated with '-', modest reactions with '+/-' and negligible or zero reaction rates with '+'.

Materials	Time (h)	MTi pebbles	OSi pebbles
AISI 321	500	+/-	+/-
	1000	+/-	-
Inconel 718	500	+/-	+/-
	1000	-	-
Eurofer97	500	+/-	-
Inconel 718 Ni-coated	500	+/-	-
15-15 Ti steel	200	-	-
	500	-	-
Pre-oxidised AISI 321	200	+/-	-
	500	-	-
Platinum	200	+	+
	1000	+	+

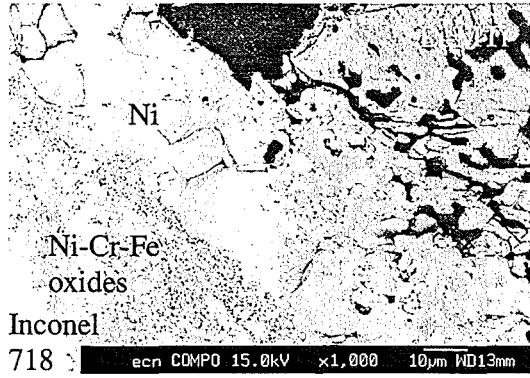


Figure 2a: Inconel 718 with nickel coating – 500 hours in contact with MTi.

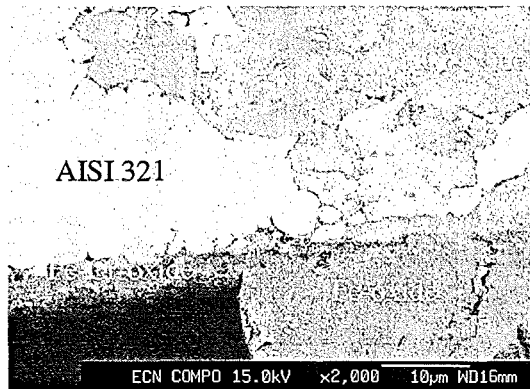


Figure 2b: Pre-oxidised AISI 321 (4 h) – 500 hours in contact with OSi.

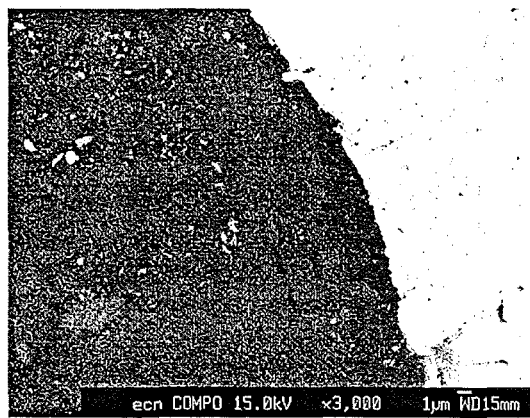


Figure 2c: Platinum in contact with OSi after 1000 hours.

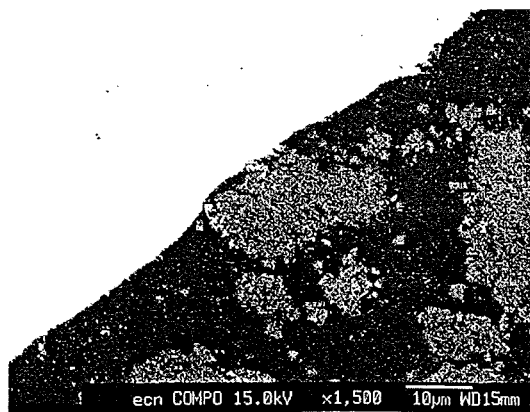


Figure 2d: Platinum in contact with MTi after 1000 hours.

3.2. Specimen design

First choice for the cladding material is Eurofer; however ODS and V-alloy may be considered too. For developing the pebble-stacks, tubular test specimens are manufactured from a high strength alloy. The inner diameter is 4, 8 or 12 mm and the pebble-stack height is either 20 or 40 mm. Pt-foil of 0.05 mm thickness will prevent direct contact with the pebble-material. First tests are to start November 1. In these tests the pebble-stack characteristics are determined, and should allow to elaborate details of filling procedure, pre-test compaction, pre-heating etc.

They are optionally pre-pressed, and subsequently isothermally heated at 800-850°C: It is necessary for determine bed structure (wall friction effects), homogeneity of deformation, and to explore PIE concepts.

4. TEST MATRIX

The test matrix considerations have not led yet to detailed proposal. The scheme under discussion is given in table 2. The number of specimens to be instrumented with thermocouples is to be balanced with redundancy and space limitations.

Table 2: HICU test matrix - tentative version September '01

		Li-6	Shield	High Constraint High Temp	High Constraint Low Temp	Low Constraint High Temp	Low Constraint Low Temp	Pressure ? High Temp
OSi-ref	FZK	20	Cd	2		1	1	1
OSi-ref	FZK	7,5	Cd	2	1	1	1	
OSi-ref	FZK	7,5	None	1				
OSi-ref	FZK	0,06	Cd			1	1	
				5		3	3	1
MTi-ref	CEA	30	Cd	2		1	1	1
MTi-ref	CEA	11	Cd	2	1	1	1	
MTi-ref	CEA	0,06	Cd			1	1	
MTi-ref	CEA	7,5	Cd	1		1	1	
MTi-ref	CEA	7,5	None	1				
MTi-ref+	CEA	7,5	Cd	1		1	1	
MTi-ref++	CEA	7,5	Cd	1		1	1	
				8		6	6	1
MTi-0%	JAERI	31	Cd	1		1	1	
MTi-5%	JAERI	31	Cd	1	1	1	1	1
MTi-10%	JAERI	31	Cd	1		1	1	
				3		3	3	1

5. MATERIALS

- OSi pebbles have been produced by Schott, subcontracted by FZK, with 20% Li-6 enrichment. Also depleted material (0.06%) has been manufactured.
- CEA has reported that the 11% and 30 % enriched as well as the 0.06 % depleted MTi material is ready for shipment. All 3 batches are denoted as 'reference' type.
- JAERI has produced batches of MTi pebbles, 3 grades with 0, 5 and 10% TiO₂ respectively, all with a 31% enrichment.

Helium pycnometry has been further developed for maximization of accuracy in case of small quantities of pebbles. The equipment has been shown reliable and stable for batches of 0,6 cm³ to 2 g.

In that case the accuracy is about 0.3 %. Table 3 shows some results for present day pebble types, e.g. from references [5-8].

Table 3: Results of helium pycnometry for some available pebble types.

Material	Helium Density (% TD)	Closed porosity (%)
Li ₄ SiO ₄ (ref)	99.4	0.6
Li ₂ TiO ₃ (ref)	95.7	4.3
Li ₂ TiO ₃ (ref-2)	94.9	5.1
MTi sintered at 1150°C	96.1	3.9
MTi annealed 3 months at 970 °C	97.1	2.9
MTi after Uni-axial Compression Test at 800 °C	93.2	6.8
JAERI large pebbles	97.8	2.2
JAERI small pebbles	99.6	0.4
MTi (CTI15C7Ti)	91.5	8.5
MTi (CTI13BOTi100)	96.0	4.0

6.PROJECT STATUS

The project status and plan by September 2001 in short:

- Detailed design analyses for specimens and rig ongoing.
- Specimen and material selection, and final test matrix proposal and definition of post-irradiation examinations by December 2001.
- Irradiation campaign from Summer 2002 onwards.
- Supportive modelling activity to launch ...

REFERENCES

- [1] J.G. van der Laan, R. Conrad, K. Bakker, S. Casadio, A.V. Fedorov, U. Fischer, S. Malang, G. Piazza, B.J. Pijlgroms, N. Roux, A. van Veen: "On the irradiation performance of HCPB candidate ceramic breeder materials to DEMO-like conditions - an approach with neutron and particle irradiations", in: A. Ying (Ed.), CBBI-8 workshop proceedings, February 2000.
- [2] U. Fischer, S. Herring, A. Hogenbirk, D. Leichtle, Y. Nagao, B.J. Pijlgroms and A. Ying: "Comparison of nuclear irradiation parameters of fusion breeder materials in high flux fission test reactors and a fusion power demonstration reactor", in: A. Ying (Ed.), CBBI-8 workshop proceedings, February 2000.
- [3] B.J. Pijlgroms & C.M. Sciolla, 'Burnup calculations for Cadmium; a case study for HFR experiments', NRG Report 20295/00.34510/P, September 2000
- [4] B.J. Pijlgroms, 'Pre-design burn-up calculations for the HICU experiment', NRG Report 20295/00.37276/I, November 2000.
- [5] J.D. Lulewicz, N. Roux, F. Pourchet, J.P. Joulin: "Status on fabrication of Li₂TiO₃ pebbles by extrusion-sphernisation-sintering process", these proceedings.
- [6] J. Reimann, J.-D. Lulewicz, N. Roux, G. Wörner: "Thermal creep of metatitanate pebble beds", these proceedings.
- [7] G. Piazza et al, CBBI-8 workshop proceedings, February 2000.
- [8] S. Kato, H. Tomimoto, T. Takayama, K. Tsuchiya and H. Kawamura: "Current Status on Li₂TiO₃ Pebble Fabrication by Wet Process", these proceedings.

Status of the In-Pile Test of HCPB Pebble-Bed Assemblies in the HFR Petten

J.G. van der Laan^a, R. Conrad^b, J.H. Fokkens^a, H.E. Hofmans^a, M. Jong^a, A.J. Magielsen^a, S. Malang^c,
B.J. Pijlgroms^a, J. Reimann^c, N. Roux^d, M.P. Stijkel^a

^a NRG, P.O. Box 25, 1755 ZG Petten, The Netherlands

^b JRC, Institute for Energy, Petten, The Netherlands

^c FZK, Karlsruhe, Germany

^d CEA Saclay, France

In the framework of developing the Helium Cooled Pebble-Bed (HCPB) blanket an irradiation test of pebble-bed assemblies is prepared at the HFR Petten. The test objective is to concentrate on the effect of neutron irradiation on the thermal-mechanical behaviour of the HCPB breeder pebble-bed at DEMO representative levels of temperature and defined thermal-mechanical loads.

The basic test elements are EUROFER-97 cylinders with a horizontal bed of ceramic breeder pebbles sandwiched between two beryllium beds. The pebble beds are separated by EUROFER-97 steel plates. The heat flow is managed such as to have a radial temperature distribution in the ceramic breeder pebble-bed as flat as reasonably possible.

The paper reports on the project status, and presents the results of pre-tests, material characteristics, the manufacturing of the pebble-bed assemblies, and the nuclear and thermo-mechanical loading parameters.

1. INTRODUCTION

In the framework of developing the Helium Cooled Pebble-Bed (HCPB) blanket an irradiation test of pebble-bed assemblies is to be performed at the HFR Petten. The performance analysis of the HCPB blanket requires knowledge of the thermo-mechanical behaviour of the pebble-beds. In this framework a number of experimental and modelling activities are being pursued in the EU programme. The thermo-mechanical performance of breeder pebble-beds appears to be characterised by: a) non-linear elasticity, b) irreversible deformation or compaction, and c) creep [1]. Early 1998 an in-pile test of pebble-bed assemblies has been defined that is to concentrate on the effect of neutron irradiation on the thermal-mechanical behaviour of the HCPB breeder pebble-bed at DEMO representative levels of temperature and defined thermal-mechanical loads. The first design has been presented at the 20th SOFT, and at CBBI-7 [2,3].

At ISFNT-5 and CBBI-8 the results of modelling and the associated SCATOLA tests were presented [4-5]. The clear evidence for fast stress relaxation in the breeder pebble-bed led to a revision of the test matrix, the fixed plate option was left to have all test-elements operate with floating plates.

At CBBI-9 several new developments were presented [6]: the problematic handling with binary beryllium beds led to the choice for a mono-disperse beryllium pebble bed. The pressure dependence of the Be bed conductivity necessitated to modify the design for pre-test bed compaction. Furthermore the instrumentation was reduced in size and number. The specific neutronics oriented test of '99 was evaluated.

This paper at CBBI-10 reports on the project status by Fall 2001, and presents the results of pre-tests, material characteristics, the manufacturing of the pebble-bed assemblies, and the nuclear and thermo-mechanical loading parameters. Details of thermal, chemical and thermo-mechanical analyses are presented in accompanying papers [7,8].

1.1. Test objectives and features

The objective for the in-pile test of Pebble-Bed Assemblies is to concentrate on the effect of neutron irradiation on the thermal-mechanical behaviour of the HCPB breeder pebble-bed at DEMO representative levels of temperature and defined thermal-mechanical loads. The basic test elements are EUROFER-97 cylinders with a horizontal bed of ceramic breeder pebbles sandwiched between two beryllium beds, see figure 1. The pebble beds are separated by EUROFER-97 steel plates, which are allowed to 'float' i.e. they are not connected to the cylinder walls but supported by the neighbouring pebble-beds only.

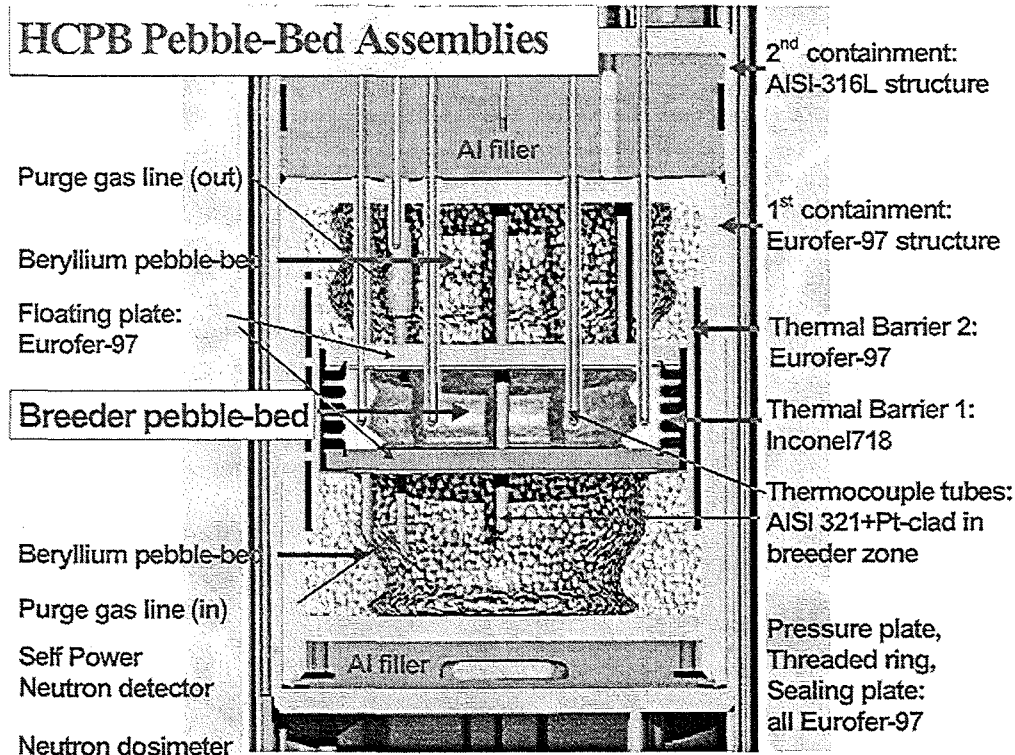


Figure 1: Schematic view of pebble-bed assembly, showing cross-section of test-element, second containment and instrumentation.

The breeder pebble beds are either Li_4SiO_4 or Li_2TiO_3 about 11 mm in height and 45 mm in diameter. Two assemblies concern Li_4SiO_4 pebble-beds with maximum breeder temperatures of 650 and 850 °C respectively. The two other assemblies are loaded with Li_2TiO_3 pebbles with a difference in sintering temperature. Their maximum breeder temperature is about 850 °C. The heat flow is managed such as to have a radial temperature distribution in the ceramic breeder pebble-bed as flat as reasonably possible. This is obtained by two thermal barriers: 1) a gas gap between the Inconel barrier and the cylindrical insert of Eurofer-97, and 2) a gas gap between the latter insert and the Eurofer-97 structure. The beryllium beds are single sized 1mm pebbles. The strong dependence of thermal conductivity on the bed compaction has required extensive analyses and pretests in order to arrive at well-defined start-up conditions for the in-pile test. This is achieved by a specific pre-test compaction procedure by pressing and heating, as demonstrated in a full-size prototypical assembly.

This in-pile test of pebble bed assemblies combines a number of inherent HCPB performance issues:

- thermal and mechanical behaviour of pebble-beds according to specific filling process and practically achievable packing density; it allows to study the possibility of gap formation and the development of modelling and predicting capabilities.
- The floating plates are in contact with breeder and multiplier. The actual bed-solid interfaces have relevant temperature and provide in-pile compatibility data.

- The experimental gas purge and tritium permeation characteristics are relevant for TBM design.
- The Eurofer-97 RAFM steel is used in a structural function during neutron irradiation.

2. LOADING PARAMETERS

2.1. Nuclear characteristics

The nuclear parameters for the in-pile test have been calculated using MCNP and applying a full model of the HFR core, see table 1 and figure 2.

Table 1: Nuclear parameters for the in-pile test of HCPB Pebble-Bed Assemblies

(n,α)power density	20-26 W/cc (average)
gamma heating	2-3 W/g
Irradiation time (planned)	300 days (12 cycles)
Lithium Burn-up	~ 3 %
Damage in RAFM Steel	~ 2.4 dpa
He-production in Beryllium	~ 600 appm He
Fast Fluence:	
> 0.1 MeV	~ $3.9 \times 10^{25} \text{ m}^{-2}$
> 1 MeV	~ $1.8 \times 10^{25} \text{ m}^{-2}$

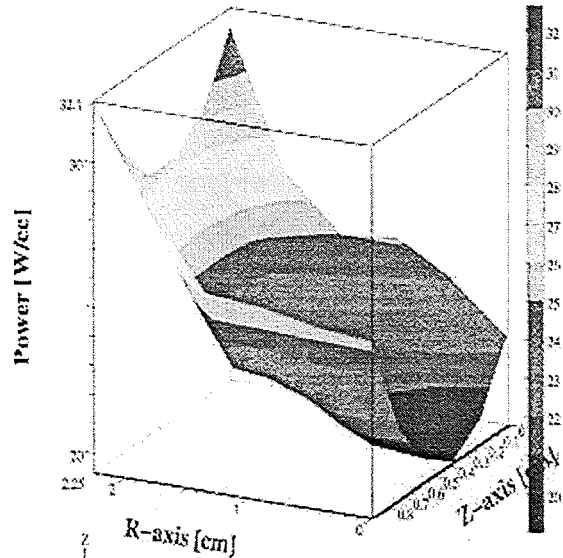


Figure 2: Nuclear power density profile for a Li-ceramic breeder bed in the PBA irradiation position. Z-axis is along height of the breeder bed.

A dedicated irradiation experiment has been performed with the objective to properly estimate the neutron flux level and profiles in the peak position for a representative nuclear configuration. Its design consists of a $\text{Ø}45 \times 11 \text{ mm}$ MTi-pebble bed contained between two plates, and a cylinder of stainless steel, and an aluminium ring, see figure 3.

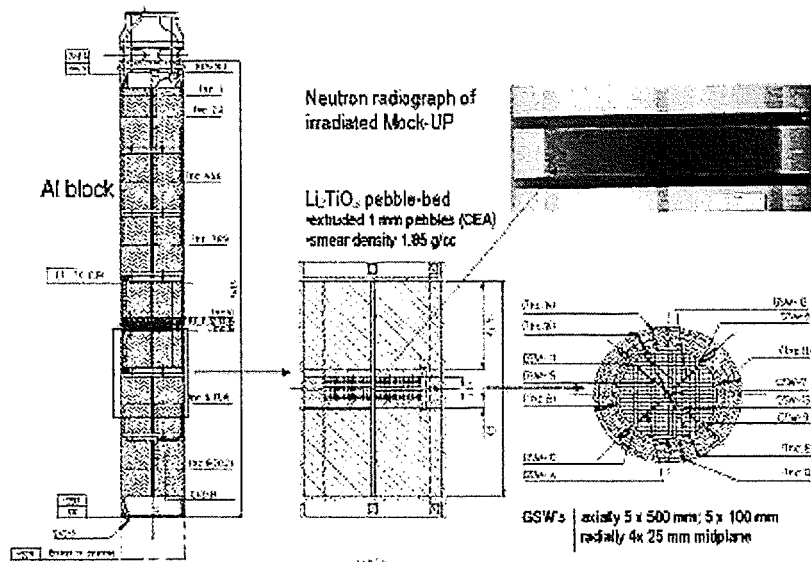


Figure 3: Axial and radial cross-sections of the in-pile mock-up experiment, showing locations of breeder section, Al-blocks and positioning of GammaScanWires. A neutron radiograph taken after irradiation is inserted.

The main body is formed by aluminium blocks, which are all placed in a stainless steel containment. The experiment has been instrumented with several neutron detector sets and a total of 15 so-called gamma scan wires. Thermocouples were arranged at the pebble-bed sides and in all Al-blocks. The latter were specifically arranged to derive the gamma heating characteristics. Irradiation has been performed in HFR for 1 cycle in 1999. Figures 4 and 5 show results from the neutron metrology along with dedicated MCNP analyses.

The HFR model used in the MCNP calculations appears fairly adequate for calculating the nuclear characteristics of the irradiation experiment in detail (axially & radially). New MCNP analyses for 4 actual PBA's (11mm bed) and estimated loading parameters are underway.

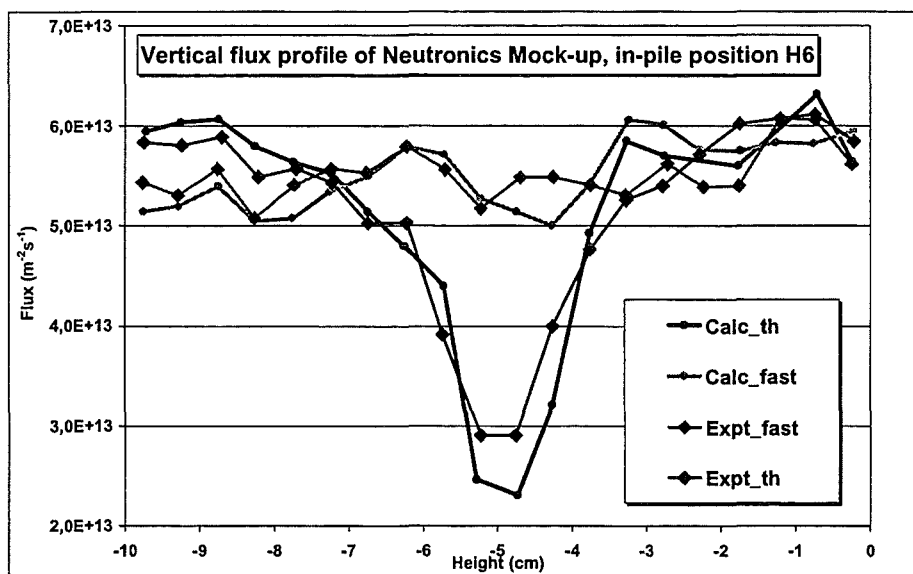


Figure 4: Axial flux profiles measured and calculated for the PBA neutronics Mock-up.

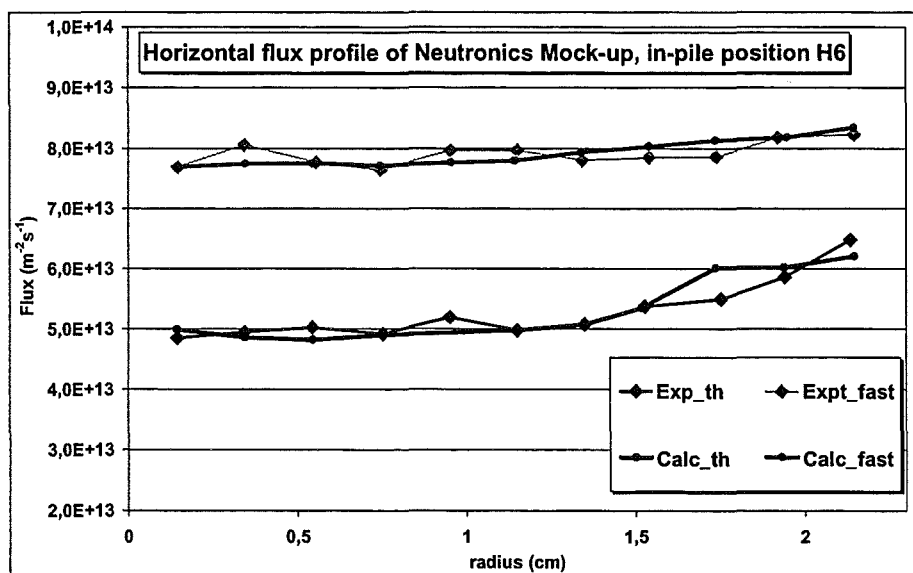


Figure 5: Radial flux profiles measured and calculated for the PBA neutronics Mock-up.

2.2. Thermal characteristics

Details of thermal, and thermo-mechanical analyses are presented in accompanying papers [7,8]. The thermal analyses have been extended to quarter sector 3-D in order to determine local temperature

field near TC-tubes. It is found that the central thermocouple reading may be up to a 100 degrees C lower than the actual 'temperature'. This reading is however responding proportionally to bed conductivity changes, which therefore should enable its quantification from in-pile measurements. The beryllium bed compaction is of the order of 0.5-1% which leads to an effective conductivity of ~ 6.7 W/mK.

Final thermal and mechanical calculations for the 4 test elements are ongoing. They concern at first the detailing of gas gap dimensions. Secondly they serve to guide in choosing the reactor start-up conditions.

3.MATERIALS

The ceramic pebble beds are Li_4SiO_4 and Li_2TiO_3 , the two candidates for the HCPB blanket concept. The test matrix has been chosen to have Li_4SiO_4 beds tested at two temperature levels, whereas the two Li_2TiO_3 pebble beds have different manufacturing histories. This choice is based on the thermal creep results of Reimann et al. [10]. Main pebble characteristics are given below in table 1, along with the beryllium pebbles. The 6Li abundance is natural for all breeder materials.

Table 1: Nominal characteristics of breeder and beryllium pebbles

Material	ID	Test-element	Pebble density (%TD)	Pebble size (mm)	Grain size (μm)	Pebble bed density (g/cc)
OSi	LOT 98/2	#1, #4	98	0.25-0.63	150-200	1.49
MTi-1	CTI 1529 Ti 1040 CTI	#2	92	0.8-1.2	1-2	1.82
MTi-2	CTI 641 Ti 1100 CEA	#3	89	0.8-1.2	1-5	1.85
Be	NGK (FZK 1999)	all		0.7-1.3		1.15

The structural material for the test elements is Eurofer-97, the available Reduced Activation Ferritic-Martensitic steel for the EU fusion programme [11]. This material has been delivered as 100mm diameter rod and as plate with thickness of 1.5, 8 and 14 mm. The main part of the test element, the 'cup', and the large thermal barrier have been manufactured from rod. The cup has been pressure tested for core quality, prior to the insertion of the thermocouple tubes. The floating discs and the pressing discs have been taken from 14mm plate material. The seal plates are manufactured from 1.5mm plate.

The 1st thermal barrier has been manufactured from Inconel 718. Rings were laser welded to form a 'bellow' like structure, i.e. high radial stiffness and low axial stiffness.

The thermo-couple tubes have been made of stainless steel type 321. They are welded at the outside to the Eurofer bottom.

Compatibility tests of the SS 321 with OSi and MTi pebbles have been performed at 800°C for 1000 hrs and more in a helium + 0.1% hydrogen purge. The results show a larger reaction rate for OSi as compared to the MTi pebbles. The preferred solution is to apply a Pt-foil cladding to the hotter parts of the tubes in contact with the breeder beds.

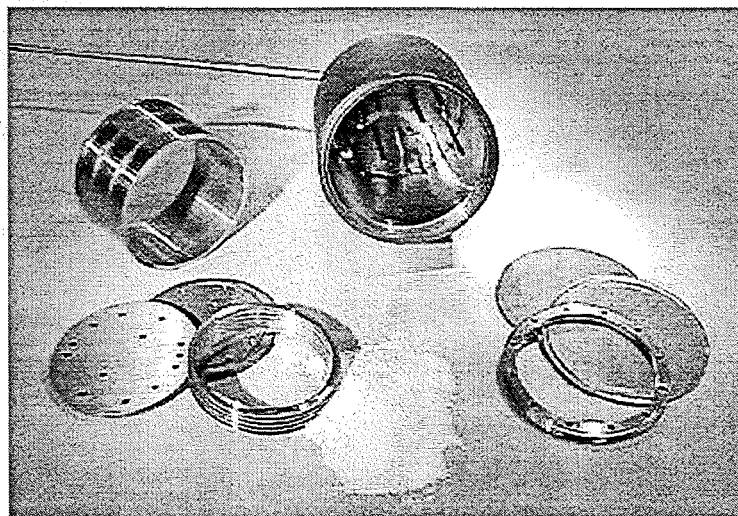
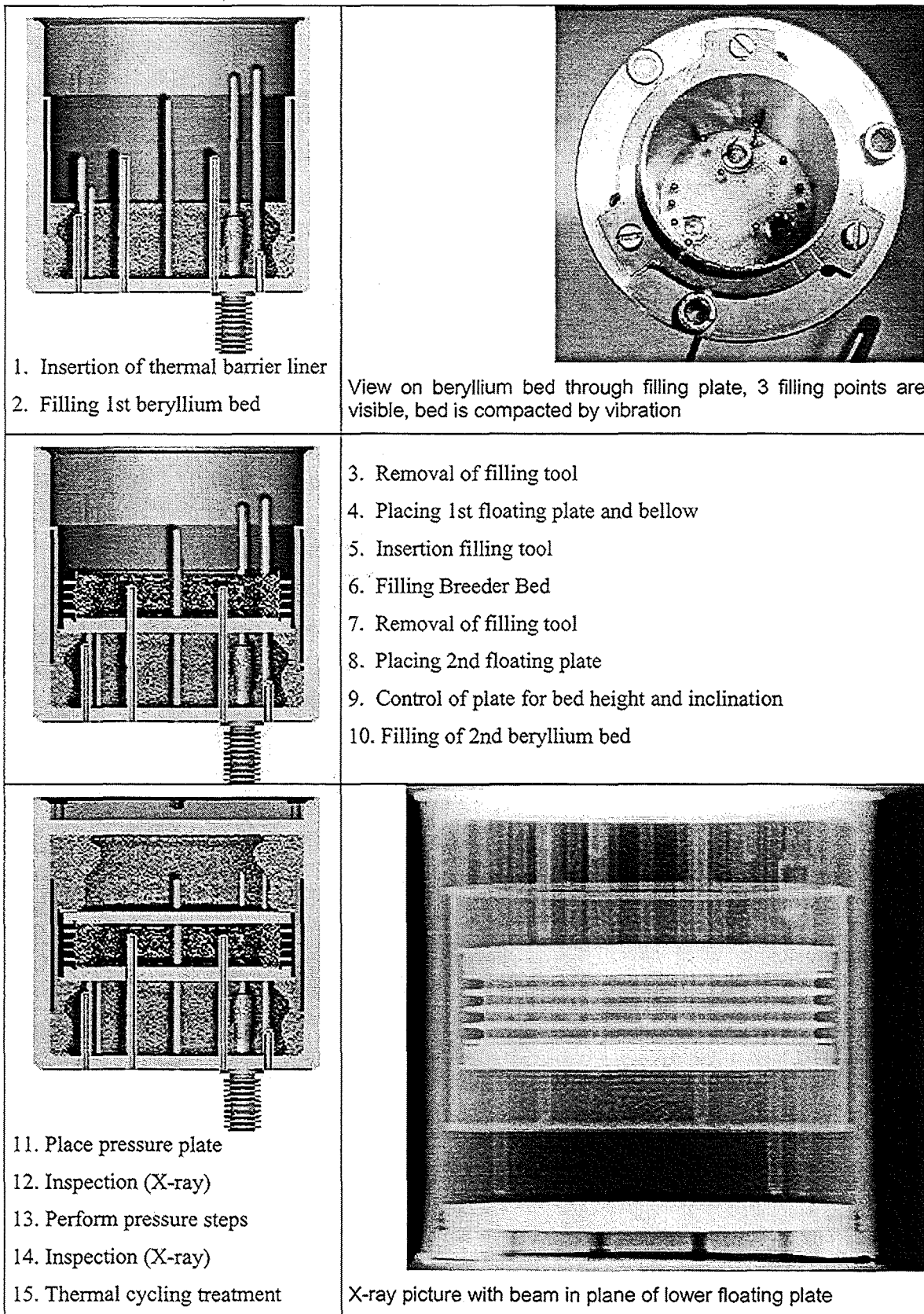


Figure 6: Parts before assembly

Figure 7: Main (15) assembly steps performed for the prototype test element



4.ASSEMBLY PROCEDURE

The pre-test compaction of the pebble beds has been developed using a prototype test-element, as depicted schematically in figure 7. After 3 cold pressing steps at 1, 2 and 3 MPa respectively, a further 3 MPa 'warm' pressing step was performed at 350 °C for 24 hours. The total plastic compaction increased from 0.16 to 0.23 mm in this last process step. A simple temperature cycling (375+/-25 C) before and after showed enhanced bed/assembly conductivity. No Be-contamination of purge lines was observed on completion of the assembly.

5.PROJECT STATUS

The project status by September 2001 was as follows:

- The 4 test-elements are about to be filled and assembled. Assembly of the whole in-pile part is to start right after.
- The Tritium Measuring Station in the HFR has been revised and adapted to provide on-line gas mixture control. The Design & Safety Report, necessary for reactor approval, is being compiled.
- Start of in-pile operation is foreseen in Spring 2002; neutron radiographs should be taken before start-up. First in-pile operation requires careful reactor start-up to allow creep compaction before reaching the maximum temperatures. Neutron radiography should be repeated after the 1st cycle.

REFERENCES

- [1] J. Reimann and S. Müller, "First experiments on the thermomechanical behaviour of Li₄SiO₄ pebble beds", Proceedings 20th SOFT, Marseille, September 1998, 1337-1340.
- [2] J.G. van der Laan R. Conrad, K. Bakker, J.H. Fokkens, S. Hermsmeyer, S. Malang, B.J. Pijlgroms, K. Schleisiek, C. Sciolla and R. van Tongeren, "In-pile testing of submodules for the HCPB DEMO blanket concept at the HFR Petten", Proc. 20th SOFT, Marseille, Sept. 1998
- [3] J.G. van der Laan R. Conrad, K. Bakker, J.H. Fokkens, S. Hermsmeyer, S. Malang, B.J. Pijlgroms, K. Schleisiek, C. Sciolla and R. van Tongeren, "In-pile testing of HCPB submodules at the HFR Petten", in: Proc. CBBI-7, NRG report 21099/99.23482/P, March 1999, 4-61.
- [4] J.G. van der Laan, R. Conrad, K. Bakker, L.V. Boccaccini, J.G. Boshoven, L. Bühler, J.H. Fokkens, M.A.C. van Kranenburg, B.J. Pijlgroms, J. Reimann: "Design analyses and pretests for the irradiation of HCPB pebble-bed assemblies", Fusion Engineering & Design 51-52 (2000) 909-918.
- [5] J.G. van der Laan, R. Conrad, K. Bakker, L.V. Boccaccini, J.G. Boshoven, L. Bühler, J.H. Fokkens, S. Hermsmeyer, M.A.C. van Kranenburg, B.J. Pijlgroms, J. Reimann, K. Schleisiek, R. van Tongeren, F. Wolf: "Thermomechanical behaviour of HCPB pebble-bed assemblies in 'SCATOLA' experiments and design analyses for irradiation in HFR", in: A. Ying (Ed.), CBBI-8 workshop proceedings, February 2000.
- [6] J.G. van der Laan et al.: *In-pile testing of submodules for the HCPB DEMO blanket concept in the HFR Petten*, paper presented at 21st SOFT, Madrid, September 2000.
- [7] J.G. van der Laan, J. Baard, K. Bakker, J.G. Boshoven, R. Conrad, J.H. Fokkens, M. Jong, S. Malang, B.J. Pijlgroms, J. Reimann, K. Schleisiek, M.P. Stijkel, F. Wolf: "The in-pile testing of HCPB pebble-bed assemblies in the HFR Petten", paper presented at CBBI-9, Toki, Oct. 2000.
- [8] A.J. Magielsen, R. Conrad, J.H. Fokkens, B.J. Pijlgroms and J.G. van der Laan, "Thermal behaviour and tritium management for in-pile testing of the pebble bed assemblies in the HFR in Petten", these workshop proceedings.
- [9] J.H. Fokkens, "Thermo-Mechanical Behaviour of Pebble-Beds by Finite Element Modelling", these workshop proceedings.
- [10] J. Reimann et al., "Thermal creep of metatitanate pebble beds", these workshop proceedings.
- [11] H.E. Hofmans, "Tensile and impact properties of Eurofer97 plate and bar", NRG Report 20023/00.38153/P

**TAZZA MOCK-UP PEBBLE BEDS.
EXPERIMENTAL AND THEORETICAL INVESTIGATIONS.**

G. Dell'Orco^a, P. A. Di Maio^b, M. Simoncini^a, G. Vella^b, D. Zito^b

^a *ENEA C.R. Brasimone P.O. 1, Brasimone 40032 Camugnano (Bo), Italy*

^b *Dipartimento di Ingegneria Nucleare, Università degli Studi di Palermo, Viale delle Scienze, 90128 Palermo, Italy*

ABSTRACT

Within the framework of the European Fusion Technology Programme 1999 - 2002, it is foreseen the use of Beryllium and Lithium ceramics in form of packed pebble beds as, respectively, neutron multiplier and Tritium breeder for the Helium Cooled Pebble Bed (HCPB) breeding blanket of a fusion power reactor operating with a D-T plasma.

The packed pebble beds are granular systems composed of quasi-spherical particles having quite complex and strictly interconnected thermal and mechanical behaviours, whose knowledge represents a pivotal issue in the design and analysis of the HCPB breeding blanket modules.

In order to investigate these behaviours, research activities have been scheduled within the above mentioned programme and, among them, experimental tests have been carried out at ENEA Brasimone labs concerning the measurement of pebble bed thermal and mechanical properties. In particular, the TAZZA test section has been set-up to investigate the Lithium ceramics and Beryllium pebble bed relevant filling procedure and their mechanical properties dependence on the bed height at room temperature.

The paper focuses on the investigation of the potential use of a simple and already tested constitutive model of the soil mechanics in the modelling of the single size Lithium Metatitanate pebble bed mechanical behaviour, observed by the TAZZA tests. The results of this investigation together with the study of the contact friction effect are herewith presented and critically discussed.

1. INTRODUCTION

Within the framework of the European Fusion Technology Programme 1999 – 2002, it is foreseen the use of Beryllium and Lithium ceramics in form of packed pebble beds as, respectively, neutron multiplier and Tritium breeder for the Helium Cooled Pebble Bed (HCPB) breeding blanket of a fusion power reactor operating with a D-T plasma.

The packed pebble beds are granular systems composed of quasi-spherical particles having quite complex and strictly interconnected thermal and mechanical behaviours, whose knowledge represents a pivotal issue in the design and analysis of the HCPB breeding blanket modules.

Therefore, intense research activities, aiming to the characterization of the pebble bed thermomechanical behaviour, have been launched in view of the qualification of the reference design of the Helium Cooled Pebble Bed (HCPB) Blanket and of its Test Blanket Module (TBM) to be tested in ITER reactor.

Within this framework, ENEA launched the design and construction of a small scale mock-up, called TAZZA, specifically intended to characterize the thermomechanical behaviour of Beryllium, Lithium Orthosilicate and Lithium Metatitanate pebble beds [1].

On the basis of the experimental results of the TAZZA Uniaxial Compressive Tests (UCTs) performed on Lithium Metatitanate pebble beds, at the Department of Nuclear Engineering of the University of Palermo, it has been investigated the potential use of a simple and already tested constitutive model of the soil mechanics in the modelling of their mechanical behaviour.

2. NOTES ON TAZZA TEST SECTION

TAZZA is a small test section (Fig. 1, 2) intended to perform UCTs and, specifically, designed to investigate Beryllium and Lithium ceramics pebble beds mechanical behaviour in a cylindrical geometry, that is simpler and more useful than the typical reactor rectangular one, to determine the pebble bed mechanical properties.

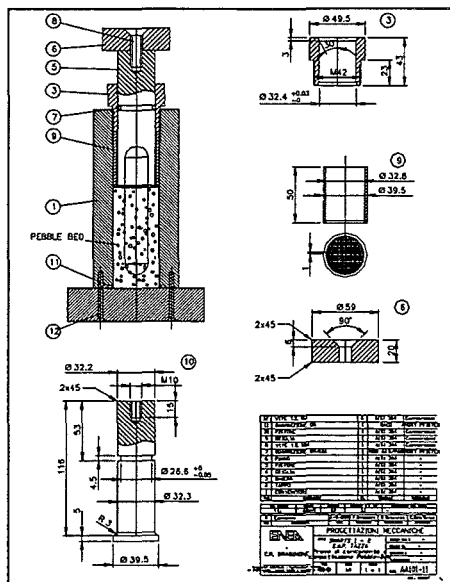


Figure 1. TAZZA test section.

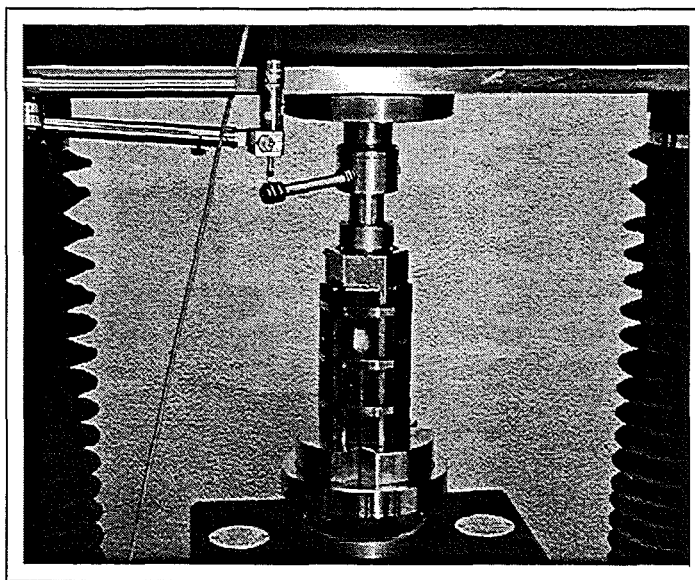


Figure 2. TAZZA test section and compressive device.

The TAZZA test section is, mainly, composed of an internal cylindrical chamber with a diameter and an height of, respectively, 40 and 160 mm, which is devoted to house pebble bed with different axial height going from 20 up to 100 mm.

The test section is filled with pebbles and, then, independently by the bed height, it undergoes for few minutes ultrasonic vibration with optimised frequencies that allow to stabilize the bed without interfering with the test section containment.

This vibration is performed in order to make bed initial states as similar as possible. In fact, the bed behaviour strongly depends on the pebble positions and on the packing factor, mainly for the first ramp-up, where the void recovering is evident. The anelastic part of this recovery, mainly depends on the initial position of the pebbles and in order to compare different experiments, it is necessary to make these initial configurations as similar as possible. Each kind of pebble bed is used for many tests in order to obtain results with a limited experimental spread.

The experiments carried out in this test section are typical UCTs composed of several loading and relaxation cycles. Each bed is loaded and unloaded for seven cycles, in order to reach the fully elastic behaviour of the pebble bed (Fig. 3).

The load is applied over a piston which can slide along the internal surface of the mock-up and for each test, the axial load together with the corresponding bed deformation are measured throughout an instrumentation consisting of a load cell at the bottom of the mock-up and an LVDT, which records the vertical displacement of the piston.

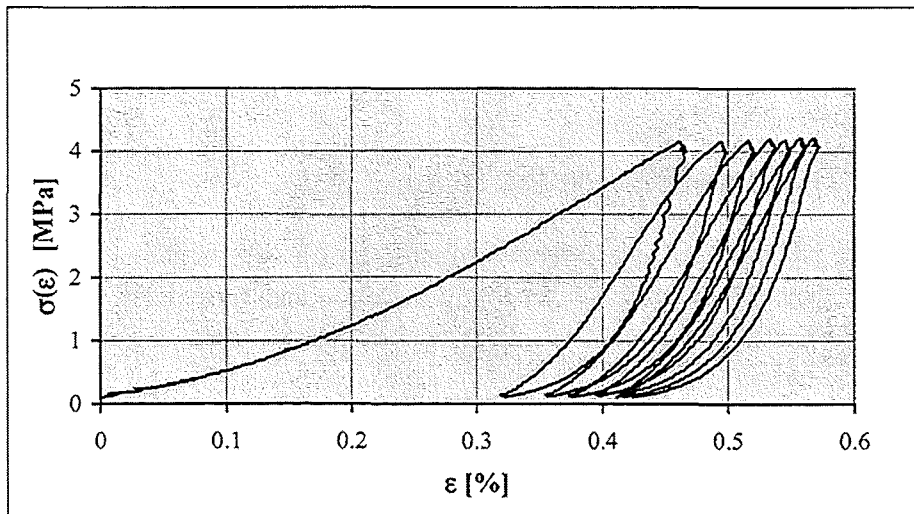


Figure 3. Typical stress – strain curves for a Lithium Metatitanate pebble bed tested in TAZZA.

The characteristic stress – strain curve of the bed (Fig. 3) and its derivative, representing the bed effective deformation modulus, are derived and, subsequently, used to theoretically model the bed behaviour.

A set of UCTs tests was launched, particularly, on Beryllium and Lithium Metatitanate (Li_2TiO_3) single size pebble bed and on Lithium Orthosilicate (Li_4SiO_4) polydisperse pebble bed. All the tests have been carried out at room temperature. Different bed height have been taken into account in order to study the effect on the pebble bed mechanical behaviour of the contact friction arising between the bed itself and the containment wall.

In Table 1 all the pebble beds tested in the TAZZA test section are reported together with their main physical characteristics and test conditions [1].

Table 1. TAZZA pebble bed main parameters.

Pebble bed	ρ_{th} [g/cm ³]	γ_p [%]	P max [MPa]	Size [mm]	Bed height [mm]	PF [%]
Li_4SiO_4	2.32-2.39	97-98	~4	0.25-0.63	~20/~50/~100	66-67
Ti_2LiO_3	3.45	88	~4	0.8-1.2	~20/~50/~100	60-62
Be	1.855	0.98	~4/~8	2.0	~20/~50/~100	64-65
Be (Bin)	1.855	0.98	~4/~8	1.6-2.4/0.1-0.2	~20/~50/~100	64+20
Glass	2.49	1	~4	2	~20/~50/~100	66-67
Glass (Bin)	2.49	1	~4	2/0.1-0.2	~20/~50/~100	67+18

The present paper is focused on the results related to the single size Lithium Metatitanate pebble bed.

3. PEBBLE BED THERMOMECHANICAL MODELLING

Pebble beds are particular granular systems composed of a very large amount of small quasi-spherical particles generally arranged in an irregular lattice and surrounded by a gas filling the interstitial space. The particles interact throughout small contact surfaces whose areas depend on the pebbles packing and on their stress and deformation state.

In general, pebble beds have thermal and mechanical behaviours that are quite different from those of a solid sample of the same size and material. They are non-linear, interconnected and strictly dependent on the bed structure and their knowledge represents a pivotal issue in the design and analysis of the HCPB breeding blanket modules [2].

From the mechanical point of view, they show a non-linear, highly load-dependent behaviour, composed of a non-linear elastic component and an irreversible one. The former, typical of all the granular systems, is characterized by a modulus of deformation depending on the system pressure and it is due to the variation of the bed stiffness with the number and the characteristics of the pebble contacts. The latter is mainly due the consolidation phenomenon which arises typically

during the compressive loading when pebbles, owing to irreversible displacements, rearrange themselves into a denser configuration, preventing the bed to recover, during the relaxation, the initial deformation and producing an increasing of its stiffness [3].

It has been, then, investigated the potential use of a semi-empirical approach adopted to describe the porous media behaviour, which results in the Porous Elasticity and in the Modified Drucker Prager/Cap constitutive models, already implemented in the ABAQUS finite element code [4].

The Porous Elasticity is a nonlinear elastic constitutive model apt to simulate the typical granular systems elastic behaviour. It is based on the experimental observation that in porous materials, during recoverable straining, the change in the void ratio, e , and the change in the logarithm of the equivalent system pressure, p , are linearly related. In the hypothesis of vanishing pebble material compressibility, it is possible to foresee a functional dependence of the pressure on the elastic volumetric strain ε_{vol}^{el} given by:

$$p(\varepsilon_{vol}^{el}) = -p_t^{el} + (p_0 + p_t^{el}) \exp\left[\frac{1+e_0}{k} (1 - \exp(\varepsilon_{vol}^{el}))\right] \quad (1)$$

where k is the logarithmic bulk modulus, p_t^{el} the tensile strength and e_0 the initial void ratio [5].

The Modified Drucker-Prager/Cap is a plasticity model able to provide a yielding surface and a flow potential rule suitable to well simulate the bed consolidation phenomenon where as plastic strain it is intended the pebble bed irreversible deformation during a loading cycle. It is based on the assumption that the elastic domain is delimited in the deviatoric and pressure stress plane by a pressure depending curve composed of a linear part, called Drucker-Prager shear failure surface, and a Cap elliptic curve (Fig. 4). The first curve delimits yielding by shear stress while the second bounds the yield surface in hydrostatic compression [3].

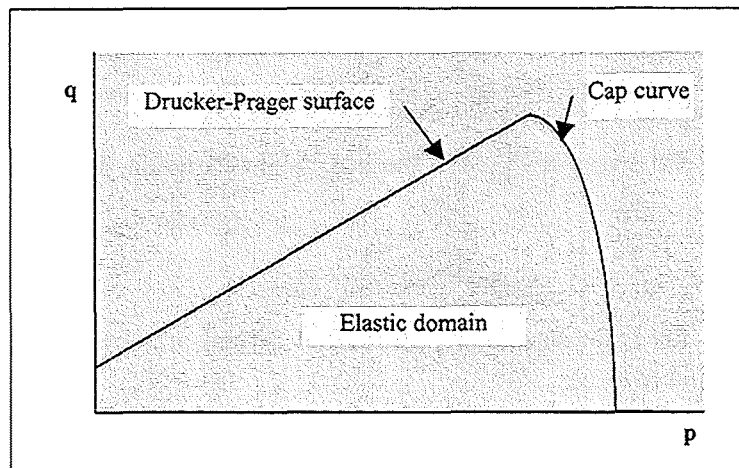


Figure 4. Drucker – Prager/Cap yielding surface in the $p - q$ plane.

3.1. The model parameters evaluation

The Porous Elasticity and the Modified Drucker – Prager/Cap models need, as input, data which can be considered as effective pebble bed mechanical properties and which can be derived by the typical tests of the soil mechanics, first of all the UCTs.

The main parameters are the logarithmic bulk modulus and the pressure tensile strength for the Porous Elasticity model and the Cap hardening law for the Modified Drucker – Prager/Cap one.

With regard to the Porous Elasticity parameters, they have been determined by supposing that the relaxation curve of the UCT first cycle is representative of the typical pebble bed non linear elastic behaviour, as the differences it shows with the corresponding curve of the seventh cycle are negligible.

In particular, a null pressure at null elastic volumetric deformation has been assumed for the bed, which means:

$$p_0 = 0 \quad (2)$$

and the values of the logarithmic bulk modulus and of the pressure tensile strength have been determined as the ones allowing the Porous Elasticity pressure function (1) to best fit the corresponding dependence of pressure on elastic volumetric deformation experimentally derived [5].

In order to find out the analytical form of this dependence, the elastic problem of a pebble bed experiencing an UCT at room temperature has been taken into account. By supposing an infinite stiffness for the test section containment wall, it has been showed [5] that the bed is characterized by an uniaxial strain state and a cylindrical stress one with the following elastic volumetric strain and cylindricity factor α :

$$\varepsilon_{vol}^{el} \equiv \varepsilon_{axial} = \frac{\Delta l}{H_{Bed}} \quad (3)$$

$$\alpha = \frac{\sigma_{transv}}{\sigma_{axial}} \quad (4)$$

both depending on the bed stress state. Δl is the bed height variation, H_{Bed} its overall height, and σ_{transv} is given by:

$$\sigma_{radial} = \sigma_{azimuthal} = \sigma_{transv} \quad (5)$$

In these hypotheses, the experimental dependence of system pressure on the elastic volumetric deformation, can be found to be [5]:

$$p_{exp}(\varepsilon_{axial}) = -\frac{1+2\alpha}{3} \sigma_{axial}(\varepsilon_{axial}) \quad (6)$$

where $\sigma_{axial}(\varepsilon_{axial})$ is the stress – strain characteristic of the UCT first relaxation phase.

By imposing the Porous Elasticity pressure curve (1) to best fit this dependence (6), the values of the logarithmic bulk modulus, k , and of the pressure tensile strength, p_t^{el} , can be derived by solving a non linear system as shown in [5]. They are found to depend, obviously, on the cylindricity factor and, through it, on the bed stress and deformation state.

With regard to the Modified Drucker Prager/Cap model and especially to the Cap hardening curve, the parameters have been determined on the basis of both the loading and relaxation curves of the UCT first cycle, by supposing that the former is representative of the typical pebble bed irreversible deformation due to the consolidation phenomenon.

In particular, the Cap hardening law gives the functional dependence of the plastic volumetric deformation on the system pressure $\varepsilon_{vol}^{pl} = \varepsilon_{vol}^{pl}(p)$, and it has been determined evaluating the residual deformation, ε_{vol}^{pl} , showed by the pebble bed at the end of a loading and relaxation cycle reaching an equivalent system pressure p . By assuming that both the first loading and first relaxation curves of the pebble bed UCT can be represented throughout a Porous Elasticity pressure curve, it is possible to obtain the following analytical expression for the Cap hardening law [5]:

$$\varepsilon_{vol}^{pl}(p) = -\ln \left\{ \frac{\left[1 - \frac{k_{load}}{1 + e_0} \ln \left(1 + \frac{p}{p_{tload}} \right) \right]}{\left[1 - \frac{k_{relax}}{1 + e_0} \ln \left(1 + \frac{p}{p_{trelax}} \right) \right]} \right\} \quad (7)$$

4. LITHIUM METATITANATE PEBBLE BED THERMOMECHANICAL MODELLING

The aforementioned procedure for the determination of the Porous Elasticity and Modified Drucker Prager/Cap model parameters has been applied to a 100 mm height Lithium Metatitanate pebble bed tested in TAZZA.

4.1. The Porous Elasticity parameters evaluation

With regard to the evaluation of the Porous Elasticity parameters, it has been assumed a constant cylindricity factor, typical of a linear elastic system, given by:

$$\alpha = \frac{\nu}{1 - \nu} \quad (8)$$

There have been, consequently, determined the following values of the logarithmic bulk modulus and of the pressure tensile strength:

$$\begin{aligned} k &= 7.08518 \cdot 10^{-4} \\ p_t &= 0.10061 \text{ [MPa]} \end{aligned} \quad (9)$$

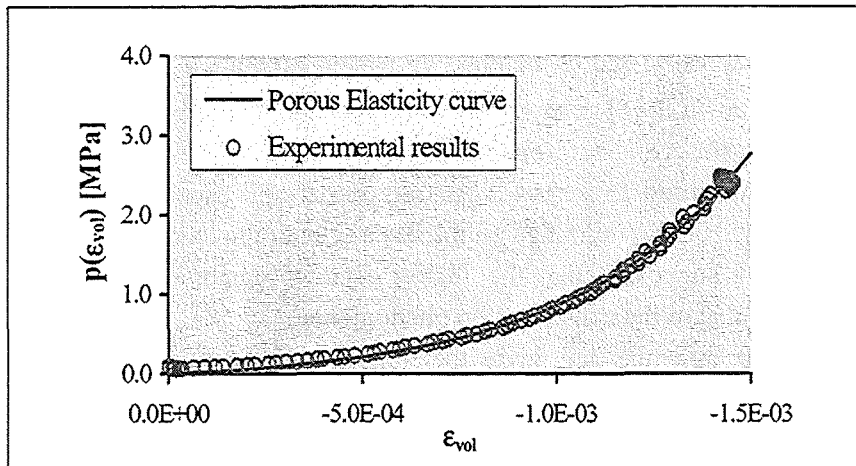


Figure 5. Comparison between the Porous Elasticity pressure curve and the experimental one.

Figure 5 shows the comparison between the Porous Elasticity pressure curve with the parameters given in (9) and the one derived directly from the experimental results.

4.2. The Modified Drucker Prager/Cap parameters evaluation

With regard to the evaluation of the Modified Drucker Prager/Cap parameters and, in particular, of the Cap hardening law (Fig. 6), the parameters reported in Table 2 have been determined:

Table 2. Cap hardening law parameters.

Phase	k	p_t [MPa]
Loading	$6.18834 \cdot 10^{-3}$	1.09877
Relaxation	$7.08518 \cdot 10^{-4}$	0.10061

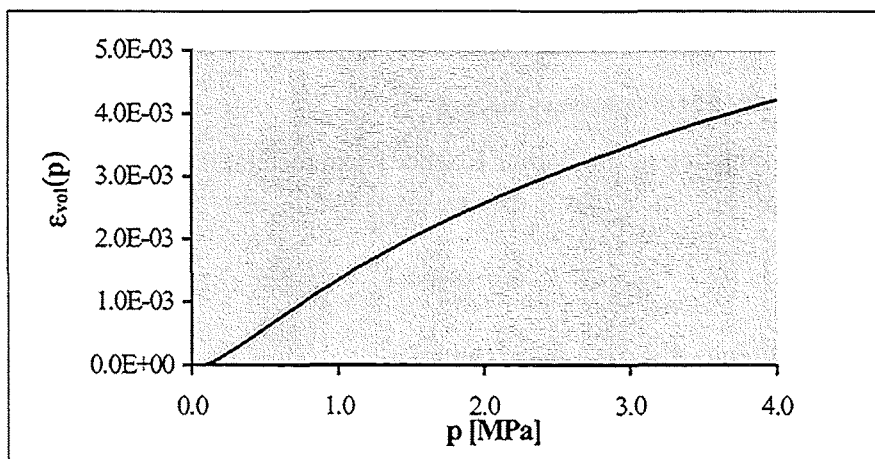


Figure 6. Cap hardening curve for the examined Lithium Metatitanate pebble bed.

5. LITHIUM METATITANATE PEBBLE BED MODEL ASSESSMENT

In order to assess the aforementioned constitutive model, a TAZZA Li_2TiO_3 pebble bed UCT first loading and subsequent relaxation has been simulated by the mean of the ABAQUS code.

The 100 mm height Li_2TiO_3 pebble bed has been taken into account and the relevant finite element model has been set up (Fig. 7), including a contact model between the bed lateral wall and the steel containing one. This allows a preliminary investigation of the effect of contact friction on the pebble bed mechanical behaviour. An ideal friction model has been assumed with a constant effective friction factor μ .

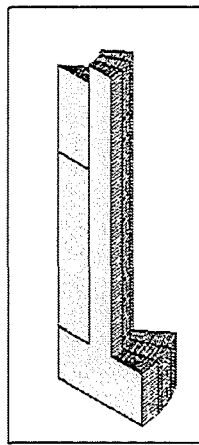


Figure 7. The adopted finite element model.

On first, a sensibility analysis has been carried out to investigate the incidence of the effective friction factor. It has been found out that the derived cap hardening law well simulates the TAZZA Li_2TiO_3 pebble bed UCT if $\mu < 0.05$, as it is shown in figure 8.

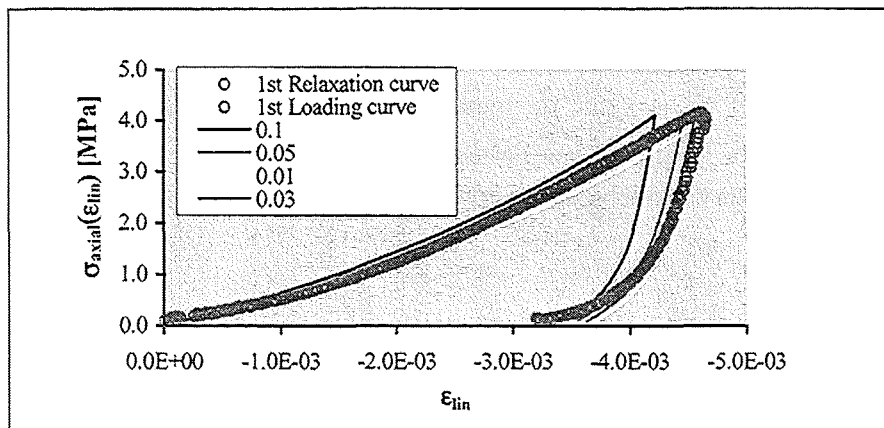


Figure 8. Comparison between experimental and numerical UCT stress-strain curves at different μ .

Moreover, it has been observed that, the contact friction between the bed and the containment wall, let bed stress state to differ from the ideal cylindrical one. In fact the axial stress depends on the axial variable in such a way that the higher is the latter the higher is the compressive axial stress (Fig. 9). As a consequence of this, the various layers of the bed located at different levels do not cooperate in the same way to counterbalance the applied load.

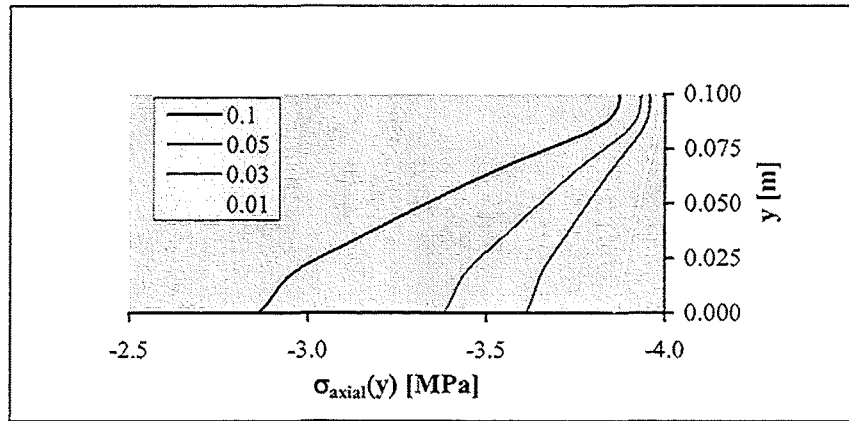


Figure 9. Axial stress profiles along the bed height at different μ .

The presence of the contact friction whose effective coefficient is higher than 0.05, let to take into account the following modified form of the Cap hardening law:

$$\varepsilon_{vol}^{pl}(p) = -C(p, \mu) \ln \left\{ \frac{\left[1 - \frac{k_{load}}{1 + e_0} \ln \left(1 + \frac{p}{p_{tload}} \right) \right]}{\left[1 - \frac{k_{relax}}{1 + e_0} \ln \left(1 + \frac{p}{p_{trelax}} \right) \right]} \right\} \quad (10)$$

which differs from (7) only as far as the amplitude function $C(p, \mu)$ is concerned.

As first attempt it has been supposed that this amplitude function does not depend on the system pressure, resulting to be $C = C(\mu)$ and thermomechanical analyses relevant to different values of the effective friction factor have been performed in order to find out an estimate of its analytical expression. There have been considered the following cases:

- I $\mu = 0.1$
- II $\mu = 0.2$
- III $\mu = 0.3$
- IV $\mu = 0.5$

The principal results obtained are reported in figures 10,11 and 12.

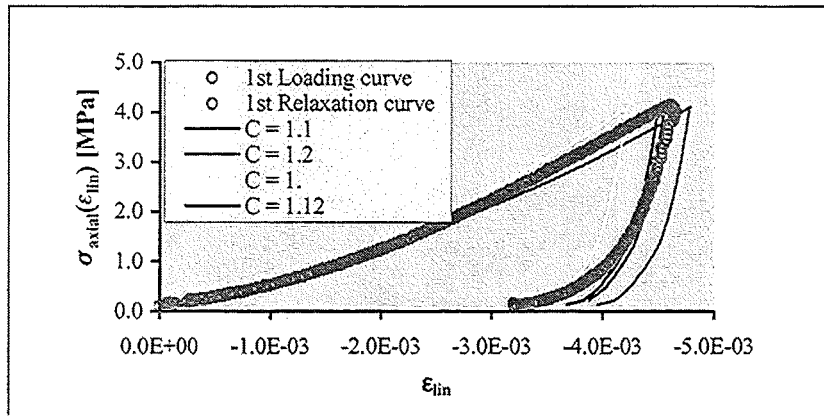


Figure 10. Comparison between experimental and numerical UCT stress-strain curves for $\mu=0.1$.

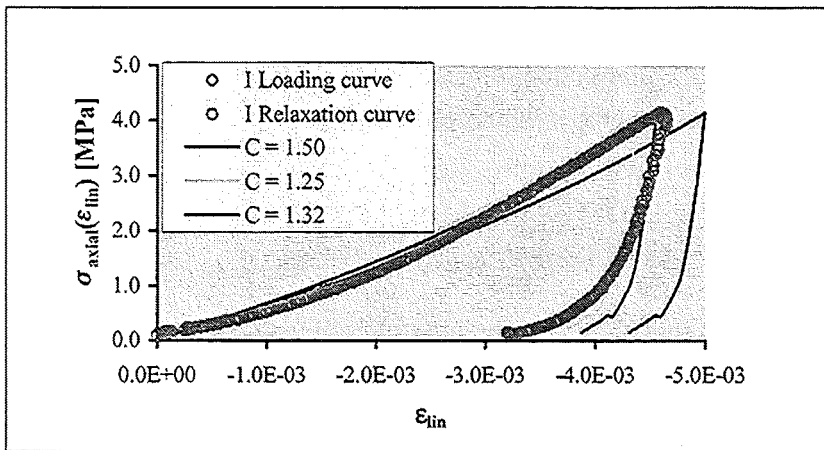


Figure 11. Comparison between experimental and numerical UCT stress-strain curves for $\mu=0.2$.

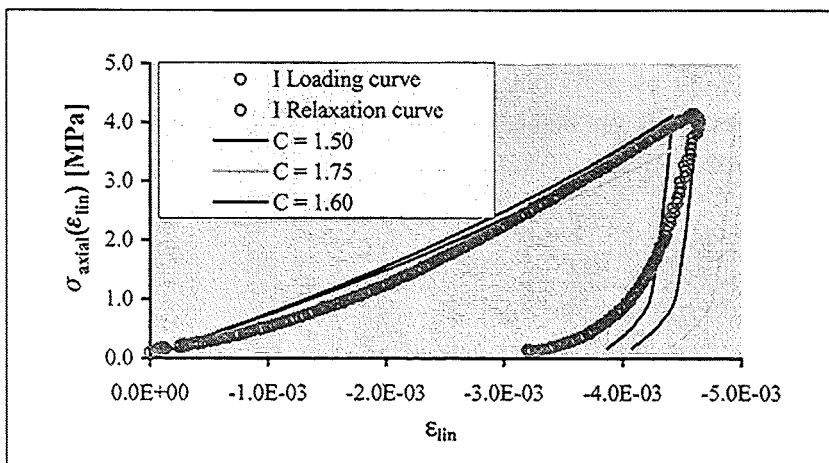


Figure 12. Comparison between experimental and numerical UCT stress-strain curves for $\mu=0.3$.

On the basis of the obtained results the following best estimate values of C have been determined:

I	$\mu = 0.1$	$C = 1.12$
II	$\mu = 0.2$	$C = 1.32$
III	$\mu = 0.3$	$C = 1.55$
IV	$\mu = 0.5$	$C = 2.25$

which suggest the following analytical expression for the $C(\mu)$ function:

$$C(\mu) = 0.925 \exp(1.7697\mu) \quad (11)$$

Obviously, repeating the same procedure for a Lithium Metatitanate pebble bed UCT having the same packing factor and a different height, another expression of the $C = C(\mu)$ function can be obtained.

Therefore, determining the intersection of these two different functions in the $C - \mu$ plane it should be, finally, possible to obtain the proper values of the effective friction factor and of the amplitude C of the Cap hardening law.

6. CONCLUSIONS AND HINTS FOR FURTHER DEVELOPMENT

The potential use of a simple and already tested constitutive model of the soil mechanics in the theoretical modelling of the Lithium Metatitanate single size pebble bed mechanical behaviour has been investigated.

The model parameters have been derived in a semi-theoretical way and they have been, subsequently, assessed on the basis of a TAZZA UCT carried out at ENEA, Brasimone on a 100 mm height Li_2TiO_3 pebble bed, taking into account the effect of the contact interaction between the bed and the containment wall.

The model seems to work properly but it depends strongly from the assumed effective friction factor and UCTs relevant to different bed heights (20, 50 mm) are needed to properly assess it.

The effect of the effective friction factor has to be furtherly investigated by simulating bi and tri-axial tests.

7. REFERENCES

- [1] G. Dell'Orco, M. Simoncini, D. Zito, G. Vella, *Optimization of filling for the improvement of the performance of beryllium pebble beds*, 14th Topical Meeting on the Technology of Fusion Energy, October 15 – 19, 2000, Park City, Utah (USA).

- [2] G. Vella, E. Oliveri, P. Di Maio, *A Thermo-Mechanical Constitutive Model Of The Lithium Orthosilicate And Beryllium Pebble Beds. An Application On The Thermo-Mechanical Study Of The Smarts Mock-Up Of The ITER Fusion Reactor Breeding Blanket*, Atti del XVIII Congresso Nazionale sulla Trasmissione del Calore, Cernobbio (CO), 28 – 30 Giugno 2000, ed. A. Niro, G. Dubini, F. Inzoli, pp. 789-800.
- [3] G. Vella, P. Di Maio, *On the use of the Porous Elasticity and the Drucker-Prager models in the numerical simulation of the pebble beds thermo-mechanical behavior*, Proceedings of the 13th Annual Worldwide ABAQUS Users' Conference, May 31st – June 2nd 2000, pp. 723-737, Newport (RI), USA.
- [4] Hibbit, Karlsson & Sorensen INC., *ABAQUS Theory Manual Version 5.8*, 4.4.1, 4.4.4, (1998).
- [5] P. A. Di Maio, *Modelli Costitutivi termomeccanico per letti di sfere in mantelli Triziogeni*, Ph. D Thesis, 2001.

Comparison of inventory of tritium in various ceramic breeder blankets

**M. Nishikawa, S. Beloglazov, N. Nakashima and K. Hashimoto,
and M. Enoeda***

*Department of New Energy, Graduate School of Engineering Science, Kyushu University
Hakozaki 6-10-1, Higashi-ku, Fukuoka 812-8581, Japan*

**Naka Establishment, JAERI, Naka, Ibaraki 319-1195, Japan*

Abstract

It has been pointed out by the present authors that it is essential to understand such mass transfer steps as diffusion of tritium in the grain of breeder material, absorption of water vapor into bulk of the grain, and adsorption of water on surface of the grain, together with the isotope exchange reaction between hydrogen in purge gas and tritium on surface of breeder material and the isotope exchange reaction between water vapor in purge gas and tritium on surface, for estimation of the tritium inventory in a uniform ceramic breeder blanket under the steady-state condition. It has been also pointed out by the present authors that the water formation reaction on the surface of ceramic breeder materials at introduction of hydrogen can give effect on behavior of bred tritium and lithium transfer in blanket.

The tritium inventory for various ceramic breeder blankets are compared in this study basing on adsorption capacity, absorption capacity, isotope exchange capacity, and isotope exchange reactions on the Li_2O , LiAlO_2 , Li_2ZrO_3 , Li_4SiO_4 and Li_2TiO_3 surface experimentally obtained by the present authors. Effect of each mass transfer steps on the shape of release curve of bred tritium at change of the operational conditions is also discussed from the observation at out pile experiment in KUR.

In order to understand the tritium behavior in a blanket system packed with sintered pebbles of micro crystal grains of ceramic breeder material, it is necessary to know the contribution of such tritium transfer steps as

- (1) tritium formation reaction in crystal grain,
- (2) diffusion of tritium in crystal grain to the grain surface,
- (3) interaction of migrating tritium with irradiation defects formed in crystal grain,
- (4) adsorption of tritium on grain surface,
- (5) absorption of tritium into bulk of crystal grain,
- (6) isotope exchange reaction between molecular form hydrogen, H_2 , in the gas stream and tritium on grain surface (isotope exchange reaction 1),
- (7) isotope exchange reaction between water vapor, H_2O , in the gas stream and tritium on grain surface (isotope exchange reaction 2),
- (8) water formation reaction on grain surface at addition of H_2 to the blanket purge gas,
- (9) transfer of hydrogen isotopes and water through pores of the sintered pebble,
- (10) transfer of hydrogen isotopes and water through boundary layer formed on the surface of a sintered pebbles to the gas stream.

Steps (1), (2) and (3) decide the diffusion inventory of tritium which corresponds to the amount of tritium in the bulk of crystal grains when no absorption occurs. Step (5) decides the absorption inventory due to absorption of water vapor or molecular form hydrogen into the bulk of grain. The present authors have observed that water vapor is absorbed into Li_2O at the higher blanket temperature and that Li_2O , $LiAlO_2$, Li_2ZrO_3 and Li_4SiO_4 have no detectable absorption capacity of water or molecular form hydrogen. Steps (4), (6), (7) and (8) decide the surface inventory of tritium which corresponds to the amount of tritium on the surface of crystal grains. Step (9) decides the tritium inventory in micro pores of sintered pebbles. Step (10) decides the tritium inventory under diffusion through the boundary layer formed around the sintered pebbles.

It has been found that the water formation reaction occurs when the purge gas with hydrogen is introduced into a bed of ceramic breeder materials have been quantified by the present authors .

Contributions of the diffusion inventory in crystal grains I_D , the absorption inventory in bulk of grains I_{ab} , the adsorption inventory on grain surface I_{ad} , and the inventory due to isotope exchange capacity on grain surface I_{ex} to the total tritium inventory in a solid breeder blanket I_{Total} are given as follows under the steady state and uniform conditions.

$$\begin{aligned}
I_{Total} &= I_D + I_{ab} + I_{ad} + I_{ex} \\
&= G_T d_p^2 / 60 D_T + Q_{ab} M P_{T_2O} / (P_{T_2O} + P_{H_2O} + P_{H_2O'}) \\
&\quad + Q_{ad} M P_{T_2O} / \left\{ (P_{H_2} / \alpha_{ex}) + (P_{T_2O} + P_{H_2O} + P_{H_2O'}) / \alpha'_{ex} \right\} \\
&\quad + Q_{ex} M P_{T_2O} / \left\{ (P_{H_2} / \alpha_{ex}) + (P_{T_2O} + P_{H_2O} + P_{H_2O'}) / \alpha'_{ex} \right\}, \quad (1)
\end{aligned}$$

where G_T : tritium generation rate in the whole blanket [mol T₂/s]
 d_p : grain diameter [m]
 D_T : apparent diffusivity of tritium in grain [m²/s]
 P_{H_2} : partial pressure of H₂ in the purge gas [Pa]
 P_{H_2O} : partial pressure of H₂O intentionally swamped to the purge gas [Pa]
 $P_{H_2O'}$: partial pressure of residual H₂O in the purge gas [Pa]
 M : amount of Li ceramics in the whole blanket [mol]
 $\alpha_{ex}, \alpha'_{ex}$: effectiveness correction factor of isotope exchange reactions [-]
 Q_{ab} : water absorption capacity in bulk [mol H₂O/mol Li compound]
 Q_{ad} : water adsorption capacity on surface [mol H₂O/mol Li compound]
 Q_{ex} : isotope exchange capacity on surface [mol H₂O/mol Li compound].

The partial pressure of tritium vapor in the purge gas, P_{T_2O} , is given as

$$P_{T_2O} = P_{He} G_T / G_{He} \quad \text{[Pa]}, \quad (2)$$

where all tritium bred in the grain of a solid breeder material is considered to be released in the chemical form of water, and P_{He} [Pa] and G_{He} [mol/s] are total pressure of helium purge gas and flow rate, respectively.

The mass transfer resistance at transfer of tritium through pores of sintered pebbles and

that at transfer through boundary layer formed around the pebble surface are considered to be negligibly small.

The average residence time of tritium at each transfer step is given by division of the each inventory by the tritium generation rate.

$$\begin{aligned} \theta_{Total} &= (I_D + I_{ad} + I_{ab} + I_{ex}) / G_T \\ &= \theta_D + \theta_{ad} + \theta_{ab} + \theta_{ex} \text{ [s].} \end{aligned} \quad (3)$$

The tritium inventory estimated for a LiAlO_2 blanket using the way proposed by the present authors considering diffusion, adsorption and isotope exchange reactions agrees well with data observed in LILA-3, TEQUILA-1, CORELLI-2, MOZART, and EXOTIC-6 experiments. The tritium inventory estimated for a Li_2ZrO_3 blanket using the same method agrees well with data reported in EXOTIC-5, EXOTIC-6, MOZART and TRINE experiments. The fair agreement is also obtained for a Li_2TiO_3 blanket reported in the EXOTIC-8 experiment.

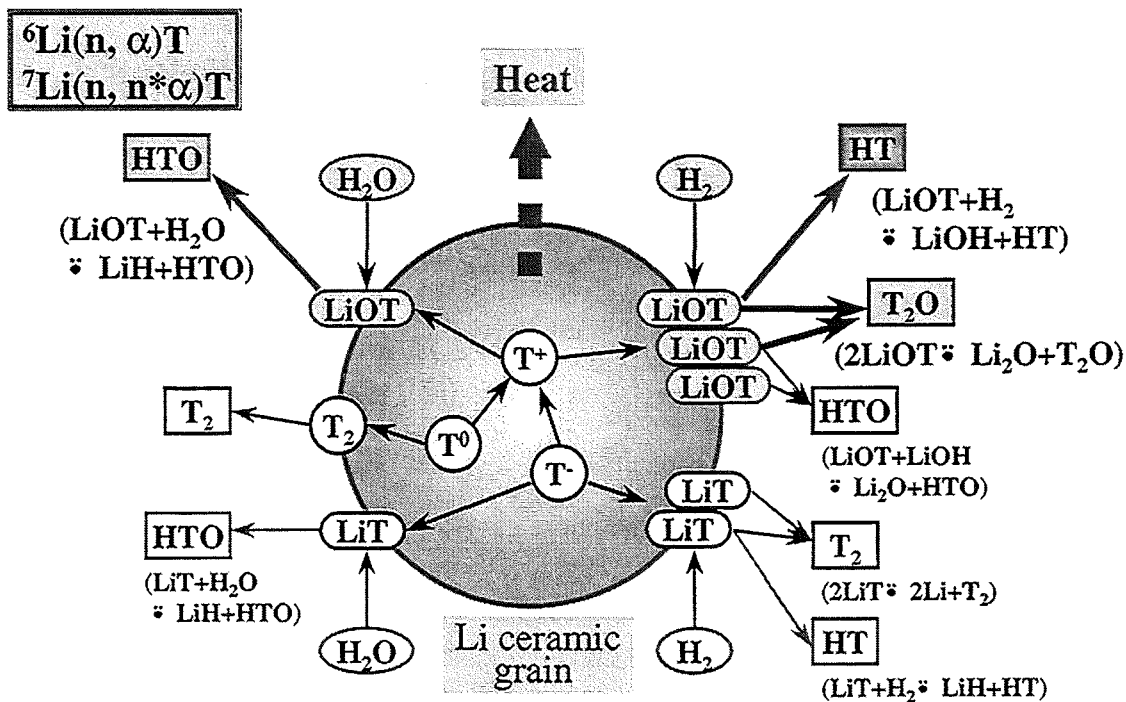


Fig. • Tritium behavior around grain of solid breeder material.

It can be seen from above discussion, the effects of tritium generation rate, temperature, grain size, partial pressure of H₂, partial pressure of water vapor or flow rate of purge gas on each tritium inventory are different. This means that the diffusion inventory controlling range, the surface inventory due to adsorption controlling range, the surface inventory due to isotope exchange capacity controlling range and the absorption inventory controlling range change with temperature, grain size or chemical compositions in the purge gas.

Figure 2 shows the comparison of the estimated tritium inventory in the solid breeder blankets of a 1GWe fusion reactor. It is known from this figure that tritium inventory in the solid breeder blanket for each blanket material does not become so large when temperature and grain size are properly selected. However, the permeation loss from the blanket system to the cooling system must not be ignored from the view point of radiation safety.

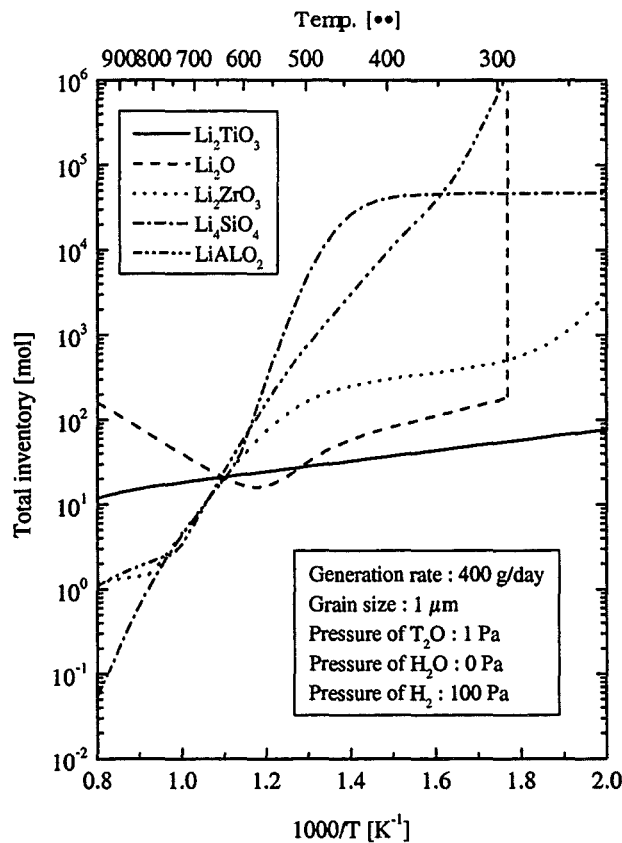


Fig. • Comparison of tritium inventory in solid breeder blanket.

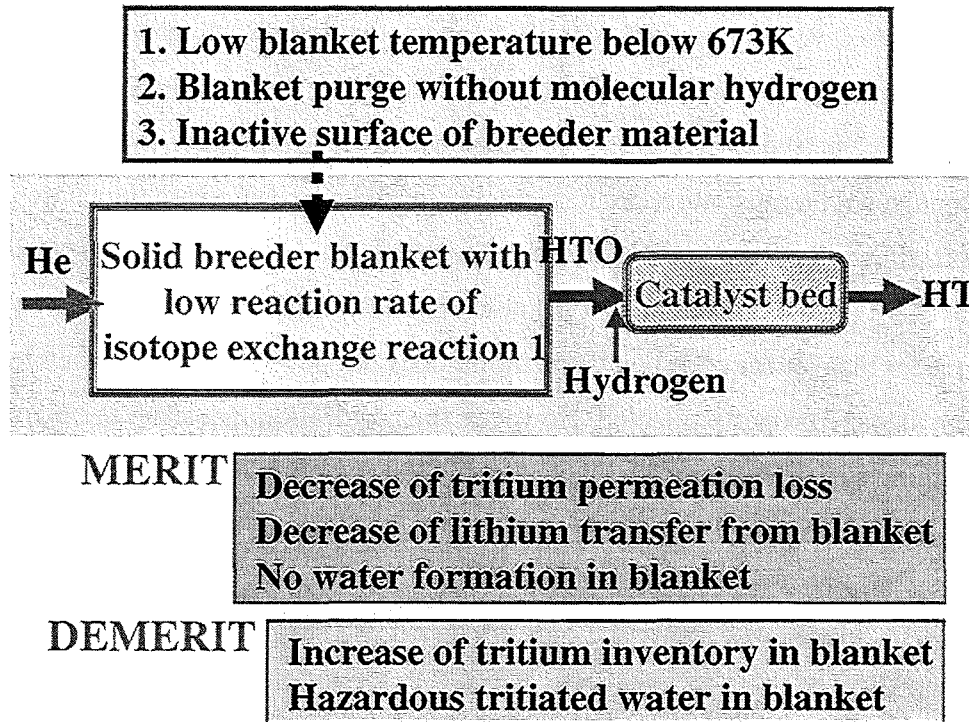


Fig. • Blanket with outside catalyst bed for conversion of tritiated water to molecular form tritium by using isotope exchange reaction 1.

In the case when the main chemical form of tritium in the blanket is oxide form, it could be effective to have a precious metal catalyst bed at outside of the blanket purge gas as is shown in Fig.3.

It must be also taken into count in the high temperature ceramic breeder blanket that some amount of lithium compound is transferred to the purge gas. Figure 4 showed that the quartz tube changed its color to white with trapping not a small amount of lithium compound from a 973K Li_2ZrO_3 bed purged by nitrogen gas with 1000ppm hydrogen for three days. The similar phenomena were obtained also at the experiment using Li_2O or Li_2TiO_3 bed.

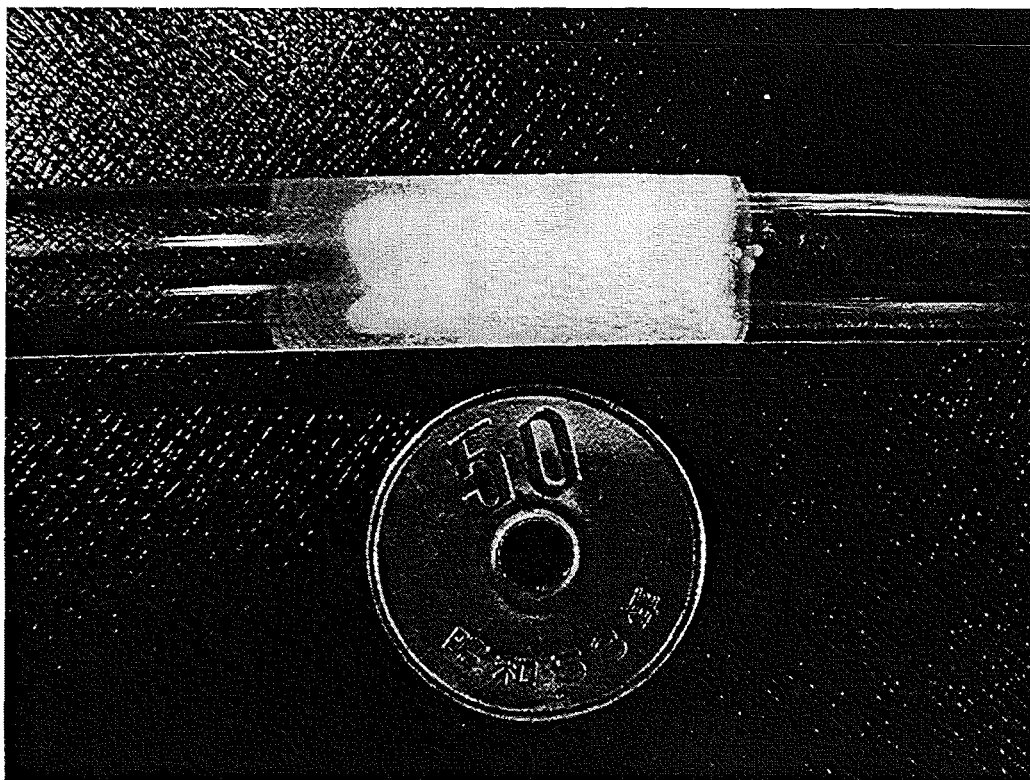


Fig. 4 Lithium compound trapped to the quartz tube from a Li_2ZrO_3 bed purged by nitrogen gas with 1000ppm hydrogen at 973K for three days

Thermal behaviour and tritium management for in-pile testing of the pebble bed assemblies in the HFR in Petten

A.J. Magielsens^a, R. Conrad^b, J.H. Fokkens^a, B.J. Pijlgroms^a and J.G. van der Laan

^aNRG, P.O. Box 25, 1755 ZG Petten, The Netherlands

^bInstitute for Energy, P.O. Box 2, 1755 ZG Petten, The Netherlands

Four pebble-bed assemblies are to be irradiated in the HFR in Petten with the objective to study the thermo-mechanical behaviour of the breeder ceramic pebble beds during irradiation.

The thermo-mechanical behaviour of the pebble bed assemblies was calculated in a 2D axi-symmetric model in MARC. In this approach there could not be accounted for the influence of thermocouple tubes on the temperature distribution in the assembly, because these are distributed in the assembly in a non axi-symmetric manner. The solution for this problem was to expand the model to a 3D model used for thermal computations only.

For safety reasons the tritium production in the breeder and permeation through the first and second containment must be estimated before the in-pile experimentation begins. In order to do so, the calculated thermal distribution is used as input for the enhanced two-dimensional finite element model in MARC. Adaptations are made in the 2D model by adding the capability of performing mass flux calculations.

This paper describes the finite element models used for computation of the temperature distribution and the tritium flux through the pebble bed assembly. The results of these calculations are critical for a safety assessment of the in-pile operation of the experiment and will give a better understanding of the in-pile behaviour on temperature and tritium management in advance.

1. INTRODUCTION

The Helium Cooled Pebble Blanket (HCPB) consists of lithium ceramic pebble beds as tritium breeding material alternating with beryllium pebble beds as neutron multiplier. The beds are separated by cooling plates with channels for the He gas coolant [1]. Design of the HCPB is set by several design criteria. Good thermo-mechanical properties of the pebble beds should prevent temperature peaks in the beds and crushing of the pebbles. Also thermal expansion/contraction and neutron induced swelling of the pebble beds should not lead to unacceptable stresses at the containment walls or to a gap between the beds and the containment walls.

In order to evaluate these criteria, four Pebble Bed Assembly test elements are developed for in-pile testing in the HFR in Petten [2]. A pebble bed assembly consists of a lithium ceramic pebble bed sandwiched by two beryllium neutron multiplier beds and is designed with a thermal barrier that provides the radial temperature profile in the tritium breeding material to be as flat as possible. Two horizontal floating plates made of Eurofer steel separate the pebble beds. The beds are placed in an Eurofer steel cylindrical inner containment. The second containment is made of AISI 316 L stainless steel.

Temperatures are controlled by a gas mixture change in the second containment and power profiles can be adjusted by a vertical displacement unit.

For temperature control, an important design parameter is the dimension of the gas gap between the first and second containment of the pebble bed assembly. During in-pile operation the second containment will be purged with a mixture of Helium and Neon. The temperature range in which the temperature of pebble bed assembly can be controlled depends on the dimension of the gas gap. To this end and to predict the in-pile behaviour of the pebble bed assembly, calculations are performed with a coupled thermo-mechanical two-dimensional axi symmetric finite element model in MARC [3]. However, in each pebble bed assembly 18 thermocouple tubes are inserted. These tubes will enhance the effective thermal conductivity in axial direction and are distributed non symmetrically over the pebble bed assembly. To adjust the thermal conductivity in the coupled model for the contribution of the thermocouple tubes, a 3D thermal finite element model was needed to model the heat flux through the tubes. Another -safety related- issue, which has to be solved before in-pile operation, is the permeation of tritium from the pebble bed through the first and second containment to the primary coolant of the HFR. In order to calculate tritium mass-flux through the steel containments the 2D FE model was modified. Tritium permeation of all assemblies during normal operation and accidental loss of purge gas flow is calculated.

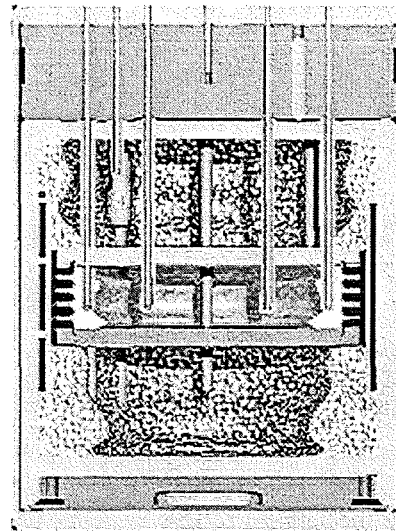


Fig. 1 Pebble bed assembly to be irradiated in the HFR in Petten.

2. THERMAL 3D AND 2D MASS FLUX MODEL

Both calculations are performed at steady state conditions, with an effective thermal conductivity of the beryllium beds of 6.7 W/m/K as used for the thermo-mechanical calculations with the 2D coupled model [3]. The thermal conductivity of the beryllium pebble beds as function of compression was used as input [4]. At steady state the compaction of the beryllium would yield a thermal conductivity of 6.7 W/m/K. Input parameters for the n, α and γ heating are taken from the MCNP calculation [5]. Material properties and the average power densities for each pebble bed assembly are tabulated in 1.

Table 1. Some input parameters for FE modelling

	material	γ heating (W/g)	average n, α heating (W/cc)	bed density (g/cc)	λ breeder (W/m/K)
PBA # 1	LiSiO ₄	2.10	21.6	1.48	$0.768+4.957 \cdot 10^{-4}T$
PBA # 2	Li ₂ TiO ₃	2.85	23.8	1.82	$2.99 \cdot 10^{-7}T^2+2.11 \cdot 10^{-5}T+0.90$
PBA # 3	Li ₂ TiO ₃	3.00	24.6	1.82	$2.99 \cdot 10^{-7}T^2+2.11 \cdot 10^{-5}T+0.90$
PBA # 4	LiSiO ₄	2.52	25.7	1.48	$0.768+4.957 \cdot 10^{-4}T$

2.1 Thermal 3D finite element model

The existing 2D FE mesh for in-pile thermo-mechanical calculations is expanded to a 90° 3D mesh to develop a model which calculates the influence of the thermocouple tubes on the temperature profile and average temperature in the pebble bed assemblies. The diameter of the first containment gas pipe and the thermocouple tube are the same, therefore the thermocouple distribution in the model is a representation of the actual thermocouple distribution as shown in figure 2 a and b.

The calculated enhanced effective conductivity is used for fine-tuning of the dimensions of the gas gaps in the pebble bed assemblies [2]. Also the local disturbance of the temperature distribution and

the influence on the average and maximum temperature is modelled, which is of relevant importance for temperature measurement during in-pile operation.

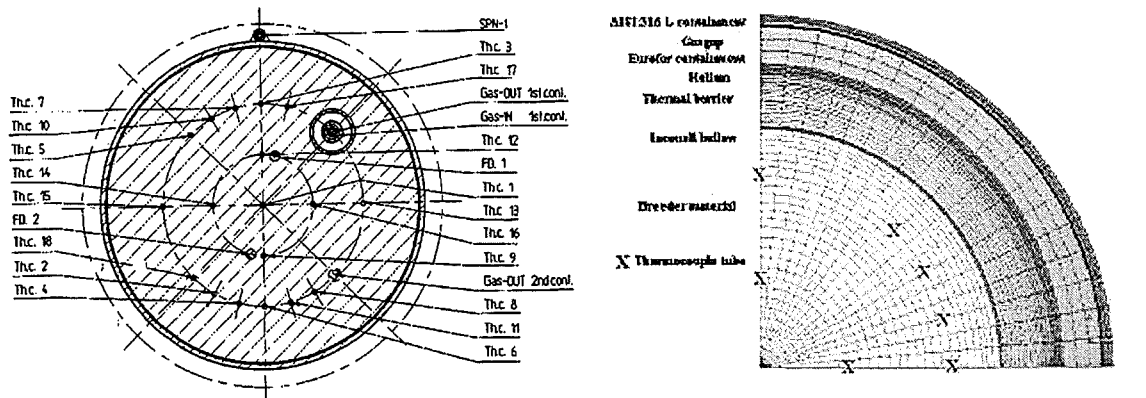


Figure 2a Actual thermocouple distribution in pebble bed assembly

Figure 2b Thermocouple distribution in 3D FE model

It is assumed that the ratio of the effective thermal conductivity of the pebble bed assembly with and without thermocouple tubes is the same for each assembly. In all pebble bed assemblies the thermocouple distribution is the same, and the difference between the thermal conductivity of the stainless steel thermocouple tubes and the conductivity of the beds is large.

2.2 2D finite element model for mass flux calculations

During in-pile operation of the pebble bed assemblies a considerable amount of tritium is generated. The first containments of the pebble bed assemblies are purged by a He + 0.1 % H₂ gas flow (flowrate 100 ml/min) which inhibit large tritium build up. However, temperatures in the assemblies are rather high (up to 850 °C) so it is important to know the tritium permeation flux through the Eurofer containment and thermocouple tubes. When incidents occur like a loss of gas flow in the first containment, it is imperative to know the tritium permeation rate to the second containment and to the primary coolant of the HFR. Calculations are therefore made for four cases:

- Normal conditions (flowrate first containment 100 ml/min, second containment 50 ml/min, P_{tot} 2.8 bar)
- Stopped flow in the first containment during 15 minutes,
- Stopped flow in the first containment during 1 hour
- Stopped flow in both containments during 1 hour

To make these calculations, the 2 dimensional thermal model is modified, based on the assumption that during steady state, heat and mass transfer are analogue transport equations[6]. The massflow of tritium through a cylindrical wall in steady state is described by [7]:

$$J = \frac{2\pi l}{\ln(b/a)} \Phi_{eff}(T) (p_{in}^{0.5} - p_{out}^{0.5}) \quad (1)$$

Where:

J= net tritium rate from medium 1 to medium 2 [mol/s],

b= outer diameter of cylinder [m]

a= inner diameter of cylinder [m]

l= lenght of cylinder [m]

p_{in} = partial pressure of tritium at the inside [Pa]

p_{out} = partial pressure of tritium at the outside [Pa]

ϵ_{eff} = Effective permeability of the DWT or TBP [$\text{mol m}^{-1} \text{s}^{-1} \text{Pa}^{0.5}$],

(1) is analogue to:

$$Q = \frac{2\pi l}{\ln(b/a)} \lambda(T) (T_1 - T_2) \quad (2)$$

Equation 1 can be used to compute the permeability of the structural material of the Pebble bed assemblies. The permeability (λ) of hydrogen in structural materials is a material property dependent on temperature described by the Arrhenius relation. Permeabilities of the materials are determined in out of pile experiments with use of deuterium. These data can be converted into tritium permeation rates by multiplication with the ratio of the square root of the weight of deuterium and tritium ($2/3$) [7]. The permeability of Eurofer is shown in figure 3 [8].

It was assumed that the permeability of AISI 316 L (material second containment) and AISI 321 are the same, this value is also plotted in figure 3 [9].

A user subroutine is written to use the outcome of the 2D thermal model as input for the calculation of the permeability of the structural materials at the calculated temperature with use of these Arrhenius relations. This model is verified by calculation of the tritium permeation through a Double Wall Tube in EXOTIC 8/9 and comparison with the in-pile data of this experiment [6].

The tritium partial pressures in the pebble bed assemblies are calculated from the average power density of the n,α heating, the operation conditions (gas flow, pressure), the packing density and the mean temperature of the pebble beds.

For numerical reason the square root of the calculated tritium partial pressure and the permeability are scaled with a factor 1000. The tritium partial pressures and average temperatures of all pebble beds are listed in table 2. The gas enters the PBA at the bottom therefore it is estimated that the tritium concentration in the lower beryllium bed is 10 times lower than the concentration in the other beds. The average ^3H production rate is calculated from the n,α heating.

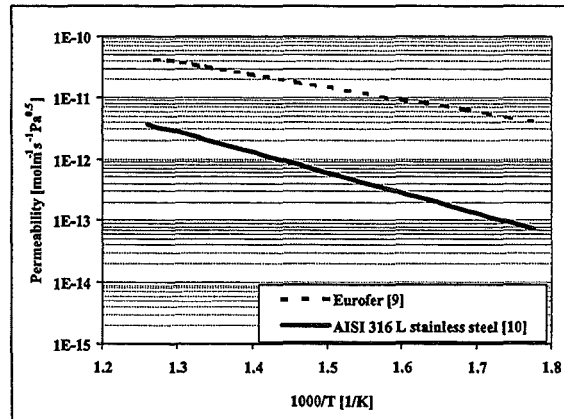


Figure 3 Permeability of Eurofer and AISI 316 L SS used as input for 2D Permeation model

Table 2. Input parameters for ^3H permeation calculation, where UBe and LBe are the Upper and Lower beryllium pebble bed respectively

	Bed	T_{av} (K)	^3H prod. rate	Tritium partial pressure (Pa)		
				Normal condition	Stop flow 15 min	Stop flow 60 min
PBA # 1	UBe	499	8.17E-10	1.8	85	340
	Breeder	850		3.1	145	580
	LBe	521		0.2	89	355
PBA # 2	UBe	545	8.99E-10	2.2	102	409
	Breeder	942		3.8	177	707
	LBe	567		0.3	106	426
PBA # 3	UBe	563	9.29E-10	2.3	109	436
	Breeder	972		4.1	188	753
	LBe	581		0.3	113	450
PBA # 4	UBe	530	9.71E-10	2.3	107	429
	Breeder	943		4.1	191	764
	LBe	553		0.3	112	448

3. RESULTS AND DISCUSSION

3.1 Influence of thermocouple tubes on temperature profile

The temperature profile of Pebble bed assembly # 3 is calculated with thermocouple tubes. The tubes are modelled as line elements. The maximum temperature of the breeder is 4 K lower when thermocouple tubes penetrate the bed. The temperature drop at the location of the tube should be less than the calculated 250 K, because the heat transfer coefficient between the pebble bed and thermocouple tube was not modelled. Instead, perfect contact is used because in this model there was no option to simulate contact areas, so the quantity of the calculated temperature drop must be taken with care. Although the temperature can be locally disturbed during in-pile operation, the desired maximum temperature does not deviate strongly. In figure 4a the cross section in the middle of the breeder bed is shown and in figure 4 b the radial temperature profile for both cases is plotted.

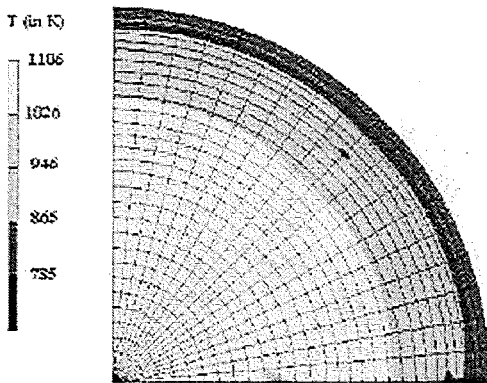


Figure 4a Cross section in the 3D model at the middle of the breeder bed, PBA # 3

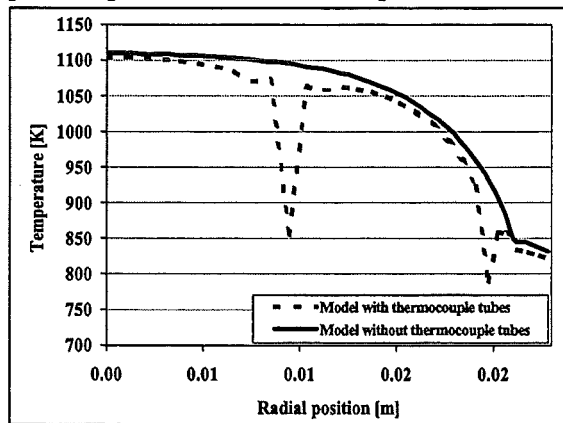


Figure 4b Radial Temperature profile in the middle breeder bed

For determination of the thermal conductivity enhancement factor calculations with the 3D thermal model without thermocouple tubes are made with the thermal conductivity as input variable. In this way the factor was iterative defined to be 1.2 for the upper beryllium bed and 1.1 for the breeder and lower beryllium bed.

3.2 Tritium permeation

Tritium permeation through the containments and thermocouple tubes is calculated for all four Pebble bed assemblies. The calculated ^3H permeation flux during normal operation and the axial temperature profile of the first containment are plotted in figure 5. The Tritium permeation flux during normal and obstructed flow conditions through all containments and thermocouple tubes is calculated and summarised in table 4. Even when the gas flows in the first and second containment are blocked during 1 hour, tritium permeation to the primary coolant of the HFR is low. The total activity of

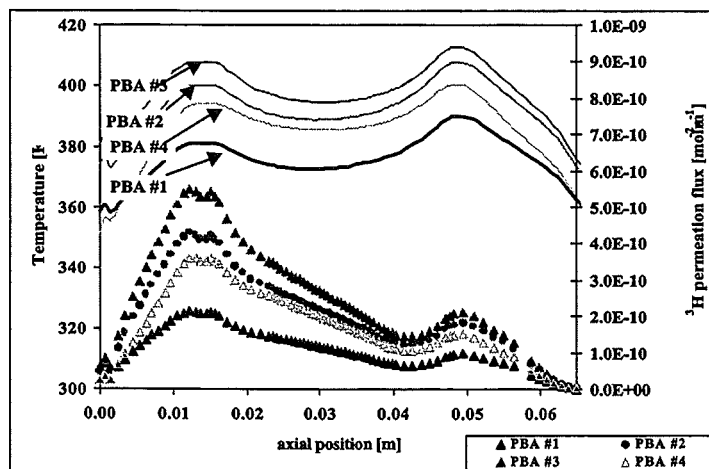


Figure 5 Axial Tritium permeation flux through the first containments of the four pebble bed assemblies

permeated tritium during the worst -case is calculated to be 100 Bq/s (summed over the four Pebble bed assemblies). Throughout these calculations the assumptions are made that analogy between mass and heat transport can be used, only Tritium will permeate through the structural material and tritium concentration outside first containment is zero.

Table 4. Tritium transport in mole/s through 1st and 2nd containment during normal operation, obstructed gas flow for 1 hour in first containment/ normal flow in 2nd and obstructed flow in both containments for 1 hour (Worst case).

	Normal operation			Stop flow in 1 st C.(60 min)			Worst case
	1 st C	TC tubes	2 nd C	1 st C	TC tubes	2 nd C	2 nd C
PBA #1	1.36E-12	1.03E-11	1.55E-16	2.84E-11	1.83E-10	6.63E-16	1.16E-14
PBA #2	2.60E-12	3.38E-11	3.07E-16	5.39E-11	4.63E-10	1.16E-15	1.80E-14
PBA #3	3.27E-12	3.43E-11	3.28E-16	6.64E-11	6.11E-10	1.39E-15	2.08E-14
PBA #4	2.19E-12	2.25E-11	2.30E-16	4.52E-11	4.06E-10	9.79E-16	1.48E-14

4. CONCLUSIONS

- Thermocouple tubes disturb the Temperature Distribution in the pebble beds locally.
- The maximum temperature of the breeder bed is lowered by 4 K, which only 0.5% of the maximum temperature
- The effective thermal conductivity is enhanced with a factor 1.2 for the Upper beryllium bed, 1.1 for the breeder bed and 1.1 for the lower beryllium bed
- To regard the tritium permeability as an analogue to thermal conductivity, tritium permeation can be calculated
- Total tritium flow rate to the primary coolant in the case in the accidental situation of a blocked flow in the first and second containment is calculated to be $6.52 \cdot 10^{-14}$ mol/s, which corresponds with an activity increase of 100 Bq/s.

REFERENCES

- [1] S. Hermsmeijer, U. Fisher, M. Fütterer et al. "An Improved European Helium Cooled Pebble Bed blanket" *Fus. Eng. Des.* vol 58-59 (2000) p 689
- [2] J.G. van der Laan, R. Conrad, J.H. Fokkens et al. "Status of the In-Pile Test of HCPB Pebble-Bed Assemblies in the HFR Petten" *these Proceedings.*
- [3] J.H. Fokkens "Thermo-mechanical Behaviour of pebble beds by finite element modelling" *these Proceedings.*
- [4] J. Reimann, S. Hermsmeijer, G. Piazza, G. Wörner. "Thermal Conductivity Measurements of Deformed Beryllium Pebble Beds By Hot Wire Method". *Proceedings CBBI-9, Toki, Japan (2000)* p199
- [5] B.J. Pijlgroms. "MCNP Calculations for the HCPB submodules In-pile test", *ECN Report, ECN-I-98-057, 1998*
- [6] A.J. Magielsen, K. Bakker, C. Chabrol, R. Conrad, J.G. van der Laan E. Rigal and M.P. Stijkel. "Irradiation performance of a double walled tube and a tritium permeation barrier." *Poster presentation at the ICFRM-10 in Baden-Baden (2001)*
- [7] M.A. Fütterer, PhD Thesis *Toulouse (1993)*
- [8] A. Aiello ICFRM-10 Proceedings to be published
- [9] K.S. Forcey, D.K. Ross and J.C.B. Simpson "Hydrogen transport and solubility in 316L and 1.4914 steels for fusion reactor applications" *J. Nucl. Mat.* vol. 160 (1988) 117-124

Thermo-Mechanical Behaviour of Pebble Beds by Finite Element Modelling

J.H. Fokkens

NRG, P.O. Box 25, 1755 ZG Petten, The Netherlands

In the framework of developing the Helium Cooled Pebble Bed (HCPB) blanket four pebble bed assemblies are to be irradiated in the HFR in Petten. The objective of these experiments is to study the thermo-mechanical behaviour of the lithium ceramic breeder and beryllium pebble beds during irradiation.

The basic test elements for the pebble bed assemblies consist of EUROFER-97 cylinders with a horizontal lithium ceramic breeder pebble bed sandwiched between two beryllium pebble beds. The breeder and beryllium pebble beds are separated by EUROFER-97 steel plates, which can float along the cylinder walls. The plates are not connected to the cylinder walls, but are supported only by the adjacent pebble beds.

The breeder pebble beds are either Lithium-Ortho-Silicate (Li_4SiO_4) or Lithium-Meta-Titanate (Li_2TiO_3). Under influence of stress, temperature, and time the breeder and beryllium pebble beds show non-linear elastic ($f(\sigma, T)$), compaction ($f(\sigma, T)$), and creep compaction ($f(\sigma, T, t)$) behaviour. Additionally, the thermal conductivity of the beryllium pebble bed depends on compaction level. All mentioned effects have to be taken into account for the evaluation of the temperatures, stresses, and strains that develop in the test elements during in-pile operation.

This paper describes how the non-linear elasticity, compaction, and creep compaction have been incorporated into the general purpose finite element program MARC. The method applied to determine the model parameters from experimental oedometer data is also described. The pebble bed model has been applied to calculate the thermo-mechanical behaviour of complete pebble bed assemblies to be irradiated in the HFR. The results of these calculations are critical for a safety assessment of the in-pile operation of the experiment and will provide a better understanding of the in-pile behaviour.

1. INTRODUCTION

In the framework of developing the Helium Cooled Pebble Bed (HCPB) blanket four pebble bed assemblies are to be irradiated in the HFR in Petten. The objective of these experiments is to study the thermo-mechanical behaviour of the lithium ceramic breeder and beryllium pebble beds during irradiation. Within the experiment two different breeder materials are to be tested: Lithium-Ortho-Silicate (OSi) and Lithium-Meta-Titanate (MTi). The maximum temperatures to be achieved in the breeder bed of each pebble bed assembly are shown in figure 1, as well as the experimental lay-out. The thermal behaviour of the pebble bed assemblies has to be predicted for the safety assessment of the in-pile operation of the experiment.

The basic test element for the pebble bed assemblies is shown in figure 2. The test element consists of a EUROFER-97 cylinder with a horizontal lithium ceramic breeder pebble bed sandwiched between two beryllium pebble beds. The breeder and beryllium pebble beds are separated by EUROFER-97 steel plates, which can float along the cylinder walls. The plates are not connected to the cylinder walls, but

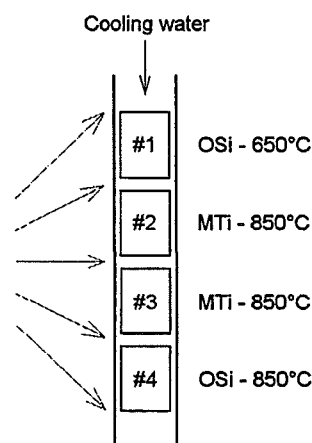


Fig. 1 Schematic view of the pebble bed assemblies during irradiation in the HFR

are supported only by the adjacent pebble-beds. The heat flow is managed in such way that the radial temperature distribution in the ceramic breeder pebble bed is as flat as possible. The EUROFER-97 cylinder is enclosed in a stainless steel containment. A gasgap between the EUROFER-97 and stainless steel cylinders controls the thermal behaviour of the test element. The dimensions of the gasgap are determined with the prediction of the thermal behaviour of the test element.

Under influence of stress, temperature, and time the breeder and beryllium pebble beds show non-linear structural behaviour. Additionally, the thermal conductivity of the beryllium pebble-bed depends on the compaction level. These effects have been taken into account in the material model used for the evaluation of the temperatures, stresses, and strains that develop in the test elements during in-pile operation. This model is incorporated in the general purpose finite element program MARC [1]. The model is based on the results of oedometer experiments performed for the breeder and beryllium pebble beds by FZK. The results of the calculations performed utilizing the material model will be used for the determination of the gasgap, the safety assessment of the in-pile operation of the experiment, and will provide a better understanding of the in-pile behaviour.

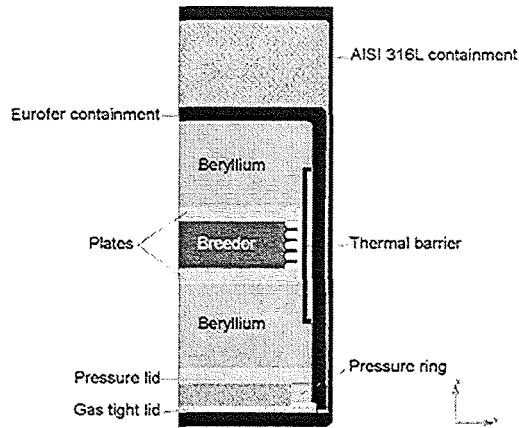


Fig. 2 The test element for the pebble bed assemblies

2. PEBBLE BED MODEL

The behaviour of OSi, MTi, and beryllium pebble beds has been investigated experimentally by FZK [2-7]. On the basis of oedometer experiments the non-linear structural behaviour of single pebble beds has been investigated at various stress and temperature levels. The experimental results have then been regressed using parametric relations. The material model used for the finite element calculations is based on these relations. In the model the observed non-linear structural behaviour is described by non-linear elastic, initial compaction, and creep compaction behaviour. The non-linear elastic and initial compaction behaviour are stress and temperature dependent. The creep compaction behaviour is stress, temperature, and time dependent. The compaction behaviours result in permanent volume change of the pebble bed. The thermal conductivity of the beryllium pebble bed is depending on the compaction level.

2.1. Non-linear elasticity and initial compaction

The experimental oedometer results are described with the following relation for the Young's modulus as a function of axial stress and temperature ('Reimann fit'):

$$E = C_1 \cdot (C_2 + C_3 \cdot T^{C_4}) \cdot \sigma^{C_5} \quad (1)$$

where:

E	: Young's modulus	[MPa]
T	: temperature	[°C]
σ	: axial stress	[MPa]

The axial strain is determined according to the following relation:

$$\varepsilon = \frac{\sigma}{E} \quad (2)$$

Table 1 The parameters for OSi and beryllium describing the experimental oedometer results

	OSi		beryllium	
	first pressure increase	first pressure decrease	first pressure increase	first pressure decrease
C_1	154.00	170.00	154.00	870.00
C_2	1.00	1.00	1.00	1.00
C_3	-8.5E-10	-8.5E-10	0.00	0.00
C_4	3.00	3.00	1.00	1.00
C_5	0.47	0.60	0.586	0.650

Separate parameters for the relation are given for the first pressure increase and the first pressure decrease. These parameters are summarized in table 1.

It is assumed that the non-linear elasticity is described by the 'fit' for the first pressure decrease. The initial compaction is described by the difference between the 'fits' for the first pressure increase and the first pressure decrease. The resulting curves for the non-linear elasticity and initial compaction are implemented as stress and temperature dependent piece-wise linear curves in the user subroutines HOOKLW and CRPLAW of the finite element program MARC.

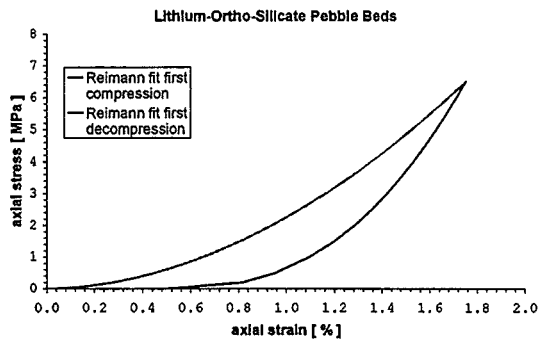


Fig. 3 The experimentally determined stress-strain curve

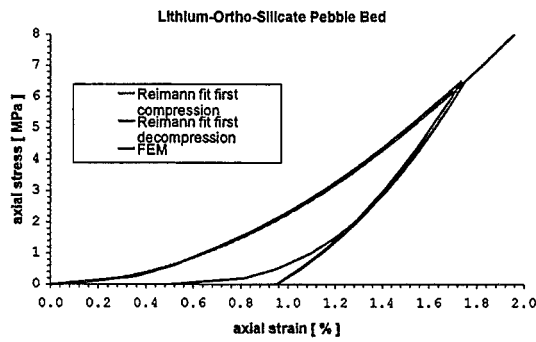


Fig. 4 Comparison between the experimental and calculated oedometer results

The pebble bed material model is used to predict the behaviour of a pebble bed (diameter 50 mm, height 25 mm) in an oedometer experiment at various temperatures. The figures 3 and 4 show the comparison between the experimentally determined and calculated stress-strain relation for OSi at one temperature level. Good agreement has been achieved between the experimental and calculated results for an OSi and beryllium pebble bed at all temperature levels.

2.2. Creep compaction

The experimental 'Reimann fit' for the creep compaction of an OSi pebble bed is given by:

$$\varepsilon^c = B_0 \cdot p^{B_1} \cdot t^{B_2} \cdot e^{\frac{B_3}{T}} \quad (3)$$

where:

- | | | |
|-----------------|---------------------------|-------|
| ε^c | : creep compaction strain | [-] |
| p | : pressure | [MPa] |
| t | : time | [s] |
| T | : temperature | [K] |

and:

$$\begin{aligned} B_0 &= 11.41 \\ B_1 &= 0.40 \\ B_2 &= 0.20 \\ B_3 &= -9741.00 \end{aligned}$$

The 'Reimann fit' has been implemented in the FEM program in the following form:

$$\varepsilon_m^c = a \cdot B_0 \cdot (\sigma_m)^{B_1} \cdot t^{B_2} \cdot e^{\frac{B_3}{T}} \quad (4)$$

where:

ε_m^c	:	mean creep compaction strain	[-]
a	:	compaction strain correction factor ($a = 1.60$)	[-]
σ_m	:	mean stress (hydrostatic stress)	[MPa]
t	:	time	[s]
T	:	temperature	[K]

and:

$$\begin{aligned} B_0 &= 11.41 \\ B_1 &= 0.40 \\ B_2 &= 0.20 \\ B_3 &= -9741.00 \end{aligned}$$

The creep compaction strain components are derived from the mean creep compaction strain according to the following relation:

$$\varepsilon_i^c = \frac{1}{3} \cdot \frac{\sigma_i}{\sigma_m} \cdot \varepsilon_m^c \quad (5)$$

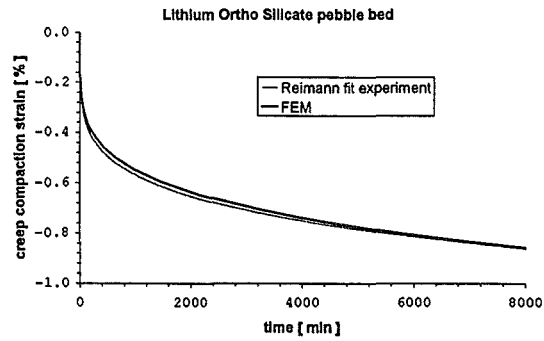


Fig. 5 Comparison between the experimental and calculated creep curve

An oedometer creep experiment has been analysed at various temperature levels above 650°C. In these analyses the non-linear elastic, initial compaction, and creep compaction behaviour have been taken into account. The pressure loading is linearly increased to 6.5 MPa in 16.25 seconds and then kept constant. For one temperature level figure 5 shows the comparison between the experimentally fitted and calculated creep behaviour.

2.3 Thermal Conductivity Beryllium

The thermal conductivity of the beryllium pebble bed depends on the compaction level in the pebble bed. Increasing compaction results in higher thermal conductivity. The relation between the thermal conductivity and the compaction is given by:

$$\lambda_{Be} = C_1 \cdot (1 - C_2 \cdot \varepsilon_{comp}) \quad (6)$$

where:

λ_{Be}	:	thermal conductivity beryllium	[W / m K]
ε_{comp}	:	compaction strain	[-]

Table 2 The parameters C_1 and C_2 in the relation for the thermal conductivity of beryllium

temperature [K]	C_1	C_2
273	1.668	505.35
298	1.700	486.00
453	1.900	366.00
648	2.100	340.00
748	2.200	314.00

The constants C_1 and C_2 are summarized in table 2 for various temperature levels. Relation 6 has been implemented in the MARC user subroutine ANKOND. The compaction dependency of the beryllium thermal conductivity can only be used in a full-coupled analysis.

3. IN-PILE TEST ELEMENT

The thermo-mechanical behaviour of test element #4 during start-up has been determined with a transient, full-coupled, axisymmetric finite element analysis. In a full-coupled analysis the interaction between the thermal and structural behaviour is directly taken into account. During start-up the reactor power is increased in four equal steps to 100%. The total start-up takes 1 hour.

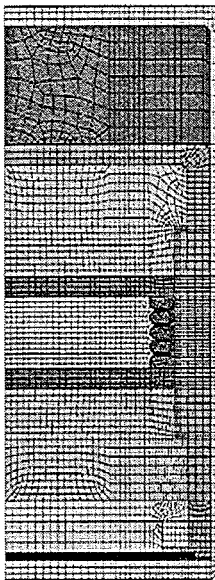


Fig. 6 Finite element model

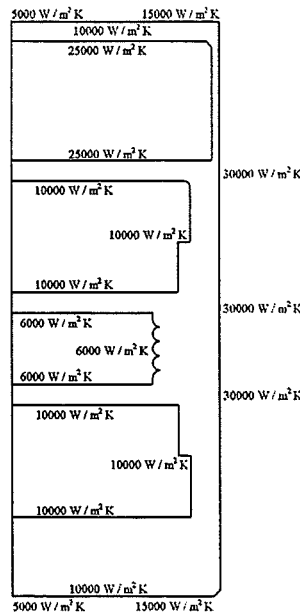


Fig. 7 Applied thermal boundary conditions

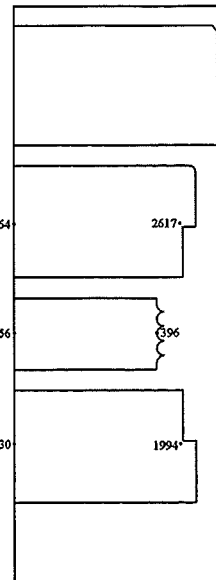


Fig. 8 Position of the characteristic nodal points

Figure 6 shows the applied axisymmetric finite element model. The model consists of 3837 four-node axisymmetric elements and 4331 nodal points. The pebble beds and the top aluminium filler are modelled as separate model parts. These parts are coupled to the main model by using the CONTACT option of MARC. At the interfaces between the various model parts (breeder bed - steel/inconel, beryllium beds - steel, and top aluminium filler - steel) heat barriers are modelled by specifying heat transfer coefficients. The applied thermal boundary conditions are shown in figure 7. The thermal loading consists of a position dependent (n , α) and γ heating. During the start-up the thermal loading is increased in four proportional steps, as already mentioned.

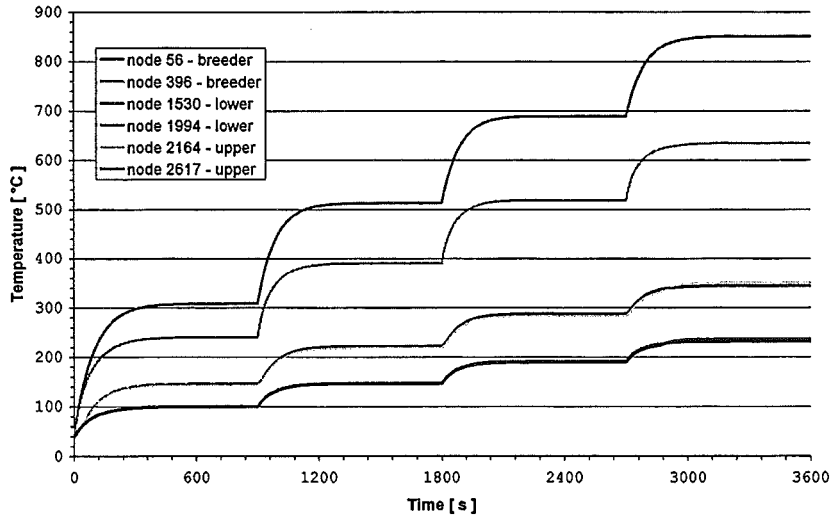


Fig. 9 The development of the temperature in the characteristic nodal points

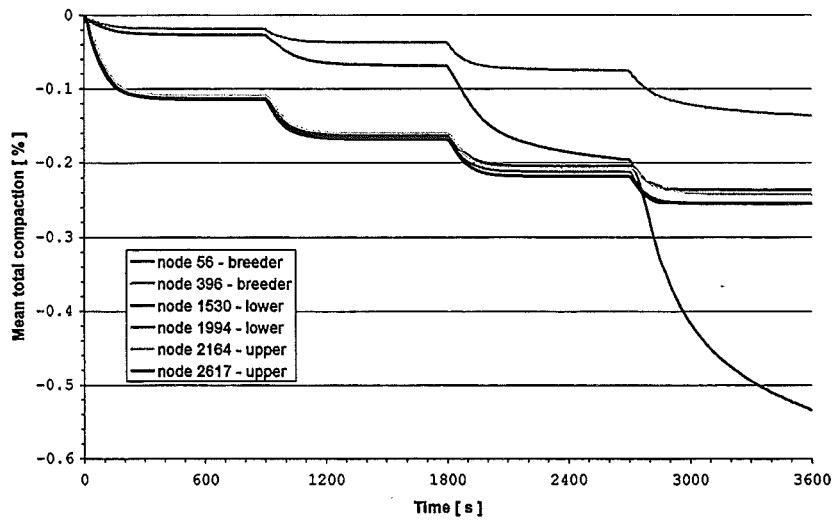


Fig. 10 The development of the total compaction strain in the characteristic nodal points

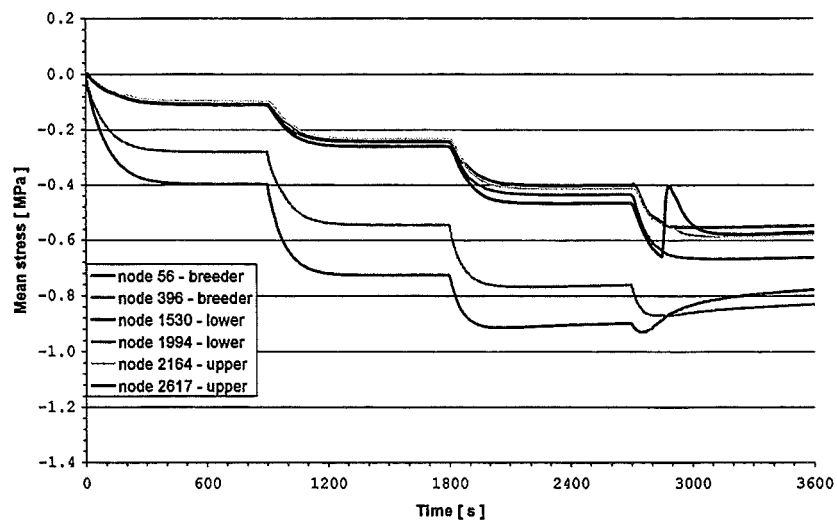


Fig. 11 The development of the mean stress in the characteristic nodal points

The figures 9 to 11 show the development of the temperature, the total compaction, and the mean stress in some characteristic nodal points during the start-up. The position of these characteristic nodal points is shown in figure 8. The test element has a rapid thermal response (figure 9). In the centre of the breeder bed the requested maximum temperature level of 850°C is reached. The radial distribution of the temperature in the breeder bed is flat (figure 12).

Initially the highest compaction levels occur in the beryllium pebble beds. After power step 3 the temperature level in the breeder bed has reached such a level that creep compaction occurs. At the end of the start-up the highest compaction levels occur in the centre of the breeder bed (figure 10).

Due to the high thermal expansion in the breeder bed, stresses build up in the pebble beds. The stress build-up decreases as soon as creep compaction occurs in the breeder bed. In the centre of the breeder bed even a stress decrease can be observed (figure 11). The increase in thermal conductivity in the beryllium pebble beds is illustrated by the figures 13 and 14.

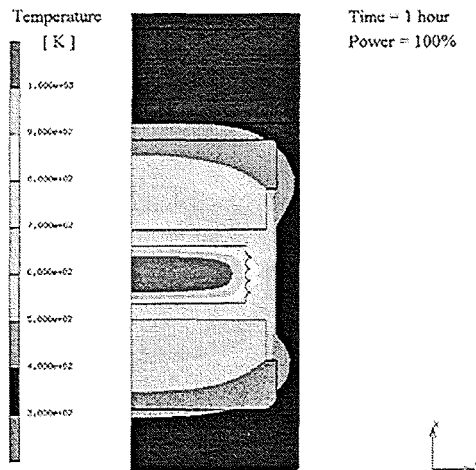


Fig. 12 Temperature distribution after the start-up

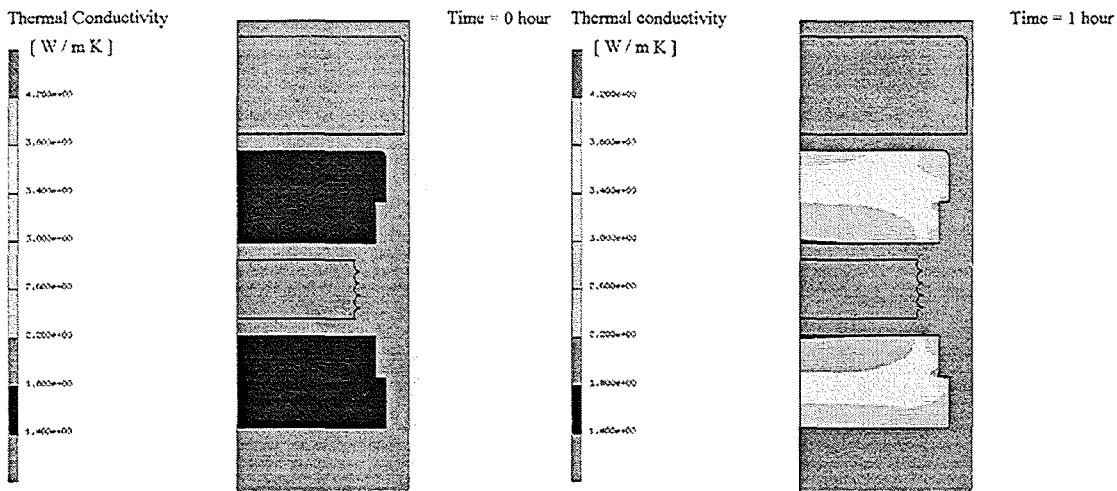


Fig. 13 The initial thermal conductivity in the beryllium Fig. 14 The thermal conductivity in the beryllium after 1 hour

The material model developed describes all relevant phenomena experimentally observed. The model gives reliable results and can be used as an engineering tool for the test elements. However, due to the fact that full-coupled analyses have to be performed, application of the material model requires large computational effort.

4. DISCUSSION

For the development of the material model a straightforward engineering approach has been chosen. The model should describe all relevant phenomena observed in the experiments and should be applicable as an engineering tool for the test elements. The model is based on the experimental oedometer results. Because the pebble bed dimensions in the oedometer experiments are comparable to the pebble bed dimensions in the test element the model can be applied directly to the test element. The model should also be applicable to other pebble bed constructions (e.g. blanket). However, this remains to be confirmed.

5. CONCLUSIONS

- the applied material model describes all relevant phenomena of the thermo-mechanical behaviour of a OSi and beryllium pebble bed;
- the material model gives reliable results, based upon the analyses undertaken;
- the material model can be used as an engineering tool to predict the response of the test elements;
- the application of the material model requires large computational efforts.

REFERENCES

- 1 *MSC MARC Users Manuals Version 2000*
MSC Software Corporation, Los Angeles; March 2000
- 2 *First Experiments on the Thermomechanical Behaviour of Li_4SiO_4 Pebble Beds*
J. Reimann; S. Müller
Proceedings 20th SOFT, Marseille; page 1337-1340; September 1998
- 3 *Thermomechanical behaviour of ceramic breeder pebble beds*
J. Reimann; E. Arbogast; S. Müller; K. Thomauske
Proceedings of CBBI-7; page 5.1-5.10; September 1998
- 4 *Thermal Creep of Li_4SiO_4 Pebble Beds*
J. Reimann; G. Wörner
Proceedings 21th SOFT, Madrid; Part B; page 647-651; September 2000
- 5 *Thermal Creep of Ceramic Breeder Pebble Beds*
J. Reimann; G. Wörner
Proceedings of CBBI-9; page 95-107; September 2000
- 6 *Particle Flow of Ceramic Breeder Beds in Bi-Axial Compression Experiments*
S. Hermsmeyer; J. Reimann
CBBI-10; paper A23; October 2001
- 7 *Thermal Conductivity of Compressed Orthosilicate and Metatitanate Pebble Beds*
J. Reimann; S. Hermsmeyer; G. Wörner
CBBI-10; paper A26; October 2001

Status and Future Plan of Breeding Blanket Development

H. Kawamura and K. Tsuchiya

Oarai Research Establishment, JAERI, Narita, Oarai, Higashi-ibaraki, Ibaraki 311-1394, Japan

Lithium titanate (Li_2TiO_3) has attracted the attention of many researchers from a point of easy tritium recovery at low temperature, chemical stability and so on. A small pebble like 0.2-2 mm diameter was proposed as the shape of tritium breeder in order to reduce thermal stress, etc. In JAERI, the fabrication development of tritium breeder pebbles and characterization of the pebbles have been carried out and concept of lithium cycle has been considered. On the other hand, the engineering data on the neutron irradiation performance of a blanket are indispensable to design the breeding blanket. Therefore, the in-pile test of a blanket mockup with Li_2TiO_3 pebbles is being started in the Japan Materials Testing Reactor (JMTR). In this paper, the status of the fabrication technology development of tritium breeder pebbles and the in-pile test of a tritium breeding blanket is described.

1. INTRODUCTION

In the development of the tritium breeding blanket for a fusion reactor, lithium-containing ceramics such as Li_2O , Li_2TiO_3 , Li_2ZrO_3 and Li_4SiO_4 were recognized as promising tritium breeders [1-2]. Recently, Li_2TiO_3 has attracted the attention of many researchers from a point of easy tritium recovery at low temperature, chemical stability and so on [3-6]. A small pebble like 0.2-2 mm diameter was proposed as the shape of tritium breeder in order to reduce thermal stress, etc. [7]. In JAERI, the fabrication development of tritium breeder pebbles has been carried out and concept of lithium cycle has been considered [8].

On the other hand, the engineering data of tritium breeders under neutron irradiation are indispensable to design the fusion blanket. It is necessary to evaluate the tritium production rate and heat generation profiles in the tritium breeder regions, and to reflect these results for the design of a fusion blanket. The major advantage of in-situ irradiation experiments is the capability to provide a neutron flux over a large volume prior to the availability of a fusion reactor. As the recent in-situ irradiation tests, CRITIC-III (Canada) [9], BEATRIX-II (US/Japan/Canada) [10-12], EXOTIC (Netherlands/EU) [13-15] and others were conducted. However, these experiments used relatively small amount of specimen for characterization of tritium breeders and the structures of a fusion blanket have not been simulated. Accordingly, the information of the in-situ irradiation behavior of tritium breeders is limited at present. In JAERI, two kinds of the blanket in-pile mockups with Li_2TiO_3 pebble bed have been developed and the in-situ tritium recovery experiments have been carried out in the Japan Materials Testing Reactor (JMTR) [16-17].

In this paper, the status of the fabrication technology development of tritium breeder pebbles and the in-pile functional test of a tritium breeding blanket is described.

2. DEVELOPMENT OF TRITIUM BREEDERS PEBBLES

2.1 Status of mass fabrication of tritium breeders pebbles

The application of small pebbles was proposed in some designs of a fusion blanket. A number of methods are available to produce pebbles, but few can simultaneously meet current shape, size, density purity, yield, and production rate requirements.

The three kinds of fabrication methods of tritium breeder pebbles, i.e. the melting granulation process, the rotating granulation process and the wet process, have been studied under paying attention to the recycle of lithium in used tritium breeder pebbles in JAERI (see Fig.1). From the preliminary

fabrication tests and characteristics (see Fig.2), it was obvious that the melting granulation process and the rotating granulation process were unfavorable from a viewpoint of the mass production. The wet process was the most advantageous for the mass production of small pebbles. In addition, reprocessing technology on irradiated tritium breeder pebbles has been developed from the viewpoints of effective use of resources and the reduction of radioactive wastes. The wet process will be also advantageous for fabricating small pebbles from the reprocessed lithium-bearing solution.

2.2 Development of indirect wet process for mass fabrication of Li_2TiO_3 pebbles

The indirect wet processes with dehydration reaction and substitution reaction were developed.

In the wet process with dehydration reaction, polyvinyl alcohol (PVA) was used as the binder of Li_2TiO_3 powder. In the wet process with substitution reaction, sodium alginate was used as the binder and zinc chloride with purity of 96wt% was prepared as the gelling agent.

Characterization of two kinds of Li_2TiO_3 pebbles fabricated above condition is tabulated in Table 1. The main features are discussed below. Average diameters of two kinds of Li_2TiO_3 pebbles were about $\phi 1.9$ mm and $\phi 0.27$ mm, respectively. Sphericity of two kinds of Li_2TiO_3 pebbles was measured by the photographic analysis method and the degrees of sphericity were as high as 1.05 to 1.1. The average grain sizes of two kinds of Li_2TiO_3 pebbles were 1.9 mm and 4.3 mm, respectively. The density of two kinds of Li_2TiO_3 pebbles was measured by mercury porosimetry and the average densities of two kinds of Li_2TiO_3 pebbles were 2.86 g/cm^3 and 2.82 g/cm^3 , respectively. Silicon (Si), sodium (Na) and carbon (C) were the highest impurities detected in the larger pebbles. On the other hand, aluminum (Al), silicon (Si), sodium (Na) and iron (Fe) were the highest impurities detected in smaller pebbles. To evaluate the strength of Li_2TiO_3 pebbles, the crushing strength was measured by a compression strength test. The average crushing load of large and small pebbles was about 73 N and 4.6 N, respectively. XRD analysis of two kinds of Li_2TiO_3 pebbles was undertaken after packing the pebbles in a polyethylene sheet and Li_2TiO_3 was the main component detected.

The results of fabrication tests and characterization of two kinds of Li_2TiO_3 pebbles were described as follows. The density of Li_2TiO_3 pebbles was controlled between 80 %T.D. and 85 %T.D. and the particle size of Li_2TiO_3 pebbles was controlled between $\phi 0.2$ and $\phi 2$ mm by two kinds of indirect wet processes. Additionally, the average grain sizes of Li_2TiO_3 pebbles were less than 5 μm . From the results, good prospects were obtained concerning mass fabrication of Li_2TiO_3 pebbles with target diameter ($\phi 0.2$ -2.0 mm) and density (80-85%T.D.) by two kinds of indirect wet processes.

2.3 Development of direct wet process for mass fabrication of Li_2TiO_3 pebbles

Fabrication tests of Li_2TiO_3 pebbles by the direct wet process were performed as a part of cooperative program on nuclear technology of fusion reactors in IEA (Task F). The direct wet process mainly consists of four processes: dissolution process of Li_2TiO_3 powder, generation process of gel-spheres, drying process of gel-spheres and sintering process. At first, the parameter survey tests were carried out in each process and optimum condition for fabrication of Li_2TiO_3 pebbles were examined.

- 1) In the dissolution process of Li_2TiO_3 powder, the solvent for dissolving the Li_2TiO_3 powder was decided. The solvents such as hydrogen peroxide (H_2O_2), citric acid ($\text{C}_6\text{H}_8\text{O}_7$) and/or other acids were selected. The dissolving was performed in a water bath controlled under 20°C with stirring.
- 2) In the generation process of gel-spheres, the gelation solvent for fabrication of gel-spheres was selected. The degassing was performed to eliminate gas (oxygen or hydrogen peroxide) dissolved in the Li_2TiO_3 solution. The Li_2TiO_3 solution was enriched by heating and a viscosity was increased by evaporating a water component in the solution. The binder such as polyvinyl alcohol (PVA) was added in the Li_2TiO_3 solution as required. The solution was dropped in gelation solvent and gel-spheres were generated.
- 3) In the drying process of gel-spheres, the drying temperature and time were selected. Additionally, solvent exchange was performed for decreasing the crack of spheres as required.
- 4) In the sintering process, the spheres were sintered in air, and Li_2TiO_3 pebbles with high density were fabricated.

The parameter survey was performed to determine each process of direct wet process and the results were as follows:

- 1) 100% Li_2TiO_3 powder could be dissolved when the holding time at more than 60°C was longer. Additionally, deposit in Li_2TiO_3 solution liquid was decreased by applying $\text{C}_6\text{H}_8\text{O}_7$ as solvent.

- 2) Good gel shape was maintained by dropping the Li_2TiO_3 condensed solution liquid in acetone.
- 3) Adjustment of a solution influenced the cracking rate of the Li_2TiO_3 pebble surface. Additionally, the solvent exchange was effective to decrease the crack of Li_2TiO_3 pebble surface and to improve the density of Li_2TiO_3 pebbles.

The future works will be to improve density by the optimization of the process parameter and to control shape by adjusting the viscosity of solution, for mass production by direct wet process.

2.4 Main material data of tritium breeders

The material data are needed for a blanket design and an analysis. Main material data of ceramic breeders are shown in Table 2. However, the material data of Li_2TiO_3 and improved materials (TiO_2 doped Li_2TiO_3) are limited. Recently, the improved materials such as TiO_2 -doped Li_2TiO_3 have been developed from viewpoints of microcrystal, moisture absorption properties and so on. Especially, the fabrication tests of TiO_2 -doped Li_2TiO_3 pebbles by indirect wet process were performed and thermal properties of TiO_2 -doped Li_2TiO_3 pellets were evaluated. From the results of these tests, it was possible to fabricate the TiO_2 -doped Li_2TiO_3 pebbles by the indirect wet process and good prospects were obtained concerning the fabrication of the TiO_2 -doped Li_2TiO_3 pebbles of diameter 0.2-2 mm by wet process. Thermal conductivity of TiO_2 -doped Li_2TiO_3 with less than 5 mol% TiO_2 powder was similar to that of Li_2TiO_3 without TiO_2 doping. On the other hand, thermal conductivity of 10mol% TiO_2 -doped Li_2TiO_3 was about 1.1 times high as that of other materials at 773K. From the result of crystal form by an X-ray diffractometer, diffraction peaks corresponding to Li_2TiO_3 appeared in TiO_2 -doped Li_2TiO_3 with less than 5 mol% TiO_2 powder. However, diffraction peaks corresponding to Li_2TiO_3 and $\text{Li}_4\text{Ti}_5\text{O}_{12}$ appeared in the 10mol% TiO_2 -doped Li_2TiO_3 . It seems that the presence of $\text{Li}_4\text{Ti}_5\text{O}_{12}$ affected the change of thermal conductivity of TiO_2 -doped Li_2TiO_3 .

3. IN-PILE FUNCTIONAL TESTS

Two kinds of blanket in-pile mockups with Li_2TiO_3 pebble bed were developed, and the in-situ tritium recovery experiments (ORIENT : Oarai Irradiation Experiment on Fusion Blanket) were carried out at the JMTR. One mock-up simulated multi-layered and pebble-packed blanket structure which has been proposed by Japan [18-19]. In these studies, effects of various parameters, i.e., irradiation temperature, sweep gas flow rate, etc., on the tritium recovery behavior from Li_2TiO_3 pebble bed were evaluated. This mockup was designed to study the tritium recovery behavior of Li_2TiO_3 pebble bed with packing fraction of about 60% under steady neutron flux. The other mockup simulated the operation pattern in the ITER pulse operation. This mockup was designed to study the tritium recovery behavior of Li_2TiO_3 pebble bed with packing fraction of about 80% under steady neutron flux and transient neutron flux. The structures and irradiation conditions of these blanket in-pile mockups are described as follows.

3.1 Irradiation test with multi-layered pebble-bed mockup (ORIENT-1)

The Li_2TiO_3 pebbles with the diameter of about 1 mm were fabricated by the rotating granulation method. Beryllium (Be) pebbles were also put into the in-pile mockup as thermal transfer medium. The schematic diagram of multi-layered pebble-bed mockup is shown in Fig. 3. The outer diameter of in-pile mockup was 65 mm. Electrical heaters for controlling irradiation temperature of Li_2TiO_3 pebble bed were installed in the in-pile mockup. The multi-paired thermocouples (T/Cs) and self powered neutron detectors (SPNDs) were also installed. There are 11 hot junction points of T/Cs and 1 measuring point of SPND in the plane of cross sections A and C. At the cross section B, there are 11 hot junction points of T/Cs and 3 measuring points of SPND. The dimension of Li_2TiO_3 pebble bed was $20\text{mm}^{\text{ID}} \times 260\text{mm}^{\text{L}}$. The in-pile mockup was irradiated in the irradiation hole of K-2 and L-3 in the JMTR for three and six operation cycles, respectively. The irradiation period of one operation cycle in the JMTR was about 25 days at 50MW. Three dimensional nuclear calculations were performed using the Monte Carlo code MCNP4B with continuous energy cross section library FSXLIBJ3R2 [20] (based on JENDL3.2). The thermal neutron flux and the fast neutron flux in the K-2 hole were about 2×10^{13} n/cm²/s and 8×10^{11} n/cm²/s. In the L-3 hole, they were about 3×10^{13} n/cm²/s and 1×10^{11} n/cm²/s, respectively. The tritium generation rate in Li_2TiO_3 pebble bed was estimated as

4.5×10^7 Bq/min and 6.9×10^7 Bq/min in the K-2 hole and L-3 hole, respectively.

3.3 Irradiation test with pulse-operation simulating mockup (ORIENT-2)

Two kinds of Li_2TiO_3 pebbles were fabricated by the wet process. The larger pebbles (diameter of about 2mm) were fabricated by the wet process with the dehydration reaction [21] and the smaller pebbles (diameter of about 0.3mm) were fabricated by the wet process with the substitution reaction [22].

The schematic diagram of pulse-operation simulating mockup is shown in Fig. 4. The outer diameter of in-pile mockup was 65 mm. This mockup has the hafnium (Hf) neutron absorber with the window for changing the thermal neutron flux. This absorber was rotated by the stepping motor installed at the top of the mockup. Electrical heaters for controlling irradiation temperature of Li_2TiO_3 pebble bed were installed in this mockup. The multi-paired thermocouples (T/Cs) and self powered neutron detectors (SPNDs) were also installed in this mockup. There are 5 hot junction points of T/Cs and 1 measuring point of SPND in the plane of cross sections A and C. At the cross section B, there are 5 hot junction points of T/Cs and 3 measuring points of SPND. Two kinds of Li_2TiO_3 pebbles with different sizes were mixed and packed into the container with the size of $20\text{mm}^{\text{ID}} \times 260\text{mm}^{\text{L}}$. The Li_2TiO_3 pebbles were fixed in the mockup by the cover plate and the spring. This in-pile mockup was irradiated in the irradiation hole M-2 hole in the JMTR for three cycles. Three dimensional nuclear calculations were performed using the Monte Carlo code MCNP4B with continuous energy cross section library FSXLIBJ3R2 (based on JENDL3.2). The thermal neutron flux and the fast neutron flux were about 2×10^{12} n/cm²/s and 5×10^{11} n/cm²/s, respectively, when the window of Hf neutron absorber was in the open condition, i.e., the window of Hf neutron absorber turned toward the reactor core. The tritium generation rate in the Li_2TiO_3 pebble bed was estimated as about 1.6×10^7 Bq/min. On the other hand, the thermal neutron flux and the fast neutron flux were about 3×10^{11} n/cm²/s and 4×10^{11} n/cm²/s, respectively, when the window of Hf neutron absorber was in the close condition, i.e., the window of Hf neutron absorber turned toward the opposite direction of reactor core. The tritium generation rate in the Li_2TiO_3 pebble bed was estimated as about 2.3×10^6 Bq/min.

3.3 Results of in-pile functional test

The effects of irradiation temperature, sweep gas flow rate, hydrogen content, etc. on tritium recovery behavior of Li_2TiO_3 pebble bed were concluded as follows by these in-situ tritium recovery experiments with JMTR.

Relationship between the temperature at outside edge of Li_2TiO_3 pebble bed and the ratio of tritium recovery rate to tritium generation rate (R/G) is shown in Fig. 5. For the data in Fig. 5, each value of R was measured in the stabilized period after 2 h. The sweep gas flow rate and the hydrogen content in sweep gas were 200 cm³/min and 1,000 ppmH₂, respectively. The moisture concentration was constant at less than 0.1 ppm. When the temperature at outside edge of Li_2TiO_3 pebble bed became more than 100°C, the tritium recovery from Li_2TiO_3 pebble bed was observed. The tritium recovery rate increased with increasing the temperature at the outside edge of Li_2TiO_3 pebble bed. From these tests, the R/G was about 1 when the temperature at the outside edge of Li_2TiO_3 pebble bed exceeded 300°C. The ratio of tritium recovery and tritium generation became saturate when the temperature at outside edge of Li_2TiO_3 pebble bed became more than 300°C. It was shown clearly that the cooling system of breeding blanket can be manufactured the same design of cooling system as a pressurized water reactor (PWR).

Sweep gas flow rate in the range of 100 cm³/min ~ 900 cm³/min dose not affect on tritium recovery from Li_2TiO_3 pebble bed in the steady state. It was shown clearly that the arrangement of thin pipes was attained in a breeding blanket since recovery of the tritium in low sweep gas flow rate had little influence. On the other hand, the change of hydrogen content was followed by positive tritium recovery peaks for increase of hydrogen content and by negative recovery peaks for decrease of hydrogen content. Hydrogen partial pressure in sweep gas has an effect on tritium recovery from Li_2TiO_3 pebble bed.

This experiment was conducted in order to evaluate the effect of continuous pulsed operation on tritium recovery from Li_2TiO_3 pebble bed. The periods of the open and close conditions were 400 s and 1310 s, respectively. The number of pulse operation cycles was 200 cycles. The result of this

experiment is shown in Fig. 6. The sweep gas flow rate and the hydrogen content in sweep gas were 200 cm³/min and 1,000 ppmH₂. The moisture concentration was constant at less than 0.1 ppm. (R/G)_{close} was about unity when the window of Hf neutron absorber turned toward the opposite direction of reactor core. When the window turned the direction of reactor core, the temperature at outside edge of Li₂TiO₃ pebble bed rose from about 300°C to 350°C and outputs of SPND also changed immediately. The tritium recovery rate fluctuated in response to pulsed operation but gradually increased in average with cycle by cycle, then became almost constant after about 20 cycles. Taking the average value of tritium generation rate over one cycle of pulsed operation (400 s of open condition + 1310 s of closed condition) as G, the ratio of tritium recovery to generation (R/G)_{av} approached to unity with time and almost saturated after 20 h, as shown in the second graph in Fig. 6. From these results, it is considered that the buildup of the tritium inventory depends on the number of pulse operation cycles when (R/G)_{av} was saturated. Tritium recovery rate increased cycle by cycle. After about 20 cycles, the average tritium recovery rate was almost constant and the ratio (R/G)_{av} was saturated. It is considered that the number of pulse operation cycles when (R/G)_{av} was saturated, depends on the buildup of the tritium inventory.

4. CONCLUSIONS

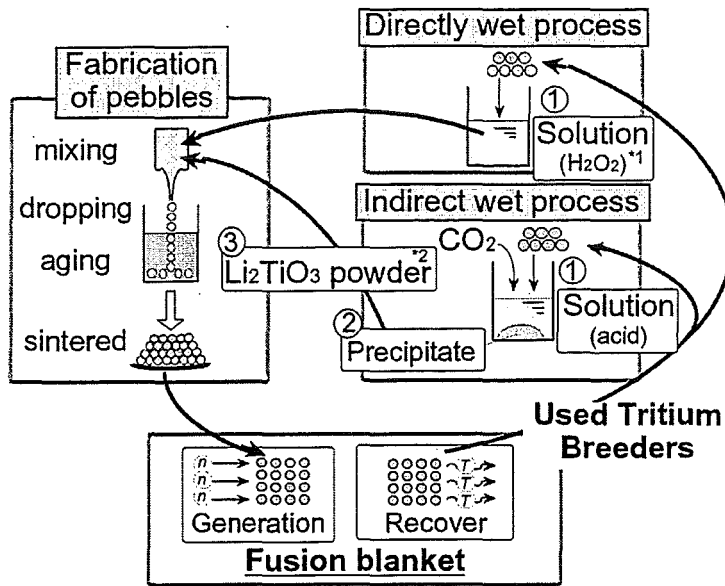
Good prospects were obtained concerning mass fabrication of Li₂TiO₃ pebbles with target diameter (φ0.2-2.0 mm) and density (80-85%T.D.) by two kinds of indirect wet processes. In the future plan, fabrication tests of Li₂TiO₃ pebbles will be carried out by the direct wet process. Additionally, high Li-burnup tests of tritium breeder pebbles will be performed for the material selection.

Two kinds of blanket in-pile mockups were developed and tritium recovery from the Li₂TiO₃ pebble bed in both conditions of the steady state and the ITER nominal pulsed operation were studied in the in-situ irradiation experiments in the JMTR. The effects of the irradiation temperature, the sweep gas flow rate, the hydrogen content, etc. were evaluated on the tritium recovery behavior from the Li₂TiO₃ pebble bed. From the results of in-situ experiments, a good prospect was obtained for the breeding blanket design using the Li₂TiO₃ pebble bed. In the future plan, tritium recovery experiments with various the pulse operation conditions will be performed, and tritium recovery behavior from the Li₂TiO₃ pebble bed will be evaluated.

REFERENCES

- [1] C.E. Johnson, K.R. Kummerer and E. Roth, *J. Nucl. Mater.*, 155-157(1988)188.
- [2] C.E. Johnson, G.W. Hollenberg, N. Roux, and H. Watanabe, *Fusion Eng. Des.*, 8(1989)145.
- [3] P.A. Finn, K. Kurasawa, S. Nasu, K. Noda, T. Takahashi, H. Takeshita, T. Tanifuji and H. Watanabe, *Proc. IEEE 9th Symp. on Engineering Problems of Fusion Research*, Vol.II, 1981, pp.1200-1204.
- [4] J.M. Miller, H.B. Hamilton and J.D. Sullivan, *J. Nucl. Mater.*, 212-215(1994)877.
- [5] P. Gierszewski, *CFFTP G-9703*(1997).
- [6] R. Roux, J. Avon, A. Floreancig, J. Mougin, B. Rasneur, S. Ravel, *J. Nucl. Mater.*, 233-237(1996)1431.
- [7] P. Gierszewski, M.D. Donne, H. Kawamura and M. Tillack, *Fusion Eng. Des.*, 27(1995)167.
- [8] K. Tsuchiya, H. Kawamura, M. Nakamichi, H. Imaizumi, M. Saito, T. Kanzawa and M. Nagakura, *J. Nucl. Mater.*, 219(1995)240.
- [9] R.A. Verrall, J.M. Miller and L.K. Jones, AECL-11768 (CFFTP G-9637), 1997.
- [10] O.D. Slagle, T. Kurasawa, R.A. Verrall, G.W. Hollenberg, *J. Nucl. Mater.*, 191-194(1992)214.
- [11] O.D. Slagle, T. Takahashi, F.D. Hobbs, K. Noda, D.L. Baldwin, G.W. Hollenberg, R.A. Verrall, *J. Nucl. Mater.*, 212-215(1994)988.
- [12] R.A. Verrall, O.D. Slagle, G.W. Hollenberg, T. Kurasawa, J.D. Sullivan, *J. Nucl. Mater.*, 212-215(1994)902.
- [13] Kwast, H., Stijkel, M., Muis, R., Conrad, R., ECN-C-95-123, (1995).

- [14] J.G. van der Laan, Stijkel, M.P., Conrad, R., JAERI-Conf 98-006, (1998)88.
- [15] J.G. van der Laan, Conrad, R., Bakker, K., Roux, N. and Stijkel, M.P., *Proc. of the 20 Symposium on Fusion Technology*, France, 1998, pp.1239-1242.
- [16] Kawamura, H., Tsuchiya, K., Nakamichi, M., Fujita, J., Sagawa, H., Nagao, Y., Gohar, Y., Ikejima, Y., Saito, T., Sakurai, S., Hisa, I., Kumahara, H. and Nemoto, N., *Proc. of the 20 Symposium on Fusion Technology*, France, 1998, pp.1289-1292
- [17] K. Tsuchiya, M. Nakamichi, Y. Nagao, J. Fujita, H. Sagawa, S. Tanaka and H. Kawamura, *Fusion Eng. Des.*, 51-52(2000)887.
- [18] T. Tone, M. Seki, A. Minato, T. Horie, T. Yamamoto, et al., *JAERI-M 87-017*, 1987
- [19] T. Kuroda, H. Yoshida, H. Takatsu, Y. Seki, K. Noda, et al., *JAERI-M 91-133*, 1991
- [20] K. Kosako, et al., *JAERI-Review 98-010*, (1998).
- [21] K. Tsuchiya, H. Kawamura, K. Fuchinoue, H. Sawada, K. Watarumi, *J. Nucl. Mater.*, 258-263(1998)1985.
- [22] K. Tsuchiya, and H. Kawamura, *J. Nucl. Mater.*, 283-287(2000)1380.



*1 : Li_2TiO_3 solution was used to directly wet process.
 *2 : Fabrication by solid-solid of Li_2CO_3 and TiO_2 powders.

Figure 1: Concept of lithium recycle.

	Fabrication Process	Photograph	Impurity	Sphericity	Cost	Mass Fabrication
Melting	 Melting Dropping (only Li_2O)	 (D=0.5~1.5mm)	E	E	G	B
Rotating	 Rolling Lithium containing ceramic powder	 (D=0.5~2.0mm)	G	G	G	G
Wet	 Mixing Dropping	 (D=0.1~2.0mm)	E	E	E	E [~150kg/y]

E : Excellent, G : Good, B : Bad

Figure 2 : Fabrication development of ceramic tritium breeder pebbles

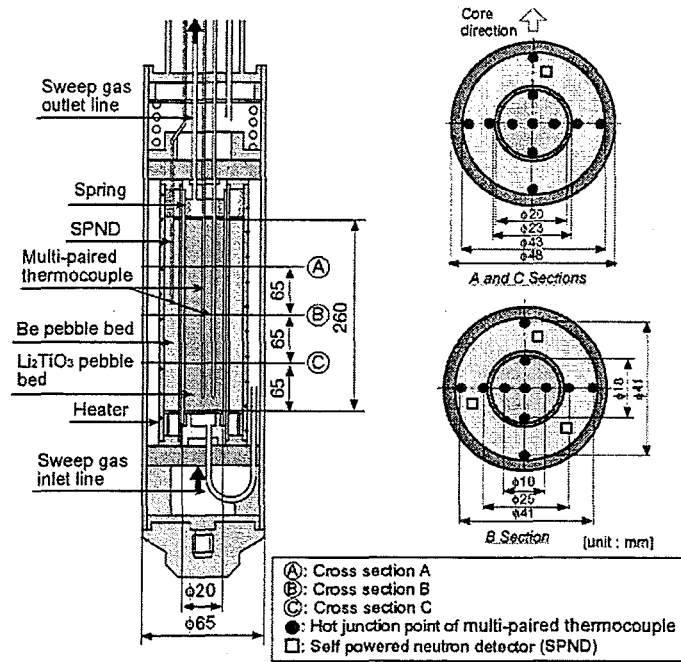


Figure 3 : Schematic diagram of the multi-layered pebble-bed mockup (ORIENT-1).

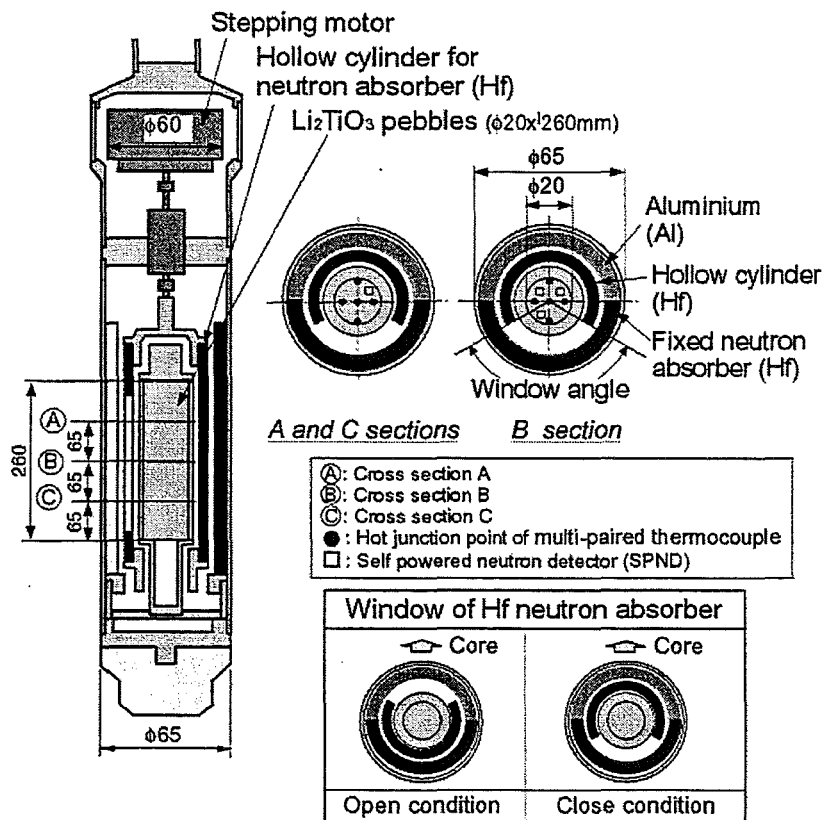


Figure 4 : Schematic diagram of the pulse-operation simulating mockup (ORIENT-2).

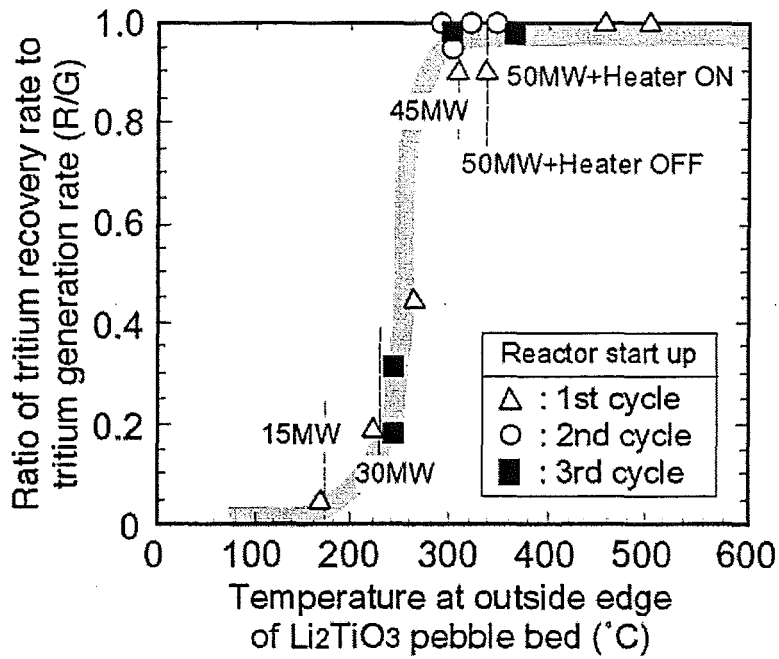


Figure 5 : Relationship between temperature at outside edge of Li_2TiO_3 pebble bed and ratio (R/G) of tritium recovery rate to tritium generation rate (R/G).

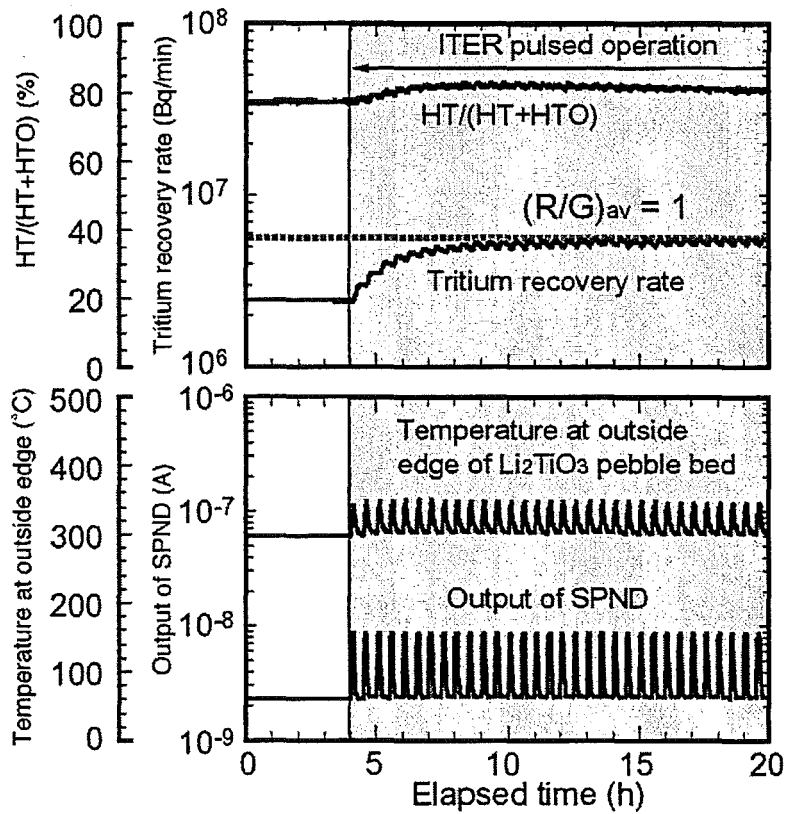


Figure 6 : Results of rotational tests under the condition of the ITER pulsed operation.

Table 1 : Characterization of two kinds of Li₂TiO₃ pebbles by the indirect wet process

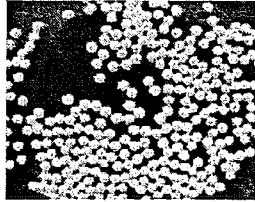
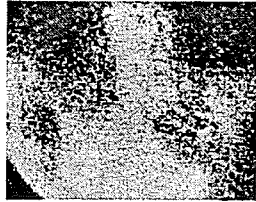
properties \ pebbles	Larger Pebbles	Smaller Pebbles
Material	Li ₂ TiO ₃	Li ₂ TiO ₃
Fabrication Method	Wet process with dehydration reaction	Wet process with substitution reaction
Diameter	φ1.7~φ2.36 mm (~φ1.9 mm av.)	φ0.25~φ0.3 mm (~φ0.27 mm av.)
Density	2.86 g/cm ³	2.82 g/cm ³
Sphericity	1.07	1.11
Grain Size	<5 μm	<5 μm
Collapse load	73 N	4.6 N
Impurity (ppm)	Ca:<2, Na:82, Al:9, Si:14	Ca:18, Na:39, Al:23, Si:73
Photograph		

Table 2 : Main material data of ceramic breeders

Items \ Materials	Li ₂ O	Li ₂ TiO ₃	Li ₂ ZrO ₃	Points
Li density (g/cm ³)	③ 0.94	② 0.43	① 0.38	×3
Thermal conductivity at 500°C (W/m/°C)	③ 4.7	② 2.4	① 0.75	×2
Thermal expansion at 500°C (ΔL/L ₀ %)	① 1.25	② 0.8	③ 0.50	×1
Reaction of water	① very	③ less	③ less	×3
Residence time at 440°C (h)	① 10	② 2	③ 1	×4
Swelling* (ΔV/V ₀ %)	① 7	③ (-)	③ <0.7	×1
Transmutation nuclides	③ ¹⁶ O(n,p):7s	② ⁴⁶ Ti(n,p):84d ⁴⁷ Ti(n,p):3.4d ⁴⁸ Ti(n,p):1.8d	① ⁹⁰ Zr(n,p):64h ⁹¹ Zr(n,p):57d ⁹² Zr(n,2n):10 ⁶ y ⁹⁶ Zr(n,2n):64d	×3
Evaluation	33	(38)	35	×

* : [⁶Li Burn up]= 3atm% (at 500°C), [Evaluation]=[point of item]•[Points]

INFLUENCE OF PEBBLE BED DIMENSIONS AND FILLING FACTOR ON MECHANICAL PEBBLE BED PROPERTIES

J. Reimann^a, D. Ericher^b, G. Wörner^a

^a Forschungszentrum Karlsruhe, PO Box 3640, D-76021 Karlsruhe, Germany

^b CEA Saclay, CEA-SPEC, F-91191 Gif/sur/Yvette, France

For the characterisation of thermomechanical properties of pebble beds, uniaxial compression tests (UCTs) are used for the determination of the strain-stress dependence, respectively, the modulus of deformation E . It is important that the results of UCTs are characteristic for blanket pebble beds.

The HCPB blanket is characterised by shallow beds which means small bed heights H compared to the other dimensions (ceramic breeder pebble beds: $H \approx 10$ mm, toroidal width ≈ 1 m; radial depth ≈ 0.5 m). Another important pebble bed quantity is the packing factor γ . Presently, blanket relevant filling procedures have not been sufficiently investigated.

Detailed UCTs have been performed at ambient temperature using different cylindrical containers (diameter D) and lithium orthosilicate pebbles (diameters $0.25 \leq d(\text{mm}) \leq 0.6$) and lithium metatitanate pebbles ($0.8 \leq d(\text{mm}) \leq 1.2$) as granular material. The influence of bed height and bed diameter on E was determined for dense pebble beds (intensively vibrated beds). For $H \approx 10$ mm, the parameter γ was varied in a wider range.

It showed that E is strongly dependent on the ratio H/D and, for orthosilicate beds, is also dependent on γ . For metatitanate beds a dependence on H/d for values $H/d \leq 10$ is observed.

In order to investigate pebble bed characteristics for relevant blanket geometries, another test section was used with a cross section of $100 \times 100 \text{ mm}^2$ and variable bed heights between 10 and 30 mm where the pebbles were filled in at one corner through a tube with a diameter of 10 mm. The UCT results agree well with those obtained with the other test containers if a homogeneous pebble distribution in the bed was reached. The achievement of homogeneous pebble distributions in blanket relevant structures requires further development work.

1. INTRODUCTION

Present ceramic breeder blanket designs are based on ceramic breeder and beryllium pebble beds. The HCPB blanket, see e.g. [1], is characterised by shallow beds which means small bed heights H (in the present design: $H \approx 10$ mm) compared to the other dimensions (toroidal width ≈ 1 m; radial depth ≈ 0.5 m).

During operation, thermal stresses arise from different thermal expansions of the pebble beds and structural materials, and from pebble bed swelling due to irradiation. The knowledge of this bed-structure mechanical interaction (BSMI) is important for the assessment of the blanket lifetime. The BSMI is predicted by finite element codes with appropriate pebble bed subroutines which as input require characteristic pebble bed properties. In this respect the strain (ϵ)-stress (σ) dependence during stress increase and stress decrease plays an important role. This strain-stress dependence is determined experimentally by uniaxial compression tests, see e.g. [2] where pebble beds with a height H are compressed by a piston in a cylindrical cavity (diameter D) in the direction of the cylinder axis and the vertical pressure p (equal to the uniaxial stress σ) and the bed strain ϵ (ratio of displacement to bed height) are measured.

Instead of using $\epsilon = f(\sigma)$, the pebble bed subroutines require the relation $E = f(\sigma)$ where E is the modulus of deformation, defined by $E = \sigma/\epsilon$. Experimentally, the following dependence is found:

$$\epsilon = A\sigma^n \quad (1a),$$

which is easily transformed to

$$E = C\sigma^m \quad (1b),$$

where, ε is given in % and E in MPa, $C = 100A$; $m = 1-n$. In general, A and C are material dependent and also change with temperature, see e.g. [2,3].

Compared to the pebble bed dimensions in the blanket, the dimension D perpendicular to the bed height in UCTs is always significantly smaller. In previous UCTs [4,5] a significantly larger bed height was used compared to in the blanket conditions. In order to obtain blanket relevant results it must be shown that that these different dimensional values do not influence the results.

In order to study the influence of bed height and diameter on the mechanical pebble bed properties a systematic investigation was performed using containers of different diameters and different bed heights and using two granular materials with different characteristic pebble diameters d : orthosilicate with a mean diameter $d=0,43\text{mm}$ and metatitanate with a mean diameter $d=1\text{mm}$.

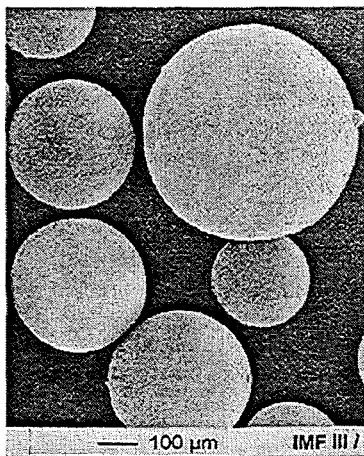
Another parameter which influences the mechanical properties is the packing factor γ , where γ is the ratio of granular material volume to total volume. It is well known that by vibration assisted filling of large cavities with granular materials packing factors of about 62% are readily achieved, quite independent of the material properties [6]. This value corresponds to a pebble arrangement dominated by a orthorhombic structure. In order to increase this value considerably, special techniques are required, e.g. ultrasonic techniques where packing factors of about 66% have been achieved in a small cylindrical cavity [5]. Up to now it is not clear which values of γ can be achieved in blanket elements or which values are desired (for very high packing factors the pebble beds become very stiff [5] and pebbles might crash). The issue of blanket relevant filling techniques has not been sufficiently discussed yet.

In the present investigations, in general, it was attempted to reach high packing factors (dense pebble beds) obtained by intense vibration. In some cases, however, the packing factor was considered as a parameter and the influence of this property on the mechanical behaviour was investigated. In order to address the issue of blanket relevant bed properties, additionally, a special test section was used with a shallow bed geometry, filled through a single pipe.

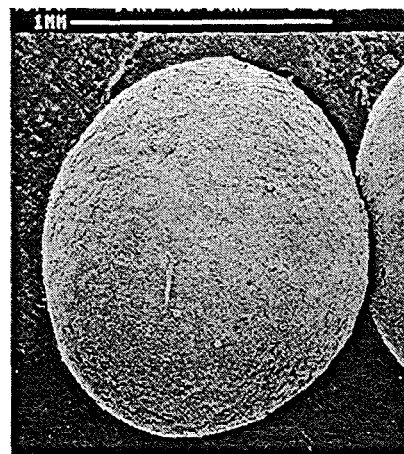
2. EXPERIMENTAL

2.1 Characterisation of Pebble Bed Materials

The orthosilicate pebbles, developed by Forschungszentrum Karlsruhe, consisted of slightly overstoichiometric lithium orthosilicate ($\text{Li}_4\text{SiO}_4 + \text{SiO}_2$) fabricated by Schott Glaswerke by melting and spraying with a gas jet. The pebbles have spherical shapes with diameters ranging from 0.25 – 0.63 mm. The mean diameter is 0.43mm. The density of the orthosilicate is 2.35g/cm^3 . After the fabrication process the pebbles have a dendritic microstructure. In order to use material which is more representative



a) FZK-orthosilicate pebbles



b) CEA-metatitanate pebbles

Figure 1. Photographs of pebbles

for the material in the blanket after some time of operation, a part of the pebbles were thermally conditioned at 1000 °C for two weeks which caused a recrystallization of the dendritic structure and resulted in grain sizes of about 50µm, for details, see [7]. The surface of these pebbles became slightly rougher due to diffusion of metasilicate to the surface, see Fig.1a. However, the present investigations proved that there is no expressed difference in the mechanical behaviour for the two types of pebbles and the data presented in the following are characteristic for both types.

The metatitanate (Li_2TiO_3), pebbles (batch CTI 1529 Ti1040) developed by CEA, were manufactured by the extrusion-spheronization-sintering process using a sintering temperature of 1050°C [8]. The pebble shapes are less spherical than the orthosilicate pebbles, some pebbles still indicate the original shape of cylindrical granules. The surface of the pebbles is rougher than those of the metasilicate pebbles, the size distribution ranges from 0.8 to 1.2 mm with a mean diameter of 1mm, see Fig. 1b. The pebbles were sintered at 1050°C; the density of the Li_2TiO_3 pebbles was 3.11g/cm³.

2.2 Test Facilities and Test Sections

The experiments described in this paper were performed at ambient temperature in different uniaxial compression test (UCT) facilities. Figure 2 (from [2]) shows schematically the set-up; the electrical furnace for experiments at elevated temperatures was not required in the present experiments. The pebble beds are compressed vertically by the piston; this pressure p (the uniaxial pebble bed stress σ) is measured by a load cell, the uniaxial bed displacements are measured by four displacement transducers, see. It proved to be very important to use more than one displacement transmitter (in the other UCT-facility three of them were used), especially for small bed heights, in order to control if the piston inclined during compression. Experimental results were discarded if for any reason significant differences between the individual displacement transmitter occurred.

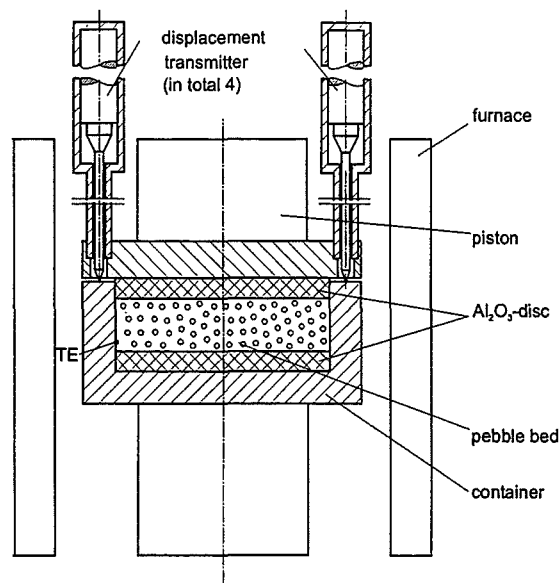


Figure 2 Test set-up for uniaxial tests

As test containers, different test sections were used:

- Test Section “T” with a diameter of 30 mm and a height of 150 mm was used to vary in a wide range the ratio H/D in order to investigate the effect of wall friction, see Fig. 3a. This test section is equipped with a strain gauge force transmitter at the bottom (effective measurement piston diameter 10mm) for the measurement of the bottom pressure. It is well known, compare e.g. [9] that due to the displacement of the transmitter membrane (30µm for full load) the local force distribution close to the measurement piston may be changed (local pebble bridging) with the effect that the measured values might be too small.
- Test Sections “S” and “N” with diameters of 60 and 90 mm. Test Section “S” with a height of $H \approx 10\text{mm}$ is being extensively used for tests at elevated temperatures [2,3], see also Fig. 2. Another test

section with $D=60\text{mm}$ and bed heights up to 60 mm was also used for heat conductance measurements using the hot wire technique [10]. Test Section "N" allows a variation of bed height up to 40mm . Test Sections "S" and "N" together with the test section described below are anticipated to investigate the influence of diameter for relatively small values of H/D where wall friction effects should be negligible.

- Test Section "B" is the test section used for biaxial experiment [11]. This test section with a rectangular cross section of $100\times 80\text{mm}$ and bed heights of 20 or 30mm was also used for UCTs.
- Test Section "F", see Fig. 3b, has been manufactured in order to study blanket relevant filling techniques. A presently favoured technique for blanket elements is the filling of the shallow bed structures through individual small pipes at the rear radial blanket region; these pipes would be required anyway for tritium removal by gas purging. Test Section "F" consists of a steel frame with an opening of $100\times 100\text{mm}^2$ and a bottom and top steel plate. By means of spacers these plates can be fixed on the frame in order to obtain bed heights between 10 and 28mm . The weight of this test section is about 30 Kg . The cavity is filled through a pipe at one corner. Due to the hexagonal shape of the test section; the test section can be placed on different sides during the vibration assisted filling. After closing the filling pipe by a screw, the test section is turned to the horizontal and positioned in a press. Then, the spacers between the upper plate and the frame are removed and an UCT is performed using the upper plate as the piston.

A special feature is that the upper steel plate can be replaced by a corresponding glass plate in order to visualise the filling process. In order to perform UCTs, the glass plate is removed after filling and replaced by a corresponding piston.

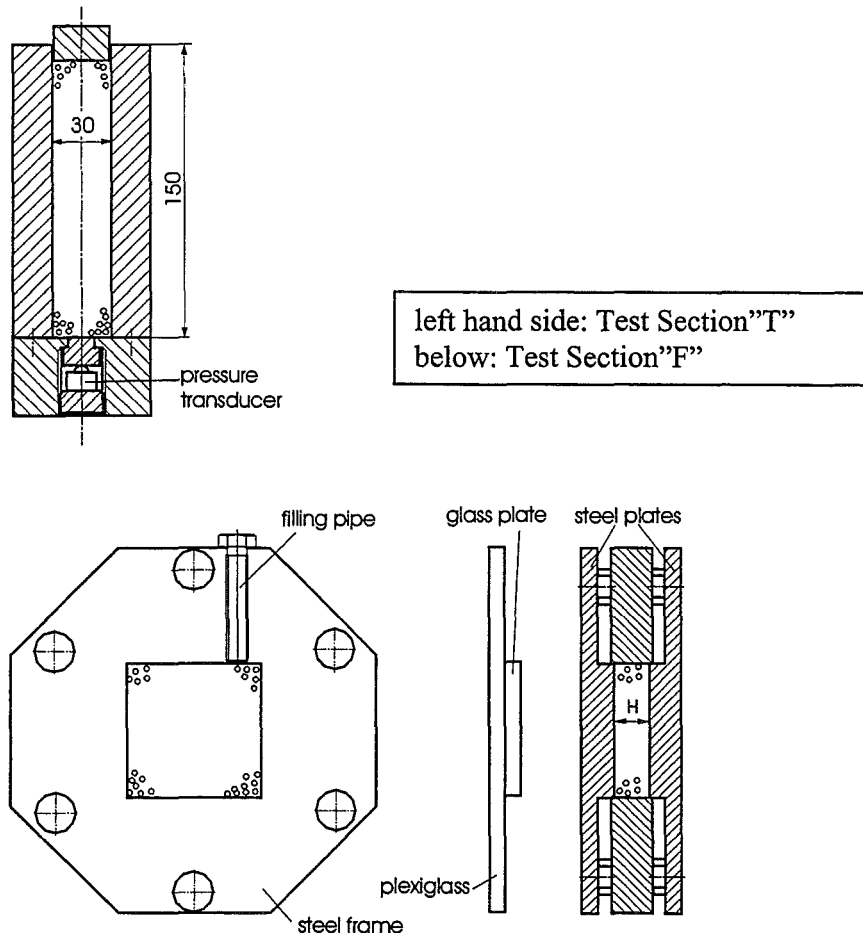


Fig.3 Schematics of Test Sections "T" and "F"

Prior to filling, the granular materials were dried in an oven at 200°C for several hours. In order to avoid the uptake of moisture, the beds were exposed as short as possible during the filling procedure to the atmosphere. Orthosilicate is much more hygroscopic than metatitanate; using the same orthosilicate pebbles for experiments during one day could influence the results, therefore, dried material was always used.

The pebbles were filled from the top in the cylindrical test sections and Test Section "B". Then a metal disc (being a part of the piston) was placed on the top and the systems were vibrated by means different mechanical vibrators where the vibration energy and amplitude were varied for the different containers in order to achieve high filling factors.

With Test Section "F" the glass plate was very helpful to optimise the filling procedure (choosing different amplitudes for the different filling steps, revolving the test section in order to fill corners etc), see Section 3.4.

As it will be seen later, there is a considerable data scattering, especially for small bed heights and for orthosilicate pebble beds. There are several reasons for this:

- the measuring inaccuracy in determining the bed height after filling by means of a slide gauge: for a bed height of $H = 10\text{mm}$ a measuring error of $\Delta H = 0.1\text{mm}$ results in an error of $\Delta\gamma \approx 0.6\%$ for packing factors slightly above 60% which is a large value taking into account the sensitivity of the mechanical properties of orthosilicate on the packing factor, see Section 3.3.
- an initial nonhomogeneous distribution in the bed or a not perfect central loading of the piston which caused an inclination of the piston during compression, as described above. This effect was much more express for orthosilicate pebble bed because the inner friction coefficient of this type of granular material is significantly smaller than for metatitanate pebble beds [10].
- moisture uptake which makes the pebble bed softer (larger strains for a given uniaxial) stress. Again this effect is much more expressed for orthosilicate pebble beds than for metatitanate pebble beds.
- pebble sedimentation: for filling of shallow beds from the top pebble segregation might occur (smaller pebbles concentrating at the bottom) and if this might influence the mechanical behaviour.

The experiments were performed in the following way: after mounting the test section in the press, the load was increased with a constant stress rate to about 4 MPa in about 5min, then the pressure (the uniaxial stress) was kept constant for 5mins. Finally, the pressure was decreased to zero in 5mins. First experiments showed that the mechanical properties did not change if the load ramp was decreased. From previous tests it was also known that a pressure of 4MPa did not cause pebble damage, therefore, the pebbles could be used for more than one experiment. Experiments where a considerable inclination of the piston occurred were discarded (measurements with $\Delta\varepsilon/\varepsilon \geq 0.5$, where $\Delta\varepsilon$ is the maximum strain difference of two displacement transducers and ε is the mean strain at maximum pressure). The data of all results are listed in the APPENDIX.

In this report, the presented results concentrate on the mechanical behaviour of pebble beds during the first pressure increase period. This period is very important for blanket operation because it determines the maximum stress build-up at the beginning of blanket operation. Data during pressure decrease and further cycles were also taken but not published in here. Results from previous experiments on the pressure decrease period are presented in [2,3].

3. RESULTS

3.1. Influence of Bed Height H

For very small bed heights, the ratio of height to pebble diameter, H/d , will effect the mechanical properties due to the fact that the pebble structure and the local packing factor are different close to the walls compared to the bulk. Generally, see e.g. [6], it is assumed that the wall influence on the packing factor becomes negligible for values H/d larger 10-20. This would mean that for blanket relevant heights of 10mm, the influence should be small for the 1mm metatitanate pebbles and negligible for the silicate pebbles. However the influence of small H/d on the mechanical properties had not been demonstrated before and will be discussed at the end of this section.

With increasing bed heights, the height to bed diameter ratio, H/D , becomes of influence due to the increasing influence of pebble friction at the cylindrical wall. Wall friction decreases the actual pressure in the bed with increasing axial distance from the piston.

Neglecting gravity and assuming a constant pressure in the bed cross section, the axial pressure distribution is described by:

$$p = p_0 \exp(-4B(h/D)) \quad (2),$$

where p_0 is the pressure (identical to the uniaxial stress σ_0) at the piston and h is the coordinate in the direction of the cylinder axis, starting at the piston. The quantity B is a friction coefficient, which depends on material properties and the filling factor.

The decrease of actual pressure with increasing h causes that the local bed strains become smaller with increasing h . By integration over the bed height H one obtains

$$\varepsilon = \varepsilon_0 \exp(-4Bn(h/D)) \quad (3),$$

where ε_0 is the strain without frictional effect which depends on the piston pressure according to Eq (1a).

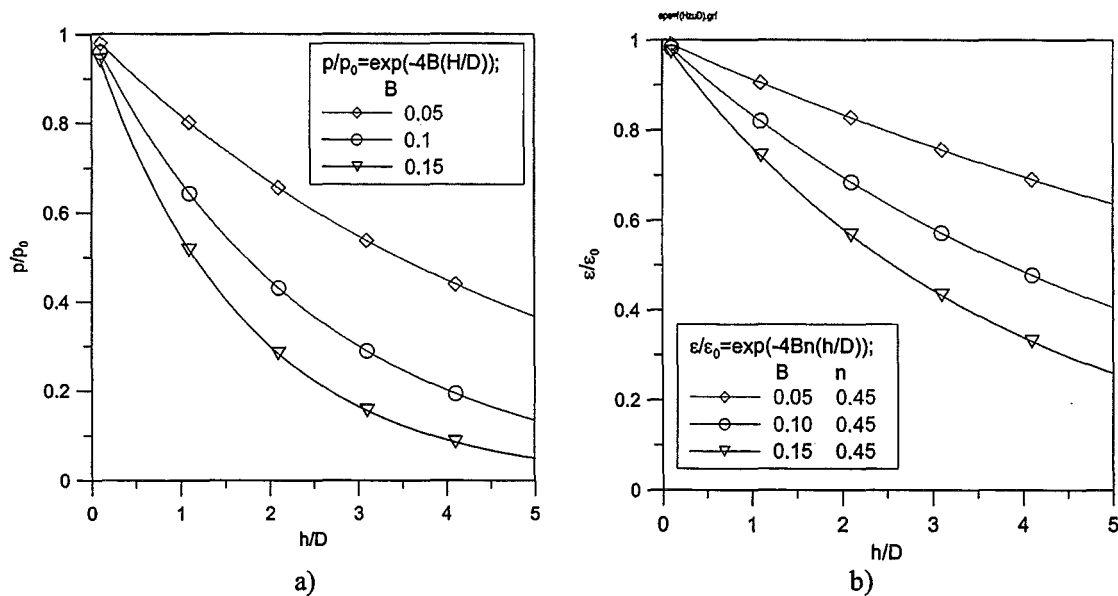


Fig.4. Calculated pressure distribution and effect on bed strains

Figure 4a shows calculated pressure distributions for different friction coefficients including the value of $B \sim 0.1$ which was assessed from previous experiments [11]. Figure 4b contains results according to Eq (3) using a value of $n=0.45$ which is also characteristic for previous experiments [2]. It is clearly seen clearly that due to the decreasing pressure the integrated bed strain becomes smaller which pretends a stiffer bed. Therefore, the ratio H/D should be significantly smaller than 1 in order to avoid a remarkable influence of wall friction.

Figure 5 contains characteristic examples for the measured pressures at the bottom of the test section and the bed strains for two UCTs performed at different bed heights. For small bed heights the difference between bottom pressure and piston pressure is not very large in contrast to the large value of H/D , see Fig. 5a. During pressure increase, the bottom pressure increases linearly with the piston pressure p_0 . During the pressure decrease phase, the influence of wall friction is clearly seen: for the small value of H/D the bottom pressure decreases much faster than for the large H/D value. Figure 5b shows characteristic results from UCTs with the softer behaviour during pressure increase (relocation of particles and elastic/plastic pebble deformation) and stiffer behaviour during pressure decrease (only elastic effects). This figure shows clearly the smaller total bed strain (stiffer behaviour) at the large value of H/D compared to the small value. Figure 5b) also demonstrates that the wall friction effects is not only influencing the bed strain during pressure increase but as well the pressure decrease curve: This curve becomes also stiffer with increasing H/D . (The linear part of the pressure decrease curves between $\approx 1\text{MPa}$ and 0MPa are due to a rapid pressure drop of the press pump).

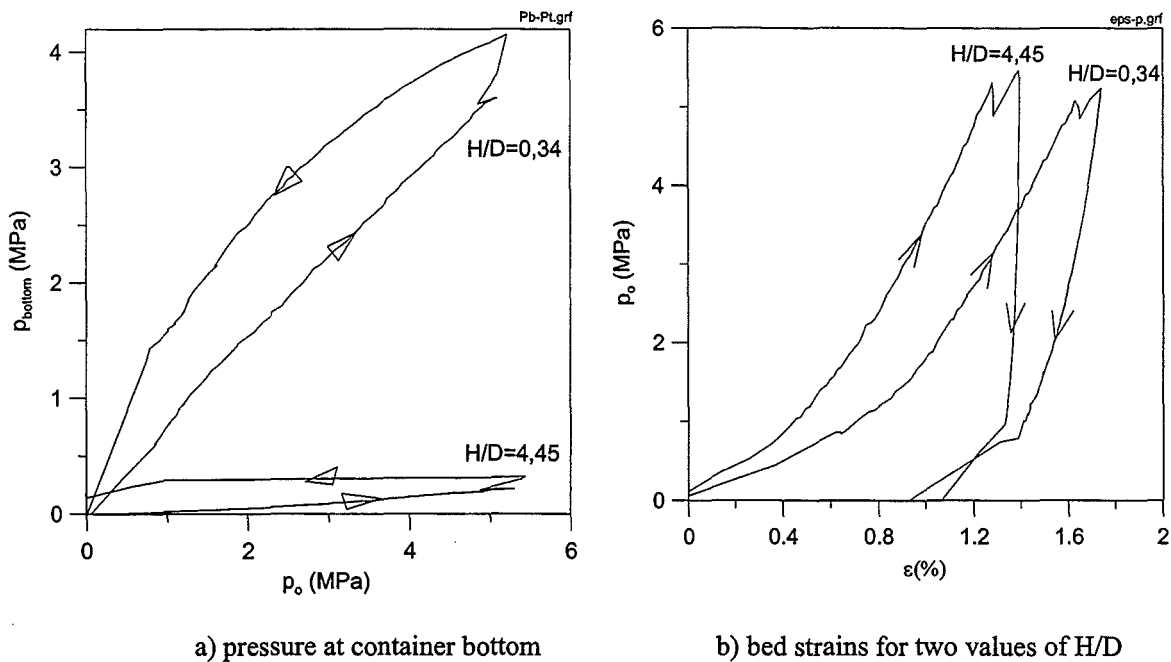


Fig.5. Measured bottom pressure and bed strains for two values of H/D (30mm test section)

Figure 6 shows the bottom pressure measurements normalised with the piston pressure as a function of H/D . The figure includes results for both granular materials using both dense beds obtained by intense vibration (orthosilicate: $\gamma = 62 \pm 0.5\%$; metatitanate: $\gamma = 60.9 \pm 0.5\%$) and loosely filled beds (orthosilicate: $\gamma = 60.9 \pm 0.5\%$; metatitanate: $\gamma = 57.2 \pm 0.5\%$). A drastic reduction of the bottom pressure is observed with increasing H/D . There is the tendency that the decrease is more expressed for titanate beds than for silicate beds. A significant dependence on the filling factor is not observed. By comparison with Fig. 3a, a friction coefficient of about 0.17 is assessed. However, it should be kept in mind that due

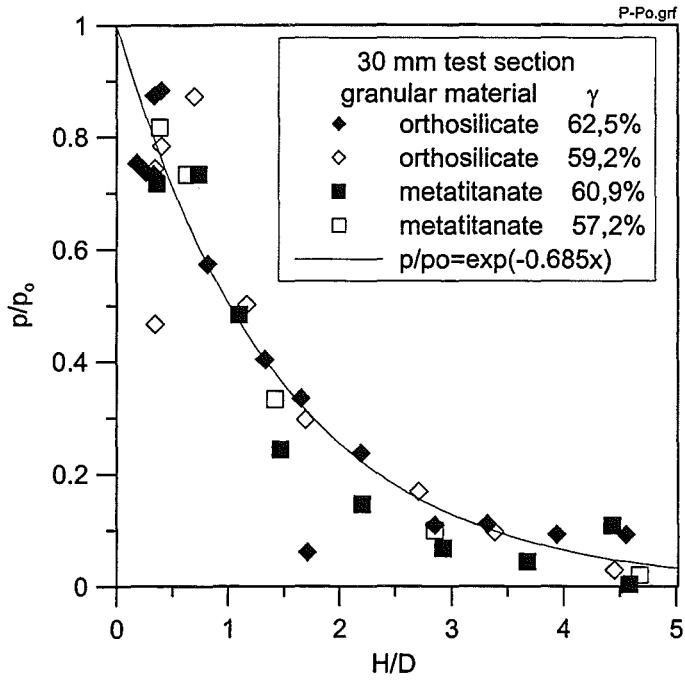


Fig.6. Measured pressure distributions $(p/p_0)=f(H/D)$

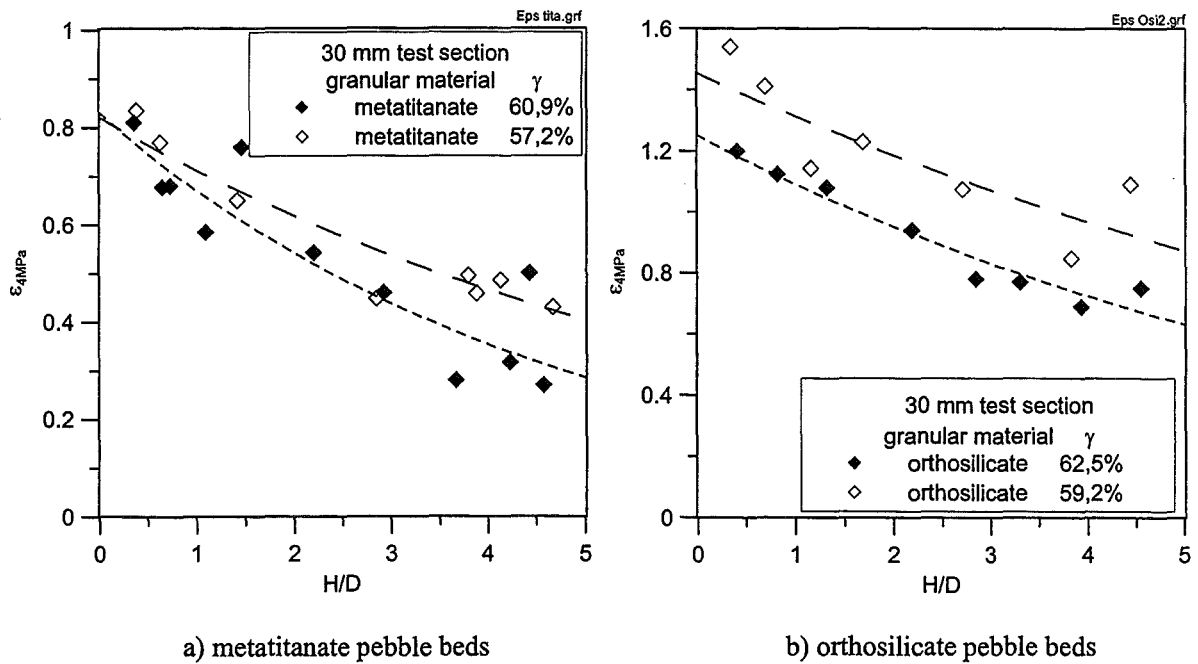


Fig.7. Measured bed strains for a piston pressure of 4MPa

to bridging effects the measured values tend to be too small which results in too high friction coefficients.

Figure 7 shows the measured strains for the maximum piston pressure of $p_0 = 4\text{MPa}$: a significant reduction with increasing H/D is also observed, for titanate beds this effect is stronger than for silicate beds. The measurements were fitted by an exponential curve in order to obtain the value ϵ_0 for $H/D = 0$. Figure 8 shows the normalised strains: by comparison with Eq(3b), friction coefficients of $B \approx 0,11$ and $B \approx 0,076$ are estimated for dense titanate beds and dense silicate beds. Here, the tendency is found that the friction factor increases with increasing packing factor.

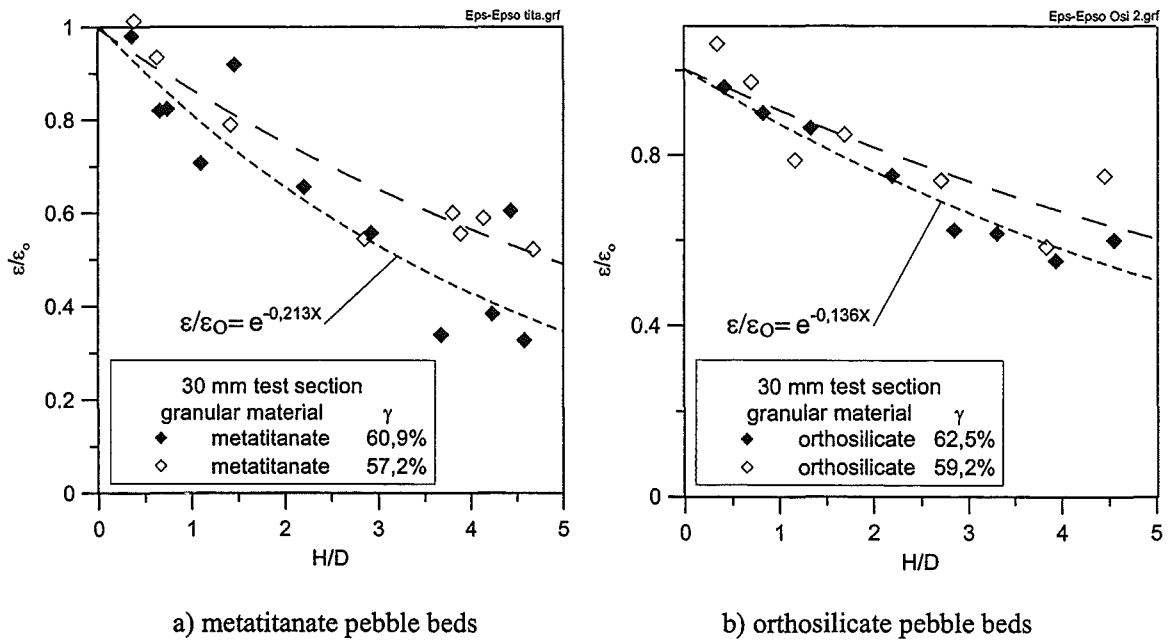


Fig. 8. Normalised bed strains for a piston pressure of 4MPa

In the following, the influence of the parameter H/d is discussed. As mentioned, this parameter becomes of influence at small values of H/D where friction effects from the circular wall can be neglected. Figure 9 shows the bed strains at 4MPa for both granular materials as a function of bed height H . These data are relevant for intensely vibrated (dense) pebble beds. There is a distinct increase below $H \approx 10\text{mm}$ for titanate pebbles with $d = 1\text{mm}$, corresponding to a value $H/d \approx 10$. For silicate beds data scattering is much larger but one can conclude that a significant effect of H/d at small heights is not observed for this material with a mean diameter of 0.43mm .

Figure 10 contains the corresponding results for the packing factor as a function of bed height for the well vibrated pebble beds. A distinct decrease of the packing factor with decreasing bed heights at $H \leq 10\text{mm}$ is not observed for the 0.4mm pebble beds (Fig. 10b) but clearly found for the 1mm pebble beds (Fig. 10a). This decrease attributed to the locally lower packing factor in the vicinity of the top and bottom walls which is more expressed for the larger pebbles (effect of H/d).

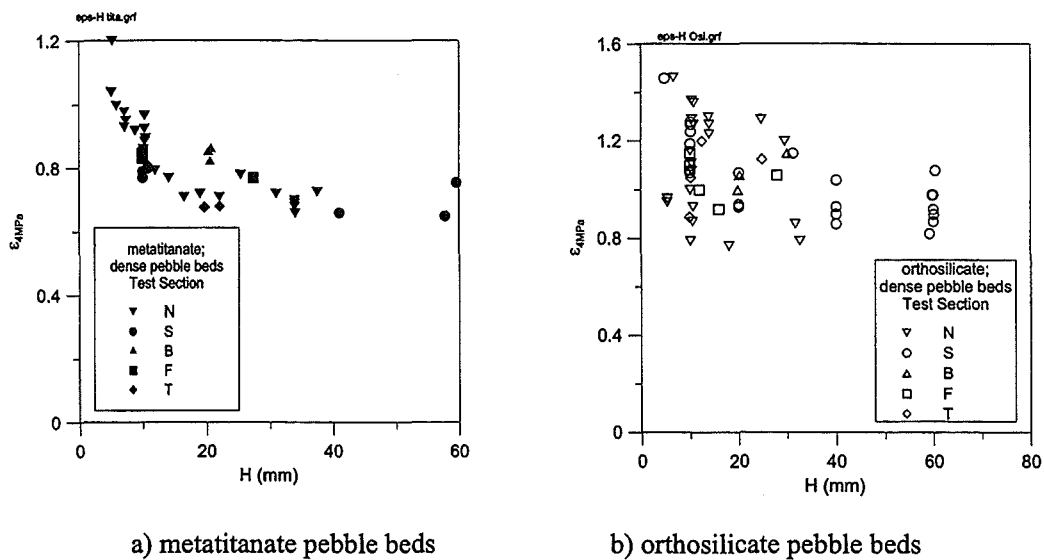
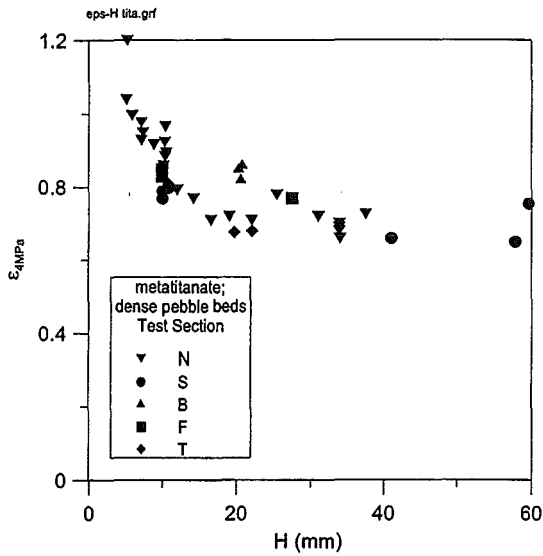
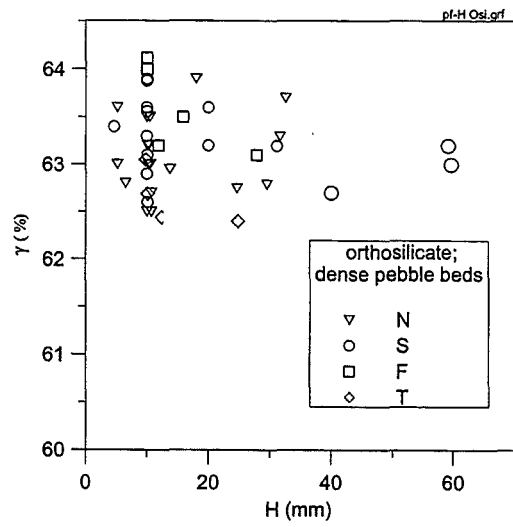


Fig. 9. Dependence of pebble bed strain on pebble diameter d and test section diameter D



a) metatitanate pebble beds

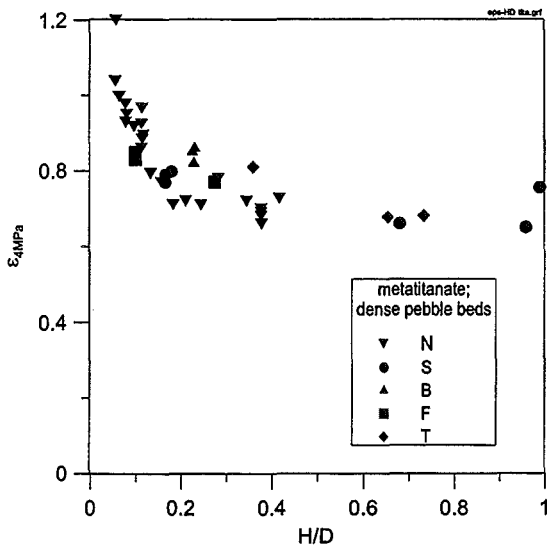


b) orthosilicate pebble beds

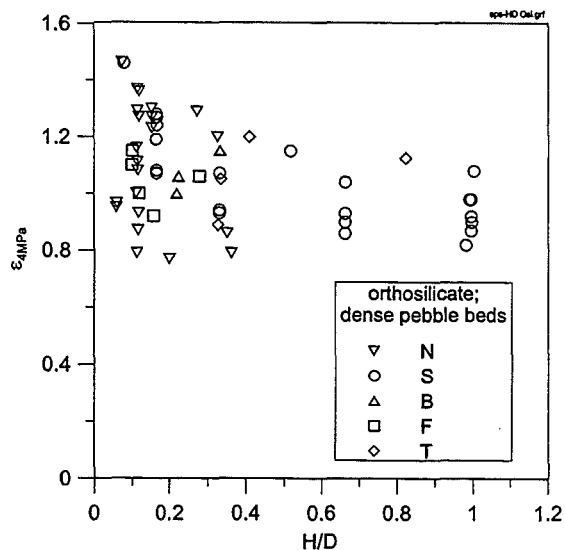
Fig.10. Dependence of packing factor γ on pebble diameter d and test section diameter D for $H/D \leq 1$

3.2. Influence of Bed Diameter D

The influence of bed diameter D on the mechanical properties is of practical interest for bed heights $H/D \leq 1$ where wall friction effects are small. Figure 11 shows the experimental results from Fig. 9 plotted as a function of H/D . For metatitanate pebble beds is clearly seen that there is no dependence on the bed diameter. For orthosilicate, the data spread is much more expressed. One reason for this is the stronger dependence of the mechanical properties on the packing factor, see Section 3.3 which is varied between 62.5 and about 64%, see Fig.10. In general, higher values of ϵ_{4MPa} are attributed to lower values of γ and vice versa. Considering this effect again one can state that there is also no diameter effect for silicate beds.



a) metatitanate pebble beds



b) orthosilicate pebble beds

Fig.11. Dependence packing factor of on pebble diameter d and test section diameter D for $H/D \leq 1$

From Fig. 10 one can also conclude that there is no dependence of the packing factor on the test section diameter. Maximum values of γ for the mechanical vibration techniques used in the present experiments are about 64% for orthosilicate pebble beds and about 62.5% for metatitanate pebble beds.

3.3. Influence of Packing Factor γ

For the blanket relevant height of $H \approx 10\text{mm}$ additional experiments were performed with loosely filled beds in order to investigate the influence of γ on the mechanical properties. Figure 11a) shows nearly no dependence of γ on $\epsilon_{4\text{MPa}}$ for titanate pebble beds. However, the variation of γ is quite small: already a modest amount of vibration results in values $\gamma \approx 62\%$. For the silicate pebble beds, Fig. 11b), the investigated γ range is larger. Again there is a considerable data scatter due to the decreased measurement accuracy at these small bed heights and the specific orthosilicate properties, discussed in Section 2.2. Nevertheless, the tendency is clearly seen that the strain $\epsilon_{4\text{MPa}}$ decreases with increasing γ .

Up to now the mechanical pebble bed behaviour during pressure increase was characterised by that strain which was obtained at a pressure of 4MPa. Of interest for the implementation in pebble bed subroutines are, compare Section 1, relationships for the modulus of deformation E of the type $E = C\sigma^m$. The present experiments show that the exponents m

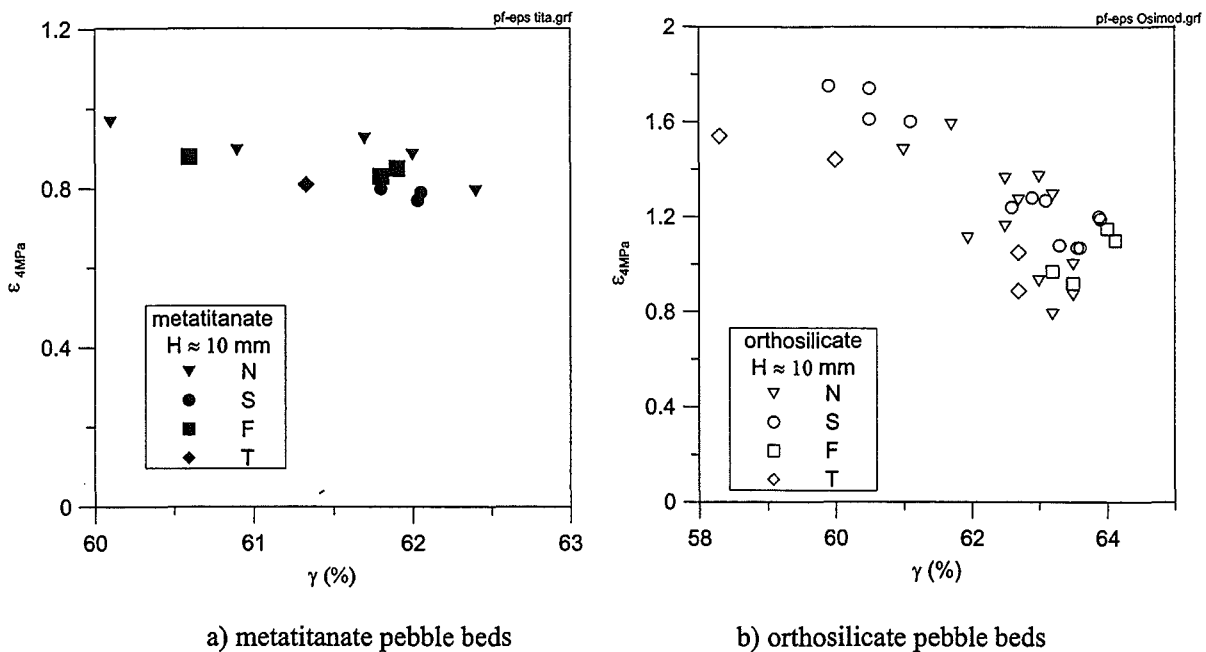


Fig.12. Dependence of pebble bed strain on packing factor for $H \approx 10\text{mm}$

are independent of γ . Then, for a constant m , the dependence of E on the packing factor can be demonstrated as $C = f(\gamma)$, see Fig. 12. For metatitanate pebble beds, C is only weakly dependent on γ for the investigated parameter range; the data are fitted by a linear relationship, see Table I. For orthosilicate pebble beds C increases significantly with increasing γ . The results for the range of packing factor between $59 < \gamma(\%) < 64$ can be fitted by the following function:

$$C = 120 + (\gamma(\%) - 59)^{2.9} \quad (59 < \gamma(\%) < 64) \quad (4)$$

For the range of practical interest for blankets ($62.5 < \gamma(\%) < 64$), C can be also expressed as a linear function of γ , see Table I.

Table I Modulus of deformation for first stress increase

Granular material	d(mm)	m	C	γ (%) range
orthosilicate (FZK)	0.25-0.6	0.45	47.5γ (%) - 2380	62.5-64
metatitanate (CEA)*	0.8-1.2	0.45	13.9γ (%) - 606	60-62.5

* CTI 1529

The values given above should not be extrapolated to packing factors considerably outside of the recommended range. The values from the present experiments predict a somewhat stiffer behaviour of the metatitanate beds compared to previous results [2,3] which were obtained using different batches of metatitanates with different pebble properties (density, surface roughness, etc). The previously proposed correlation for orthosilicate [2,3] was established for a filling factor of $\approx 62\%$. There is a good agreement with the new correlation according to Eq (4).

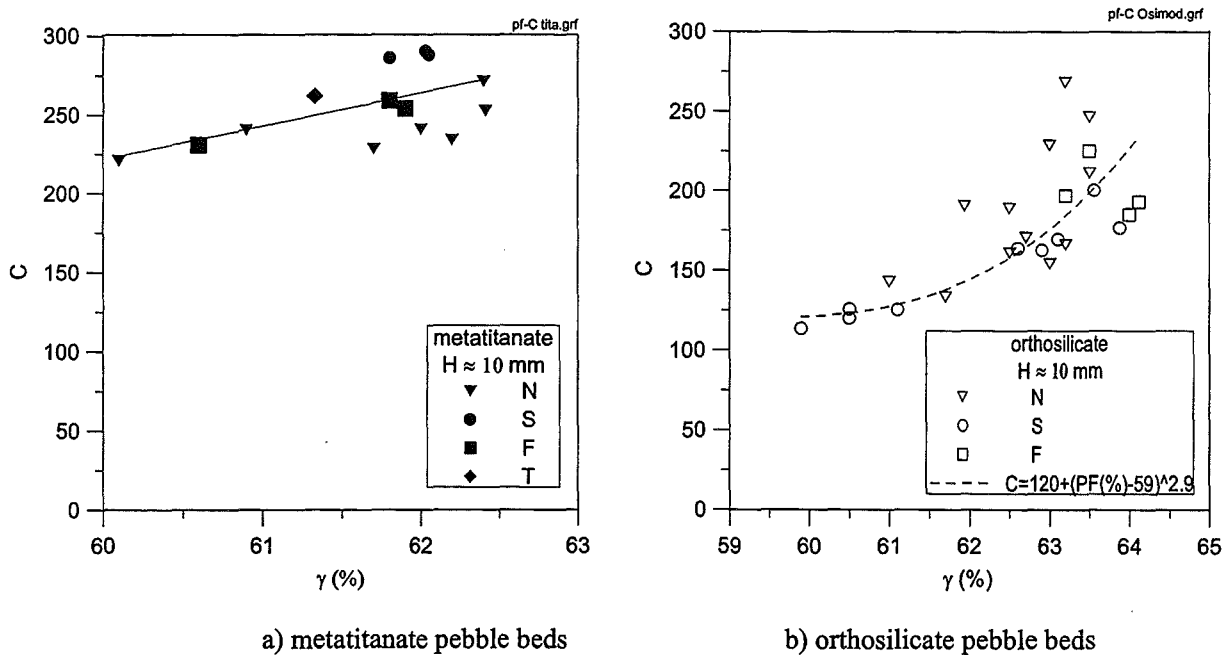


Fig.13. Dependence of C on packing factor for $H \approx 10$ mm

3.4. Filling of Blanket Relevant Cavities

The purpose of Test Section "F" was, as mentioned in Section 2, to investigate the mechanical pebble bed behaviour for blanket relevant bed geometries and filling techniques. In conventional UCT sections the bed is filled from the top side (the piston side). In the present UCTs with the circular test sections a metal disc (being a part of the piston) was placed on the top side before starting bed vibration in order in order to generate a good contact of the uppermost layer of pebbles with the piston. However, the question still existed if the local pebble bed structure is comparable to blanket conditions. Another concern for the blanket relevant filling shallow beds is if a homogeneous packing in the total bed can be achieved.

In order to optimise the filling procedure with Test Section "F", the use of the glass plate was very helpful. First, the test section was put on that side of the hexagonal structure that the filling opening was nearly at the highest point. The bed was filled assisted by mechanical vibration. As long as a free pebble bed surface existed in the cavity, already small vibration energies were sufficient to generate a circulating flow of pebbles in a part of the bed. Filling the test section in this position was not sufficient in order to fill the cavity completely. The test section had to be placed several times on different sides in order to achieve this. As soon as a filling without free pebble surface was achieved, the vibration energy was considerably increased in order to densify the bed, however, the vibration energy was kept below that level where a circulating flow of pebbles could occur (such a pebble flow is connected with locally lower packing factors). Finally, the test section was closed by the screw. The maximum filling factors of

$\gamma \approx 64\%$ obtained in this way were about the same as obtained with the other test sections, see previous figures. It was also demonstrated previously that the results from the UCTs with Test Section "F" agreed well with the other results. This is an important result because it proves that UCTs performed with relatively small cylindrical containers are representative for blanket pebble beds.

In order to investigate the homogeneity of the pebble distribution in the bed, before filling, the bottom side of the test section cavity was covered with a pressure sensitive foil (FUJI PRESCALE FILM). Figure 14a) shows that for the optimised filling procedure a fairly homogeneous distribution is obtained in the total bed including the zones close to the side walls.

As described above, the maximum packing factors were achieved by a visually controlled filling procedure with varying vibration energies and changing test section positions. Using this optimised filling procedure, the same high packing factors were also obtained if the glass plate was covered with a piece of cardboard (blind filling).

Using the same filling procedure but replacing the glass plate by the steel plate, only filling factors of $\gamma \approx 62\%$ were achieved. Figure 14b) shows the corresponding pebble distribution: There are distinct zones with smaller pebble densities. UCT's with these kinds of beds resulted in smaller strains compared to homogeneously filled beds with the same packing factor. A nonhomogeneous pebble distribution was also detected by different values of the displacement transmitter signals.

The exchange of the plates caused a significant change of the test section weight which would have required another optimisation of the vibration procedure. This optimisation would have been more difficult to develop because a direct optical control is not possible. For the pebble bed geometries relevant for blanket components the achievement of homogeneous pebble distributions is, therefore, not trivial.

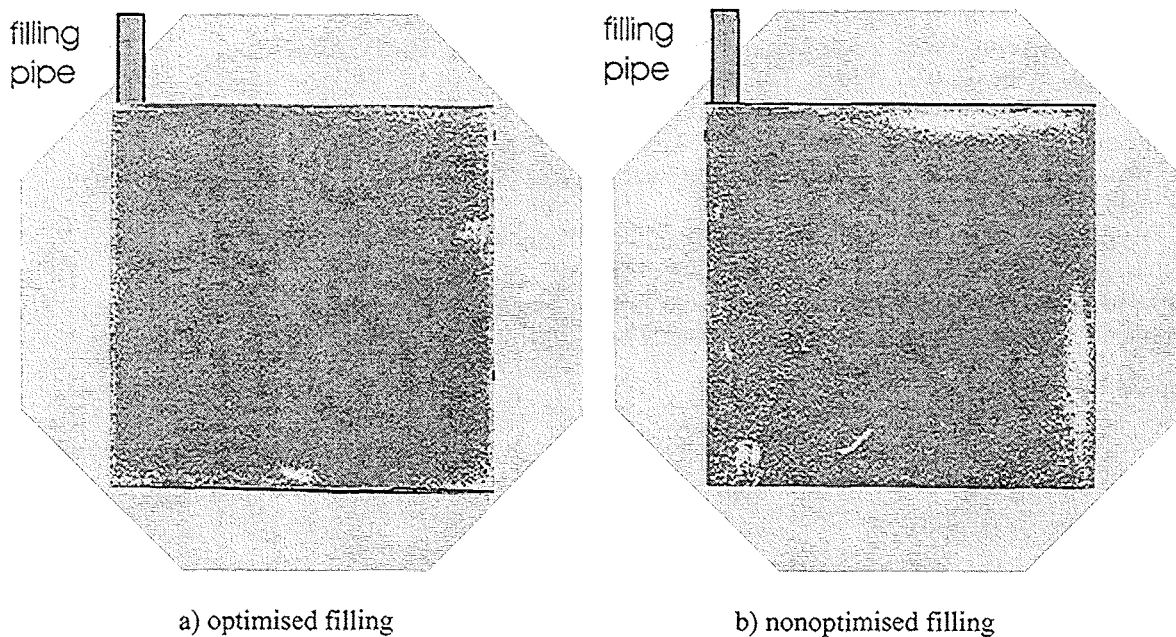


Fig. 14. Pebble distribution in Test Section "F"

4. CONCLUSIONS

For the generation of a data base on thermomechanical properties of pebble beds uniaxial compression tests (UCTs) play an important role. These UCTs must be appropriate for blanket relevant pebble beds characterised by shallow beds.

It has been shown that a very important requirement is that the UCT test sections have a height to diameter ratio of $H/D \leq 1$ in order to avoid influences due to wall friction on the mechanical pebble bed behaviour both during the pressure increase and pressure decrease period.

For $H/D \leq 1$ it has been demonstrated that test section diameters as small as at least 60mm do not influence the results for the investigated granular materials with maximum pebble diameters of $d \approx 1\text{mm}$.

It has been shown that for $H/d \leq 10$ an influence of the pebble diameter on the packing factor and the mechanical pebble bed behaviour occurs.

It has been demonstrated further that results from UCTs with a blanket relevant bed geometry and filling system agree well with standard UCTs where the pebbles are filled from the top if a homogeneous pebble distribution in the bed is obtained.

REFERENCES

- [1] S. Hermsmeyer, U. Fischer, K. Schleisiek, Improved helium cooled pebble bed blanket, : HCPB blanket, 21th SOFT 2000, Madrid, Spain, Sept.11-15, 2000.
- [2] J. Reimann, G. Wörner: Thermal creep of Li_4SiO_4 pebble beds, 21th SOFT 2000, Madrid, Spain, Sept.11-15, 2000.
- [3] J. Reimann, G. Wörner: Thermal creep of ceramic breeder pebble beds, CBBI-9, Toki, Japan, Sept.27-29, 2000.
- [4] A. Ying, Z. Lu, M. A. Abdou, Mechanical behaviour and properties of solid breeder blanket packed beds; ISFNT-4, Tokyo, Japan, April 1997.
- [5] G. Dell'Orco et al., Optimization of the filling for the improvement of the performance of reference ITER/DEMO ceramic and beryllium pebble beds, Proc. 14th Top. Meeting on Technology of Fusion Energy, Vol.39, Nr. 2, Part 2 Fuste 8 (3) ,p.644-648, Park City Oct. 15-19, 2000.
- [6] R. K. McGeary, Mechanical packing of spherical particles, J. Am. Ceram. Soc., 44 10, 513, 1961.
- [7] G. Piazza, M. Dalle Donne, H. Werle, E. Günter, R. Knitter, N. Roux, J.D. Lulewicz, Long Term Annealing of Ceramic Breeder Pebbles for the HCPB DEMO Reactor, Proc. of the CBBI-7, Petten, The Netherlands, September 14-16, 1998.
- [8] J.D.Lulewicz, Advances in the pre-industrial fabrication of Li_2TiO_3 pebbles by the extrusion-speronization-sintering process, CBBI-9, Toki, Japan, Sept. Sept.27-29, 2000.
- [9] L.Vanel, E.Clement, Pressure screening and fluctuations at the bottom of a granular column, Eur. Phys. J. B 11, 525-533 (1999).
- [10] J Reimann, S. Hermsmeyer, Thermal conductivity of compressed ceramic breeder pebble beds, CBBI-10, Karlsruhe, Germany, Oct. 22-24, 2001.
- [11] S. Hermsmeyer, J. Reimann, Particle flow of ceramic breeder beds in biaxial compression experiments, CBBI-10, Karlsruhe, Germany, Oct. 22-24, 2001.

THERMAL CREEP OF METATITANATE PEBBLE BEDS

J. Reimann¹⁾; J.-D. Lulewicz²⁾; N. Roux²⁾; G. Wörner¹⁾

1) Forschungszentrum Karlsruhe, Institut für Kern- und Energietechnik,
P.O. Box 3640, D-76021 Karlsruhe, Germany

2) CEA Saclay; DRT/DECS/SE2M/LECMA; F-91191 Gif/sur/Yvette, France

Present ceramic breeder blanket designs are based on ceramic breeder and beryllium pebble beds. During operation, thermal stresses arise from different thermal expansions of the pebble beds and structural materials, and pebble bed swelling due to irradiation. Thermal creep of pebble beds will partly release the build-up of stresses, might improve heat transfer due to increased contact areas between the pebbles and might compensate a further stress build-up due to irradiation induced swelling. On the other hand, plastic pebble deformation might cause gap formation during blanket shutdown and heat-up phases. The knowledge of the thermal creep behaviour, therefore, is important for the blanket design.

Previous experiments showed that the thermal creep behaviour differed significantly for two types of metatitanate pebble beds differing only by grain size. In this paper, results of detailed experiments are presented using other batches of metatitanate pebbles developed by CEA and JAERI. These granular materials differed in sintering temperature, grain size and density. The experiments were performed in an uniaxial test facility with a maximum pressure of 8MPa and a maximum temperature of 850°C.

It was confirmed again that thermal creep strains are the largest for materials with very small grains. Creep strains also tend to increase with decreasing pebble density. Thermal creep of the group of the materials with small creep rates can be described sufficiently well by the correlation proposed previously. For materials with larger creep rates in a second creep regime, data are also presented to be used in codes to describe the thermomechanical pebble bed behaviour.

1. INTRODUCTION

In recent papers [1,2], results of investigations on pebble bed thermal creep for three types of ceramic breeder pebbles were presented: orthosilicate pebbles from FZK with pebble diameters d between 0.25 to 0.6mm, metatitanate pebbles ($d \approx 1$ mm) from JAERI (denominated in Table II as Ti-I) and two different types of metatitanate pebbles ($d \approx 1$ mm) from CEA. The CEA metatitanate pebbles originated from the same batch. The granular material denominated in Table II as Ti-D was used as received in the thermal creep experiments whereas Ti-D Ita was investigated after being subjected to a long time annealing test for 3 months at 970°C [3] during which the grain size of the material increased considerably.

The experiments [2] showed a similar creep behaviour for orthosilicate, Ti-I and Ti-D Ita whereas thermal creep was much larger for Ti-D at large creep times, see Fig. 1. The first three materials have in common quite large grain sizes g_s (orthosilicate pebbles $g_s \approx 50\mu\text{m}$; for other granular materials, see Table II) whereas Ti-D is characterised by grain sizes of 1-2 μm .

The previous investigations work concentrated on the materials with large grains. Normally, creep data are plotted as a function of time where the time axis starts when σ_{max} is reached, see Fig. 1a. In such a plot the slopes of the curves first are changing and become constant for large times. However, it was already demonstrated earlier for orthosilicate [1] that by taking into account the initial creep during the stress increase period the thermal creep strain becomes proportional to t^n for approximately the total creep period. It showed that the exponent n is independent of temperature. In [2] it was demonstrated that such

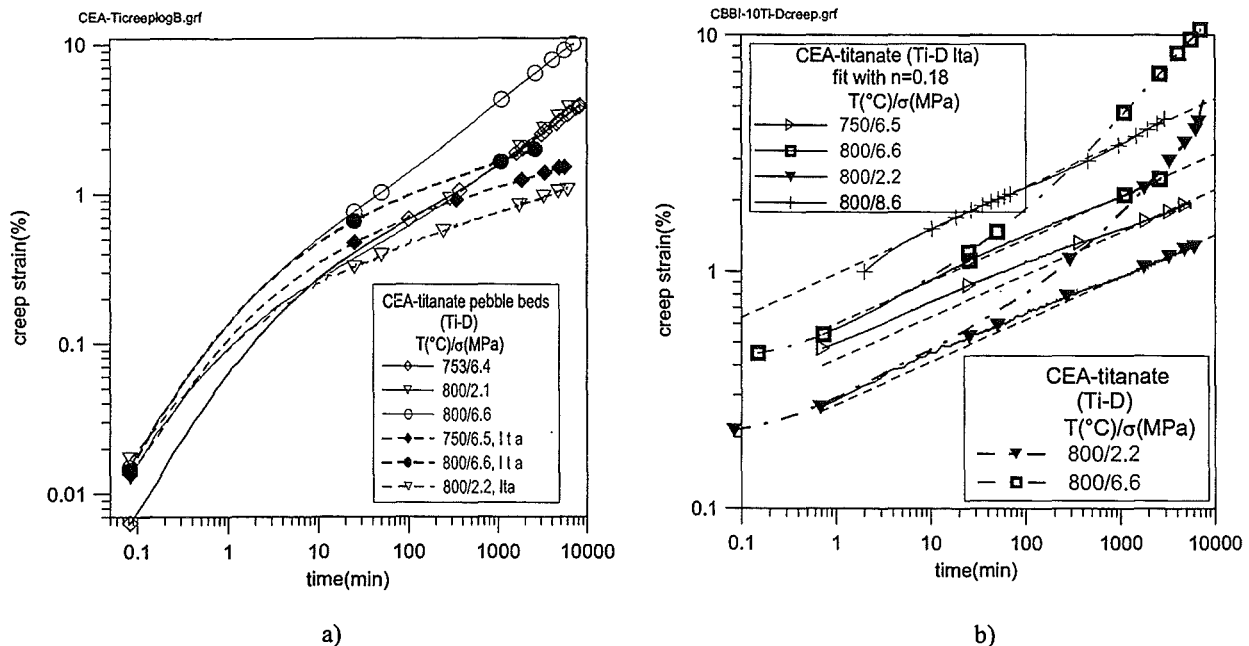


Figure 1. Thermal creep strains of CEA metatitanate Ti-D before and after long term annealing tests (from [2])

Table I Thermal creep correlations (from [2])

Granular material	$\epsilon_{cr}(t) = A \exp(-B/T(K)) \sigma(\text{MPa})^p t(\text{s})^n$			
	A	B	p	n
FZK-Li ₄ SiO ₄	12.12	10220	0.65	0.2
CEA-Li ₂ TiO ₃ (lta)	0.67	7576	0.65	0.18
JAERI-Li ₂ TiO ₃	0.37	6947	0.65	0.19

a behaviour exists also for the titanate pebbles with large grain sizes, compare Fig. 1b. Table I (from [2]) contains the proposed thermal creep correlations for the materials with large grain sizes.

Figure 1b again demonstrates the different behaviour of Ti-D: there is a characteristic change in the slope after about hundred minutes of creep time, indicating that a different creep mechanism becomes dominant. Further experiments with Ti-D in the frame of the present investigations show clearly that the slopes of the curves in this "second creep regime" are temperature dependent as outlined in Section 3.3.

One goal in the optimisation of the manufacturing process of the CEA metatitanate pebbles was to obtain pebbles with small grain sizes in order to facilitate tritium release. Other aims were a high pebble density in order to reach a high Li content and a large crush load of the pebbles. From the manufacturing procedure[4], the sintering temperature T_s is an important parameter; increasing T_s generally increases the grain size and density. Density can also be adjusted by adapting the composition of the extrusion paste (example of the latter is Ti-E and Ti-G). Since some metallic impurities, even at the 10 ppm level, act as sintering aids, the decrease of the amount of these impurities was one objective of the optimisation of the fabrication process. This required to increase T_s in order to maintain the density. Because of the recent creep strain results the question now arises if one should aim at very small grain sizes if it shows that large creep rates are unfavourable.

In this paper experimental thermal creep results are presented for new batches of CEA metatitanate pebbles where the manufacturing parameters were varied in such a way to obtain different grain sizes and pebble densities. Additionally, experiments were also performed with new batches of JAERI metatitanate pebbles (diameters of 2mm and 1mm) produced by different techniques.

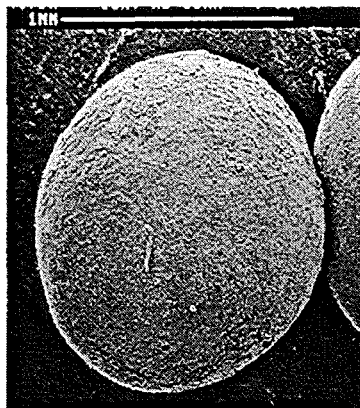
2. EXPERIMENTAL

2.1 Characterisation of pebble bed materials

Table II shows characteristic values of the investigated pebbles. Both CEA and JAERI pebbles are non-stoichiometric metatitanates but their exact composition is slightly different. The CEA metatitanate

Table II. Characterisation of investigated metatitanate pebbles

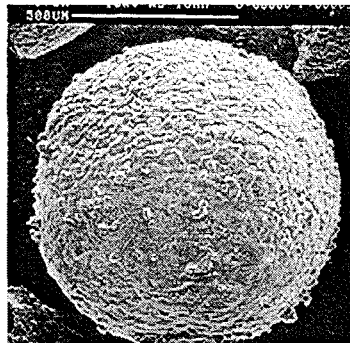
Type	Association	pebble diameter d(mm)	density ratio δ (%)	Grain size gs(μ m)	sint. temp. T_s ($^{\circ}$ C)
TiA	CEA	0.8-1.2	94,9	1.5-2.5	1050
Ti-B	CEA	0.8-1.2	83,1	0.5-1	950
Ti-C	CEA	1.1-1.5	93		1100
Ti-D	CEA	0.8-1.2	90	1-2	1050
Ti-D Ita	CEA	0.8-1.2	92	50	1050
Ti-E	CEA	0.8-1.2	86	1-5	1100
Ti-F	CEA	0.8-1.2	90	2-7	1140
Ti-G	CEA	0.8-1.2	89	1-5	1100
Ti-H	CEA	0.7-1.0	91	1-3	1100
Ti-I	JAERI	0.85-1.15	92	10-50	1200
Ti-J	JAERI	2	84	1-3	1200
Ti-K	JAERI	1	83	1-3	1200



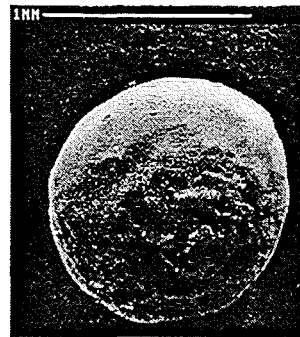
a) Ti-D



b) Ti-H



c) Ti-I



d) Ti-K

Figure 2. Photographs of pebbles

pebbles were manufactured by the extrusion-spheronization-sintering process [4]. The pebble shapes are mostly fairly spherical, however, some pebbles still show the original shape of cylindrical granules. The surface of the pebbles is slightly rough. Figure 2a shows pebbles of the Type Ti-D with a mean diameter of ≈ 1 mm. Pebbles from other batches, see Table II, differed slightly in shape and roughness. The pebbles with diameters between 0.7 and 1 mm (Ti-H), (Fig. 1b), are more spherical than those with larger diameters.

The JAERI metatitanate pebbles from batch Ti-I (Fig 2c) were manufactured by the rotating granulation method with pebble diameters between 0.85 and 1.2 mm [5]; the surface is significantly rougher than those of the CEA pebbles. The pebbles from batches Ti-J and Ti-K (Fig.2d) were manufactured by the wet process [6] with somewhat smaller surface roughnesses than those of Ti-I.

Important pebble properties are, as already mentioned, pebble density and grain size. The pebble density is expressed in the following by the ratio $\delta(\%)$ of actual pebble density to the density of metatitanate (3.43 g/cm^3 for non-stoichiometric metatitanate). Open porosity was measured by the mercury intrusion method or porosimetry. Closed porosity was measured by helium pycnometry. Taking into account both open and closed porosity, pebbles density is determined. The accuracy is 0.01 g/cm^3 on the density, which results in an error of $\approx 0.3\%$ in the determination of pebble density. Scanning Electron Microscopy was used for evaluation of grain size of the pebbles by image analysis.

2.2 Testing

The experiments were performed in the uniaxial compression test (UCT) facility, described previously [1,2], which consists of a hydraulic press and an electrical 3-zone furnace (Fig.3). The pebbles were filled in a cylindrical container with an inner diameter of $D = 60$ mm using Al_2O_3 top and bottom discs, the bed heights were adjusted to about $H = 10$ mm. This bed height is characteristic for blanket conditions; it was recently demonstrated [7] that the ratio of H/D should be significantly smaller than unity in order not to influence the results by pebble friction at the cylindrical container wall.

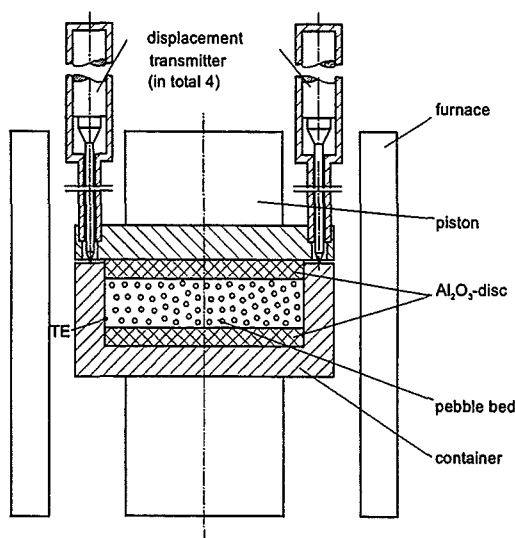


Figure 3. Test set-up for uniaxial compression tests and creep tests

For fusion reactor blankets, dense pebble beds (large packing factors γ), are of interest. In order to achieve this, the pebble beds were mechanically vibrated. Table I shows the obtained packing factors γ . The differences are primarily caused by different pebble shapes and surface conditions. The vertical pressure p on the pebble bed, equal to the uniaxial pebble bed stress σ , was measured by a load cell; the uniaxial bed displacements were measured by four displacement transducers. The uniaxial strain is the ratio of the mean displacement to bed height. The present experiments were carried out at temperatures up to 800 °C and pressures up to 9 MPa. During the pressure increase period the load ramp was in general

1MPa/min; maximum creep time periods were about one week. This is a small time period compared to conventional creep experiments using homogeneous materials. However, for blanket pebble beds smaller time periods might be of prime interest due to significant stress relaxation processes occurring already at small creep times [8].

3. RESULTS

3.1 Stress-strain dependence

Figure 4 shows for some granular materials the stress(σ)-strain(ϵ) dependences measured by UCTs. The differences of the curves for the different materials are primarily caused by the different pebble shapes and surface conditions. The most important parts of the curves are those for the first stress increase. As characteristic values, the strains measured at $\sigma = 4\text{MPa}$ are listed in Table III both for ambient temperature and 750°C . For ambient temperature, the stress(σ)-strain(ϵ) dependence differs most for Ti-I which is characterised by a much softer behaviour (larger strain for constant stress) probably due to the larger surface roughness connected with a smaller filling factor. At high temperatures, the beds become softer, compare Table III, partially due to creep occurring during the stress increase phase. For the thermomechanical description of blanket elements it was proposed previously [1,2] to neglect this temperature dependence in the stress-strain relationship but to take it into account in the thermal creep correlation.

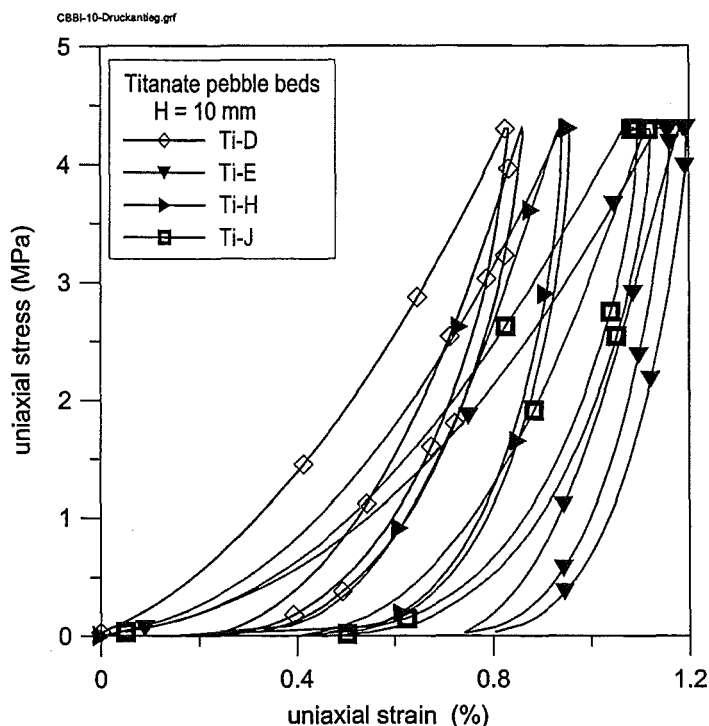


Figure 4. Stress-strain dependence of first stress increase at ambient temperature.

The functional relationship between σ and ϵ can be converted to the form $E = \sigma/\epsilon = f(\sigma)$ where E is denominated as modulus of deformation. This module E is often experimentally fitted by an expression of the type

$$E = C\sigma^m \quad (1).$$

The values for the constant C and the exponent m are different for the different types of pebbles and are additionally dependent on the packing factor γ (C increases with γ). Different values were proposed in the

Table III: Characteristic results

Type	pebble diameter d(mm)	density ratio δ (%)	grain size gs(μ m)	sintering temp. T_s ($^{\circ}$ C)	packing factor γ (%)	ϵ_{4MPa} (%)		C	creep rate
						25 $^{\circ}$ C	750 $^{\circ}$ C		
TiA	0.8-1.2	94.9	1.5-2.5	1050	60	1.27	1.35	172	medium
Ti-B	0.8-1.2	83.1	0.5-1	950	61.4	1.34	2.0	160	large
Ti-C	1.1-1.5	93		1100			1.76		small
Ti-D	0.8-1.2	90	1-2	1050	63	0.8	1.15	268	medium
Ti-D lta	0.8-1.2	92	50	1050	65.4	0.97	1.2	220	small
Ti-E	0.8-1.2	86	1-5	1100	63.2	1.05	1.4	205	medium
Ti-F	0.8-1.2	90	2-7	1140	62	0.95	1.52	225	small
Ti-G	0.8-1.2	89	1-5	1100	62	0.98	1.66	219	small
Ti-H	0.7-1.0	91	1-3	1100	64.4	0.85	1.35	251	small
Ti-I	0.85-1.15	92	10-50	1200	57	1.55	1.8	138	small
Ti-J	2	84	1-3	1200	64.3	0.94	1.3	230	medium
Ti-K	1	83	1-3	1200	64.8	1.11	1.18	195	small

past [1,2] for specific materials. Very recently [6], detailed experiments were performed with Ti-D and a correlation was established where as exponent a value of $m=0.45$ was determined and C was expressed as a function of γ . Table III shows the values of C for the investigated granular materials, again assuming $m=0.45$. Although C is dependent on pebble properties; the tendency that C increases with γ can be observed.

3.2 Thermal creep

The following figures show creep strain as a function of creep time; the initial creep strain occurring during stress increase[1,2] is taken into account. Log-log plots are used because then, the relation $\epsilon_{cr} \sim t^m$ corresponds to curves with a constant slope. Figure 5 shows results for Ti-E characterised by larger grains compared to Ti-D, see Table III. Again, two characteristic creep regimes are observed: the first which is

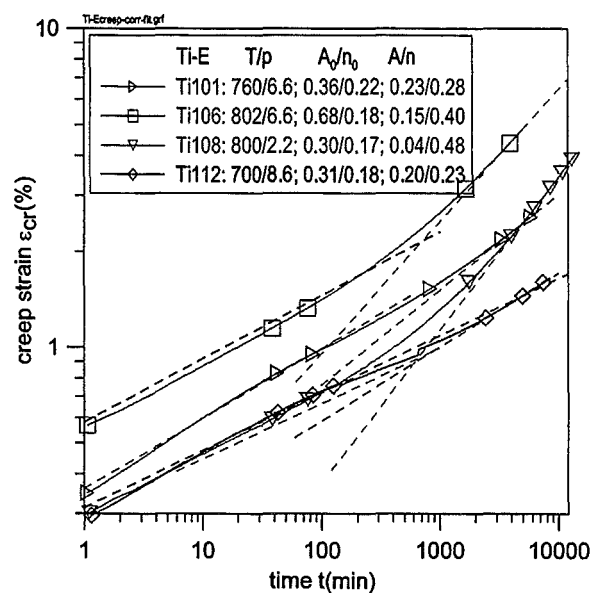


Figure 5. Thermal creep of Ti-E at different temperatures

identical with that creep regime which is observed for the large grain sizes materials and a second one which starts at about 100min and where the creep strain again follows a power law but with a larger exponent. This figure demonstrates that the slopes in this "second creep regime" are strongly temperature dependent. The legend of Fig. 5 contains the values of the exponents n both for the first regime (exponent n_0) and the second regime. It shows that for Ti-E the exponent in the first regime is again quite close to 0.18 as found for the materials with large grains.

Figure 6 contains data for larger creep times for the different materials at 750°C. The pebble bed consisting of Ti-B pebbles creeps by far the largest. This granular material is characterised by the lowest sintering temperature, a low density and the smallest grains. The lowest creep strains are observed for Ti-D Ita but the creep strains of batches Ti-F, Ti-G, Ti-H and Ti-I are quite close to those of Ti-D Ita. There are three granular materials with somewhat higher creep strains: Ti-D, Ti-E and Ti-J.

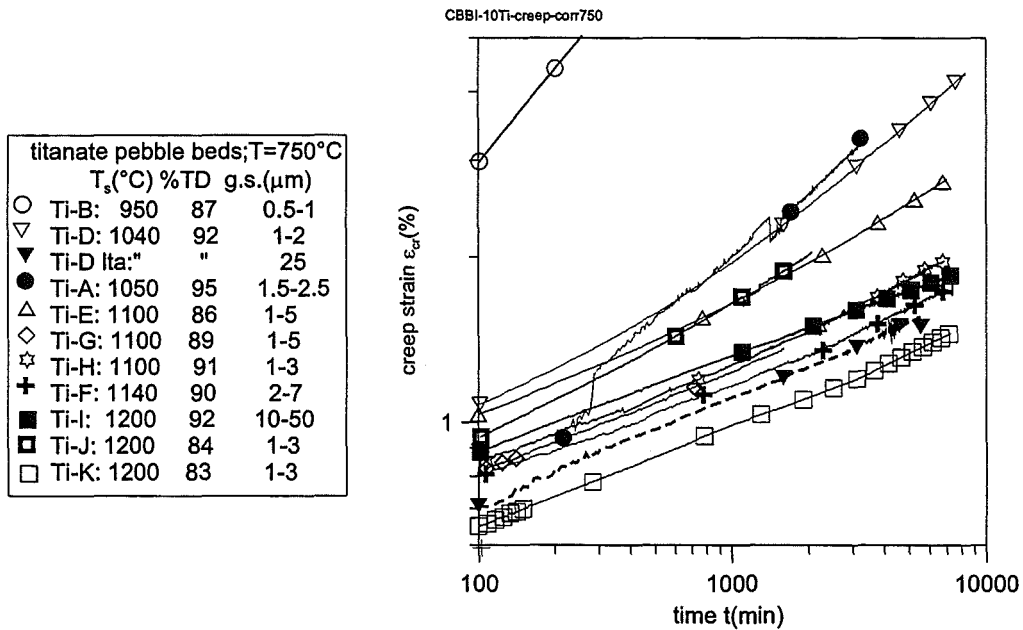


Figure 6. Thermal creep strain at large creep times of metatitanate pebble beds at 750°C and 6.6MPa

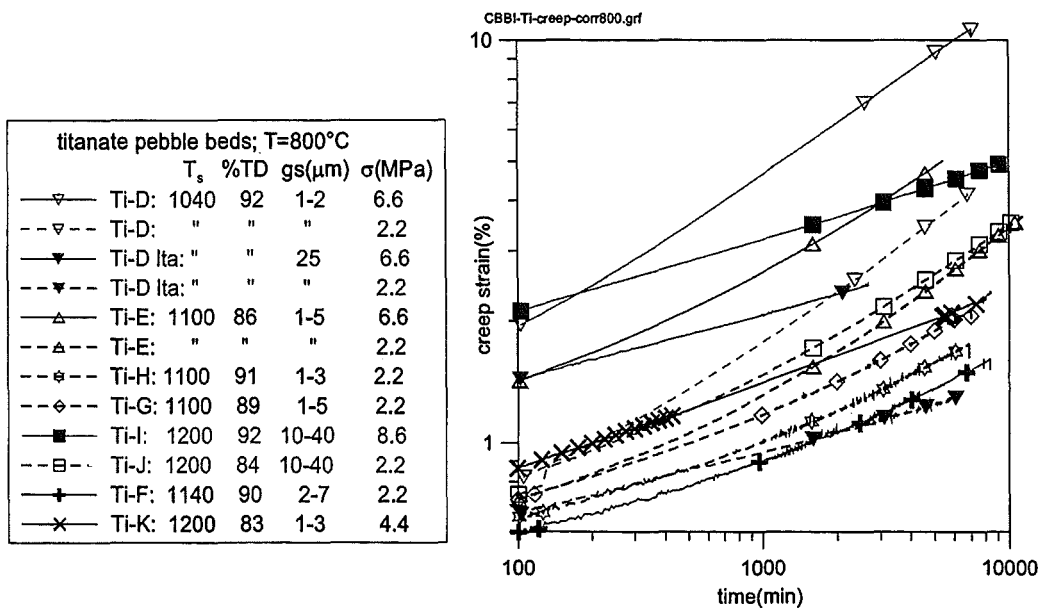


Figure 7. Thermal creep strain at large creep times of metatitanate pebble beds at 800°C

Figure 7 shows corresponding results for 800°C: for a constant stress, again Ti-D lta exhibits the smallest creep strains and Ti-D the largest (measurements for Ti-B were not performed at this temperature), followed by Ti-E and Ti-J.

In the following it is discussed which of the three parameters, sintering temperature T_s , pebble density δ , and grain size g_s , is best suited to describe the observed trends.

Sintering temperature: There is a trend that creep strain decreases with increasing T_s , however, exceptions exist: The most pronounced exception is Ti-D and Ti-D lta, being produced at the same T_s . Ti-E and Ti-G differ in creep strain although T_s is the same, however, they were obtained from different extrusion pastes. Ti-J is associated with a very high value of T_s and creep rate is quite large, however, the density is relatively low. Therefore, one might conclude that T_s is not sufficiently suited to correlate the experimental results.

Pebble density: One could suppose that creep strain increases with decreasing density. In fact, some materials with low density seem to confirm this effect: Ti-B, Ti-E, Ti-J. However, Ti-D is an example which does not follow this trend.

Grain size: This parameter is perhaps the most important although, again, there is not a unique trend: Ti-E and Ti-G do not differ in grain size but the creep rate of Ti-G is smaller than that of Ti-E. Possibly, this difference is caused by the influence of pebble density. An exception represents also Ti-H which shows a quite small creep although the grain size is quite small. Ti-H differs from the other CEA titanates by the smaller pebble size and the large packing factor which can be achieved with these pebbles.

A preliminary conclusion is that grain size influences the most the thermal creep behaviour; however, this influence becomes small for grain sizes above 5µm; additionally, there is the tendency that creep increases with decreasing density. However, there might be other parameters which were not considered in sufficient detail at the present stage of the investigations (e.g impurity contents and pebble sphericity and surface roughness).

3.3 Recommended thermal creep correlations

The present results have confirmed that the previously proposed thermal creep correlations (Table I) are sufficiently well suited to describe thermal creep of the metatitanate pebbles batches Ti-F, Ti-G, Ti-H and Ti-I. For Ti-B, Ti-D, Ti-E and Ti-J the correlation according to Table I can be applied up to creep times of about 2hr. For the second creep regime, correlations would be required where the exponent n is a function of temperature. Many more experiments than performed up to now are necessary.

At present some results are available for Ti-D and Ti-E. It proved that a stress dependence of $\epsilon_{cr} \sim \sigma^{0.65}$ again fitted quite well the experiments. Using a relationship of the type

$$\epsilon_{cr} = A^* \sigma^{0.65} t^{n^*},$$

the values of the temperature dependent quantity A^* and the exponents n are given for different temperatures in Table IV.

Table IV Thermal creep of second creep regime

T (°C)	Ti-D		Ti-E	
	A*	n*	A*	n*
650	0.00022	0.190	0.000114 ^{a)}	0.180 ^{a)}
700	0.00026	0.250	0.00022	0.230
750	0.00022	0.391	0.00026	0.270
800	0.00027	0.485	0.00029	0.425

^{a)} from correlation according to Table I

For Ti-D and temperatures $T \leq 600^\circ\text{C}$ the correlation according to Table I should be used (thermal creep might be ignored at these low temperatures); for Ti-E the values of Table I should be used for $T \leq 650^\circ\text{C}$.

The necessity of establishing thermal creep correlations for the second creep regime would decrease remarkably if it proves that stress relaxation processes in blanket structures in essential take place during the first hours. Figure 8 (from [8]) shows experiments and theoretical predictions for the case that after reaching the maximum uniaxial pressure (which is identical to the stress σ_{yy} in Fig. 8) of 8MPa the pebble bed volume was kept constant and the pressure decrease is determined. For 770°C, the uniaxial pressure drops to $\approx 25\%$ of the initial value in only 2 hr which indicates that relaxation processes are very fast.

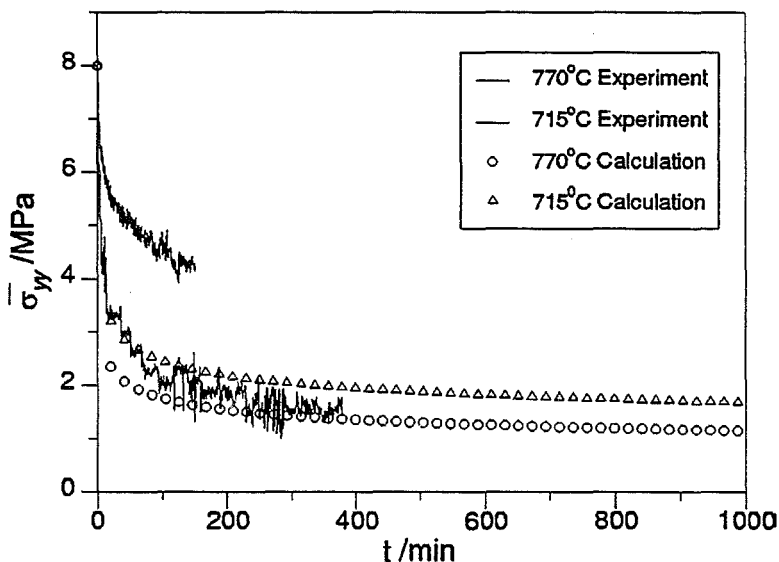


Figure 8 Stress relaxation experiment and calculation (from [8])

4. CONCLUSIONS

The present experiments proved that thermal creep of metatitanate pebble beds can vary significantly depending on the microstructural characteristics of the pebbles. These were varied in a large range as part of the optimisation study. The most significant parameter appears to be grain size. The largest creep rates were determined for a material with very small grains (1-2 μ m), a low pebble density ($\approx 83\%$ of theoretical density), produced at a low sintering temperature ($T_s = 950^\circ\text{C}$). For small creep rates, grains should be $> 5\mu\text{m}$, the percentage of theoretical density $> 90\%$. This would probably require a sintering temperature of $> 1100^\circ\text{C}$. However, other pebbles characteristics, such as shape, size, and surface roughness, should be also considered before clear conclusions can be drawn on the relevant parameters governing the thermal creep behaviour of metatitanate pebbles.

The most recently produced metatitanate pebbles by CEA, Ti-H, with smaller pebbles ($d = 0.7\text{-}1\text{mm}$) compared to other batches (0,8-1,2mm) showed very satisfactory results (although grain size was smaller than the value recommended above). This might be caused by the larger achievable packing factor which is also desired for other reasons (breeding ratio, heat transfer).

For the group of materials characterised by quite small creep rates, thermal creep can be described sufficiently well by correlations proposed in a previous paper. There is another group of materials which exhibit a second creep regime connected with higher creep rates. Data are also presented for these materials to be used in numerical codes to describe the thermomechanical interaction between pebble beds and structural materials.

REFERENCES

- [1] J. Reimann, G. Wörner, Thermal creep of Li_4SiO_4 pebble beds, 21th Symp Fusion Technology, Madrid, Spain, Sept. 11-16, 2000.
- [2] J. Reimann, G. Wörner; Thermal creep of ceramic breeder pebble beds, CBBI-9, Toki, Japan, Sept. 27-29, 2000.
- [3] G. Piazza, M. Dalle Donne, H. Werle, E. Günter, R. Knitter, N. Roux, J.D. Lulewicz, Long Term Annealing of Ceramic Breeder Pebbles for the HCPB DEMO Reactor, Proc. of the CBBI-7, Petten, The Netherlands, Sept. 14-16, 1998.
- [4] J. D. Lulewicz, Advances in the pre-industrial fabrication of Li_2TiO_3 pebbles by the extrusion-speronization-sintering process, CBBI-9, Toki, Japan, Sept. 27-29, 2000.
- [5] M. Enoeda, personal communication, 2000.
- [6] K. Tsuchiya, H. Kawamura, S. Tanaky, Characteristics of TiO_2 -doped Li_2TiO_3 , CBBI-9, Toki, Japan, Sept. 27-29, 2000.
- [7] J. Reimann, D. Ericher, G. Wörner, Influence of pebble bed dimensions and filling factor on mechanical pebble bed properties, CBBI-10, Karlsruhe, Germany, Oct.22-24, 2001.
- [8] L. Bühler, J. Reimann, Thermal creep of granular breeder materials in fusion blankets, ICRFM 10, Baden-Baden, Germany, Oct. 14-18, 2001.

THERMAL CONDUCTIVITY OF COMPRESSED ORTHOSILICATE AND METATITANATE PEBBLE BEDS

J. Reimann; S. Hermsmeyer, G. Wörner

Forschungszentrum Karlsruhe, Postfach 3640, D-76021 Karlsruhe, Germany

For the thermomechanical design of ceramic breeder blankets the effective thermal conductivity of pebble beds is an important design parameter for the layout of optimum temperatures in the breeder and multiplier pebble beds. Ceramic breeder blankets generally use pebble beds both for the breeder material and the beryllium required as multiplier. For power reactor blankets maximum temperatures in the breeder and the beryllium pebble beds are in the range of 900°C and 650°C, respectively. Because of different thermal expansions of the pebble beds and the structural material and irradiation effects, large compressive stresses occur in these beds which might cause considerable plastic deformations of pebbles. For the proper thermodynamic design the thermal conductivity of these deformed beds, therefore, is of prime importance.

A large variety of measurements were performed to determine the thermal bed conductivity for uncompressed pebble beds or pebble beds where only a small degree of compression was reached. In these experiments the bed deformation was not measured. Only recently, results for strongly deformed beryllium pebble beds were obtained where significant increases of the conductivity were found for bed deformations of about 1%.

For ceramic breeder beds, the increase of the bed conductivity with increasing bed deformation is expected to be much smaller compared to beryllium pebble beds due to the much smaller difference of the solid material conductivity and the conductivity of the surrounding gas. Quantitative results, however, were still missing.

This paper presents results on the thermal conductivity of orthosilicate and different metatitanate pebble beds for bed deformations up to 4% and maximum temperatures of 800°C using the pulsed hot wire technique. Most of the measurements at high temperatures were performed in air; at ambient temperature also helium and argon was used. Again, a distinct increase of thermal conductivity with bed deformation was found, however this effect is quite small and becomes negligible at high temperatures.

The conductivity measurements are compared to predictions made by the Schlünder-Bauer-Zehner Model.

1. INTRODUCTION

For the thermomechanical design of ceramic breeder blankets the effective thermal conductivity of pebble beds is an important design parameter for the layout of optimum temperatures in the breeder and multiplier pebble beds. Ceramic breeder blankets generally use pebble beds both for the breeder material and the beryllium required as multiplier [1]. For power reactor blankets maximum temperatures in the breeder and the beryllium pebble beds are in the range of 900°C and 700°C, respectively. Because of large temperature differences between pebble beds and the structural material, different thermal expansion coefficients and irradiation effects, constrained strains occur which give rise to large compressive stresses in these beds which might result in plastic deformations of pebbles. These deformations influence the thermal conductivity of the beds which determines the temperature distribution. For the thermomechanical blanket design, therefore, the relationship between bed stress and bed strain must be known as well the relationship between thermal conductivity and strain and stress, respectively.

At present, a considerable amount of data exists for the mechanical behaviour of ceramic pebble beds (stress-strain relationships, thermal creep) at blanket relevant conditions, obtained by uniaxial compression tests (UCTs), see e.g. [2,3]. The measurements of the thermal conductivity of ceramic breeder pebble beds, however, concentrated either on uncompressed pebble beds [4-6] or moderately compressed pebble beds without recording the corresponding bed strains [7]. The only heat conductivity measurements with an independent variation of temperature ($25 \leq T(^{\circ}\text{C}) \leq 480$) and bed pressure ($p_{\text{max}} = 8\text{MPa}$) with the measurement of bed strains were performed recently with beryllium pebble beds [8] in helium atmosphere using the hot wire technique. These experiments showed drastic increases of the thermal conductivity with increasing bed strain due to the large conductivity ratio of beryllium to helium; a linear relation between conductivity and bed strain was observed.

For ceramic breeder pebble beds, the conductivity increase with increasing pressure is expected to be much less expressed due to the smaller conductivity ratio of pebble material to surrounding gas. In previous experiments [6] in helium at ambient temperature and pressures up to 1.4MPa the change of conductivity was negligible. However, no remarkable elastic and plastic pebble deformations occurred at these operating conditions which is different at high temperatures where large strains due to thermal creep are observed [2,3]. Therefore, the present investigations were performed both at ambient temperature and at elevated temperatures (750 and 800°C); the maximum pressure was 6.5MPa.

2. EXPERIMENTAL SET-UP

The pulsed hot wire method (HWM) has become a standard technique for the measurement of materials with small thermal conductivities. In respect to pebble bed fusion blankets the HWM has been extensively used by Enoeda et al. [4,5]. In their experiments, no external pressure was applied, however, a certain stress build-up might not be excluded at higher temperatures due to different thermal expansions of the pebble beds and the test container structure. Very good agreement between the results obtained by the HWM and steady-state methods was obtained.

The HWM is based on the use of a long, thin wire embedded in the material to be investigated. At the time $t=0$, the electric power is switched on and the measured temperature differences at two times t_2 and t_1 are used to determine the conductivity k by

$$k = q / (4\pi \ln(t_2/t_1) / (\Delta T_2 - \Delta T_1)) \quad (1)$$

where q is the electrical power per unit length, $q = Q/L$, where L is the heated wire length. For data evaluation it is convenient to plot the temperature difference $\Delta T = T(t) - T(t=0)$ versus the logarithm of the time t . Then, Eq.(1) results in a straight curve with the slope $(\Delta T_2 - \Delta T_1) / \ln(t_2/t_1)$.

Eq. (1) is valid for an infinitely long thin wire with no thermal inertia and with no heat resistance between wire and surrounding material. A very favourable feature of the HWM, however, is that Eq (1) is also the asymptotic solution if thermal inertia of the wire and heat resistance wire/bed are taken into account.

Figure 1 (from [8]) shows characteristic HW temperature signals for two types of pebble beds:

- an aluminium pebble bed which is characterised by a large thermal conductivity of the pebbles and significant plastic pebble deformations during compression,
- and,
- an orthosilicate pebble bed, characterised by a small thermal pebble conductivity and negligible plastic pebble deformations during compression.

After switching on the electrical power in the inner wire, the thermal response is first dominated by the heat resistance between heater and pebble bed. After a certain time period the heat conductivity of the surrounding material becomes dominating and a fairly straight curve in the half-logarithmic plot develops after about 20s for the Al pebble bed and after less than 10s for the orthosilicate pebble beds. For the orthosilicate beds there is no significant influence of pressure on the bed conductivity and the influence of the heat resistance is not so clearly observed because of the small thermal conductivity. The figure shows that for a large conductivities (Al beds at high pressures), the slope of the curve becomes

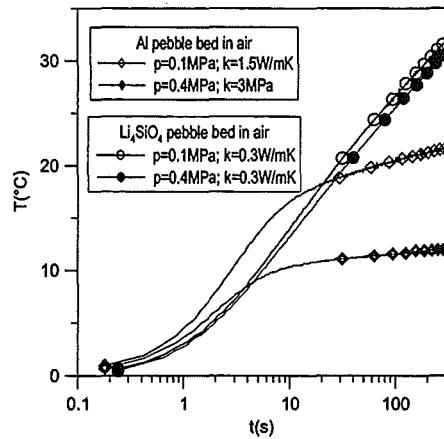


Fig. 1. Measured temperature response for Li_4SiO_4 and Al pebble beds

quite flat and with this the accuracy of the conductivity evaluation decreases (this is the reason why the HWM is favourably used for materials with small conductivities).

In the experiments the hot wire consisted of an indirectly heated element with 1mm outer diameter (diameter of the inner electrically heated wire $d_i = 0.3\text{mm}$, MgO insulator thickness of $s_i = 0.3\text{mm}$, thickness of outer stainless steel tube $s_s = 0.1\text{mm}$, heated length within the pebble bed: 90mm). This heater penetrated the cylindrical container (diameter 60mm, height 60mm) horizontally at a height of 30mm, see Fig. 1. Two thermocouples with a diameter of 0.25mm, being 10 mm apart, were brazed on the heater surface.

First, the pebbles were filled into the cavity of a cylindrical container supported by mechanical vibration in order to obtain a high packing factor γ . Then, the container was positioned in the press which is part of the UCT facility described previously [1,2]. In this facility, experiments at elevated temperatures can only be performed in air atmosphere. At ambient temperature, a plastic hood was also used which could be purged with helium or argon. Therefore, UCT experiments at ambient temperature were performed in an air, helium or argon atmosphere and UCT experiments at 750 and 800°C in air. In some of the experiments at 750 and 800°C the pebble beds were stepwise cooled down under load, therefore, keeping the maximum strain constant. At ambient temperature, the gas atmosphere could be changed, still keeping the strain constant.

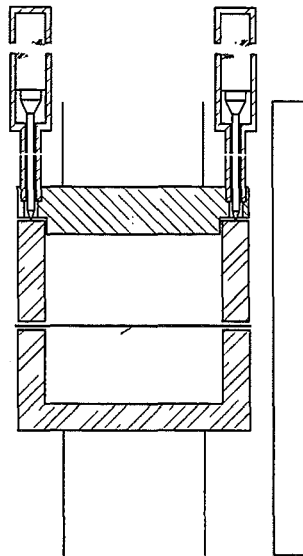


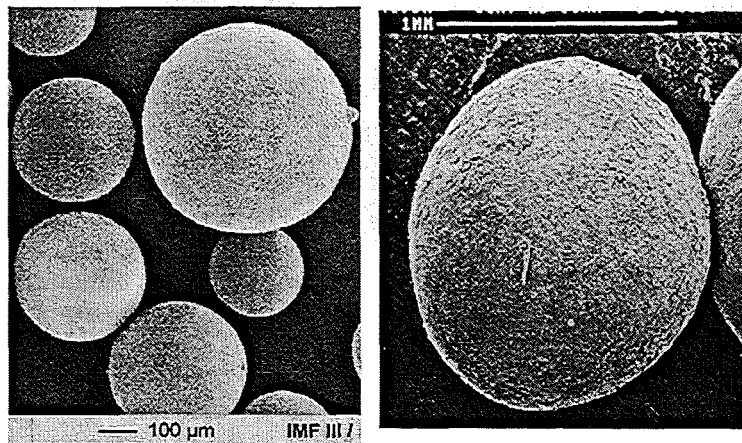
Fig. 2. Experimental set-up

There is one single UCT experiment with orthosilicate in helium at 480°C. This experiment was performed in the facility positioned in a glove-box used for the previous beryllium experiments, for details see [8].

The experiments were performed with orthosilicate pebble beds (Osi) and different kinds of metatitanate pebble beds (Ti-D ect.); Fig.3 shows photographs of two different pebbles, characteristic values of all materials are given in Table I, for details, see [3].

Table I. Characterisation of investigated granular materials

Type	Assoc.	pebble diameter d(mm)	dens. ratio $\delta(\%)$	grain size gs(μm)	sint.temp. $T_{\text{sinter}}(^{\circ}\text{C})$	packing factor $\gamma(\%)$
Osi	FZK	0.25-0.6	98	50		64
Ti-D	CEA	0,8-1,2	90	1-2	1050	63
Ti-E	CEA	0,8-1,2	86	1-5	1100	63,2
Ti-J	JAERI	≈ 2	84	1-3	1200	64,3
Ti-J-bin	JAERI	0.2+2	84	1-3	1200	81.2



a) b)
Fig. 3. Orthosilicate (a) and metatitanate pebbles (Ti-D) (b)

3. RESULTS

3.1 Parameter sensitivity analyses using SBZ-Model

There are different models to predict the thermal conductivity, k , of pebble beds. In the present work the Schlünder-Bauer-Zehnder-Model (SBZ-Model) [9] has been used. The SBZ-Model takes into account the influences of various pebble bed parameters such as thermal conductivities of the pebble material, k_p , and gas, k_g , pebble diameter d , bed porosity, λ , and normalised contact area between pebbles, $\rho_k^2 = (d_c/d)^2$, where d_c is the diameter of the contact area. In practice, the value of ρ_k^2 is not known and this value is used to fit the model to experimental data.

Figure 4 shows the thermal conductivities of different pebble bed materials (orthosilicate and metatitanate pebbles) and different gases (helium and air) as a function of temperature. For a temperature increase from 25°C to 800°C, the conductivities k of the pebble materials decrease from about 4 to 2 (for beryllium the values vary between 160 and 80 W/mK) whereas the helium conductivity increases from 0.154 to 0.4.

Figure 5 contains some parameter variations using the SBZ-Model for orthosilicate pebble beds: Fig. 5a demonstrates the influence of pebble deformation ρ_k^2 as a function of temperature for two gases, helium and air. For zero deformation ($\rho_k^2 = 0$), k increases moderately with temperature T due to the increasing gas conductivity. For a deformation of $\rho_k^2 = 0.02$, the bed conductivity has increased; however, the temperature effect is negligible due to the competing influence of the pebble material conductivity, decreasing with temperature.

In Figure 5b the thermal conductivity is presented as a function of the normalised contact area with T as a parameter: relationships exist where the slope decreases with increasing T .

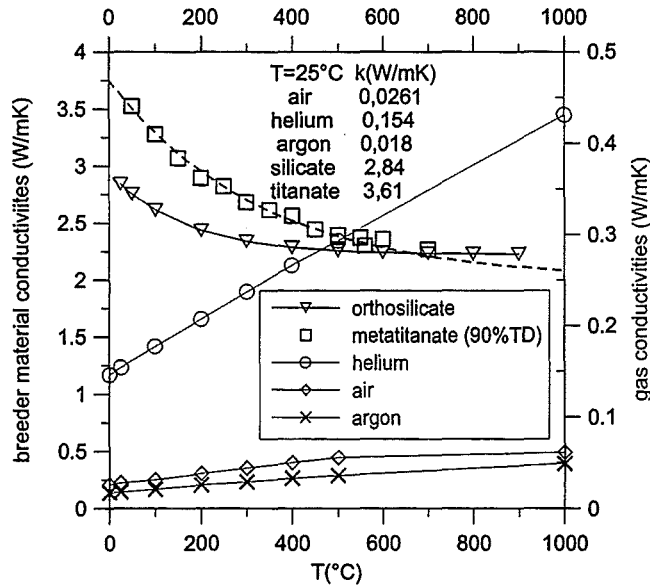


Fig. 4. Thermal conductivity of ceramic breeder materials and helium and air

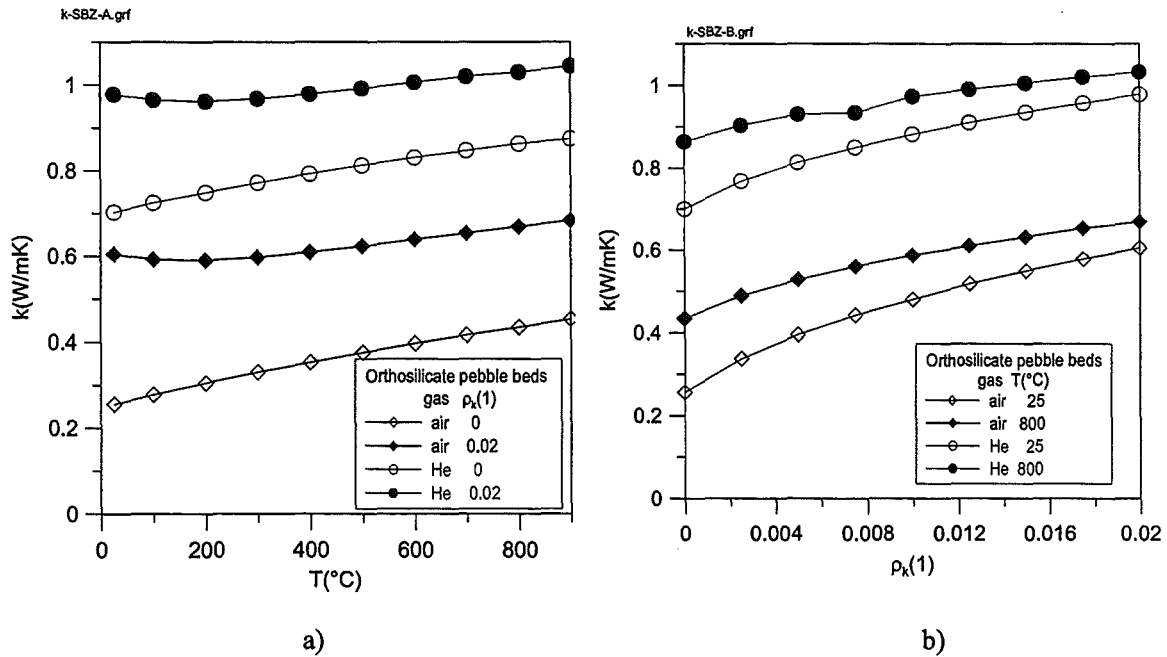


Fig. 5. Influence of temperature and contact area ratio on pebble bed conductivity

4.2 Pebble bed results

Figure 6 shows for metatitanate at two temperatures measurements of the stress-strain dependence together with the corresponding measured bed conductivities: for ambient temperature, the conductivity increases very moderately by about 10% during stress increase; in the experiment at 800°C, the pressure

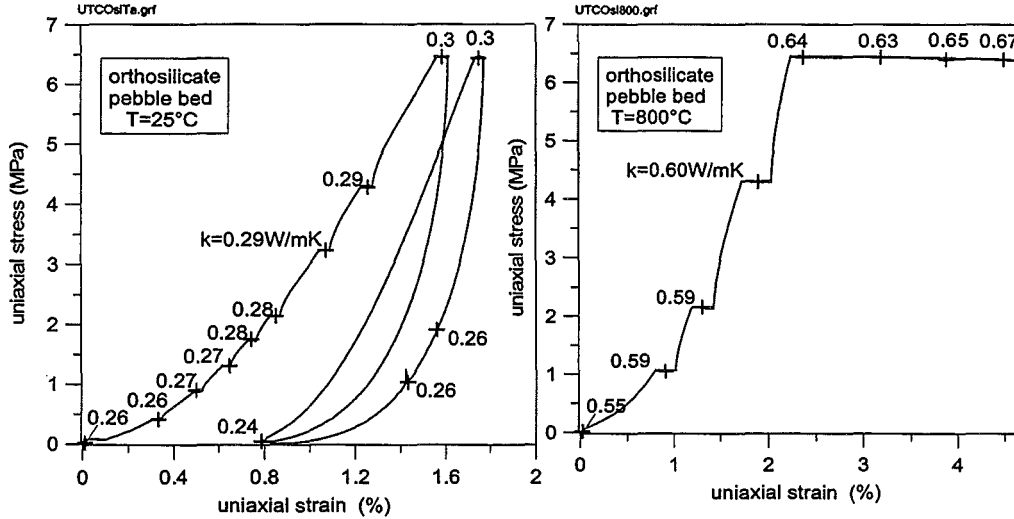


Fig. 6. Stress-strain dependence and measured conductivities for orthosilicate pebble beds in air at $T=25^{\circ}\text{C}$ and at 800°C

was kept constant after having reached the maximum value of 6.4MPa and strain increased due to thermal creep to a value of about 4.5%. During the pressure increase phase the conductivity again only increased modestly; interestingly, this increase is also not very expressed during the creep phase where strain is supposed to be caused primarily by plastic deformation (strains during the pressure increase period are also supposed to be caused by pebble relocation).

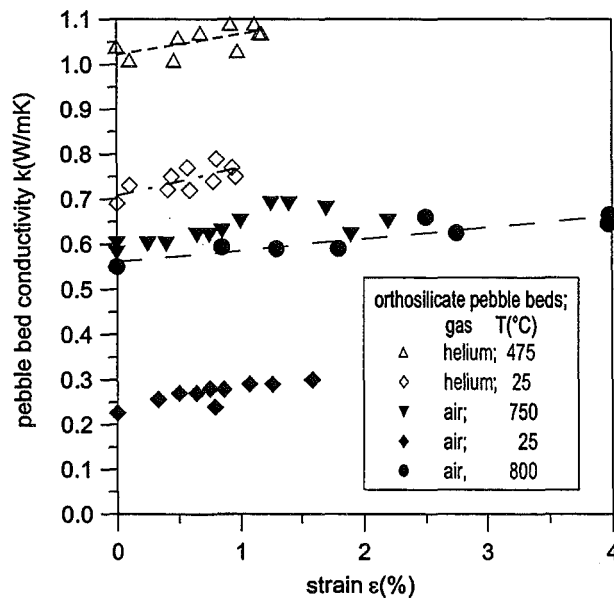


Fig.7. Thermal conductivity $k=f(\epsilon)$ for Li_4SiO_4 pebble beds

Figure 7 summarizes all results for orthosilicate during the first pressure increase period: as for beryllium pebble beds [8], a linear increase of conductivity with strain is observed although this increase is quite small. Table II contains the coefficients of these relationships. For non-deformed pebble beds, the Table II. Correlations for thermal conductivity of deformed orthosilicate pebble beds

granular material	gas	T(°C)	k(W/mK)=a+bε(%)		k _{SBZ} ρ _k ² =0	k _{DD} ¹⁾
			a	b		
orthosilicate	helium	485	1.02	0.045	0.84	1.0
	helium	25	0.72	0.045	0.74	0.78
	air	25	0.24	0.038	0.27	
	air	750	0.59	0.036	0.45	
	air	800	0.56	0.025	0.46	

¹⁾ Dalle Donne et al.[6] $k(\text{W/mK})=0.768+4.96 \cdot 10^{-4}T(^{\circ}\text{C})$

SBZ-model (with $\rho_k^2 = 0$) agrees quite well with the results in air and helium at ambient temperature but under-estimates conductivities with increasing temperature. The present measurement in helium at 485°C agrees well with the prediction from the correlation from Dalle Donne et al. [6], established for helium at elevated temperatures.

Figure 8 presents a summary of the results for metatitanate pebble beds: for small gas conductivities (air or argon atmosphere at ambient temperature) the increase of conductivity with strain is more expressed than for orthosilicate. This might be due to both the large surface roughness and smaller sphericity of the titanate pebbles compared to the orthosilicate pebbles, see Fig. 2: with increasing stress, the surface roughness might be decreased and during stress increase the pebbles might relocate in such a way that contact zones increase. However, with increasing gas conductivity these influences become smaller. Table 2 shows that for non-deformed pebble beds the agreement between measurements and SBZ-model is quite good for air at ambient temperature while the SBZ-model predicts too low values in the other cases. Enoeda et al. [5] obtained good agreement between their measurements for non-deformed metatitanate pebble beds in helium at elevated temperatures and the SBZ-model by assuming a value of $\rho_k^2 = 0.0049$. Using this value, the agreement atmosphere is also quite good for the present experiment in helium atmosphere, however, the agreement becomes worse for air at low temperatures.

In Fig. 9, experiments are presented where large strains were obtained after the thermal creep period, compare Figs. 7 and 8, the stress was kept constant during cooling down and with this the strain

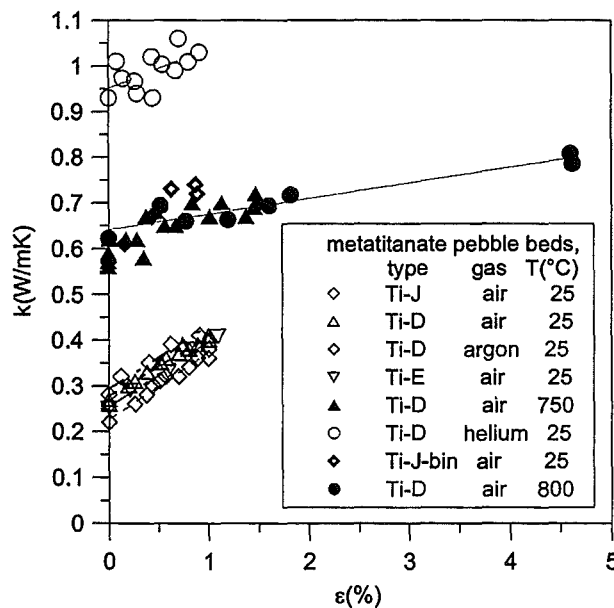


Fig. 8. Thermal conductivity $k=f(\epsilon)$ for Li_2TiO_3 pebble beds

Table III. Correlations for thermal conductivity of deformed metatitanate pebble beds

granular material	gas	T(°C)	k(W/mK)=a+bε(%)		k _{SBZ} ρ _k ² =0	k _{SBZ} ρ _k ² =0.0049 ¹⁾
			a	b		
Ti-D	air	800	0.64	0.034	0.49	0.59
Ti-J	air	25	0.28	0.13	0.26	0.37
Ti-D	air	25	0.25	0.14	0.29	0.36
Ti-D	helium	25	0.98	0.046	0.86	1.00

¹⁾ value recommended by Enoeda [5]

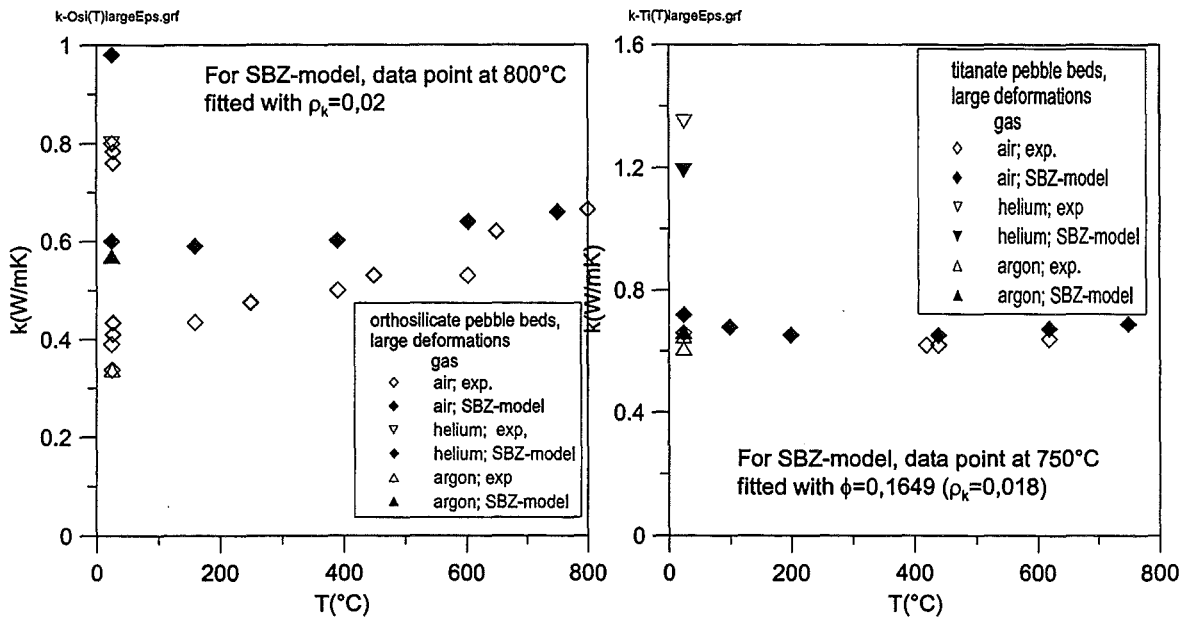


Fig. 9. Thermal conductivity $k=f(T)$ for constant large strains (SBZ fitted at max. T)

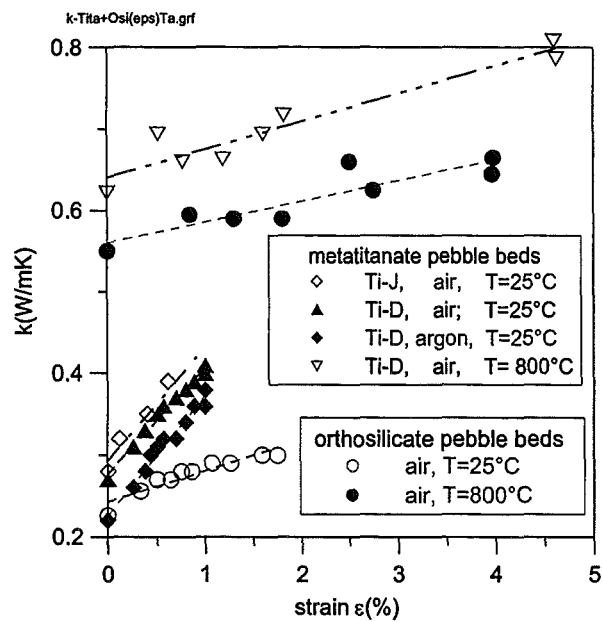


Fig. 10. Comparison between Li_4SiO_4 and Li_2TiO_3 pebble beds

was kept constant. The measurement at the highest temperature was used to adjust ρ_k^2 in order to obtain the same value with the SBZ-model. For metatitanate pebble beds the agreement for the following measurements during cooling-down is very good; for the orthosilicate pebble bed the measurements are lower than the SBZ-predictions; one reason could be that during cooling down pebble contacts get lost due to the much higher thermal expansion coefficient of orthosilicate compared to metatitanate.

Figure 10 shows a comparison between orthosilicate and metatitanate pebble bed results: for air at ambient temperature, the increase of conductivity with strain is more expressed for metatitanate pebble beds than for orthosilicate pebble beds; for air at 800°C the conductivity of metatitanate pebble beds is higher by about 20% than that of orthosilicate pebble beds and the increase of conductivity with strain is about equal in both cases; about 20% for a strain of 4.5%.

CONCLUSIONS

Measurements of the thermal conductivity of considerably deformed ceramic breeder pebble beds were performed at pressures up to 6 MPa and temperatures up to 800°C. At the maximum temperature the thermal conductivity increases only by about 20 % for an air atmosphere; for a helium atmosphere this value is expected to be even less. With decreasing temperatures, this effect is somewhat more expressed. Correlations are given for the thermal conductivity as a function of strain and temperature.

For non-deformed pebble beds in helium at elevated temperatures, the correlation of Dalle Donne et al [5] for orthosilicate beds is confirmed, for metatitanate pebble beds the SBZ-model with the value for ρ_k^2 as used by Enoeda [5] is recommended.

REFERENCES

- [1] S. Hermsmeyer, U. Fischer, K. Schleisiek, Improved helium cooled pebble bed blanket, 21st Symp Fusion Techn., Madrid, Spain, Sept. 11-15, 2000.
- [2] J. Reimann and G. Wörner, Thermal Creep of Li₄SiO₄ Pebble Beds, 21st Symp. Fusion Techn., Madrid, Spain, Sept. 11-15, 2000.
- [3] J. Reimann, G. Wörner; Thermal creep of ceramic breeder pebble beds, CBBI-9, Toki, Japan, Sept.27-29, 2000.
- [4] M. Enoeda, K. Furuya, H. Takatsu, S. Kikuchi, T. Hatano, Effective thermal conductivity measurements of the binary pebble beds by hot wire method for the breeding blanket, Fusion Technology, Vol. 34, Nov. 1998.
- [5] M. Enoeda, Y. Ohara, N. Roux, A. Ying, S. Malang, Effective thermal conductivity measurements of the ceramic breeder pebble beds using the hot wire method under IEA collaboration program, CBBI-8, Colorado Springs, USA, Oct.6-8, 1999.
- [6] Dalle Donne et al., Measurements of the effective thermal conductivity of a Li₄SiO₄ pebble bed, 5th Int. Symp. Fusion Nuclear Technology, Roma, Italy, Sept.19-25, 1999.
- [7] F. Tehranian and M. Abdou, Experimental study of the effect of external pressure on particle bed effective thermal properties, Fusion Techn. Vol. 27, May 1995, pp. 298-313.
- [8] J. Reimann, S. Hermsmeyer, G. Piazza, G. Wörner, Thermal conductivity measurements of deformed beryllium pebble beds by hot wire method, CBBI-9, Toki, Japan, Sept.27-29, 2000.
- [9] E.V. Schlünder, Particle heat transfer, Proc 7th Int. Heat Transfer Conf., München, Germany, 1982, Vol1, RK10, 195-212, 1982.

PARTICLE FLOW OF CERAMIC BREEDER PEBBLE BEDS IN BI-AXIAL COMPRESSION EXPERIMENTS

S.Hermsmeyer, J.Reimann

Forschungszentrum Karlsruhe

Pebble beds of ceramic material are investigated within the framework of developing solid breeder blankets for future fusion power plants. A thermo-mechanical characterisation of such pebble beds is mandatory for understanding the behaviour of pebble beds, and thus the overall blanket, under fusion environment conditions.

The mechanical behaviour of pebble beds is typically explored with uni-axial, bi-axial and tri-axial compression experiments. The latter two types of experiment are particularly revealing since they contain explicitly, beyond a compression behaviour of the bed, information on the conditions for pebble flow, i.e. macroscopic relocation, in the pebble bed.

Previous compression experiments at the Forschungszentrum Karlsruhe focussed on blanket relevant bed geometry, which meant that they were mostly limited to ceramic breeder bed heights of 10 mm. Under this condition, the bed is stiff and pebble flow perpendicular to the main compression direction occurs only at large ratios of main direction and perpendicular direction pressures.

New experiments on 20 and 30 mm high pebble beds show much pronounced pebble flow effects that were negligible in 10 mm beds. Owing to the greater bed height, conditions are reached where the bed fails in horizontal direction and fast flow of the pebbles occurs. The paper presents measurements for the orthosilicate and metatitanate breeder materials that are envisaged to be used in a solid breeder blanket. The data are accompanied by calculations made with a Drucker-Prager soil model within the finite-element code ABAQUS. It is tried to answer empirically the questions of what feedback such a model can have on the calibration of a Drucker-Prager model and if it is possible to replace the information from tri-axial models, that is hard to gain particularly at high temperatures, by simpler, less temperature-limited, bi-axial compression tests.

Introduction

The proposed use of breeder ceramics and Beryllium in the form of pebbles within breeding blankets for nuclear fusion plants has led to various activities of developing suitable particle materials, and measuring/modelling their pebble bed behaviour. The soil behaviour that these beds show, and the models to predict it, are not new, e.g. [1]; however, applications tend to be stationary soils or the handling of granular materials in industry, both quite different from volumetrically heated pebble beds in a neutron environment, where thermal conductivity, thermal expansion, thermal creep and swelling are main effects to be considered.

The majority of mechanical pebble bed experiments with relevant materials has in the past stayed very close to the shallow bed geometry dictated by volumetric heating and the expected thermal conductivities. These, mostly isothermal, results suggest predominantly one-dimensional behaviour perpendicular to the shallow bed, although it is expected that, at least locally, the

thermal gradients found in a fusion environment would imply a deviation from one-dimensionality.

The bi-axial compression tests on higher-than-standard ceramic breeder pebble beds presented in this paper exhibit two- or three-dimensional physics much stronger than shallow-bed experiments. While their results cannot be applied directly to shallow pebble beds, they prove to be useful in both extending the understanding of pebble bed behaviour and providing better information for the determination of parameters in the Drucker-Prager cap model applied within finite element simulations of the pebble bed [2].

This paper gives a broad view of bi-axial compression tests of 20 and 30mm-high ceramic breeder pebble beds by (i) discussing recent measurements, (ii) comparing them with finite element simulations and (iii) proposing the use of measurements for improvements to model parameter determination.

Bi-axial compression experiment

The test section for bi-axial compression tests (BCT's) consists of a rectangular cavity with a horizontal cross section $L \times W$ and a vertical bed height H , see Figure 1(a). The bed is compressed by a vertical piston (corresponding to the poloidal direction in a fusion blanket) with a constant load ramp; the load is induced momentum-less on the centre of the piston. One side wall (cross section $W \times H$) consists of a movable piston which can be preloaded with a given radial pressure, p_h . The horizontal piston displacement s_h is measured with an inductive displacement transmitter. In the following, experiments are described where the pebble bed and the movable piston are the same height, H . In previous experiments, a bed of $H = 10$ mm was used [3] and the other dimensions L and W were 100mm. For the present experiments with $H = 20$ and 30 mm, the dimension W was also 100 mm but L was reduced to 80 mm. The test apparatus can be used for uni-axial compression tests (UCT's), if the horizontal piston is fixed by a screw. An important feature of this arrangement is that during the performance of a UCT the horizontal pressure on the piston can be measured.

The vertical pressure is measured by three strain gauge force transmitters; the positions are shown in Figure 1(a). The displacement of the vertical piston is measured with three displacement transmitters. It proved that the displacements s_2 and s_3 agreed fairly well. All displacements are normalised with the bed height H in order to obtain strains. With the vertical strain ε_{v1} (determined from s_1) and ε_{v2} (determined from $(s_2+s_3)/2$) the inclination of the piston can also be determined. The mean vertical strain ε_v is evaluated from $(\varepsilon_{v1} + \varepsilon_{v2})/2$.

Two granular materials were used: orthosilicate pebbles with diameters d between 0.25 and 0.6 mm and metatitanate pebbles with d between 0.8 and 1.2 mm. The orthosilicate pebbles were of spherical shape with a smooth surface, whereas the sphericity of the metatitanate pebbles was smaller and the surface was rougher.

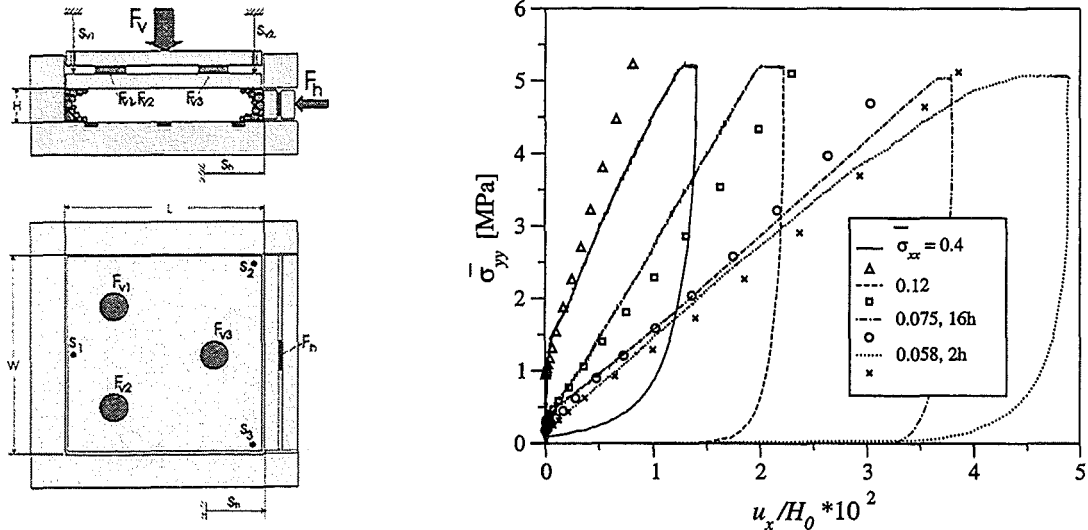


Figure 1 (a) Test section for bi-axial compression experiments. (b) Bi-axial compression test results for 10mm-high orthosilicate pebble beds.

Previous results on shallow beds

Characteristic BCT results from previous experiments with orthosilicate pebble beds ($H = 10\text{mm}$) are shown in Figure 1(b) with the vertical pressure plotted as a function of the horizontal strain. The horizontal strain increases with vertical pressure; strain levels depend strongly on the pressure applied to the horizontal piston – held constant for each of the for curves -, with larger strains achieved for smaller horizontal pressure. As shown in [3], larger strains are produced by increasing packing factor γ , too. These results show particle flow expected in a pebble bed, but they suggest that horizontal pressures as small as 1% of the vertical load, in conjunction with wall friction, inhibit the free particle flow, or perfect plasticity, seen in tri-axial experiments.

It should be noted that after reaching the maximum vertical pressure there is, depending on the load ramp, still some movement of the horizontal piston until the final position is reached. Frictional effects between individual pebbles cause this non-equilibrium behaviour; a quasi-steady loading was reached when the load was increased to the maximum value in about 16 hours.

The results on 10 mm-high beds are relevant for a fusion plant, since they match the bed heights that a blanket in such a machine will have. They confirm that only local, limited pebble flow is to be expected, and seem to suggest a simple form of bed behaviour. However, it is the need to model pebble bed behaviour, to understand and quantify pebble flow in the bed that drive bi-axial experiments on higher pebble beds. In particular, higher beds exhibit a greater level of shear failure than shallow beds, which is a harder test for the shear failure part in the Drucker-Prager model. In reversing the argument, it is proposed that the shear failure information in bi-axial experiment results is so strong that these results can be employed for model calibration.

New results for higher beds

Figure 2(a) demonstrates the differences found for bed heights of $H = 10, 20$ and 30mm at identical horizontal pressures and packing fractions; in all cases the vertical pressure was increased with a constant load of about $0.15\text{MPa}/\text{min}$. In contrast to the shallow bed, horizontal

strain in the 20 and 30 mm beds increases strongly from vertical pressures as small as 0.5 MPa on and reach a stage of horizontal particle flow at constant vertical pressure. This process is similar to the state of perfect plasticity seen in tri-axial compression tests [4], the key differences being the two-dimensionality of the present experiment and the presence of wall friction. The dependence of the critical vertical pressure on bed height is due to this wall friction.

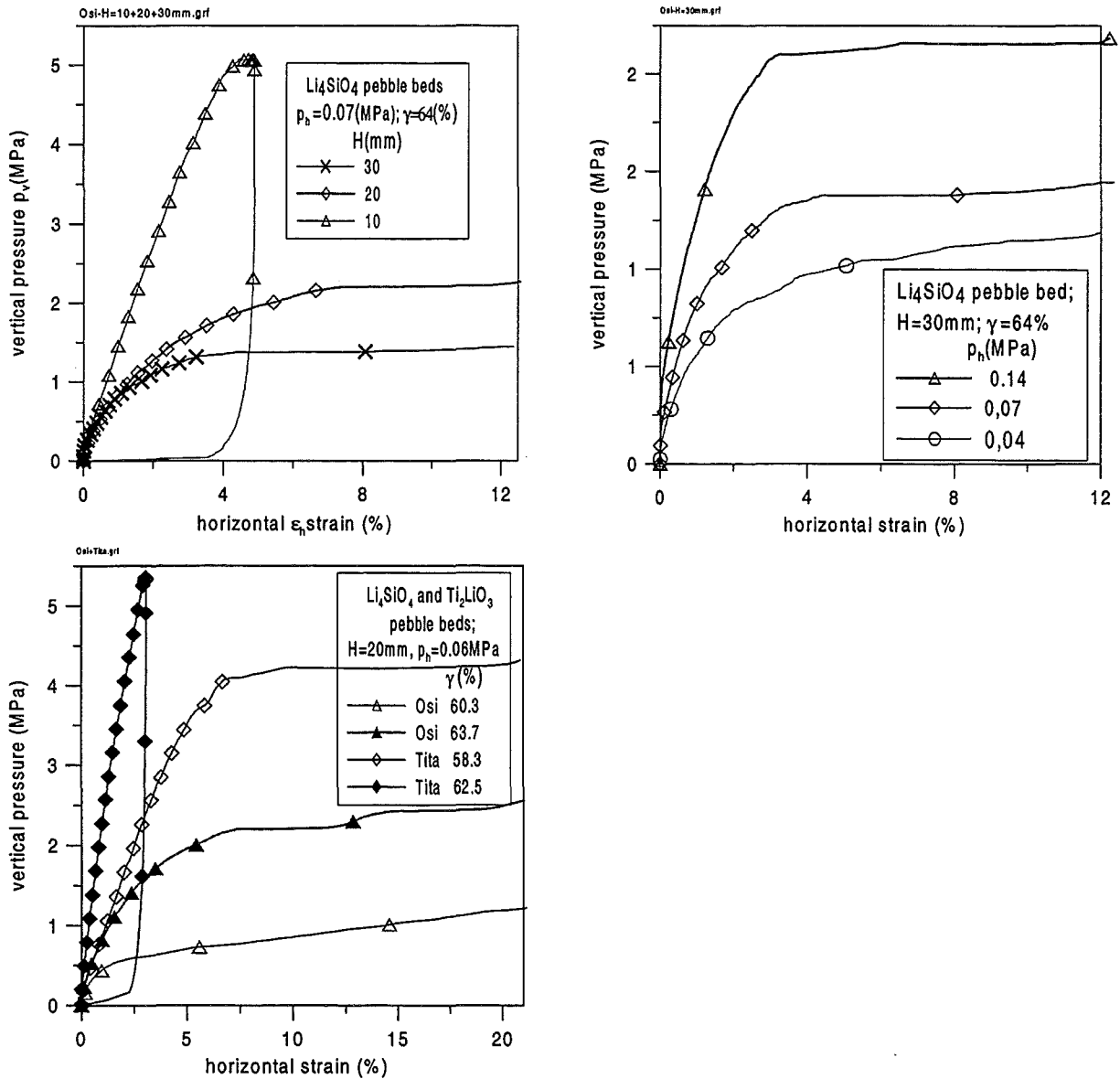


Figure 2 Perfect plasticity in bi-axial experiments. Variation of (a) bed heights, (b) horizontal threshold pressure and (c) pebble material and packing fraction.

Experimental results displayed in Figure 2 (b) and (c) confirm the expected trends, that smaller horizontal pressure leads to an earlier appearance of perfect plasticity, as do larger sphericity and surface smoothness that are seen in orthosilicate as opposed to metatitanate material, and looser packing of the bed.

Finite-element simulation

Predicting the behaviour of pebble beds by means of finite element models is a capability that has been, and still is, developed at the Forschungszentrum alongside pebble bed experiments, and that will become crucial for future design analyses of a solid breeder blanket. The simulation of bi-axial compression experiments on beds higher than 10 mm is particularly demanding, because of the extent of pebble flow that occurs.

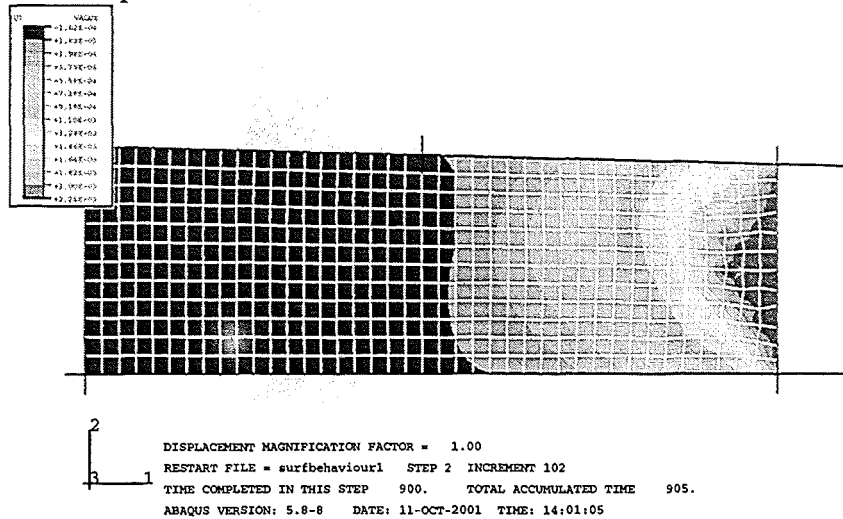


Figure 3 Finite element model of the bi-axial compression test. Mesh display, deformations and contour plot of horizontal displacements.

Figure 3 shows the mesh of the two-dimensional model with $40 \times 12 = 480$ elements. The dimensions are identical to the 30 mm-high pebble experiment; the initial and boundary conditions chosen try to match the reality as closely as possible, with contact surfaces between bed and container including friction, and the top plate free to tilt while the right-hand wall “piston” is not. The vertical displacement of the top plate’s central node was imposed. The piston wall was assumed fixed up to a reaction force threshold of 0.5 MPa; after reaching this conditions, the analysis was continued with a condition of constant horizontal pressure of these 0.5 MPa. The pebble bed is described by a Drucker-Prager-cap continuum model that covers physics of elastic and plastic deformation, and shear failure, known to occur in soils. The model was calibrated with data from uni-axial compression tests, and with internal friction angles found in tri-axial compression experiments.

The distorted mesh together with the horizontal displacements contour plot illustrate qualitatively the physics in the experiment: the horizontal flow of particles is largest at the piston wall, at half the height of the bed, while friction reduces flow in the vicinity of the wall. In the figure, the horizontal piston has started giving way, which leads to (i) a particle flow towards the, moving, right-hand side piston wall; (ii) a tilting of the top plate towards the piston; and, (iii) a pebble re-circulation, and possibly a detachment of bed and tilted top plate, on the left side of the model.

Figure 4 depicts some results from the analysis. Comparing Figure 4(a) to the experimental measurement displayed in Figure 2(a) shows that the level of vertical stress in the simulation is off by a factor of 2, while the horizontal strain corresponding to the critical vertical stress is reasonably close. Similarly, the tilting of the top plate as expressed by vertical displacements of the left and right corner of the plate, Figure 4(c), is qualitatively in agreement with the

experimental data, Figure 4(d). The predicted displacements exceed measured data, but they are close enough to expect that a model calibrated with more relevant data could come close.

The state of perfect plasticity for the bi-axial experiment has as yet proved to be difficult to simulate: The negative displacements in Figure 4(c) mean that indeed the top plate lifts off the pebble bed on that side, creating a free surface that the soil model is not prepared for. By defining an artificial interaction of top plate and pebble bed after contact is lost, the point where numerical problems stop the computation could be moved to larger horizontal strains, and a critical vertical stress reached in the present analysis.

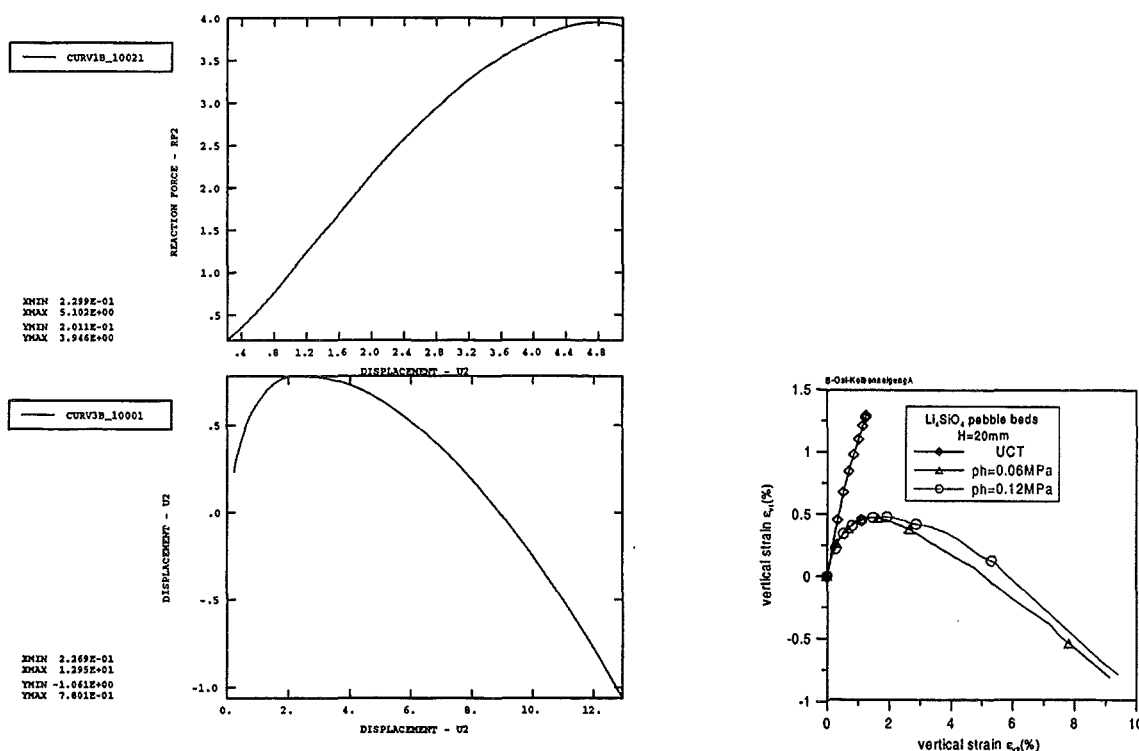


Figure 4 Bi-axial experiment simulation results. (a) Vertical pressure over horizontal strain; (b) Mises stress in the pebble bed; (c) Vertical strain of top plate left over right corner; (d) experimental data for (c).

Determination of internal friction angles

The internal friction angle is an important quantity for the determination of the macroscopic movement of pebbles (particle flow) in blanket structures with inhomogeneous stress distributions. Measurements of the inner friction angle α are usually performed in tri-axial compression tests; in the past, such measurements for ceramic breeder pebbles were performed in different facilities [5]. Even so, it is clear from the results presented above that measurements from the bi-axial compression test section are informative about the friction processes inside the pebble bed, too. This information should be used for the characterisation of pebble beds. In the following we will use an adhoc approach to determining internal friction angles, and compare results to TCT friction angles to establish the merit of the achievable results.

At the beginning of a BCT or UCT the horizontal piston is fixed in the zero strain position ($\epsilon_h=0$), preloaded with the value p_h . Increasing the vertical pressure, the horizontal piston stays in its zero position until the threshold p_h is exceeded. On reaching this pressure, the pebbles start to

move macroscopically and the horizontal strain increase. Similar to the definition of friction between two materials (the angle at which a block of material A starts moving on an inclined surface of material B) the values of $p_{h,0}$ and of the vertical pressure $p_{v,0}$ at the first movement characterise inner friction of the pebble bed. The friction angle β is defined by

$$\beta = \arctan(3(p_{v,0} - p_{h,0})/p_{v,0} + 2 p_{h,0})$$

Figure 5(a) and (b) show the evolution of pressure values, together with the horizontal strain, from representative bi-axial and uni-axial compression experiments. The characteristic change of the slope of ϵ_h is more pointed in the UCT than in the BCTs, although in both cases it is rather a range than a certain time instant of initial horizontal strain that can be determined from these data. Once a the initial time instance of pebble movement has been determined from ϵ_h , the pressure values needed for the determination of the friction angle can be read from the two pressure measurements.

One might be surprised that non-zero strains are recorded for UCTs; This strain can only occur due to elastic deformation of the force transmitter which is about 50 μm for 100% load. Although this maximum strain is very small it is sufficient to produce incorrect results for p_h if data are used for significant transmitter deformations due to pebble bridging, see [4].

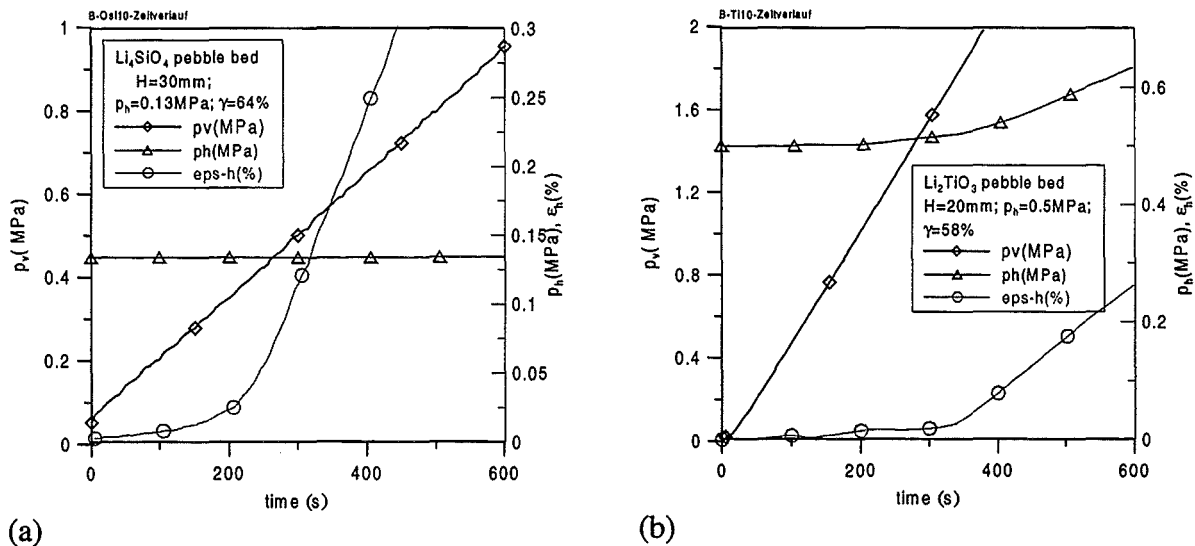


Figure 5 Determination of horizontal pebble bed pressure (a) from a bi-axial compression test, (b) from a uni-axial compression test.

Figure 6 depicts a host of friction angles that were calculated from uni- and bi-axial compression tests. The choice of initial time instant was somewhat arbitrary, but based on a subjective judgment on the available horizontal strain measurement. The data points for orthosilicate and metatitanate breeding materials are reasonably well correlated as linear functions of packing fraction, even though scatter of the data is considerable. Metatitanate has consistently larger friction angle than orthosilicate, which is due to its pebbles' smaller sphericity and its larger surface roughness.

The comparison of values calculated from BCTs and UCTs with data from TCTs does not reject the hypothesis that the presented method of determining friction angles is feasible. However, the large scatter of TCT results sheds a light on the large sensitivity to experimental conditions, and on the poor quality, of the existing database.

Current Status on Li_2TiO_3 Pebble Fabrication by Wet Process

S.Kato¹, H.Tomimoto¹, T.Takayama¹, K.Tsuchiya² and H.Kawamura²

¹Nuclear Fuel Industries, Ltd., Tokai, Naka, Ibaraki, 319-1196, Japan

²Oarai Research Establishment, JAERI, Narita, Oarai, Higashi-ibaraki, Ibaraki, 319-1394, Japan

In the joint program with JAERI and Nuclear Fuel Industries, Ltd. (NFI) concerning fabrication development of the tritium breeder pebbles, two kinds of pebble fabrication method, the wet process with dehydration reaction and with substitution reaction were developed. On the other hand, from the results of the irradiation damage and tritium breeder ratio (TBR) by the calculation codes (MCNP code, etc.), ^6Li enriched Li_2TiO_3 pebbles have been suggested for the purpose of increasing the TBR. Among others, ^6Li enrichment was optimized to approximately 30at% from the viewpoint of the irradiation test.

In this study, the fabrication tests of 30at% ^6Li enriched Li_2TiO_3 pebbles and TiO_2 doped Li_2TiO_3 pebbles with 1mm in diameter by the wet process with dehydration reaction were carried out, and their characteristics were evaluated.

1. Introduction

In 1994, JAERI and Nuclear Fuel Industries, Ltd. (NFI) started the joint research program concerning fabrication development of the tritium breeder pebbles. In this joint program, two kinds of pebble fabrication method, the wet process with dehydration reaction and with substitution reaction were developed. The wet process is the most advantageous from a viewpoint of mass fabrication, lithium recycle, etc. [1-3].

On the other hand, irradiation damage and tritium breeder ratio (TBR) of Li_2TiO_3 pebbles with the structure of DEMO breeding blanket was established by the calculation codes (MCNP code, etc.). From the calculation results, ^6Li enriched Li_2TiO_3 pebbles have been suggested for the purpose of increasing the TBR. Among others, ^6Li enrichment was optimized to approximately 30at% from the viewpoint of the irradiation test with the material testing reactor [4].

In this study, the fabrication tests of ^6Li enriched Li_2TiO_3 pebbles with 1mm in diameter by the wet process with dehydration reaction were carried out, and characteristics of ^6Li enriched Li_2TiO_3 pebbles were evaluated. In addition, for researching the relationship between doped TiO_2 and grain sizes of pebbles ^6Li enriched TiO_2 doped Li_2TiO_3 pebbles were fabricated and their characteristics were evaluated [5-6].

2. Experimental

^6Li enriched Li_2TiO_3 pebbles and ^6Li enriched TiO_2 doped Li_2TiO_3 pebbles were fabricated by the wet process with dehydration reaction. Flow chart for the fabrication process of pebbles is shown in Fig.1. The procedure includes the fabrication of ^6Li enriched Li_2TiO_3 powder and gel spheres, calcination process and sintering process, and the fabrication procedure was based on the following phenomena.

- 1) Fabrication of ^6Li enriched Li_2TiO_3 powder: Flow chart for the fabrication of ^6Li enriched Li_2TiO_3 powder is shown in Fig.2. 95at% ^6Li enriched Li_2TiO_3 powder is converted by solid phase reaction with ^6Li enriched Li_2CO_3 powder and TiO_2 powder. 95 at% ^6Li enriched Li_2TiO_3

powder is mixed with 7.5at% ^6Li natural Li_2TiO_3 powder, and ^6Li enrichment is adjusted to 30at%.

- 2) Fabrication of gel spheres: At first, liquid mixture is prepared from ^6Li enriched Li_2TiO_3 powder, PVA binder and water. It is dropped through the nozzles into acetone. At this time, liquid mixture changes by itself to the shape of sphere by its surface tension, and they are gelled in acetone by dehydration reaction. After that, gel pebbles are dried.
- 3) Calcination of gel spheres: Dried gel pebbles are calcined in air for removed PVA.
- 4) Sintering: Calcined pebbles are sintered in air for increased their density.

The fabrication tests of Li_2TiO_3 pebbles for researching the relationship between content of Li_2TiO_3 powder in mixture and pebble diameter and the relationship between sintering temperature and pebble density were carried out.

At last, ^6Li enriched Li_2TiO_3 pebbles and ^6Li enriched TiO_2 doped Li_2TiO_3 pebbles with 1mm in diameter were fabricated by the wet process with the condition selected by the fabrication tests, and their characteristics were evaluated.

3. Results and Discussions

3.1. Fabrication of ^6Li enriched Li_2TiO_3 powder

Characteristics of ^6Li enriched Li_2TiO_3 powder are shown in table 1. ^6Li enrichment of fabricated powder was 31at%, content of Li_2TiO_3 was not less than 99.97% and average particle size was $0.43\mu\text{m}$. And, impurities in pebbles were nearly same content as in starting powder. From the results of X-ray diffraction, the detected diffraction peaks were corresponded with the diffraction peaks of Li_2TiO_3 , and the diffraction peaks of Li_2CO_3 and TiO_2 were not detected.

3.2. Fabrication tests of Li_2TiO_3 pebbles

As the first fabrication test of Li_2TiO_3 pebbles, the relationship between content of Li_2TiO_3 powder in mixture and pebble diameter was researched. The result of test is shown in Fig.3. As the result, pebble diameter increased with increasing content of Li_2TiO_3 powder. And since Li_2TiO_3 pebbles with 1mm in diameter have the target diameter in the range of 0.85 to 1.18mm, content of Li_2TiO_3 powder in mixture can be selected $25 \pm 5\text{wt}\%$ for the target diameter.

As the second fabrication test of Li_2TiO_3 pebbles, the relationship between sintering temperature and pebble density was researched. The result of test is shown in Fig.4. As the result, pebble density increased with increasing sintering temperature. And, 5mol% TiO_2 doped Li_2TiO_3 pebbles increased their density at the lower sintering temperature than pebbles without doped TiO_2 . Contrary, 10mol% TiO_2 doped Li_2TiO_3 pebbles increased their density at the higher sintering temperature than pebbles without doped TiO_2 . And since Li_2TiO_3 pebbles have the target density in the range of 80 to 85%T.D. from a viewpoint of tritium breeder property, sintering temperature for the target density can be selected $1220 \pm 20^\circ\text{C}$ for Li_2TiO_3 pebbles, $1150 \pm 20^\circ\text{C}$ for 5mol% TiO_2 doped Li_2TiO_3 pebbles, and $1260 \pm 20^\circ\text{C}$ for 10mol% TiO_2 doped Li_2TiO_3 pebbles.

3.3. Characteristics of ^6Li enriched Li_2TiO_3 pebbles and TiO_2 doped Li_2TiO_3 pebbles

Characteristics of ^6Li enriched Li_2TiO_3 pebbles and ^6Li enriched TiO_2 doped Li_2TiO_3 pebbles is shown in table 2. ^6Li enrichment was 31at% as same as Li_2TiO_3 raw powder. Diameter as shown in Fig.5 and density of fabricated pebbles were well controlled within the target range by wet process with dehydration reaction. Average grain sizes of three kinds of pebbles calculated by Fig.6 were all less than $5\mu\text{m}$, and although doped TiO_2 intends to research the relationship between doped TiO_2 and grain size, it wasn't appeared clearly. As the results of X-ray diffractometry, the detected diffraction peaks of fabricated Li_2TiO_3 pebbles were corresponded with that of Li_2TiO_3 . At last, impurities in fabricated pebbles are shown in table 3. In these elements, sodium was detected a lot. A cause of result is thought that sodium in PVA remained in fabricated pebbles and the rate of PVA against Li_2TiO_3 was high.

4. Conclusion

The results of fabrication tests and characteristics of ^6Li enriched Li_2TiO_3 pebbles and ^6Li enriched TiO_2 doped Li_2TiO_3 pebbles were described as follows. The relationships between content of Li_2TiO_3 powder in mixture and pebble diameter and between sintering temperature and pebble density were obtained, and pebble diameter and pebble density was well controlled in target range by the wet process. Additionally, the average grain sizes of three kinds of ^6Li enriched Li_2TiO_3 pebbles were all less than $5\mu\text{m}$.

In the future, fabrication of ^6Li enriched Li_2TiO_3 pebbles with various enrichment will become possible. Further, fabrication of ^6Li enriched Li_2TiO_3 pebbles with not only 1mm but between 0.3 and 2mm in diameter will become possible.

References

- [1] K.Tsuchiya, H.Kawamura, K.Fuchinoue, H.Sawada and K.Watarumi, *J.Nucl.Mater.*, 258-263 (1998) 1985.
- [2] K.Tsuchiya and H.Kawamura, *J.Nucl.Mater.*, 283-287, (2000), 1380.
- [3] C.Alvani, S.Casadio, V.Contini, P.Bruno, E.Marmo and S.Lagos, Presented at 7th International Workshop on Ceramic Breeder Blanket Interactions, 1998, Petten, the Netherlands.
- [4] U.Fischer, S.Herring, A.Hogenbirk, D.Leichtle, Y.Nagao, B.J.Pijlgroms and A.Ying, Proceeding of the 8th International Workshop on Ceramic Breeder Blanket Interactions, 1999, Colorado Springs, USA.
- [5] K.Tsuchiya and H.Kawamura, *Fusion Technology*, vol.39, p.624-628, (2001)
- [6] K.Tsuchiya and H.Kawamura, Proceeding of 8th International Workshop on Ceramic Breeder Blanket Interactions, 1999, Colorado Springs, USA.

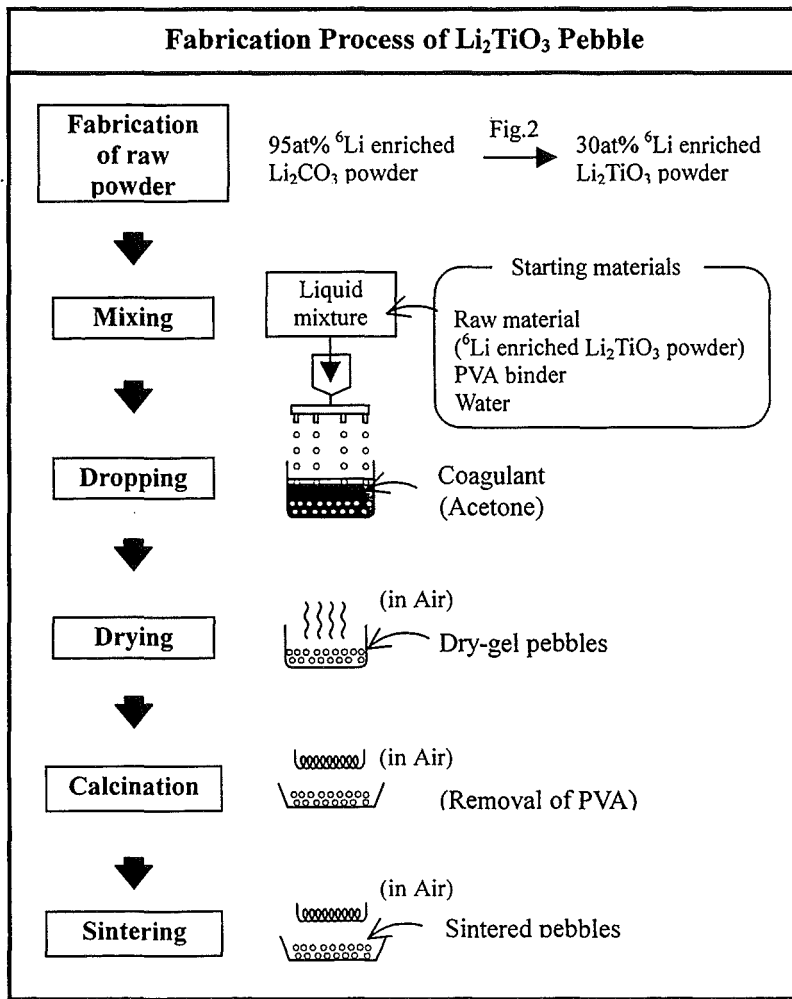


Fig.1 Flow chart of fabrication process of Li_2TiO_3 pebbles by the wet process.

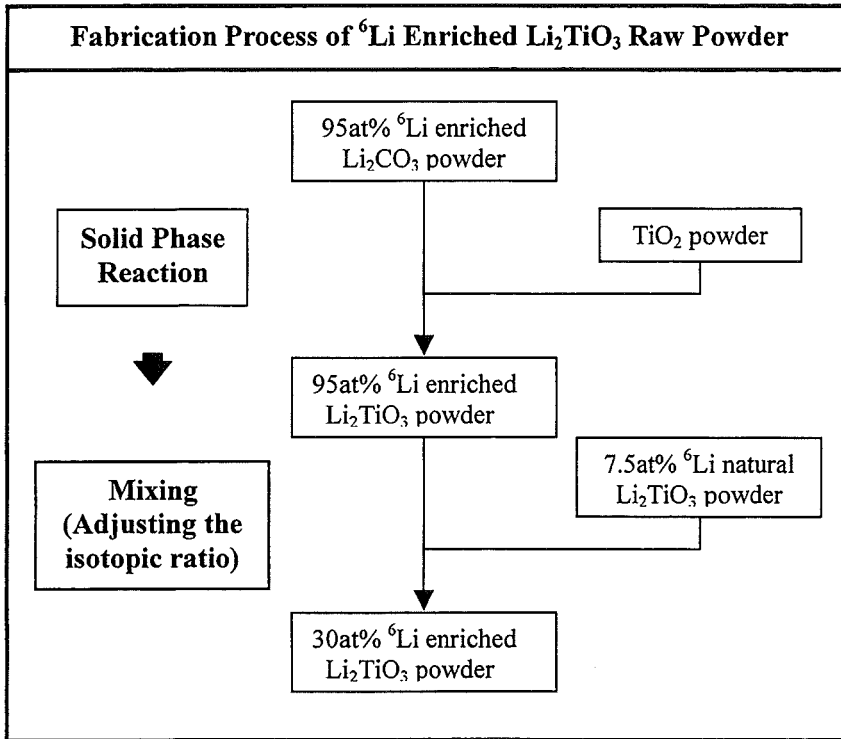


Fig.2 Flow chart of fabrication process of ${}^6\text{Li}$ enriched Li_2TiO_3 raw powder

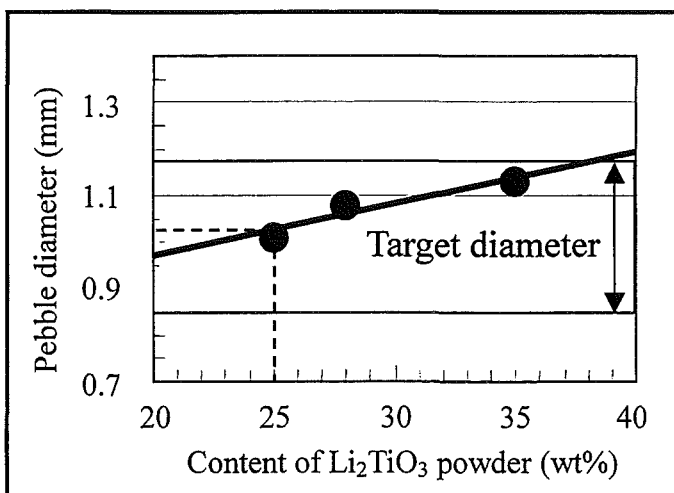


Fig.3 Relationship between content of Li_2TiO_3 powder in mixture and pebble diameter

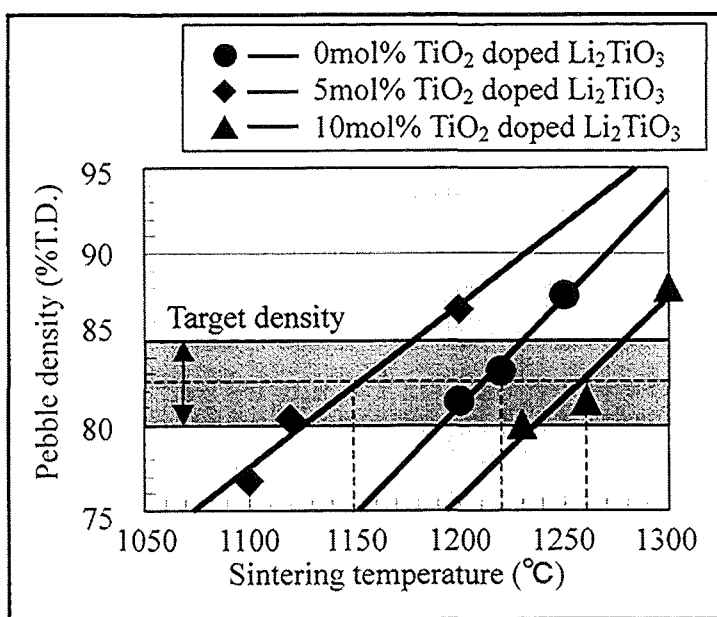


Fig.4 Relationship between sintering temperature and pebble density

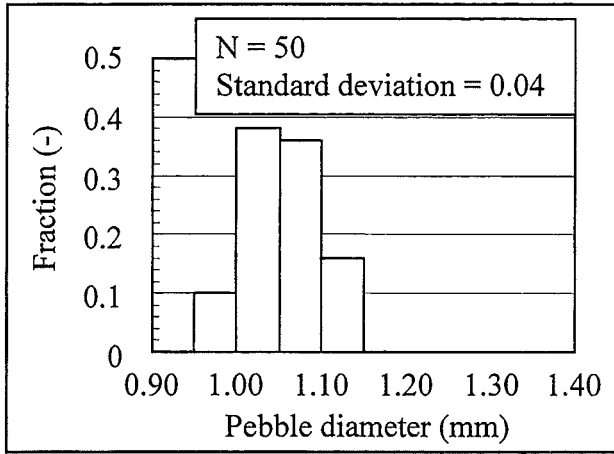


Fig.5 Distribution of pebble diameter of ${}^6\text{Li}$ enriched Li_2TiO_3 pebbles

Table 1 Characteristics of ^6Li enriched Li_2TiO_3 powder

Property	Value
^6Li enrichment	31 at%
Content of Li_2TiO_3	$\geq 99.97\%$
Particle size	Av. $0.43\ \mu\text{m}$

Table 2 Characteristics of ^6Li enriched Li_2TiO_3 pebbles and ^6Li enriched TiO_2 doped Li_2TiO_3 pebbles

Property	0mol% TiO_2 doped Li_2TiO_3 pebbles	5mol% TiO_2 doped Li_2TiO_3 pebbles	10mol% TiO_2 doped Li_2TiO_3 pebbles
^6Li enrichment	31 at%	31 at%	31 at%
Diameter	1.05 mm	1.06 mm	1.05 mm
Sphericity	1.08	1.06	1.08
Density	83.9 %T.D.	81.5 %T.D.	80.3 %T.D.
Fracture load	24 N	33 N	24 N
Grain size	$3.9\ \mu\text{m}$	$3.8\ \mu\text{m}$	$4.7\ \mu\text{m}$

Table 3 impurity in ^6Li enriched Li_2TiO_3 pebbles and ^6Li enriched TiO_2 doped Li_2TiO_3 pebbles

Element	0mol% TiO_2 doped Li_2TiO_3 pebbles	5mol% TiO_2 doped Li_2TiO_3 pebbles	10mol% TiO_2 doped Li_2TiO_3 pebbles
Ca	23	28	17
Na	610	460	550
K	< 5	< 5	< 5
Mg	< 5	< 5	< 5
B	< 5	< 5	< 5
Co	4.5	4.3	4.1
Al	26	24	25
Si	80	78	73
Zr	< 5	< 5	< 5
Fe	23	22	22
Mn	< 5	< 5	< 5